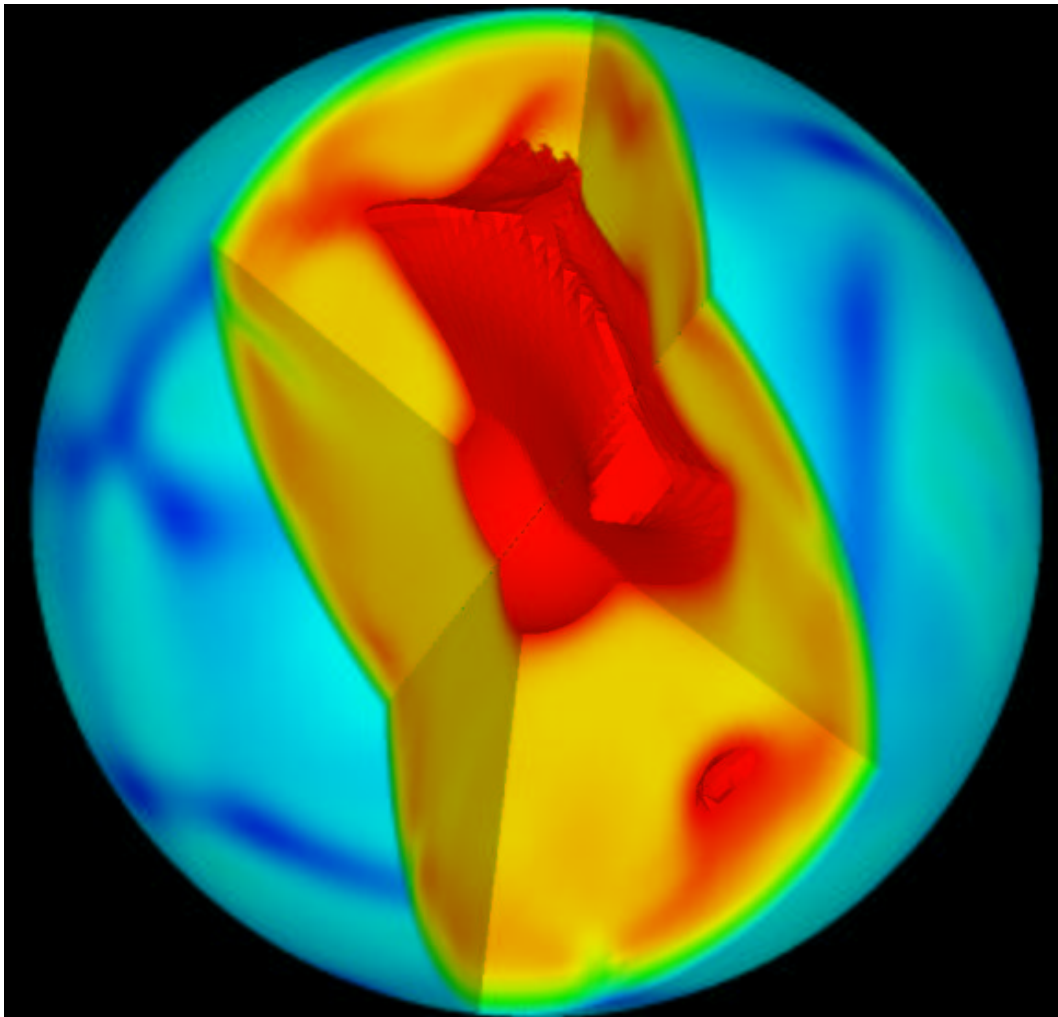


Berkeley Seismological Laboratory



Annual Report July 2002 - June 2003

Contents

- I Introduction 5**
- 1 Director’s Report 6**
 - 1. Background and Facilities 6
 - 2. Highlights of 2002-2003 7
 - 3. Acknowledgements 10
 - 4. Glossary of Common Acronyms 11

- II Operations 13**
- 2 California Integrated Seismic Network 14**
 - 1. Introduction 14
 - 2. CISN Background 14
 - 3. 2002-2003 Activities 15
 - 4. Acknowledgements 19
 - 5. References 19
- 3 Berkeley Digital Seismic Network 20**
 - 1. Introduction 20
 - 2. BDSN Overview 20
 - 3. 2002-2003 Activities 23
 - 4. Acknowledgements 29
 - 5. References 29
- 4 Northern Hayward Fault Network 31**
 - 1. Introduction 31
 - 2. NHFN Overview 31
 - 3. 2002-2003 Activities 33
 - 4. Acknowledgements 38
 - 5. References 38
- 5 Parkfield Borehole Network 40**
 - 1. Introduction 40
 - 2. HRSN Overview 40
 - 3. 2002-2003 Activities 42
 - 4. Acknowledgements 49
 - 5. References 49
- 6 Parkfield-Hollister Electromagnetic Monitoring Array 51**
 - 1. Introduction 51
 - 2. MT Overview 51
 - 3. 2002-2003 Activities 51
 - 4. Data Processing 52
 - 5. Acknowledgements 53

6.	References	54
7	Bay Area Regional Deformation Network	56
1.	Introduction	56
2.	2002-2003 Activities	59
3.	Data Analysis and Results	62
4.	Real-Time Processing	64
5.	Acknowledgements	64
6.	References	64
8	Plate Boundary Deformation Project	65
1.	Introduction	65
2.	New Site Installations	65
3.	Broadband Deformation Data	69
4.	Acknowledgements	70
9	Data Acquisition and Quality Control	72
1.	Introduction	72
2.	McCone Hall Facilities	72
3.	Data Acquisition	73
4.	Seismic Noise Analysis	75
5.	Sensor Testing Facility	75
6.	Sensor Testing in 2002-2003	76
7.	UrEDAS Project	78
8.	Acknowledgements	80
9.	References	80
10	Northern California Earthquake Monitoring	81
1.	Introduction	81
2.	Northern California Management Center	81
3.	2002-2003 Activities	82
4.	Routine Earthquake Analysis	85
5.	Acknowledgements	88
6.	References	89
11	Northern California Earthquake Data Center	90
1.	Introduction	90
2.	NCEDC Overview	90
3.	2002-2003 Activities	90
4.	Data Collections	91
5.	Data Quality Control	96
6.	Database Development	97
7.	Data Access & Distribution	97
8.	Acknowledgements	99
12	Outreach and Educational Activities	100
1.	Introduction	100
2.	Outreach Overview	100
3.	2002-2003 Activities	101
4.	Acknowledgements	102
III	Ongoing Research Projects	103
13	Finite Source Modeling of Great Earthquakes	104

14 Accuracy of the Hypocenter Location and Fault Plane Orientation for Near Realtime Finite Fault Inversion	109
15 Historical Earthquake Re-analysis Project	112
16 Northern California Seismicity Project	115
17 Parkfield Research	118
18 The Evolution of the Seismic-Aseismic Transition during the Earthquake Cycle: Constraints from the Time-Dependent Depth Distribution of Aftershocks	121
19 Detection of Seismic Stress-Drop Anomalies in the Mendocino Transform Using Coda-Derived Spectra	124
20 Long-Period Microtremor Observations in the Santa Clara Valley, California	127
21 Fluid Influenced Faulting in the Long Valley Volcanic Region	129
22 Source Mechanisms of Volcanic Induced Seismicity – Miyakejima, Japan, 2000	132
23 Identifying and Removing Noise from the Ocean Bottom Broadband Seismic Data	136
24 Detection of Long Period Surface Wave Energy	139
25 Automated Moment Tensor Software for Monitoring the Comprehensive Test Ban Treaty	142
26 The Bay Area Velocity Unification (BĀVŪ); Bringing Together Crustal Deformation Observations from throughout the San Francisco Bay Area	144
27 Crustal Deformation Along the Northern San Andreas Fault System	147
28 Surface Creep Measurements from a Slow Earthquake on the San Andreas Fault Using InSAR	150
29 Evidence of Powerlaw Flow in the Mojave Mantle	153
30 Intraplate Strain Accumulation in the New Madrid Seismic Zone	156
31 The Adriatic Region: An Independent Microplate within the Africa-Eurasia Collision Zone	159
32 Global Waveform Tomography with Spectral Element Method	161
33 Global Anisotropy and the Thickness of Continents	164
34 Large Scale Anisotropy Near the Core-Mantle Boundary from Global Waveform Inversion	168
35 Towards Forward Modeling of 3D Heterogeneity in D” region	170
36 Constraints on Density and Shear Velocity Contrasts at Inner Core Boundary	174
37 Investigating Mantle’s Density Resolution Using the Neighborhood Algorithm	177
38 Thermochemical Convection Models of Lunar Evolution	181

Part I

Introduction

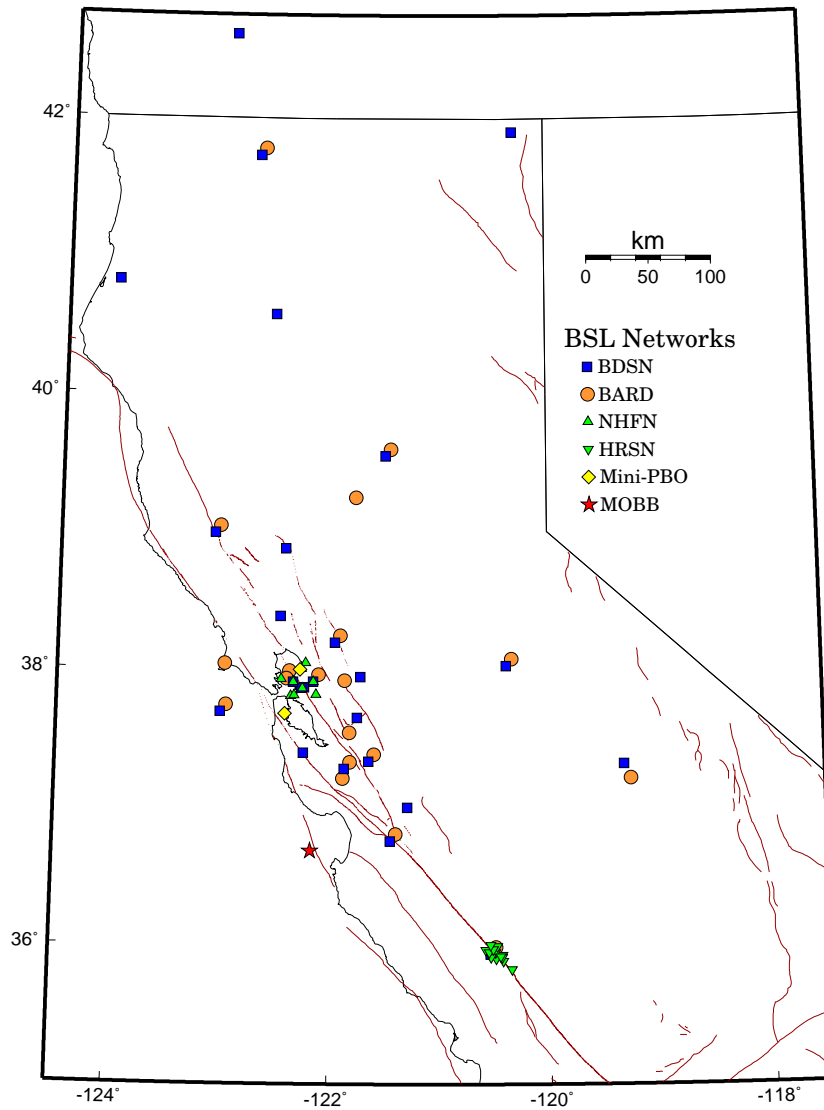


Figure 1: Map illustrating the distribution of stations in the BDSN, NHFN, HRSN, BARD, and Mini-PBO networks in northern and central California. A star indicates the location of the MOBB deployment.

Chapter 1

Director's Report

1. Background and Facilities

The Berkeley Seismological Laboratory (BSL), formerly the Berkeley Seismographic Station (BSS), is the oldest Organized Research Unit (ORU) on the U. C. Berkeley campus. Its mission is unique in that, in addition to research and education in seismology and earthquake-related science, it is responsible for providing timely information on earthquakes (particularly those that occur in northern and central California) to the UC Berkeley constituency, the general public, and various local and state government and private organizations. The BSL is therefore both a research center and a facility/data resource, which sets it apart from most other ORUs. A major component of our activities is focused on developing and maintaining several regional observational networks, and participating, along with other agencies, in various aspects of the collection, analysis, archival and distribution of data pertaining to earthquakes, while maintaining a vigorous research program on earthquake processes and Earth structure. In addition, the BSL staff spends considerable time with public relations activities, including tours, talks to public groups, responding to public enquiries about earthquakes and, more recently, World-Wide-Web presence (<http://www.seismo.berkeley.edu/seismo/>).

U.C. Berkeley installed the first seismograph in the Western Hemisphere at Mount Hamilton (MHC) in 1887. Since then, it has played a leading role in the operation of state-of-the-art seismic instruments and in the development of advanced methods for seismic data analysis and interpretation. Notably, the installation, starting in 1927, of Wood-Anderson seismographs at 4 locations in northern California (BKS, ARC, MIN and MHC) allowed the accurate determination of local earthquake magnitude (M_L) from which a unique historical catalog of regional earthquakes has been maintained to this day, providing crucial input to earthquake probabilities studies.

Over the years, the BSS continued to keep apace of technological improvements. The first centrally telemetered network using phone lines in an active seismic region was installed by BSS in 1960. The BSS was the

first institution in California to operate a 3-component "broadband" system (1963). Notably, the BSS played a major role in the early characterization of earthquake sources using "moment tensors" and source-time functions, and made important contributions to the early definitions of detection/discrimination of underground nuclear tests and to earthquake hazards work, jointly with UCB Engineering. Starting in 1986, the BSS acquired 4 state-of-the-art broadband instruments (STS-1), while simultaneously developing PC-based digital telemetry, albeit with limited resources. As the telecommunication and computer technology made rapid progress, in parallel with broadband instrument development, paper record reading could be completely abandoned in favor of largely automated digital data analysis.

The current modern facilities of BSL have been progressively built over the last 13 years, initiated by significant "upgrade" funding from U.C. Berkeley in 1991-1995. The BSL currently operates and acquires data, continuously and in real-time, from over 60 regional observatories, housing a combination of broadband and strong motion seismic instrumentation installed in vaults, borehole seismic instrumentation, permanent GPS stations of the BARD network, and electromagnetic instrumentation. The seismic data are fed into the BSL real-time processing and analysis system and are used in conjunction with data from the USGS NCSN network in the joint earthquake notification program for northern California, started in 1996. This program capitalizes on the complementary capabilities of the networks operated by each institution to provide rapid and reliable information on the location, size and other relevant source parameters of regional earthquakes. In recent years, a major emphasis in BSL instrumentation has been in densifying the state-of-the-art seismic and geodetic networks, while a major on-going emphasis in research has been the development of robust methods for quasi-real time automatic determination of earthquake source parameters and predicted strong ground motion, using a sparse network combining broadband and strong motion seismic sensors, as well as permanent geodetic GPS receivers.

The backbone of the BSL operations is a regional net-

work of 25+ digital broadband and strong motion seismic stations, the Berkeley Digital Seismic Network (BDSN), with continuous telemetry to UC Berkeley. This network provides the basic regional data for the real-time estimation of location, size and rupture parameters for earthquakes of M 3 and larger in central and northern California, within our Rapid Earthquake Data Integration (REDI) program and is the Berkeley contribution to the California Integrated Seismic Network (CISN). It also provides a fundamental database for the investigation of three-dimensional crustal structure and its effects on regional seismic wave propagation, ultimately crucial for estimating ground shaking for future earthquakes. Most stations also record auxiliary temperature/pressure channels, valuable in particular for background noise quality control. Complementing this network is a 25 station "high-resolution" network of borehole seismic sensors located along the Hayward Fault (HFN) and under the Bay Area bridges, operated jointly with the USGS/Menlo Park and linked to the Bridge Safety Project of the California Department of Transportation (Caltrans). The latter has facilitated the installation of sensor packages at 15 bedrock boreholes along 5 east-bay bridges in collaboration with LLNL. A major science goal of this network is to collect high signal-to-noise data for micro-earthquakes along the Hayward Fault to gain insight into the physics that govern fault rupture and its nucleation. The BSL is also involved in the operation and maintenance of the 13 element Parkfield borehole seismic array (HRSN), which is yielding enlightening results on quasi-periodic behavior of micro-earthquake clusters and important new constraints on earthquake scaling laws and is currently playing an important role in the characterization of the site for the future San Andreas Fault Observatory at Depth (SAFOD). Since April 2002, the BSL is also involved in the operation of a permanent broadband ocean bottom station, MOBB, in collaboration with MBARI (Monterey Bay Aquarium Research Institute).

In addition to the seismic networks, the BSL is involved in data archival and distribution for the permanent geodetic BARD (Bay Area Regional Deformation) Network as well as the operation and maintenance, and data processing of 22 out of its 70+ sites. Whenever possible, BARD sites are collocated with BDSN sites in order to minimize telemetry costs. In particular, the development of analysis methods combining the seismic and geodetic data for the rapid estimation of source parameters of significant earthquakes has been one focus of BSL research.

Finally, two of the BDSN stations (PKD, SAO) also share data acquisition and telemetry with 5-component electromagnetic sensors installed with the goal of investigating the possibility of detection of tectonic signals.

Archival and distribution of data from these and other regional networks is performed at the Northern Cali-

fornia Earthquake Data Center (NCEDC), operated at the BSL in collaboration with USGS/Menlo Park. The data reside on a mass-storage device (2.5+ Terabyte capacity), and are accessible "on-line" over the Internet (<http://www.quake.geo.berkeley.edu>). Among others, data from the USGS Northern California Seismic Network (NCSN), are archived and distributed through the NCEDC. The NCEDC also maintains, archives and distributes the ANSS/CNSS earthquake catalog.

Core University funding to our ORU has suffered from permanent budget cuts to research programs from the State of California, and currently provides salary support for 2 field engineers, one computer expert, 2 data analysts, 1 staff scientist and 2 administrative staff. This supports a diminishing portion of the operations of the BDSN and provides seed funding for our other activities. All other programs are supported through extramural grants primarily from the USGS and NSF, and in the past two years, the Governor's Office of Emergency Services (OES). We acknowledge valuable recent contributions from other sources such as Caltrans, the CLC program, PEER, as well as our Earthquake Research Affiliates.

2. Highlights of 2002-2003

2.1 Infrastructure and Earthquake Notification

In 2002-2003, the BSL has continued its involvement in several major projects, including the CISN, and the installation and operation of *Mini-PBO* instrumentation. We have also taken initial steps in preparation of our involvement in the deployment in California of the *BigFoot* component of USArray/Earthscope.

We are entering the 3rd year of our participation in the efforts of the CISN, for which we received support in 2002-2003 from the State of California through the Office of Emergency Services (OES) (Chapter 2).

The main goal of the CISN is to ensure a more uniform system for earthquake monitoring and reporting in California. The highest priority, from the point of view of emergency responders in California, is to improve the robustness of statewide real-time notification and to achieve a uniform interface across the State to the California OES and other emergency responders. This represents a major challenge, as the CISN started as a heterogeneous collection of networks with disparate instrumentation, software systems and culture. Therefore, in the past year, the emphasis has been on software development for seamless data exchange between institutions, the establishment of redundant links to data sources, as well as the construction of a single interface to access the different products, such as earthquake locations, magnitudes and, most importantly "ShakeMaps".

Another goal of the CISN program is to improve the

seismic infrastructure in northern California. Because funding is limited, this goal is currently pursued at a slower pace. Nevertheless, two new broadband/strong motion stations have been installed in 2002-2003, and three additional sites have been selected and permitted. They are currently at different stages of completion. The CISN has held its first Northern California outreach workshop on "ShakeMaps" in January 2003, with BSL participation, and has been actively engaged in working with its Advisory Committee towards meeting the needs of the users, among which Caltrans as well as utilities companies.

BSL staff spend considerable efforts in organizational activities for CISN, notably by participating in the CISN Project Management Group (Gee), which includes weekly 2 hour phone conferences, and the Standards Committee (Neuhauser-chair, Gee, Lombard), which strives to define and coordinate software development tasks. Romanowicz and Gee serve on the CISN Steering Committee, which was chaired by Romanowicz in 2001. The CISN also represents California as a designated region of ANSS (Advanced National Seismic System) and the BSL is actively involved in planning activities for the ANSS.

This past year has seen progress in the installation efforts of the *Mini-PBO* project (Chapter 8), a project supported partly by a grant from the NSF/MRI program, in collaboration with CIW, UCSD and USGS/Menlo Park, with matching from participating institutions (including UCB) as well as Caltrans (http://www.seismo.berkeley.edu/seismo/bdsn/mpbo_overview.html). This project's focus is the installation of a network of multi-parameter stations in the San Francisco Bay Area to monitor the evolution of tectonic strain in time and space - a pilot project for the Plate Boundary Observatory (PBO) component of Earthscope (a national infrastructure program funded by NSF within its Major Research Equipment program). *Mini-PBO* instrumentation comprises 3 component borehole strainmeters and seismometers, GPS receivers and auxiliary sensors (such as pore pressure, temperature, and tilt). The data are telemetered to UC Berkeley and distributed through the NCEDC. Five holes have now been drilled and instrumented with considerable involvement of BSL staff (Murray, Basset, W. Johnson, Karavas, Friday, Rapkin, Thomas). The initial goal of 10 stations has been reduced to 6 due to budgetary constraints and delays related to considerable difficulties and cost-overruns in drilling. We are still hoping that the 6th and last hole will be drilled with Caltrans's help, as a "hole of opportunity", in 03-04. Meanwhile, all existing 5 stations now have borehole strainmeters and seismometers, as well as tiltmeters. Two sites are completed, while the remaining three are in the final stages of the installation of GPS receivers, Quanterra data loggers and/or

power and communications systems.

The MOBB (Monterey Ocean bottom Broad Band observatory) is a collaborative project between the BSL and MBARI and builds upon the experience gained in 1997 through the MOISE project, which involved the temporary deployment of a broadband ocean bottom system in Monterey Bay. MOBB is now a permanent installation and comprises a broadband seismic package (Guralp CMG-1), a battery and recording package, as well as auxiliary sensors: a current-meter and a DPG (differential Pressure Gauge). The system was assembled and tested at BSL in early 2002, and successfully deployed in April 2002 (Chapter 3). In particular, extensive testing and seismometer insulation procedures, which were developed at Byerly Vault on the UCB campus prior to MOBB deployment (Chapter 9) have now been applied to three similar systems destined for the KECK project (Juan de Fuca plate), in collaboration with University of Washington at Seattle. There have been 4 dives in 2002-2003 to recover and exchange battery packages and recording systems from the seafloor. Software problems have unfortunately led to the loss of much data during the first part of 2003. We will know after the next dive, scheduled for 09/15/03, whether these problems have definitely been fixed.

In the past year, the BSL has continued to be involved in the coordination of site characterization for the SAFOD drilling project (another component of Earthscope) in the Parkfield area (Chapter 5). A new central data acquisition system with near real time transmission to Berkeley of event data and waveform samples allows routine checks of quality of operation, and more timely response to failures and sources of noise. The resulting dataset is of primary importance for monitoring the evolution of microseismicity, particularly in the SAFOD drilling zone, where the new triggering scheme allows detection of events down to magnitude -1.0, a three-fold higher detection rate compared to the local surface seismic network, in a 30 km stretch around the M6 earthquake of 1966.

Other accomplishments in the past year include the completion of a new BDSN station (HUMO - Chapter 3) in southern Oregon, in collaboration with USGS/NSN and IRIS programs, and, as mentioned previously in the framework of CISN, the installation of two new broadband stations.

The NHFN network project has seen the upgrade of infrastructure at 7 stations on the Bay Bridge (Chapter 4), in anticipation of the deployment of the Quanterra recording systems and associated telemetry to UC Berkeley. Stations BBEB and W02B are now online, and the remaining five sites will be brought up this fall. In parallel, we have been working on improvement of data processing techniques. The datastreams from the borehole seismometers of the *Mini-PBO* project are progressively

being integrated with those of the NHFN (Chapter 8).

On the NCEDC front (Chapter 11), we continue archiving and distribution on-line of data from expanding BDSN, NHFN, HRSN, BARD, Mini-PBO, and other networks and data collections in northern California and Nevada. There has been progress in the construction of the "metadata" for the NCSN and a major "revamping" of the NCEDC Webpage. The NCEDC is participating in the UNAVCO-sponsored GPS Seamless Archive Centers (GSAC) initiative, which is developing common protocols and interfaces for the exchange and distribution of continuous and survey-mode GPS data, and is now both a primary provider for BARD/BSL data, a wholesale collection point for other northern California GPS data, and a retail center for all GSAC data.

The BSL continues to collaborate with the USGS/Menlo Park in the generation of ShakeMap for northern California and has been developing and implementing successive upgrades to this system, integrated within the REDI environment (Chapter 10). ShakeMap is calculated routinely for magnitude 3.5 and larger events in northern California. Any magnitude 5.0 or larger will now also trigger the finite-fault processing. In 2002-2003, a 2nd ShakeMap system has been installed at UC Berkeley, to provide redundancy for northern California earthquakes. Also in the past year, we have implemented a database within the real-time system and have been involved in redesigning the Northern California operations, to achieve a single system at USGS/Menlo Park and UCB.

Finally, we have been routinely monitoring electric and magnetic field at two of our observatories since 1995. In 2002-2003, efforts in this direction have been stepped up: an automated quality control software has been implemented and a time domain processing software is currently being developed and perfected (Chapter 6).

In 03-04, a major new component of our activities will be coordinating with IRIS on the deployment in northern California of 50 temporary broadband stations of the BigFoot array of Earthscope. The BSL will contribute many (15+) of its existing sites to this effort. Likewise, we anticipate helping out with some aspects of the Plate Boundary Observatory component of Earthscope. In particular, we have received funding from NSF for the support of routine operations of the BARD GPS network for the next 1.5 years, as part of a collaborative proposal coordinated by UNAVCO Inc. We will be actively engaged in the next year in planning the integration of existing permanent GPS networks into the PBO.

2.2 Research Accomplishments

Chapter III documents the main research contributions of the past year. Research at the BSL spans a broad range of topics, from the study of microseismicity at the local scale to global deep earth structure, and includes

seismological, geodetic and remote sensing (InSAR) techniques.

In the general area of earthquake source studies, a major earthquake (M 7.9) occurred in Alaska on the Denali Fault on 11/03/2002. This has been an opportunity for Professor Dreger and collaborators to combine his broadband waveform source tomography approach with GPS and surface displacement observations to study the complex fault geometry of this unusual event, documenting in particular evidence for discontinuous rupture propagations (III.1). Professor Dreger and graduate students Wucheng Chi (III.2), Dennise Templeton (III.9) and Gilead Wurman (III.7), as well as undergraduate student Sarah Minson (III.10) have pursued the study of various earthquake source problems in California, Taiwan, and Japan, in particular with a continued interest in the characterization of earthquakes related to fluid migrations in volcanic areas. Graduate student David Dolenc is using microtremors to illuminate basin structure in the San Francisco Bay Area to anticipate ground motions in large earthquakes (III.8), while Dr. Robert Uhrhammer has continued his efforts to characterize historical seismicity in the San Francisco Bay Area (III.3) as well as Northern California (III.4). Dr. Robert Nadeau continues to discover and analyze new sequences of micro-earthquakes at Parkfield (III.5) in an effort to better understand how the fault works. In particular, he has documented evidence for periodic pulsing along the central San Andreas Fault between Parkfield and the southern end of the Loma Prieta earthquakes. In collaboration with Dr. Nadeau and Professor Bürgmann, post-doctoral associate Frédérique Rolandone has been studying the time variations of the maximum depth of seismicity around major earthquakes during the earthquake cycle (III.6). With graduate student David Dolenc, we have started to analyze the background noise at the ocean bottom MOBB site with the goal of a-posteriori noise reduction using correlations with current, pressure and other auxiliary data (III.11). Dr. Peggy Hellweg has completed the installation and testing of our automated moment tensor inversion codes at the Center for Monitoring Research, in the framework of efforts to monitor the CTBT (III.13). With graduate student Junkee Rhie, we are perfecting a very low frequency event detection method, with the ultimate goal of trying to characterize sources of the continuous background excitation of earth's free oscillations (III.12).

The BSL has also been actively involved in studying active deformation using various geodetic techniques. Working with Professor Roland Bürgmann, graduate students Matt d'Alessio and Ingrid Johanson have been analyzing campaign GPS data and InSAR to monitor fault slip and strain accumulation in the San Francisco Bay region, characterizing creep events and delineating rigidly behaving crustal blocks (III.14,III.16). Studies of strain

accumulation and distribution have also been pursued by Dr. Mark Murray in northern California (III.15) and the New Madrid Seismic Zone (III.18), while post-doctoral associate Maurizio Battaglia documented the existence of a microplate in the Adriatic region (III.19). Finally, Dr. Andy Freed used GPS data to characterize the nature of viscous flow associated with the coupled 1992 Landers and 1999 Hector Mine earthquakes (III.17).

With graduate students Yuancheng Gung, Mark Panning, Akiko To, Sébastien Rousset and post-doctoral Miller fellow Yann Capdeville, Professor Romanowicz has been pursuing various aspects of wave propagation in the 3D spherical earth, adapting the coupled Spectral Element/normal mode method to study complex structure at the base of the mantle (III.20, III.23), experimenting with a neighborhood algorithm to explore the range of possible large scale variations in density in the mantle using normal mode observations (III.25) and implementing anisotropic parameterization in global mantle tomography (III.21, III.22). With graduate student Aimin Cao, Romanowicz has pursued the study of core structure, revisiting this past Spring the issue of the density jump at the Inner Core Boundary (III.24). Also included in this report is a contribution from graduate student David Stegman, working with Professor Mark Richards on a model of convection of the moon (III.26) featured this year on the cover of our Annual Report.

We are proud to note that Yuancheng Gung, Wuchen Chi and David Stegman successfully completed their Ph.D.'s in the summer of 2003, and will pursue post-doctoral appointments at BSL, Caltech and Canberra, Australia, respectively. Last but not least, post-doctoral fellow Andy Freed left last Fall to take a faculty position at Purdue University, while Miller Fellow Yann Capdeville went back to Paris, France at the end of August to join the research staff at the CNRS.

3. Acknowledgements

I wish to thank our technical and administrative staff, scientists and students for their efforts throughout the year and their contributions to this annual report. Individual contributions to activities and report preparation are mentioned in the corresponding sections, except for the Appendix section, prepared by Christina Jordan and Eleanor Blair.

Starting July 1st, 2002, Professor Douglas Dreger has been appointed Associate Director of the BSL. In particular, Doug has assumed overall responsibility, with help from Bob Nadeau, for the HRSN and NHFN programs, following Professor McEvelly's death.

I also wish to specially thank the individuals who have regularly contributed to the smooth operation of the BSL facilities: André Basset, Sierra Boyd, Rich Clymer, Doug Dreger, John Friday, Lind Gee, Wade Johnson, Bill Kar-

avas, Pete Lombard, Rick McKenzie, Mark Murray, Bob Nadeau, Doug Neuhauser, Charley Paffenbarger, David Rapkin, Cathy Thomas, Bob Uhrhammer, and Stephane Zuzlewski. To our regret, Cathy Thomas went back home to the East Coast in March 2003.

In 2002-2003, there have been some changes in the BSL administrative office. Eleanor Blair, and Christina Jordan continue to provide critical support to the administration of our lab, but Heather Reed left in 11/2002. We welcome Myriam Cotton, who joined the administrative office in 11/2002, helping with accounting. They are assisted by part-time student employees Morgan Weibel, Patty Villa and Loan Pham.

I also wish to thank our undergraduate assistants Tom Fournier, Alex Goines, Lisa Krain, Edwin Kwan, Sarah Minson, and Gabriel Treves, for their contributions to our research and operational activities. Lisa left in December 2002 to follow her newly acquired husband and pursue graduate studies in southern California, and Sarah left in August 2003, to become a graduate student in Geophysics at Caltech.

As every year, I am particularly thankful to Lind Gee and Christina Jordan for their help in putting together this Annual Report.

The Annual Report of the Berkeley Seismological Laboratory is available on the WWW at http://www.seismo.berkeley.edu/seismo/annual_report/.

Barbara Romanowicz
Sept 15, 2003

4. Glossary of Common Acronyms

Table 1.1: Standard abbreviations used in this report.

Acronym	Definition
AGU	American Geophysical Union
ANSS	Advanced National Seismic System
BARD	Bay Area Regional Deformation
BDSN	Berkeley Digital Seismic Network
BSL	Berkeley Seismological Laboratory
BSS	Berkeley Seismographic Station
CISN	California Integrated Seismic Network
CGS	California Geological Survey
CLC	Campus Laboratory Collaboration
CNSS	Council of the National Seismic System
EM	Electromagnetic
EPRI	Electric Power Research Institute
FBA	Force Balance Accelerometer
FIR	Finite Impulse Response
FRAD	Frame Relay Access Device
GPS	Global Positioning System
HFN	Hayward Fault Network
HRSN	High Resolution Seismic Network
IGS	International Geodetic Service
IMS	International Monitoring System
InSAR	Interferometric Synthetic Aperture Radar
IRIS	Incorporated Research Institutions for Seismology
ISC	International Seismological Center
ISTAT	Integrating Science, Teaching, and Technology
JPL	Jet Propulsion Laboratory
LBNL	Lawrence Berkeley National Laboratory
LLNL	Lawrence Livermore National Laboratory
MBARI	Monterey Bay Aquarium Research Institute
MHH	Murdoch, Hutt, and Halbert
MOBB	Monterey Ocean Bottom Broadband observatory
MOISE	Monterey Bay Ocean Bottom International Seismic Experiment
MPBO	Mini-Plate Boundary Observatory
MRI	Major Research Initiative
MRE	Major Research Equipment
MT	Magnetotelluric
NCEDC	Northern California Earthquake Data Center
NCSN	Northern California Seismic Network
NEHRP	National Earthquake Hazards Reduction Program
NEIC	National Earthquake Information Center
NHFN	Northern Hayward Fault Network
NGS	National Geodetic Survey
NSF	National Science Foundation
NSN	National Seismic Network
OES	Office of Emergency Services
ORU	Organized Research Unit
PBO	Plate Boundary Observatory
PEER	Pacific Earthquake Engineering Center
PH	Pilot Hole
PPE	Parkfield Prediction Experiment

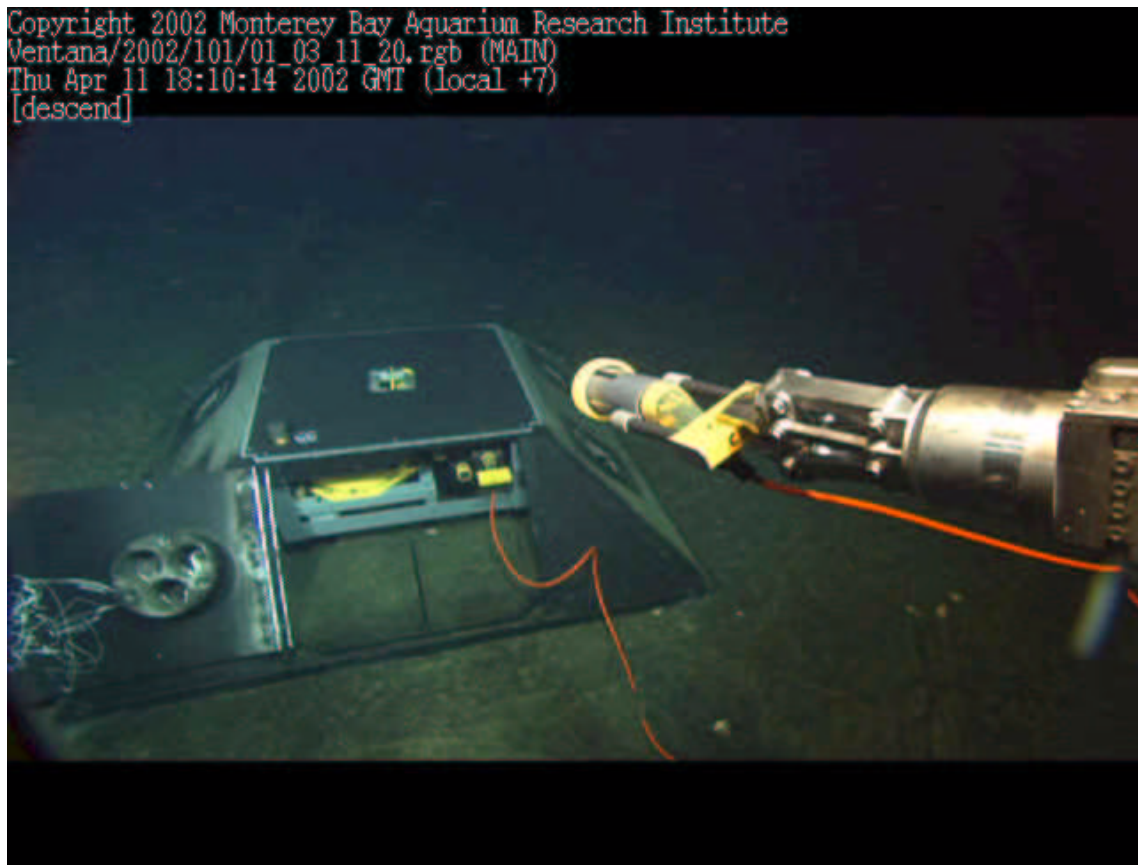
continued on next page

Table 1.1: *continued*

Acronym	Definition
PREM	Preliminary Reference Earth Model
PSD	Power Spectral Density
REDI	Rapid Earthquake Data Integration
SAF	San Andreas Fault
SAFOD	San Andreas Fault Observatory at Depth
SAR	Synthetic Aperture Radar
SCEC	Southern California Earthquake Center
SCEDC	Southern California Earthquake Data Center
SCIGN	Southern California Integrated GPS Network
SEED	Standard for the Exchange of Earthquake Data
SEM	Spectral Element Method
SHFN	Southern Hayward Fault Network
SIO	Scripps Institutions of Oceanography
SNCL	Station Network Channel Location
SSA	Seismological Society of America
STP	Seismogram Transfer Program
UCB	University of California at Berkeley
UNAVCO	University NAVSTAR Consortium
UrEDAS	Urgent Earthquake Detection and Alarm System
USGS	United States Geological Survey

Part II

Operations



Chapter 2

California Integrated Seismic Network

1. Introduction

Advances in technology have made it possible to integrate separate earthquake monitoring networks into a single seismic system as well as to unify earthquake monitoring instrumentation. In California, this effort was initiated under the TriNet Project in southern California, where Caltech, the then California Division of Mines and Geology, and the USGS combined their efforts to create a unified seismic system for southern California. With major funding provided by FEMA, OES, and the USGS, the TriNet project provided the opportunity to upgrade and expand the monitoring infrastructure, combining resources in federal, state, university partnership. More recently, the California Geological Survey, Caltech Seismological Laboratory, Berkeley Seismological Laboratory, USGS Menlo Park, and the USGS Pasadena have agreed to cooperate on a statewide basis, because of the obvious benefit to the state.

In the 2000-2001 Annual Report, we described the efforts to create this collaboration through the establishment of a memorandum of agreement and the development of the CISN strategic and implementation plans. Last year, we reported on the first steps toward establishing a statewide system with funding provided by the OES. This year we continued our efforts to move forward with the CISN.

2. CISN Background

2.1 Organization

The core CISN institutions (California Geological Survey, Berkeley Seismological Laboratory, Caltech, USGS Menlo Park, USGS Pasadena) and OES have signed a MOA (included in the 2000-2001 Annual Report) that describes the CISN organizational goals, products, management, and responsibilities of member organizations. To facilitate coordination of activities among institutions, the CISN has formed three management centers:

- Southern California Management Center: Caltech/USGS Pasadena

- Northern California Management Center: UC Berkeley/USGS Menlo Park
- Engineering Management Center: California Geological Survey/USGS National Strong Motion Program

A goal of the CISN is for the Northern and Southern California Management Centers to operate as twin earthquake processing centers. The Engineering Management Center has the lead responsibility for producing engineering data products.

The Steering Committee oversees CISN projects and is comprised of two representatives from each core institution and a representative from OES. The position of chair rotates among the institutions; Barbara Romanowicz served as the first chair of the Steering Committee; the position has rotated to the California Geological Survey and Jim Davis served as chair from January 2003 until his retirement in the end of June. Mike Riechle is the new chair of the Steering Committee.

An external Advisory Committee, representing the interests of structural engineers, seismologists, emergency managers, industry, government, and utilities, has been formed for review and oversight. The Advisory Committee is chaired by Bruce Clark of the California Seismic Safety Commission. The Advisory Committee held its first meeting in July 2001 and met most recently in January of 2003.

The Steering Committee has formed other committees, including a Program Management Group to address planning and coordination, a Strong Motion Working Group to focus on issues related to strong-motion data, and a Standards Committee to resolve technical design and implementation issues.

In addition to the core members, several organizations contribute data that enhances the capabilities of the CISN. Contributing members of the CISN include: University of California, Santa Barbara; University of California, San Diego; University of Nevada, Reno; University of Washington; California Department of Water Resources; Lawrence Livermore National Lab; and Pacific Gas and Electric.

2.2 CISN and ANSS

The USGS Advanced National Seismic System (ANSS) is being developed along a regionalized model. 8 regions have been organized and the CISN represents the "California region". Over the last 4 years, ANSS funding in California has primarily been directed to the USGS Menlo Park to expand the strong-motion instrumentation in the San Francisco Bay Area. As a result, instruments at over 100 sites have been installed or upgraded, significantly improving the data available for ShakeMaps.

The CISN is currently developing plans for the FY03/04 ANSS program. As the ANSS moves forward, committees and working groups are being established to address issues of interest. Currently, Lind Gee and David Oppenheimer represent the CISN on an ANSS working group for business rules for earthquake reporting (developing figures of merit for selecting the "best" location, magnitude, and other earthquake products when multiple solutions are available).

2.3 CISN and OES

The California Governor's Office of Emergency Services has had a long-term interest in coordinated earthquake monitoring. The historical separation between northern and southern California and between strong-motion and weak-motion networks resulted in a complicated situation for earthquake response.

OES has been an advocate of increased coordination and collaboration in California earthquake monitoring and encouraged the development of the CISN Strategic and Implementation Plans. In FY01/02, Governor Gray Davis requested support for the CISN, to be administered through OES. Funding for the California Geological Survey, Caltech and UC Berkeley was made available in spring 2002, officially launching the statewide coordination efforts.

Despite the dire budget situation in the state of California in FY02/03, OES support led to the establishment of 3-year contracts to the BSL, Caltech, and the California Geological Survey for CISN activities. Although at a reduced level of support from the previous year, these funds are critical to continued efforts in statewide integration.

3. 2002-2003 Activities

The CISN funding from OES facilitated a number of activities at the BSL during the past year.

3.1 Expanded Instrumentation

In 2001-2002, the BSL purchased equipment for 5 BDSN stations, including STS-2 seismometers, Episensors, and Q4120 data loggers and initiated efforts to identify potential sites, considering such factors as the current

distribution of stations, private versus public property, location of power and telecommunications, and geologic materials. Two sites were permitted - McLaughlin Mine Natural Reserve and Alder Springs Conservation Camp.

In 2002-2003, the BSL permitted a 3rd site at Pacheco Peak with the California Department of Forestry and Fire. This site is located in south Santa Clara County. The BSL installed two sites during this year, at McLaughlin Reserve and Pacheco Peak, complementing the BDSN installations in the San Francisco Bay Area. The efforts for site preparation and installation are more fully described in Chapter 3.

Other areas under consideration for future installations include the Pt. Reyes area, the Santa Cruz Mountains (in collaboration with UC Santa Cruz), Placerville (in collaboration with Davey Jones and Lava Cap Winery), near Pinehurst (in collaboration with Peggy Hellweg), Hat Creek (in collaboration with UC Berkeley Department of Astronomy), and Carmel Valley (UC Berkeley Hastings Preserve). We hope to install two more sites in FY03/04.

3.2 Network Operations

As part of the CISN project, the BSL purchased a number of upgrade kits for their Q4120 data loggers with the goal of improving remote diagnostic capabilities last year. Three different kits were purchased - power board only, calibration board only, and combined power and calibration boards - in order to ensure that every Q4120 has a power board and that every 8-channel Q4120 also has a calibration board. The power boards provide the capability to monitor battery voltage, allowing staff to discriminate between power and telemetry problems remotely. The calibration boards provide the capability to monitor mass position as well as allow remote calibration of the seismic sensors. Both boards also record data logger temperature.

The boards were received in the winter of 2002. BSL staff, particularly Dave Rapkin, began to work on installing the upgrade kits. Of the 23 kits purchased, 11 have been installed as of June 30th and 9 of these data loggers have been reinstalled in the field. In addition to the installation of these boards, the BSL staff must also prepare new cables in order to record these new channels. That effort is also underway.

3.3 Statewide Communications

One of the major accomplishments in FY01/02 was the design and initial implementation of a CISN communications infrastructure. Doug Neuhauser of the BSL took the lead in investigating options and the CISN partners decided to establish a "ring" of T1 communication links (Figure 2.1) with dual routers at each node.

The implementation of the CISN ring was completed in early 2003, when the last problem (a bad wire in building

11 at the USGS Menlo Park) was resolved. All links are now fully operational and the ring is being used to push data among the CISN partners such as waveforms, picks, and ground motions. In addition, the CISN partners have migrated the transmission of ShakeMaps to OES to the ring. Use of the ring for sending ShakeMaps to OES has been a long-standing goal for the CISN but required coordination with OES personnel to configure machines. This effort was accelerated by the failure of the computer at OES that had been the recipient of ShakeMaps via the Internet. When the computer failed, BSL staff worked with OES and CISN partners to set up an interim system where ShakeMaps were transmitted to a UC Berkeley-maintained computer at OES. This stop-gap provided a local site within OES where the ShakeMaps could be retrieved while more permanent solutions were developed. OES replaced the failed computer and set up a new recipient system on the CISN ring. As of the end of May, ShakeMaps are being pushed to two separate OES machines, one on the CISN ring and one on the public Internet.

Early in 2003, Doug Neuhauser of the BSL installed the Multi Router Traffic Grapher (MRTG) software package to monitor the CISN ring. This package collects data for graphical display of traffic on the CISN router interface. More recently, Stan Schwartz of the USGS began using the Big Brother software to establish alarming capabilities - that is, to notify personnel when a problem with the ring is detected. The alarming system is running in Pasadena and will be installed at Berkeley soon. Two separate instances of the alarming software should provide reliable notification of problems with the ring.

The remaining outstanding issues with the ring include the connection of the OES routers to the Internet and the development of a security document.

3.4 Northern California Management Center

As part of this effort within the CISN, the BSL and the USGS Menlo Park have begun to plan for the next generation of the northern California joint notification system. Chapter 10 describes the operations of the existing Management Center and reports on design discussions.

Communications Infrastructure

In order to migrate to a design such as Figure 10.7, the BSL and the USGS Menlo Park need to enhance the communications infrastructure between their sites. Presently, data and information are shared on a dedicated connection, with fallback to the Internet.

Last year, the BSL commissioned Telecommunications Design Services, Inc. to perform a feasibility study for a microwave communication link between Berkeley and Menlo Park. The goal of the study was to evaluate options for a microwave communication link between the

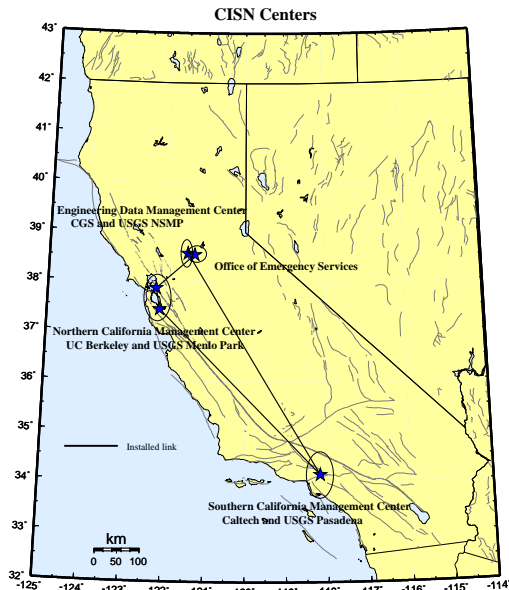


Figure 2.1: Map showing the geographical distribution of the CISN partners and centers. The communications "ring" is shown schematically with installed links (solid lines).

BSL and USGS elements of the Northern California Management Center. The report concludes that a repeater site will be required, given the length of the path and the obstructions (buildings, bridges, etc.). According to the report, the Space Sciences Laboratory at UC Berkeley will be a good site for the repeater.

Unfortunately, funding to establish this microwave link has not been identified. As a modest step to improve the communications links between the BSL and Menlo Park, the BSL installed a dedicated T1 connection this year, similar to the one established last year for the CISN ring. This dedicated T1 replaces the previous frame-relay connection as a more cost effective alternative. The second T1 provides the necessary bandwidth between the Berkeley and Menlo Park elements of the Northern California Management Center. The original frame-relay T1 will be reused by the BSL as a second link for connections to its seismic networks.

Computing Upgrade

The current data acquisition and processing computers used as part of the Northern California Management Center at the BSL are nearly 4 years old. As part of the OES project, the BSL purchased computers to replace these aging systems.

In the past year, the five Sun 280R computers have been brought online. Two of them were used to replace the data acquisition and processing computers. One is being used to generate ShakeMaps for northern California.

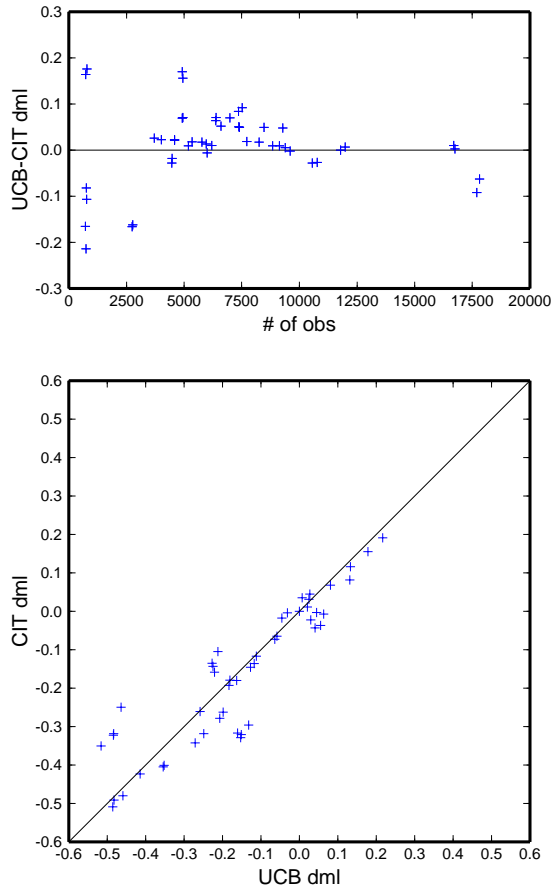


Figure 2.2: Comparison of M_L station adjustments estimated for BDSN stations from independent inversions of Wood Anderson amplitudes, using methodologies developed at UCB and Caltech (CIT).

And two are being setup as as pilot system for statewide earthquake processing. In addition to the 280R computers, the BSL purchased two Sun StorEdge RAID disk systems. The additional disk systems are required by the expanded waveform exchange among the centers.

3.5 Statewide Integration

BSL staff are involved in many elements of the statewide integration effort. In FY02/03, the Standards Committee of the CISN addressed a number of topics critical to this effort such as the software calibration issues discussed below. The Standards Committee continues to define and prioritize projects necessary to develop a prototype system and established working groups to address them (see the minutes from meetings and conference calls at <http://www.cisn.org/standards/meetings.html>).

Software Calibration

The CISN partners are working together on the problem of software calibration, particularly as it pertains to automated earthquake processing. Currently, the software implemented in the Northern and Southern California Management Centers is very different. Eventually, there may be standardization of software across the management centers, but in the short term, the focus is on calibrating the software to produce the same answers, given the same input data.

In the last year, effort was continued to focus on phase pickers, the association algorithm (binder), the location algorithm (hypoinverse), and magnitude estimation (various).

The CISN continued evaluation of data from a test system that is performing statewide earthquake notification using seismic data from all CISN partners. These tests are structured so that both northern and southern California are operating a statewide system in parallel with their current "regional" system. A recent 2-week evaluation of results from an exchange of data between northern and southern California networks showed that approximately 95% of the earthquakes were identical. Of the remaining 5%, most were "noise" associations on one system that were rejected on the other. The discrepant behavior can be attributed to differences in the order in which travel-time information is received by the two systems. This type of algorithm behavior may be difficult to eliminate without significant revision to the software design. We have identified several other issues and continue to improve the behavior of the statewide associator.

In parallel, the CISN has been working on issues related to magnitude. Here, the CISN is working in several areas. Pete Lombard of the BSL and Caltech staff have been working together to resolve issues in the original TriNet software that computes magnitude related to the selection of time windows and stations used in the estimation. Bugs in the codes that compute travel time have been identified and are being corrected. Once these issues have been resolved, then the Northern California Management Center will implement the magnitude codes for computing M_L and M_e . Similarly, the Southern California Management Center is working on the implementation of codes to estimate M_w and the seismic moment tensor that were developed in Northern California.

Also part of the magnitude calibration effort is the computation of station adjustments for M_L and M_e on a statewide basis. This effort is underway by BSL and Caltech staff. Figure 2.2 shows the results from two separate inversions of Wood Anderson amplitudes from the BDSN to estimate local magnitude adjustments. Bob Uhrhammer of the BSL and Jascha Polet of Caltech have been comparing their independent results as a first step to determine a common set of adjustments. The method Jascha employs estimates the adjustments and attenu-

ation relationship simultaneously, while Bob's approach a differential approach while fixing the attenuation relationship. The good agreement between the estimates of the adjustments provides confidence in the first step of the process. The next step is a joint inversion of BDSN and TriNet data for magnitude adjustments and a unified statewide attenuation relationship. In parallel, the BSL has worked to develop a collection of energy magnitude estimates in order to determine M_e station adjustments.

A final component of the magnitude efforts is the designation of a magnitude reporting hierarchy. There is general agreement at the low end and at the high end, but the working group is still reviewing issues relation to transition points from one magnitude type to another. More details about the magnitude calibration effort are documented in Chapter 10.

Metadata Exchange

The CISON is also working on issues related to metadata exchange. This is an important component of CISON activities, as correct metadata are required to insure valid interpretation of data. A Standards Working Group has developed and initiated testing of a model for database replication of metadata, and is currently reviewing how much of the schema to exchange and how to address metadata from partners such as CGS, who do not currently maintain their metadata in a database.

The Metadata Working Group has compiled a list of metadata necessary for data processing and developed a model for exchanging metadata. In this model, each CISON member is responsible for the metadata of their stations and other stations that enter into CISON processing through them. For example, Menlo Park is responsible for the NSMP, Tremor, and PG&E stations and Caltech is responsible for the Anza data. The Working Group believes that metadata exchange should proceed on a timely basis, not just when data are generated, and is testing an approach using database replication.

The core of the model is to have a master database at each organization and use multi-master replication to propagate the changes between the different data centers. Within a data center, it is proposed to use an interim database as the staging area. This database would contain snapshots of the master tables and the changes would be pushed manually to the master database by using snapshot replication. The use of such a staging area is particularly important because of the way Northern and Southern California currently load their databases. The current programs usually delete some or all the metadata before repopulating the updated data. This will introduce a latency period where the users will see inconsistent information in the database. The working group believes that this period should be relatively small and acceptable in our model. However, a longer term solution will certainly include the coding of new population

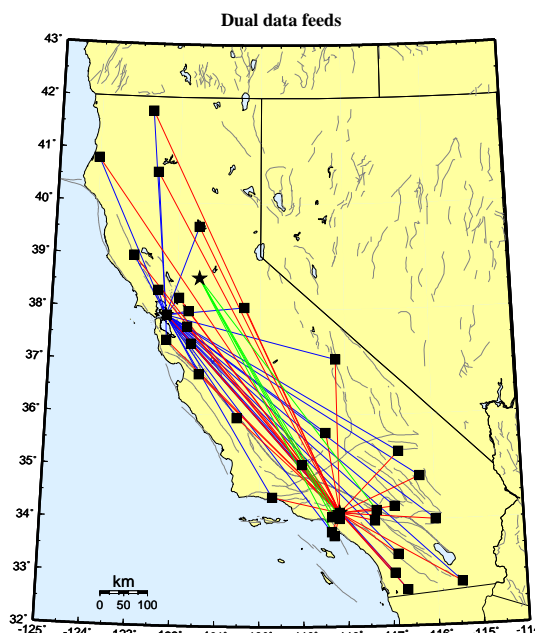


Figure 2.3: Map showing the 30 stations selected to send data directly to the Northern and Southern California processing centers, and the 5 stations that send data directly to the Engineering Data Center and the Southern California processing center.

programs. This model is currently being tested.

Dual Station Feeds

One of the major accomplishments last year was the establishment of "dual station feeds" from 20 stations (10 in northern California and 10 in southern California). To achieve this, the BSL and Caltech both ordered the DLCIs (data link connection identifier) that allow the 2nd center to establish a PVC (permanent virtual circuit) to each station using the frame-relay network.

The Northern California Management Center is using data from the 10 Southern California stations to estimate magnitudes on a routine basis. A subset of these stations are being used for the moment tensor inversions, a computation that is more sensitive to the background noise level.

This initial set of 20 stations was expanded to 30 this year (Figure 2.3), providing a broad sampling of the state. The next step for the BSL is to test these stations in their automated processing system. This direct feed of data from the station to two processing centers is an important step to improving the robustness of earthquake monitoring statewide.

Data Exchange

Pick exchange was initiated between the Northern and Southern California Management Centers last year. Al-

though the CISN has developed software to exchange the reduced amplitude timeseries, this aspect of data exchange has been delayed while certain problems in the codes that generate the time series are addressed. We hope to begin exchanging these timeseries in the fall of 2003.

The CISN partners completed the first stage of a system to exchange peak ground motion data this year. Using a common format, the CISN partners are exchanging observations with one another following an event or a trigger. This step increases the robustness of generating products such as ShakeMap, since all CISN partners are now exchanging data directly with one another. It also improves the quality of ShakeMaps on the boundary between northern and southern California, such as the recent events in Lompoc, by allowing all data to be combined in a single map. Finally, it is a necessary step toward the goal of generating statewide ShakeMaps.

3.6 Earthquake Information Distribution

In response to a request from the PMG, USGS and OES management established an *Ad Hoc* panel to develop specifications for an earthquake information system and to review existing systems as well as systems under development. Lind Gee of the BSL and David Oppenheimer of the USGS were asked to co-chair this panel and to provide a written report within 90 days. The panel was put together in May and a meeting took place on July 9-10th at the BSL. The report is due in early September.

3.7 Outreach

The CISN hosted an outreach workshop on ShakeMaps in January 2003, targeting the media. "ShakeMap for the News Media" was held at the USGS Menlo Park and attended by a number of print, radio, and television media in northern California. The purpose of the workshop was to raise awareness of ShakeMaps as an important tool in earthquake reporting. As part of the workshop, Lind Gee gave a talk on the CISN and its activities.

The CISN Web site <http://www.cisn.org> is continuing to develop. As part of the Web updating of the NCEDC and BSL this year, the CISN Web site was revamped and reorganized. In March, the Web site was updated to conform with USGS usage of their logo.

One of the major changes this year was the addition of "Seismology Data Reports". Both the Northern and Southern California Management Centers have generally produced special reports following earthquakes of note. These reports have generally provided tectonic and seismological context for the event and have included detailed maps showing background seismicity and figures showing waveforms of interest. We developed a prototype for a standard CISN report, and had the opportunity to try it out during the November 24, 2002 San

Ramon swarm as well as the February 2, 2003 Dublin swarm and the February 22, 2003 Big Bear earthquake.

Plans are underway to expand the capabilities and services of CISN Web site. This year, the BSL purchased two computers for Web servers, in order to improve response. This upgrade is critical to insure that the CISN Web site can respond to post-earthquake traffic. Once the upgrade is complete, the BSL will migrate the recenteqs and ShakeMap pages from the NCEDC server to the CISN server. That will make these products available directly from cisn.org. In addition, we are working with Caltech to setup a system to mirror the CISN Web site in southern California in order to distribute the load.

We have also moved forward with the development of a "myCISN". The ability to personalize earthquake content on a Web site was suggested at an early CISN Advisory Committee meeting. This year, Ionut Iordache developed a prototype for myCISN and we have just started testing this feature.

4. Acknowledgements

CISN activities at the BSL are supported by funding from the Governor's Office of Emergency Services.

Barbara Romanowicz and Lind Gee are members of the CISN Steering Committee. Lind Gee is a member of the CISN Program Management Committee and she leads the CISN project at the BSL. Doug Neuhauser is chair of the CISN Standards Committee, which includes Lind Gee and Pete Lombard as members.

Because of the breadth of the CISN project, many BSL staff have been involved including: John Friday, Lind Gee, Ionut Iordache, Wade Johnson, Bill Karavas, Pete Lombard, Doug Neuhauser, Charley Paffenbarger, Dave Rapkin, Cathy Thomas, and Stephane Zuzlewski. Lind Gee contributed to this chapter. Additional information about the CISN is available through reports from the Program Management Committee (*Hauksson et al.*, 2002; 2003a; 2003b).

5. References

Hauksson, E., L. Gee, D. Given, D. Oppenheimer, and T. Shakal, Report to the CISN Advisory and Steering Committees, #4, <http://www.cisn.org/oes/2003.05.09.pdf>, 2003b.

Hauksson, E., L. Gee, D. Given, D. Oppenheimer, and T. Shakal, Report to the CISN Advisory and Steering Committees, #3, <http://www.cisn.org/oes/2003.01.17.pdf>, 2003a.

Hauksson, E., L. Gee, D. Given, D. Oppenheimer, and T. Shakal, Report to the CISN Advisory and Steering Committees, #2, <http://www.cisn.org/oes/2002.10.25.pdf>, 2002.

Chapter 3

Berkeley Digital Seismic Network

1. Introduction

The Berkeley Digital Seismic Network (BDSN) is a regional network of very broadband and strong motion seismic stations spanning northern California and linked to UC Berkeley through continuous telemetry (Figure 3.1 and Table 3.1). This network is designed to monitor regional seismic activity at the magnitude 3+ level as well as to provide high quality data for research projects in regional and global broadband seismology.

The network upgrade and expansion initiated in 1991 has continued, and it has grown from the original 3 broadband stations installed in 1986-87 (BKS, SAO, MHC) to 28 stations in 2003, including the ocean-bottom seismometer in Monterey Bay. Two new stations were added in the past year (PACP and MNRC).

We take particular pride in high quality installations, which involves often lengthy searches for appropriate sites away from sources of low-frequency noise as well as continuous improvements in installation procedures and careful monitoring of noise conditions at existing stations.

Future expansion of our network is contingent on the availability of funding and coordination with other institutions for the development of a denser state-of-the-art strong motion/broadband seismic network and joint earthquake notification system in this seismically hazardous region.

2. BDSN Overview

Twenty-five of the BDSN sites are equipped with 3 component broadband seismometers and strong-motion accelerometers, and a 24-bit digital data acquisition system or data logger. Two additional sites (RFSB and SCCB) consist of a strong-motion accelerometer and a 24-bit digital data logger. Data from all BDSN stations are transmitted to UC Berkeley using continuous telemetry. In order to insure against data loss during utility disruptions, each site has a 3-day supply of battery power and is accessible via a dialup phone line. The combination of high-dynamic range sensors and digital data log-

gers ensures that the BDSN has the capability to record the full range of earthquake motion for source and structure studies. Table 3.2 lists the instrumentation at each site.

Most BDSN stations have Streckeisen three-component broadband sensors (*Wielandt and Streckeisen, 1982; Wielandt and Steim, 1986*). Guralp CMG-3T downhole broadband sensors contributed by LLNL are deployed in post-hole installations at BRIB and FARB. The strong-motion instruments are Kinemetrics FBA-23 or FBA-EST with ± 2 g dynamic range. The recording systems at all sites are either Q730, Q680, Q980 or Q4120 Quanterra data loggers, with 3, 6, 8, or 9 channel systems. The Quanterra data loggers employ FIR filters to extract data streams at a variety of sampling rates and these have been implemented as acausal filters in the BDSN. In general, the BDSN stations record continuous data at .01, 0.1, 1.0, and 20.0 samples per second and triggered data at either 80 or 100 samples per second using the Murdock, Hutt, and Halbert event detection algorithm (*Murdock and Hutt, 1983*) (Table 3.3). In addition to the 6-channels of seismic data, signals from thermometers and barometers are recorded at nearly every site (Figure 3.2).

In parallel with the upgrade of the broadband network, a grant from the CalREN (California Research and Education Network) Foundation enabled the BSL to convert data telemetry from analog leased lines to digital frame-relay connections. The frame-relay network uses digital phone circuits that can support 56 Kbit/s to 1.5 Mbit/s throughput. Since frame-relay is a packet-switched network, a site may use a single physical circuit to communicate with multiple remote sites through the use of "permanent virtual circuits". Frame Relay Access Devices (FRADs), which replace modems in a frame-relay network, can simultaneously support multiple interfaces such as RS-232 async ports, synchronous V.35 ports, and ethernet connections. In practical terms, the upgrade to frame relay communication provides faster data telemetry between the remote sites and the BSL, remote console control of the data loggers, additional services such as FTP and telnet to the data loggers, data transmission to

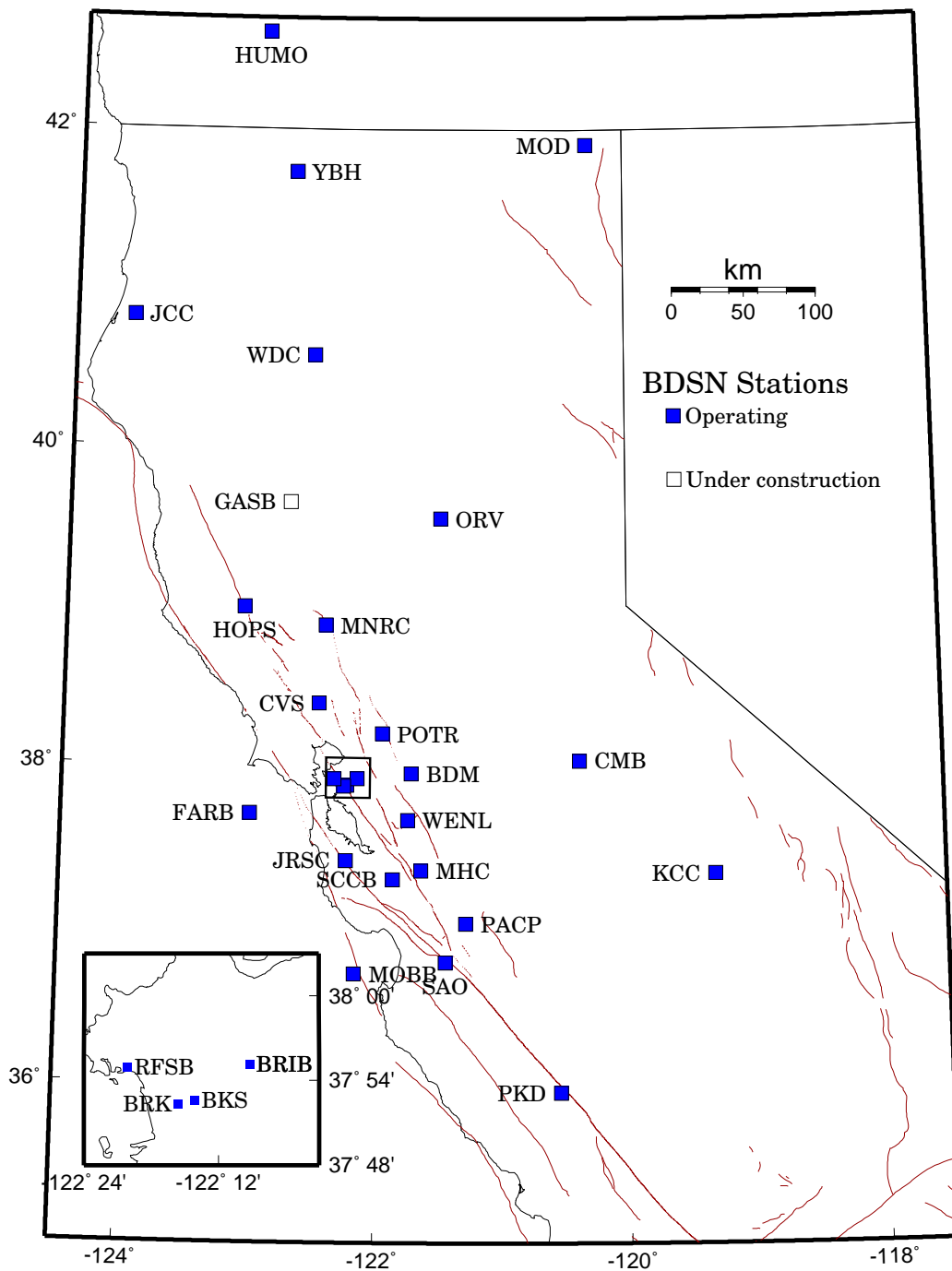


Figure 3.1: Map illustrating the distribution of operational (filled squares), planned (open squares), and closed (grey squares) BDSN stations in northern and central California.

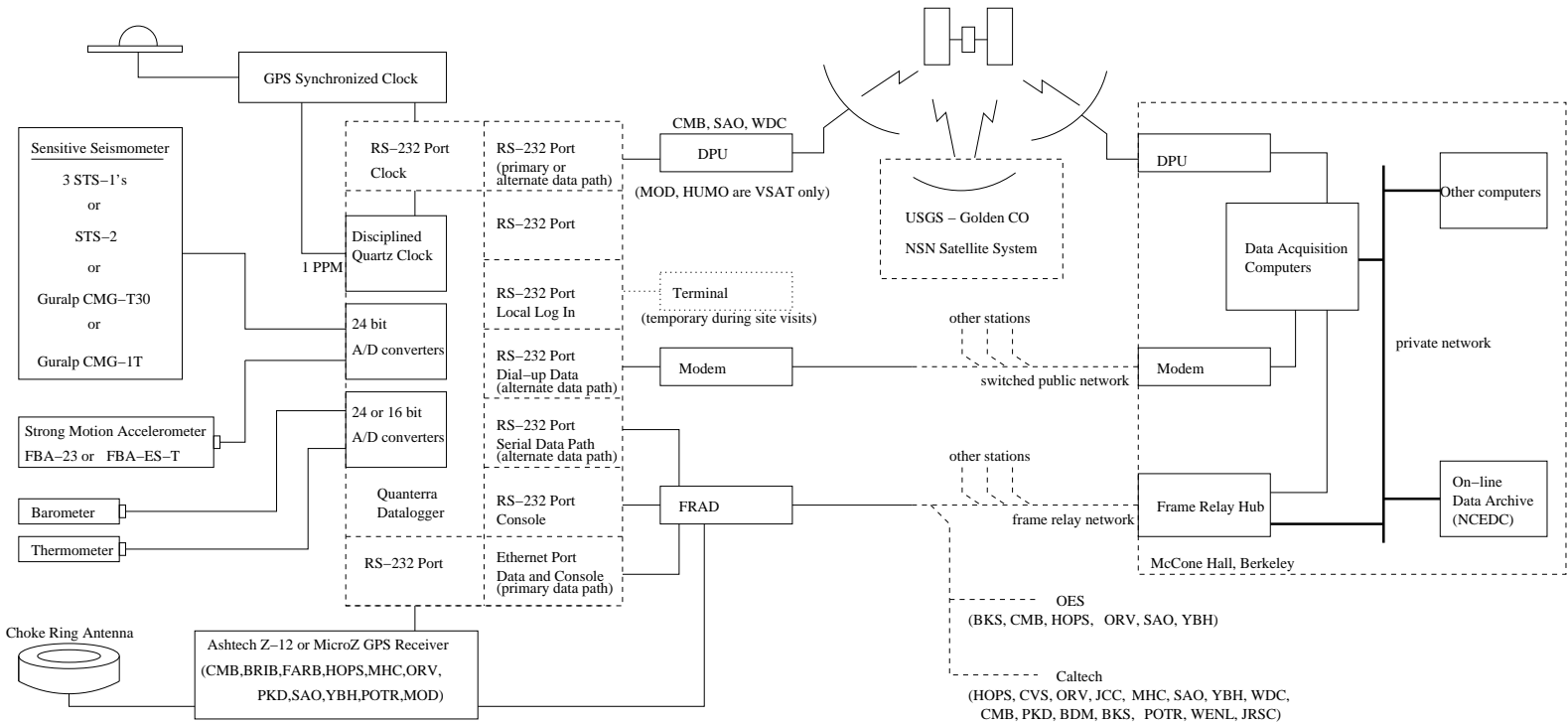


Figure 3.2: Schematic diagram showing the flow of data from the sensors through the data loggers to the central acquisition facilities of the BSL.

multiple sites, and the ability to communicate and transmit data from multiple instruments such as GPS receivers and/or multiple data loggers at a single site. Today, 20 of the BDSN sites use frame-relay telemetry for all or part of their communications system.

As described in Chapter 9, data from the BDSN are acquired centrally at the BSL. These data are used in the Rapid Earthquake Data Integration System as well as in routine earthquake analysis (Chapter 10). As part of routine quality control (Chapter 9), power spectral density analyses are performed weekly and Figure 3.3 shows a summary of the results for 2002-2003. The occurrence of a significant teleseism also provides the opportunity to review station health and calibration and Figure 3.8 displays the response of the BDSN to a M_w 7.3 deep focus earthquake in the Fiji Islands region.

BDSN data are archived at the Northern California Earthquake Data Center and this is described in detail in Chapter 11.

Sensor	Channel	Rate (sps)	Mode	FIR
Broadband	UH?	0.01	C	Ac
Broadband	VH?	0.1	C	Ac
Broadband	LH?	1.0	C	Ac
Broadband	BH?	20.0	C	Ac
Broadband	HH?	80.0/100.0	T	Ac
Strong-motion	LL?	1.0	C	Ac
Strong-motion	BL?	20.0	C	Ac
Strong-motion	HL?	80.0/100.0	C	Ac
Thermometer	LKS	1.0	C	Ac
Barometer	LDS	1.0	C	Ac

Table 3.3: Typical data streams acquired at BDSN stations, with channel name, sampling rate, sampling mode, and the FIR filter type. C indicates continuous; T triggered; Ac acausal. The LL and BL strong-motion channels are not transmitted over the continuous telemetry but are available on the Quanterra disk system if needed.

3. 2002-2003 Activities

3.1 Station Maintenance

Given the remoteness of the off-campus stations, BDSN data acquisition equipment and systems have been designed, configured, and installed for both cost effectiveness and reliability. As a result, the need for regular station visits has been reduced. Most station visits are necessitated by some catastrophic failure. The 2002-2003 fiscal year was no exception.

YBH Upgrades

The seismic vault at Yreka, CA (YBH) is sited in an abandoned hard rock mining drift in the Klamath Na-

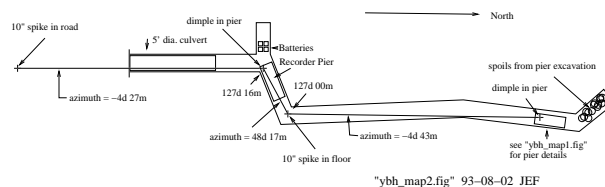


Figure 3.4: Map showing layout of YBH seismic vault. The location of the STS-2 seismic pier is shown in the right central part of the figure.

tional Forest in northern California. YBH was previously chosen as an alternative monitoring station by both IMS and DTRA. In collaboration with the IMS, BSL installed a VSAT data link, long-period microbarograph, separate battery back-up, a stand-alone data validation computer and door switch in 2001-2002.

This year, an STS-2 seismometer was deployed, bringing YBH into compliance as an auxiliary station of the IMS. This seismometer (0.0083-50 Hz passband) joins the three-component set of Streckeisen STS-1 broadband seismometers (0.0027-5 Hz passband), a three-component Kinematics FBA-23 strong motion accelerometer (0-32 Hz passband; 2g full scale); an Ashtech Z-XII3 geodetic GPS receiver; a YSI 44031 thermistor (to sense seismic pier temperature); a Motorola MPX-2010 pressure transducer and a Druck PTX-1240 microbarograph (to sense atmospheric pressure); and a Quanterra GPS clock for an accurate time base. Additionally, the sensor temperature, data logger temperature, broadband sensor mass position, clock quality, and telemetry through-put are utilized for status of health monitoring.

The STS-2 became operational as a part of the BDSN and telemetry of the signals to CTBTO and to BSL commenced on 27 November 2002. The three-component STS-2 and STS-1 data are continuously telemetered at 80, 20, 1, 0.1 and 0.01 samples per second.

As one part of BSL routine testing, the vertical-component background noise levels observed by the STS-1 and STS-2 were compared (see Figure 3.5). From the manufacturers specifications, the self noise of the high-gain STS-2 is lower that of the STS-1 at frequencies above 1 Hz. Here the high-gain STS-2 noise floor rises above the background earth noise observed by the STS-1 at 0.5 Hz and there are also narrow band spectral peaks at 1 Hz and its harmonics present with amplitudes of up to 20 dB. We suspect that the abnormally high noise levels observed on the STS-2 signals are related to the installation of the IMS satellite transmitter and computer equipment in the YBH vault. We also need to track down the source of the 0.7-8 Hz frequency noise peaks on the STS-1 (see Figure 3.5) which we suspect are also related to the installation of the IMS equipment.

In the coming year, we need to trouble shoot and cure

BDSN PSD Low Noise Synopsis (2002–2003)

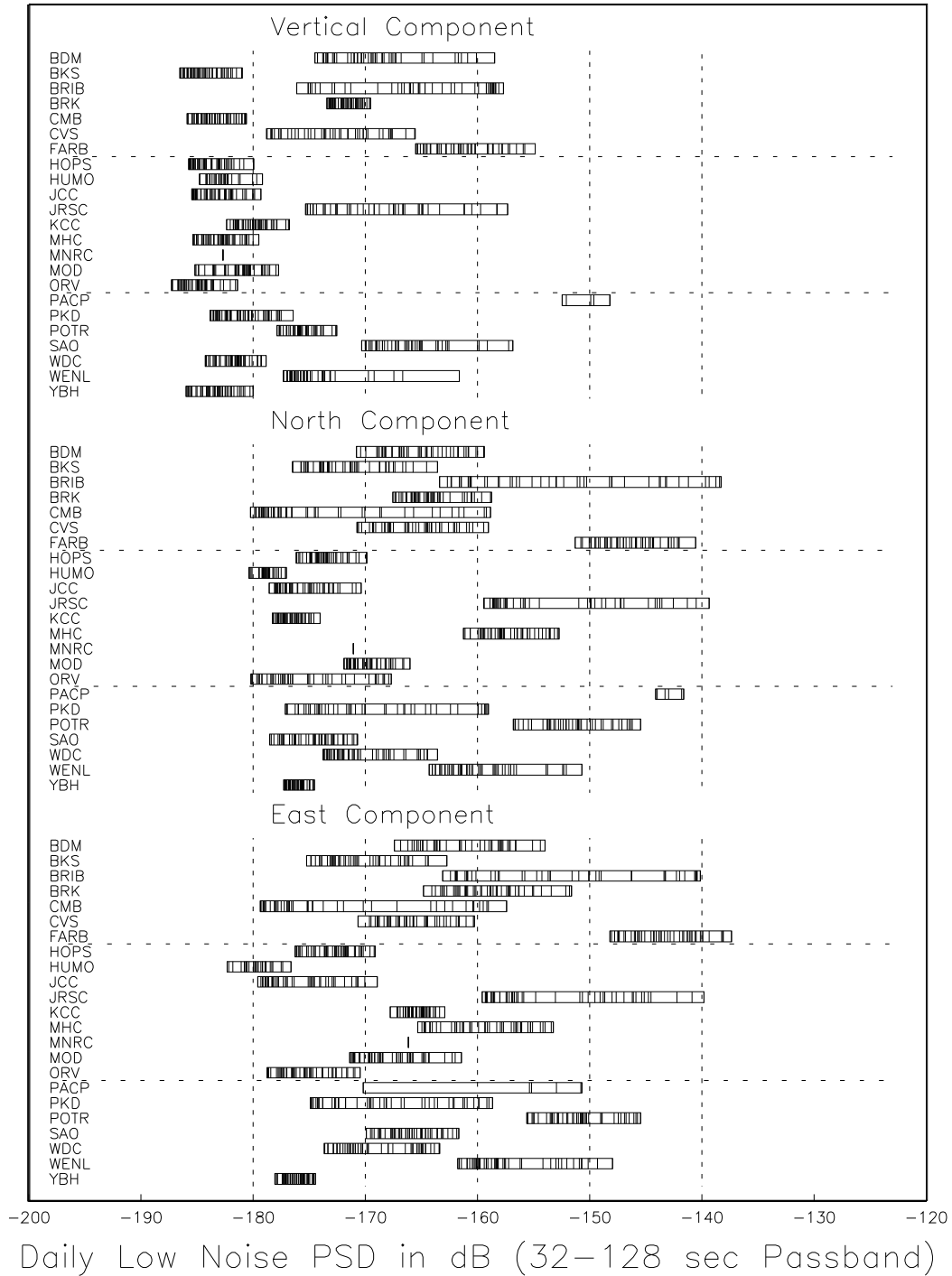


Figure 3.3: PSD noise analysis for BDSN stations, by channel, in the period range from 32-128 sec. PKD stands out in terms of its high noise level variation, which was caused by a problem in the sensor. FARB, sited on the Farallon Islands, stands out as the station with the highest average background noise level. BRIB, sited in a shallow borehole on a hillside prone to seasonal tilting, is also relatively noisy. YBH, sited in a remote and abandoned hard rock mining drift, stands out as exceptionally quiet site.

Code	Net	Latitude	Longitude	Elev (m)	Over (m)	Date	Location
BDM	BK	37.9540	-121.8655	219.8	34.7	1998/11 -	Black Diamond Mines, Antioch
BKS	BK	37.8762	-122.2356	243.9	25.6	1988/01 -	Byerly Vault, Berkeley
BRIB	BK	37.9189	-122.1518	219.7	2.5	1995/06 -	Briones Reservation, Orinda
BRK	BK	37.8735	-122.2610	49.4	2.7	1994/03 -	Haviland Hall, Berkeley
CMB	BK	38.0346	-120.3865	697.0	2	1986/10 -	Columbia College, Columbia
CVS	BK	38.3453	-122.4584	295.1	23.2	1997/10 -	Carmenet Vineyard, Sonoma
FARB	BK	37.6978	-123.0011	-18.5	0	1997/03 -	Farallon Island
HOPS	BK	38.9935	-123.0723	299.1	3	1994/10 -	Hopland Field Stat., Hopland
HUMO	BK	42.6071	-122.9567	554.9	50	2002/06 -	Hull Mountain, Oregon
JCC	BK	40.8175	-124.0296	27.2	0	2001/04 -	Jacoby Creek
JRSC	BK	37.4037	-122.2387	70.5	0	1994/07 -	Jasper Ridge, Stanford
KCC	BK	37.3236	-119.3187	888.1	87.3	1995/11 -	Kaiser Creek
MHC	BK	37.3416	-121.6426	1250.4	0	1987/10 -	Lick Obs., Mt. Hamilton
MNRC	BK	38.8787	-122.4428	704.8	3	2003/06 -	McLaughlin Mine, Lower Lake
MOBB	BK	36.6907	-122.1660	-1036.5	1	2002/04 -	Monterey Bay
MOD	BK	41.9025	-120.3029	1554.5	5	1999/10 -	Modoc Plateau
ORV	BK	39.5545	-121.5004	334.7	0	1992/07 -	Oroville
PACP	BK	37.0080	-121.2870	844	0	2003/06 -	Pacheco Peak
PKD	BK	35.9452	-120.5416	583.0	3	1996/08 -	Bear Valley Ranch, Parkfield
POTR	BK	38.2026	-121.9353	20.0	6.5	1998/02 -	Potrero Hill, Fairfield
RFSB	BK	37.9161	-122.3361	-26.7	0	2001/02 -	RFS, Richmond
SAO	BK	36.7640	-121.4472	317.2	3	1988/01 -	San Andreas Obs., Hollister
SCCB	BK	37.2874	-121.8642	98	0	2000/04 -	SCC Comm., Santa Clara
WDC	BK	40.5799	-122.5411	268.3	75	1992/07 -	Whiskeytown
WENL	BK	37.6221	-121.7570	138.9	30.3	1997/06 -	Wente Vineyards, Livermore
YBH	BK	41.7320	-122.7104	1059.7	60.4	1993/07 -	Yreka Blue Horn Mine, Yreka

Table 3.1: Currently operating stations of the Berkeley Digital Seismic Network. Each BDSN station is listed with its station code, network id, location, operational dates, and site description. The latitude and longitude (in degrees) are given in the WGS84 reference frame and the elevation (in meters) is relative to the WGS84 reference ellipsoid. The elevation is either the elevation of the pier (for stations sited on the surface or in mining drifts) or the elevation of the well head (for stations sited in boreholes). The overburden is given in meters. The date indicates either the upgrade or installation time.

the high-frequency noise observed on the STS-2 channels and on the STS-1 channels. The LD2 channel was configured to record the output from the Druck microbarograph in early January. We have experimented with installing opto-isolators in all digital signal lines at BSL in order to minimize the number of potential ground loop paths and the results are very encouraging. We will install opto-isolators in all digital signal lines at YBH, the next time the station is visited, to break the ground loop paths which are most likely contributing to the high noise level observed on the STS-2.

STS-1 Hinges

In November of 2001, Bob Uhrhammer reported observations of 1-sided steps on the STS-1 North component at station BKS. In January and early February of 2002, BSL staff replaced the electronics box and tested the baseplates, and concluded that rust on the sensor hinge was the source of the noise. Small rust spots were

observed on another STS-1 sensor (both sensors had not been evacuated in their early history).

Since replacement hinges are not available from Streck-eisen - and since as many as 20 BDSN sensors could develop this problem, BSL staff began efforts to manufacture replacement hinges. During a visit to BSL, Erhard Wielandt recommended replacing all 4 hinges simultaneously, using material similar to the original. BSL staff has spent time attempting to develop a reproducible recipe for the hinges, including laser cutting the edges for smoothness.

The first set of replacement hinges was tested and found to be too thin. In order to center the mass of the horizontal seismometers, the feet are adjusted such that the glass bell jar no longer clears the instrument itself. A second attempt at fabricating the hinges is ongoing.

Code	Broadband	Strong-motion	Data logger	T/B	GPS	Other	Telemetry	Dial-up
BDM	STS-2	FBA-23	Q4120	X			FR	
BKS	STS-1	FBA-23	Q980	X		Baseplates	FR	X
BRIB	CMG-3T	FBA-23	Q980		X	Vol. Strain	FR	X
BRK	STS-2	FBA-23	Q680				POTS	
CMB	STS-1	FBA-23	Q980	X	X	Baseplates	FR/NSN	X
CVS	STS-2	FBA-23	Q4120	X			FR	
FARB	CMG-3T	FBA-23	Q4120	X	X		R-FR/R	
HOPS	STS-1	FBA-23	Q980	X	X	Baseplates	FR	X
HUMO	STS-2	FBA-ES-T	Q4120	X			NSN	X
JCC	STS-2	FBA-23	Q980	X			FR	X
JRSC	STS-2	FBA-23	Q680				FR	X
KCC	STS-1	FBA-23	Q980	X		Baseplates	R-Mi-FR	X
MHC	STS-1	FBA-23	Q980	X	X		FR	X
MNRC	STS-2	FBA-ES-T	Q4120	X			None	X
MOBB	CMG-1T		GEOsense			Current meter, DPG	None	
MOD	STS-1	FBA-ES-T	Q980	X	X	Baseplates	NSN	X
ORV	STS-1	FBA-23	Q980	X	X	Baseplates	FR	X
PACP	STS-2	FBA-ES-T	Q4120	X			Mi/FR	
PKD	STS-2	FBA-23	Q980	X	X	EM	R-FR	X
POTR	STS-2	FBA-ES-T	Q4120	X	X		FR	X
RFSB		FBA-ES-T	Q730				FR	
SAO	STS-1	FBA-23	Q980	X	X	Baseplates, EM	FR/NSN	X
SCCB		FBA-ES-T	Q730		X		FR	
WDC	STS-2	FBA-23	Q980	X			FR/NSN	X
WENL	STS-2	FBA-23	Q4120	X			FR	
YBH	STS-1 & STS-2	FBA-23	Q980	X	X	Baseplates	FR	X

Table 3.2: Instrumentation of the BDSN as of 06/30/2003. Every BDSN station consists of collocated broadband and strong-motion sensors, with the exception of PKD1, RFSB and SCCB which are strong-motion only, with a 24-bit Quanterra data logger and GPS timing. Additional columns indicate the installation of a thermometer/barometer package (T/B), collocated GPS receiver as part of the BARD network (GPS), and additional equipment (Other) such as warpless baseplates or electromagnetic sensors (EM). The obs station MOBB has a current meter and differential pressure gauge (DPG). The main and alternate telemetry paths are summarized for each station. FR - frame relay circuit, R - radio, Mi - microwave, POTS - plain old telephone line, NSN - USGS NSN satellite link, None - no telemetry at this time. An entry like R-Mi-FR indicates multiple telemetry links, in this case, radio to microwave to frame relay.

3.2 New Installations

In the past year, one installation was completed and two new sites were installed. At Pacheco Peak in south Santa Clara County, the BSL permitted and built an observatory at the site of a State of California radio tower and vault. North of the Bay Area, the BSL installed a site at the McLaughlin Mine Natural Reserve.

Hull Mountain, Oregon (HUMO)

In the fall of 2000, we began a search for a site to extend BDSN north of the California/Oregon border, as part of a collaboration with the USGS National Seismic Network and the Global Seismic Network of IRIS, to be located north of the midpoint between the existing sites at MOD and YBH.

During the fall of 2002, VSAT connection to the National Seismic Network VSAT was established. Because the equipment is underground and the site is located within a mature forest, it was necessary to locate the VSAT dish approximately 300 meters away from the data logger in a location with a view of the southern sky (where the NSN satellite is located). To achieve digital telemetry over this distance, power lines and fiber optic cable were trenched and buried. The fiber optic link connects the data logger with the VSAT hardware. Additionally, the station is accessible via a dial-up phone line.

HUMO is a collaborative effort; the USGS/NSN provided the STS-2 seismometer, the BSL supplied the Episensors and the Quanterra data logger, and IRIS provided additional installation funding. The US Bureau

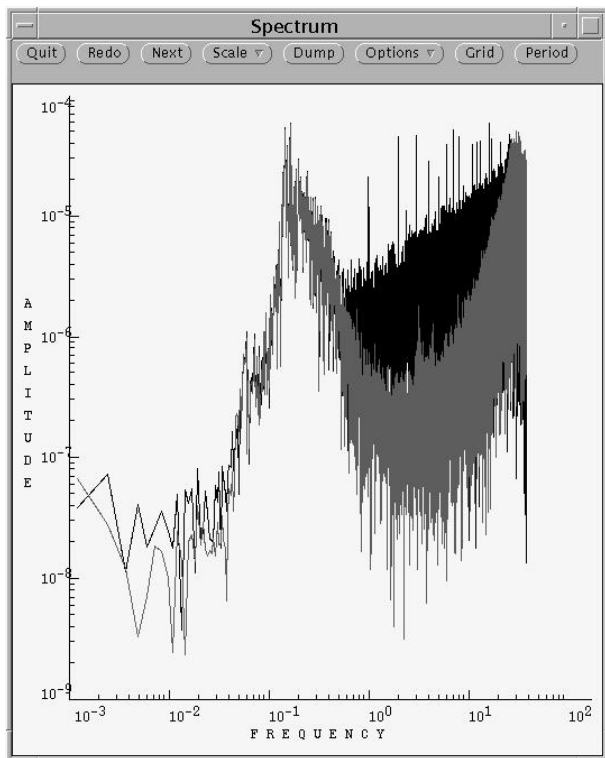


Figure 3.5: Comparison of the STS-1 (lower trace) and STS-2 (upper trace) derived background noise levels at YBH. The spectra are absolute ground acceleration (the respective instrument responses have been deconvolved). The nearly identical spectral amplitudes in the 0.05-0.5 Hz microseismic band indicates that the absolute calibrations of the two sensors are consistent with each other.

of Land Management assisted in locating the historical mine adit, and provides the site permit.

Pacheco Peak

During 2002-2003, BSL acquired a permit from the State of California, Department of Forestry and Fire Protection to install a broadband observatory at Pacheco Peak in south Santa Clara County. The mountain top site has two existing concrete radio vaults and 30 meter antenna towers. Police, fire, and state, and county communication equipment are housed there. Santa Clara County has furnished BSL a microwave channel from the site to transmit data back to their main facility in San Jose where the BSL station SCCB was previously installed in 2000. There data from both stations (PACP and SCCB) are aggregated with two BARD stations (LUTZ and SODA) onto a single digital data circuit.

Data from the Pacheco Peak station was first recorded in late June of 2003. At this time, additional efforts to minimize site, and thermally induced noise is being undertaken, such as the insulation over the seismometer.

The mutual cooperation of the State of California, Department of Forestry and Fire Protection (CDF), Santa Clara County Communications, together with BSL made this site possible.

McLaughlin Mine

The McLaughlin Mine site is on property owned and formerly operated by Homestake Mining Company as a surface gold mine. The geology of the area is extremely varied and complex. With the conclusion of mining operations, the property will be managed as a UC-Davis reserve for research. The seismographic vault is the first new research project on the reserve. The site is located approximately 20 kilometers east of the town of Lower Lake, California in an area of Franciscan sandstone.

A steel and concrete vault from a shipping container similar to those found at stations JCC, PKD, and HOPS was constructed. Power and telephone lines were trenched approximately 300 meters to the site. Because of the remoteness of the site, digital telephone data circuits are not available. To address our desire for continuous telemetry, BSL engineers have proposed and applied for permits to install a wireless radio bridge to a site 50 km away where digital phone service is offered. If and when permits are acquired, data would reach the Berkeley hub via a combination of land telco lines and spread spectrum radios. Continuous telemetry should be achieved in 2003-2004. In the meantime, data are being retrieved by dial-up access.

3.3 New Site Development

Alder Springs

At the Alder Springs site, located approximately 35 kilometers west of the central valley town of Williams, a short period observatory is operated by the California Department of Water Resources. Rocks are mostly serpentine in nature. Again, a seismographic vault similar to those at JCC, PKD, and HOPS will be built. The BSL vault will house the Department of Water Resources equipment presently installed in a fiberglass enclosure. This site has been named GASB by the BSL.

3.4 Ocean Floor Broadband Station

The Monterey Ocean Bottom Broadband observatory (MOBB) is a collaborative project between the Monterey Bay Aquarium Research Institute (MBARI) and the BSL. Supported by funds from the Packard Foundation to MBARI, NSF/OCE funds and UC Berkeley funds to BSL, its goal has been to install and operate a permanent seafloor broadband station as a first step towards extending the on-shore broadband seismic network in northern California, to the seaside of the North-America/Pacific plate boundary, providing better azimuthal coverage for regional earthquake and structure

studies. It also serves the important goal of evaluating background noise in near-shore buried ocean floor seismic systems, such as may be installed as part of temporary deployments of "leap-frogging" arrays (e.g. Ocean Mantle Dynamics Workshop, September 2002). In this context, evaluating the possibility of a posteriori noise deconvolution using auxiliary data (e.g. current meter, differential pressure gauge) as well as comparison with land based recordings.

This project follows the 1997 MOISE experiment, in which a three component broadband system was deployed for a period of 3 months, 40 km off shore in Monterey Bay, with the help of MBARI's Point Lobos ship and ROV Ventana (Figure 3.6). MOISE was a cooperative program sponsored by MBARI, UC Berkeley and the INSU, Paris, France (*Stakes et al.*, 1998; *Romanowicz et al.*, 1998; *Stutzmann et al.*, 2001). During the MOISE experiment, valuable experience was gained on the technological aspects of such deployments, which contributed to the success of the present MOBB installation.

The successful MOBB deployment took place April 9-11, 2002 and the station is currently recording data autonomously (e.g. *Romanowicz et al.*, 2003). In the future, it may be linked to the planned (and recently funded) MARS (Monterey Accelerated Research System; <http://www.mbari.org/mars/>) cable, or to the MBARI MOOS buoy, and provide real-time, continuous seismic data to be merged with the rest of the northern California real-time seismic system, although there are plans to eventually replace it by a quieter bore-hole installation.

Instrumentation

The ocean-bottom MOBB station currently comprises a three-component seismometer package, a current-meter, and a recording and battery package. A differential pressure gauge (DPG) with autonomous recording (e.g. *Cox et al.*, 1984) was deployed in the vicinity of the seismometer package in December 2002.

The seismic package contains a low-power (2.2W), three-component CMG-1T broadband seismometer system, built by Guralp, Inc., with a three-component 24-bit digitizer, a leveling system, and a precision clock. The seismometer package is mounted on a cylindrical titanium pressure vessel 54 cm in height and 41 cm in diameter, custom built by the MBARI team and outfitted for underwater connection.

Because of the extreme sensitivity of the seismometer, air movement within the pressure vessel must be minimized. In order to achieve this, after extensive testing at BSL (Chapter 9), the top of the pressure vessel was thermally isolated with two inches of insulating foam and reflective Mylar. The sides were then insulated with multiple layers of reflective Mylar space blanket, and the vessel was filled with argon gas.

The current-meter is a Falmouth Scientific 2D-ACM

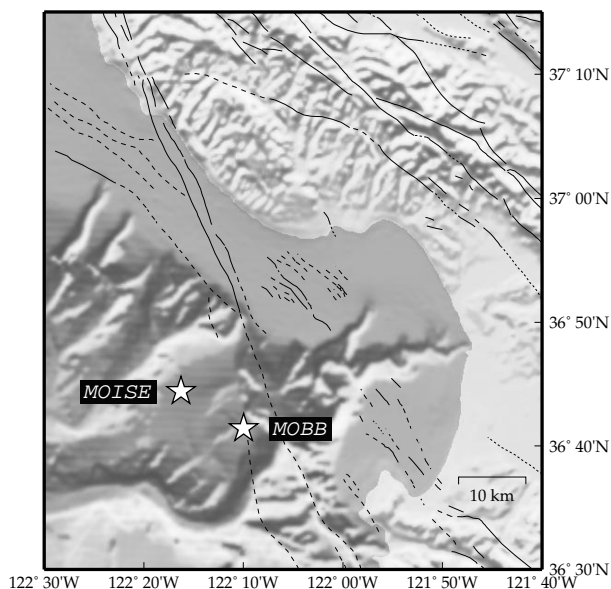


Figure 3.6: Location of the MOBB and MOIS stations in Monterey Bay, California, against seafloor and land topography. Fault lines are from the California Geological Survey database. MOBB is located at 1000 m below sea-level.

acoustic current meter. It is held by a small standalone fixture and measures the magnitude and direction of the currents about 1 meter above the seafloor.

The recording system is a GEOSense LP1 data logger with custom software designed to acquire and log digital data from the Guralp system and digital data from the current meter over RS-232 serial interfaces. The seismic data are sampled at 20 Hz and current-meter data at 1 Hz, and stored on a 3 GB, 2.5 in disk drive. All the electronics, including the seismometer and the current meter, are powered by a single 10kWh lithium battery.

All installations were done using the MBARI ship Point Lobos and the ROV Ventana. Prior to the instrumentation deployment, the MBARI team manufactured and deployed a 1181 kg galvanized steel trawl-resistant bottom mount to house the recording and power systems (Figure 3.7), and installed a 53 cm diameter by 61 cm deep cylindrical PVC caisson to house the seismometer pressure vessel. The bottom mount for the recording system was placed about 11m away from the caisson to allow the future exchange of the recording and battery package without disturbing the seismometer. Prior to deployment, the seismometer package was tested extensively at BSL, then brought to MBARI where its internal clock drift was calibrated in the cold room against GPS time. The details of the deployment which took place on 04/09/02-04/11/02 were described in the 2001-2002 BSL Annual Report.

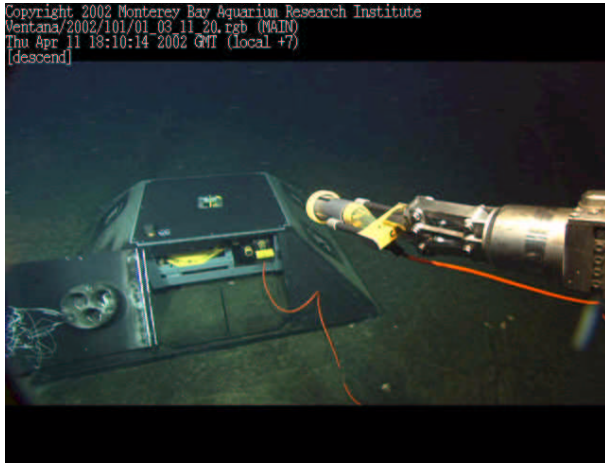


Figure 3.7: Snapshot showing underwater connection of cable from the seismometer system to the recording package inside the trawl-resistant mount. The robotic arm of the ROV is seen holding the connector from the right. Such an underwater connection was successfully performed for the first time during the MOISE experiment. The Point Lobos crew has now gained much experience, reducing the time it takes to successfully connect from over 2.5 hours to 10-15 mn at most.

Since the installation in April 2002, 5 data recovery dives have taken place (Jun 22, 2002; Sep 20, 2002; Jan 7, 2003; Mar 24, 2003; and Jun 9, 2003). Each time, the data recording and battery packages are exchanged for new ones, and the data transferred to BSL for analysis. While the seismometer package functioned well since installation, we have experienced several serious problems with malfunction of the data loggers, so that since that time, new seismic data are available only over short intervals. Both hardware and software problems appear to be involved, but BSL and MBARI staff are optimistic that the problems have been identified and corrected in the June 2003 deployment. We are hoping that the recovery dive scheduled for Sept 16th will result in augmenting our existing 2002 collection with 3 months of valuable uncorrupted MOBB seismic, DPG and current meter data.

Available MOBB data are being systematically analyzed to assess the data quality and possible improvements, through post-processing and/or installation adjustments. We plan to evaluate the long term time evolution of background noise, as the system continues to settle and stabilize, and the shorter term noise fluctuations in relation to tides and currents as recorded by the current-meter as well as the DPG. Since the auxiliary data are sampled at sufficiently high rates (1 sps) compared to what was available for the MOISE experiment, we are investigating ways to reduce the background noise correlated with the pressure and current data at periods longer than 10 sec

(see the Research contribution in Chapter III)

4. Acknowledgements

Under Barbara Romanowicz's general supervision, Lind Gee and Doug Neuhauser oversee the BDSN data acquisition operations and Bill Karavas is head of the engineering team. John Friday, Dave Rapkin, Cathy Thomas, and Bob Uhrhammer contribute to the operation of the BDSN. Bill Karavas, Bob Uhrhammer, and Lind Gee contributed to the preparation of this chapter.

Support for the installation of HUMO was provided by the USGS/NSN and IRIS. The California Governor's Office of Emergency Services provided funding toward the development of sites MNRC and PACP as part of the CISN.

MOBB is a collaboration between the BSL and MBARI, involving Barbara Romanowicz, Bob Uhrhammer, and Doug Neuhauser from the BSL and Debra Stakes and Paul McGill from MBARI. The MBARI team also includes Steve Etchemendy (Director of Marine Operations), Jon Erickson, John Ferreira, Tony Ramirez and Craig Dawe. The MOBB effort at the BSL is supported by funds from NSF/OCE and UC Berkeley.

5. References

- Cox, C., T. Deaton and S. Webb, A deep-sea differential pressure gauge, *J. Atm. Ocean. Tech.*, 1, 237-245, 1984.
- Murdock, J., and C. Hutt, A new event detector designed for the Seismic Research Observatories, *USGS Open-File-Report 83-0785*, 39 pp., 1983.
- Romanowicz, B., D. Stakes, J. P. Montagner, P. Tarits, R. Uhrhammer, M. Begnaud, E. Stutzmann, M. Pasyanos, J.F. Karczewski, S. Etchemendy, MOISE: A pilot experiment towards long term sea-floor geophysical observatories, *Earth Planets Space*, 50, 927-937, 1999.
- Romanowicz, B., D. Stakes, R. Uhrhammer, P. McGill, D. Neuhauser, T. Ramirez and D. Dolenc, The MOBB experiment: a prototype permanent off-shore ocean bottom broadband station, *EOS Trans A.G.U.*, Aug 28 issue, 2003.
- Stakes, D., B. Romanowicz, J.P. Montagner, P. Tarits, J.F. Karczewski, S. Etchemendy, D. Neuhauser, P. McGill, J-C. Koenig, J.Savary, M. Begnaud and M. Pasyanos, MOISE: Monterey Bay Ocean Bottom International Seismic Experiment, *EOS Trans., A.G.U.*, 79, 301-309, 1998.
- Stutzmann, E., J.P. Montagner et al., MOISE: a prototype multiparameter ocean-bottom station, *Bull. Seism. Soc. Am.*, 81, 885-902, 2001.
- Wielandt, E., and J. Steim, A digital very broad band seismograph, *Ann. Geophys.*, 4, 227-232, 1986.

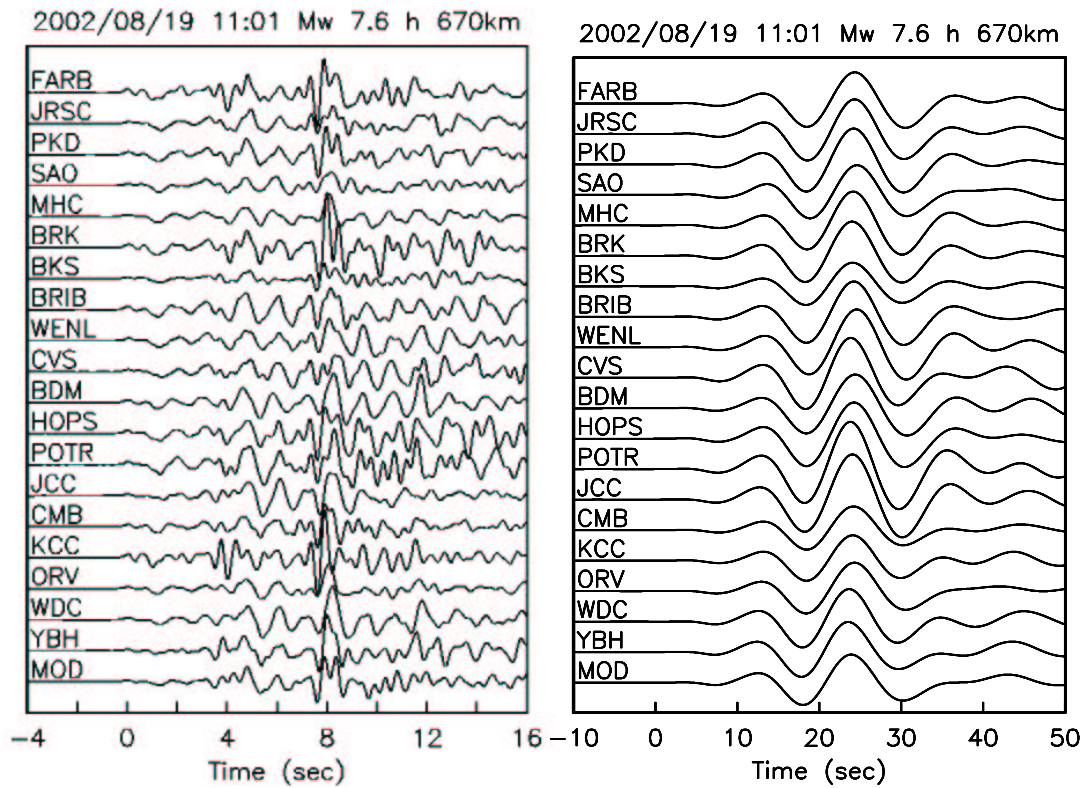


Figure 3.8: it Left: BDSN Z-component broadband recording of the P waveforms from a large deep focus teleseism the occurred in the Russia-northeast China border region (M_w 7.6; 2002.231,11:01; depth 670 km; 75° SW of Berkeley). The waveforms have been bandpass filtered (0.03-3.0 Hz), deconvolved to absolute ground acceleration, ordered by distance from the epicenter and aligned on the first peak in the P waveform (at 0 seconds). The differences in the waveforms in the BDSN broadband records are due primarily to differences in the response of the local crustal structure in the vicinity of each BDSN station. *Right:* Low-pass filtered version of the BDSN Z-component broadband P waveforms shown at left. The waveforms have been bandpass filtered (0.03-0.3 Hz), deconvolved to absolute ground acceleration, ordered by distance from the epicenter and aligned with 0 seconds the same absolute time. The similarities in the waveforms in the BDSN broadband records indicates that the sensors are all performing nominally within their specifications and that their calibrations are internally consistent. The variation in the waveforms correlates with variation in the crustal structure with generally larger amplitudes observed at BDSN stations in the Central Coast Ranges and smaller amplitudes observed at BDSN stations sited in the Sierra Nevada and elsewhere.

Wielandt, E., and G. Streckeisen, The leaf spring seismometer: design and performance, *Bull. Seis. Soc. Am.*, 72, 2349-2367, 1982.

Chapter 4

Northern Hayward Fault Network

1. Introduction

Complementary to the regional broadband network, a deployment of borehole-installed, wide-dynamic range seismographic stations is being established along the Hayward Fault and throughout the San Francisco Bay toll bridges network. This network is a cooperative development of the BSL and the USGS, with support from USGS, Caltrans, EPRI, the University of California Campus/Laboratory Collaboration (CLC) program, LLNL, and LBNL (Figure 4.1 and Table 4.1). Efforts at ongoing development of the network have also recently been enhanced by through coordinated efforts with the Mini-PBO project (Chapter 8, which is partially funded by NSF and by the member institutions of that project).

The purpose of the network is threefold: 1) to lower substantially the threshold of microearthquake detection, 2) to increase the recorded bandwidth for events along the Hayward fault, and 3) to obtain bedrock ground motion signals at the bridges from small earthquakes for investigating bridge responses to stronger ground motions. A lower detection threshold increases the resolution of the fault-zone seismic structure; allows seismologists to monitor the spatial and temporal evolution of seismicity at magnitudes down to $M \sim -1.0$, where earthquake rates are many times higher than those captured by the surface sites of the NCSN; allows researchers to look for pathologies in seismicity patterns that may be indicative of the nucleation of large damaging earthquakes; and allows scientists to investigate fault and earthquake scaling, physics and processes in the Bay Area of California. This new data collection will also contribute to improved working models for the Hayward fault. The bedrock ground motion recordings are also being used to provide input for estimating the likely responses of the bridges to large, potentially damaging earthquakes. Combined with the improved Hayward fault models, source-specific response calculations can be made, as well.

The Hayward Fault Network (HFN) consists of two parts. The Northern Hayward Fault Network (NHFN) is operated by the BSL and currently consists of 25 stations, including those located on Bay Area bridges and at

borehole sites of the Mini-PBO (MPBO) project. This network is considered part of the BDSN and uses the network code BK. The Southern Hayward Fault Network (SHFN) is operated by the USGS and currently consists of 5 stations. This network is considered part of the NCSN and uses the network code NC. This chapter is primarily focused on the NHFN and activities associated with the BSL operations.

2. NHFN Overview

The five MPBO sites have 3-component borehole geophone packages. All the remaining HFN sites have six-component borehole sensor packages. The packages were designed and fabricated at LBNL's Geophysical Measurement Facility by Don Lippert and Ray Solbau, with the exception of site SFAB. For the HFN sites three channels of acceleration are provided by Wilcoxon 731A piezoelectric accelerometers and three channels of velocity are provided by Oyo HS-1 4.5 Hz geophones. Velocity measurements for the MPBO sites are provided by Mark Products L-22 2 Hz geophones (Table 4.2). Sensors are generally installed at depths of about 100 m, but several sites have sensors emplaced at depths of over 200 m and the Dumbarton bridge sites have sensors at multiple depths (Table 4.1). During initial stages of the project, the NHFN sensors provided signals to on-site Quanterra Q730 and RefTek 72A-07 data loggers. In the current NHFN configuration on-line data logging is being done by on-site Quanterra Q4120 instrumentation. The SHFN sensors have been providing signals to Nanometrics HRD24 data loggers since initiation of data collection.

The 0.1-400 Hz Wilcoxon accelerometers have lower self-noise than the geophones above about 25-30 Hz, and remain on scale and linear to 0.5 g. In tests performed in the Byerly vault at UC Berkeley, the Wilcoxon is considerably quieter than the FBA-23 at all periods, and is almost as quiet as the STS-2 between 1 and 50 Hz.

Thirteen of the NHFN sites have Quanterra data loggers with continuous telemetry to the BSL. Similar to BDSN sites, these stations are capable of on-site recording and local storage of all data for more than one day

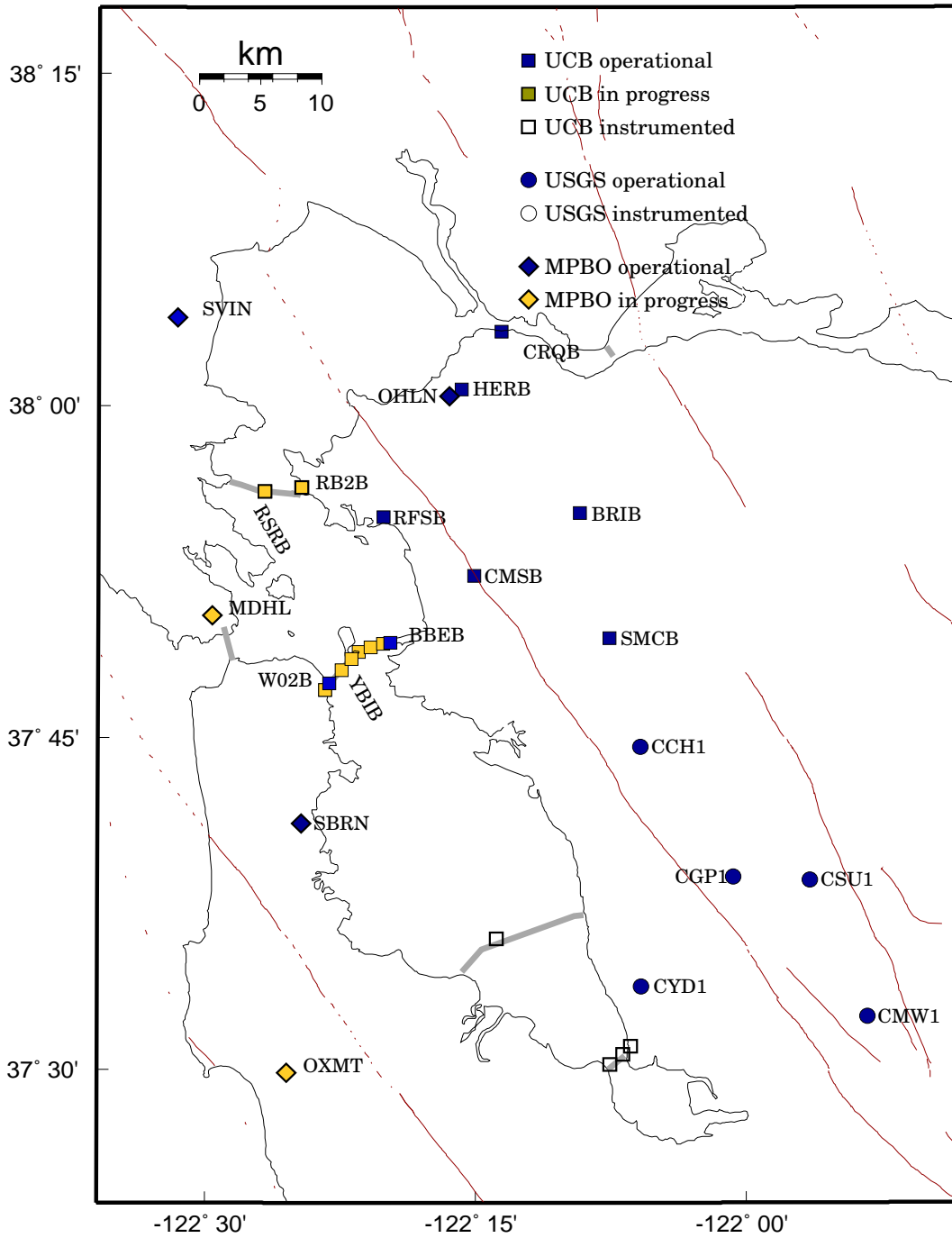


Figure 4.1: Map showing the locations of the HFN stations operated by the BSL (NHFN - squares) and the USGS (SHFN - circles) and Mini-PBO stations (diamonds) in the San Francisco Bay Area. Operational sites are filled, while sites in progress are grey. Other instrumented boreholes are indicated as open symbols.

and have batteries to provide backup power. Signals from these stations are digitized at a variety of data rates up to 500 Hz at 24-bit resolution (Table 4.3). In contrast to the BDSN implementation, the NHFN data loggers employ casual FIR filters at high data rates and acausal FIR filters at lower data rates. Because of limitations in telemetry bandwidth and disk storage, these 13 sites transmit triggered data at 500 sps, using the Murdock, Hutt, and Halbert (MHH) event detection algorithm (*Murdock and Hutt, 1983*), and continuous data at reduced rates (100, 20 and 1 sps) to the BSL.

The remaining 12 sites of the NHFN have in the past recorded data using RefTek data loggers. These sites do not have continuous telemetry for acquisition and required visits from BSL staff for data recovery. Collection of data from these sites has been discontinued, but efforts are underway to upgraded them with Quanterra Q4120 data loggers and continuous telemetry.

Signals from the 5 SHFN stations are digitized by Nanometrics data loggers at 100 sps and transmit continuous data to Menlo Park by radio. These digital data streams are processed by the Earthworm system with the NCSN data and waveforms are saved when the Earthworm detects an event.

Experience has shown that the MHH detector does not provide uniform triggering across the NHFN on the smallest events of interest. In order to insure the recovery of 500 sps data for these earthquakes, a central-site controller has recently been implemented at the BSL using the 500 sps vertical component geophone data for event detection. Originally the 100 sps vertical component geophone data was used for event detection but the bandwidth proved to be inadequate for detection of the smaller events where most of the seismic wave energy was at frequencies above 40 Hz. Triggers from this controller are being used to recover the 500 sps data from the NHFN data loggers.

Data from the NHFN and SHFN are archived at the NCEDC. At this time, the tools are not in place to archive the Hayward fault data together. The NHFN data are archived with the BDSN data, while the SHFN are archived with the NCSN data (Chapter 11). However, the new central-site controller will provide the capability to both include SHFN data in the event detection and extract SHFN waveforms for these events in the future.

As originally planned, the Hayward Fault Network was to consist of 24 to 30 stations, 12-15 each north and south of San Leandro, managed respectively by UCB and USGS. This is not happening quickly, although west of the fault, Caltrans has provided sites along the Bay bridges. This important contribution to the Hayward Fault Network has doubled the number of sites with instrumentation. At times, Caltrans provides holes of opportunity away from the bridges (e.g., HERB), so we have plans for additional stations that will bring the net-

Sensor	Channel	Rate (sps)	Mode	FIR
Accelerometer	CL?	500.0	T	Ca
Accelerometer	HL?	100.0	C	Ca
Accelerometer	BL?	20.0	C	Ac
Accelerometer	LL?	1.0	C	Ac
Geophone	DP?	500.0	T	Ca
Geophone	EP?	100.0	C	Ca
Geophone	BP?	20.0	C	Ac
Geophone	LP?	1.0	C	Ac

Table 4.3: Typical data streams acquired at each NHFN site, with channel name, sampling rate, sampling mode and FIR filter type. C indicates continuous; T triggered; Ca causal; and Ac acausal. The 100 sps channels (EP & HL) are only archived when the 500 sps channels are not available.

work geometry to a more effective state for imaging and real-time monitoring of the fault.

As a check on the calibration and an example of the capabilities of a borehole installed network, we compare the bandpass filtered (0.3-2 Hz) ground velocity data recorded at HERB, RFSB, BBEB, CMSB, BRIB, and SMCB for a M 6.9 deep focus teleseism that occurred in the vicinity of the Rat Islands in the Aleutian Islands chain at a depth of 685 km. in Figure 4.2.

3. 2002-2003 Activities

In addition to routine maintenance, operations and data collection; activities of the NHFN project over the past year have also included numerous efforts at network expansion, quality assurance, performance enhancement and catalog development.

3.1 Station Maintenance

Shown in Figure 4.3 are power spectral density (PSD) distributions of background noise for a sample of 8 NHFN land and bridge site stations. In general, background noise levels of the borehole HFN stations is more variable and generally higher than that of the Parkfield HRSN borehole stations (Figure 5.3). This is due in large part to the significantly greater level of cultural noise in the Bay Area, and to the fact that noise reduction efforts on the much more recently installed NHFN stations are still underway. For example the two noisiest stations (i.e. BBEB and W02) are located on the Bay Bridge which is currently undergoing earthquake retrofit and east span reconstruction. These stations have also only recently come back on-line with upgraded infrastructure and instrumentation, so the full complement of noise reduction modifications have not yet been completed.

On average the MPBO NHFN sites are more consistent and quieter (Figure 8.6). This is due in large part to

Code	Net	Latitude	Longitude	Elev (m)	Over (m)	Date	Location
CRQB	BK	38.05578	-122.22487	-25.0	38.4	1996/07 - current	CB
HERB	BK	38.01250	-122.26222	-25.0	217.9	2000/05 - current	Hercules
BRIB	BK	37.91886	-122.15179	219.7	108.8	1995/07 - current	BR, Orinda
RFSB	BK	37.91608	-122.33610	-27.3	91.4	1996/01 - current	RFS, Richmond
CMSB	BK	37.87195	-122.25168	94.7	167.6	1994/12 - current	CMS, Berkeley
SMCB	BK	37.83881	-122.11159	180.9	3.4	1997/12 - current	SMC, Moraga
SVIN	BK	38.03325	-122.52638		158.7	2003/08 - current	MPBO, St. Vincent's school
OHLN	BK	38.00742	-122.27371		196.7	2001/07 - current	MPBO, Ohlone Park
MDHL	BK	37.84227	-122.49374		160.6	in progress	MPBO, Marin Headlands
SBRN	BK	37.68562	-122.41127		157.5	2001/08 - current	MPBO, San Bruno Mtn.
OXMT	BK	37.498	-122.425		194.2	in progress	MPBO, Ox Mtn.
BBEB	BK	37.82167	-122.32867		150.0	2002/05 - current	BB, Pier E23
E17B	BK	37.82086	-122.33534		160.0	1995/08 - current *	BB, Pier E17
E07B	BK	37.81847	-122.34688		134.0	1996/02 - current *	BB, Pier E7
YBIB	BK	37.81420	-122.35923	-27.0	61.0	1997/12 - current *	BB, Pier E2
YBAB	BK	37.80940	-122.36450		3.0	1998/06 - current *	BB, YB Anchorage
W05B	BK	37.80100	-122.37370		36.3	1997/10 - current *	BB, Pier W5
W02B	BK	37.79120	-122.38525		57.6	2003/06 - current	BB, Pier W2
SFAB	BK	37.78610	-122.3893		0.0	1998/06 - current *	BB, SF Anchorage
RSRB	BK	37.93575	-122.44648	-48.0	109.0	1997/06 - current *	RSRB, Pier 34
RB2B	BK	37.93	-122.41		133.8	2003/07 - current *	RSRB, Pier 58
SM1B	BK	37.59403	-122.23242		298.0	not recorded	SMB, Pier 343
DB3B	BK	37.51295	-122.10857		1.5	1994/09 - 1994/11	DB, Pier 44
					62.5	1994/09 - 1994/09	
					157.9	1994/07 - current *	
DB2B	BK	37.50687	-122.11566			1994/07 - current *	DB, Pier 27
					189.2	1992/07 - 1992/11	
DB1B	BK	37.49947	-122.12755		0.0	1994/07 - 1994/09	DB, Pier 1
					1.5	1994/09 - 1994/09	
					71.6	1994/09 - 1994/09	
					228.0	1993/08 - current *	
CCH1	NC	37.7432	-122.0967	226		1995/05 - current	Chabot
CGP1	NC	37.6454	-122.0114	340		1995/03 - current	Garin Park
CSU1	NC	37.6430	-121.9402	499		1995/10 - current	Sunol
CYD1	NC	37.5629	-122.0967	-23		2002/09 - current	Coyote
CMW1	NC	37.5403	-121.8876	343		1995/06 - current	Mill Creek

Table 4.1: Stations of the Hayward Fault Network. Each HFN station is listed with its station code, network id, location, operational dates, and site description. The latitude and longitude (in degrees) are given in the WGS84 reference frame. The elevation of the well head (in meters) is relative to the WGS84 reference ellipsoid. The overburden is given in meters. The start dates indicate either the upgrade or installation time. The abbreviations are: BB - Bay Bridge; BR - Briones Reserve; CMS - Cal Memorial Stadium; CB - Carquinez Bridge; DB - Dumbarton Bridge; MPBO - mini-Plate Boundary Observatory RFS - Richmond Field Station; RSRB - Richmond-San Rafael Bridge; SF - San Francisco; SMB - San Mateo Bridge; SMC - St. Mary's College; and, YB - Yerba Buena. The * for stations indicates that the stations are not currently recording data. RSRB is shut down while Caltrans is retrofitting the Richmond-San Rafael bridge (as of April 19, 2001) and YBIB has been off-line since August 24, 2000 when power cables to the site were shut down. Other off-line stations are in the process of being upgraded as funding for equipment becomes available. The table also includes 2 MPBO stations which became operational in the last 2 years, and 3 MPBO borehole sensors that have recently been installed.

Site	Geophone	Accelerometer	Z	H1	h2	Data logger	Notes	Telem.
CRQB	Oyo HS-1	Wilcoxon 731A	-90	251	341	Q4120		FR
HERB	Oyo HS-1	Wilcoxon 731A	-90	TBD	TBD	Q4120		FR
BRIB	Oyo HS-1	Wilcoxon 731A	-90	79	349	Q4120	Acc. failed, Dilat.	FR
RFSB	Oyo HS-1	Wilcoxon 731A	-90	256	346	Q4120		FR
CMSB	Oyo HS-1	Wilcoxon 731A	-90	19	109	Q4120		FR
SMCB	Oyo HS-1	Wilcoxon 731A	-90	76	166	Q4120	Posthole	FR
SVIN	Mark L-22		-90	TBD	TBD	Q4120	Tensor.	FR/Rad.
OHLN	Mark L-22		-90	TBD	TBD	Q4120	Tensor.	FR
MDHL	Mark L-22		-90	TBD	TBD	None at present	Tensor.	
SBRN	Mark L-22		-90	TBD	TBD	Q4120	Tensor.	FR
OXMT	Mark L-22		-90	TBD	TBD	None at present	Tensor.	
BBEB	Oyo HS-1	Wilcoxon 731A	-90	TBD	TBD	Q4120	Acc. failed	Radio
E17B	Oyo HS-1	Wilcoxon 731A	-90	TBD	TBD	None at present		
E07B	Oyo HS-1	Wilcoxon 731A	-90	TBD	TBD	None at present		
YBIB	Oyo HS-1	Wilcoxon 731A	-90	257	347	Q4120	Z geop. failed	FR/Rad.
YBAB	Oyo HS-1	Wilcoxon 731A	-90	TBD	TBD	None at present		
W05B	Oyo HS-1	Wilcoxon 731A	-90	TBD	TBD	None at present		
W02B	Oyo HS-1	Wilcoxon 731A	-90	TBD	TBD	Q4120		Radio
SFAB	None	LLNL S-6000	TBD	TBD	TBD	None at present	Posthole	
RSRB	Oyo HS-1	Wilcoxon 731A	-90	50	140	Q4120	2 acc. failed	FR
RB2B	Oyo HS-1	Wilcoxon 731A	-90	TBD	TBD	None at present	1 acc. failed	
SM1B	Oyo HS-1	Wilcoxon 731A	-90	TBD	TBD	None at present		
DB3B	Oyo HS-1	Wilcoxon 731A	-90	TBD	TBD	None at present	Acc. failed	
DB2B	Oyo HS-1	Wilcoxon 731A	-90	TBD	TBD	None at present		
DB1B	Oyo HS-1	Wilcoxon 731A	-90	TBD	TBD	None at present	Acc. failed	
CCH1	Oyo HS-1	Wilcoxon 731A	-90	TBD	TBD	Nanometrics HRD24	Dilat.	Radio
CGP1	Oyo HS-1	Wilcoxon 731A	-90	TBD	TBD	Nanometrics HRD24	Dilat.	Radio
CSU1	Oyo HS-1	Wilcoxon 731A	-90	TBD	TBD	Nanometrics HRD24	Dilat.	Radio
CYD1	Oyo HS-1	Wilcoxon 731A	-90	TBD	TBD	Nanometrics HRD24	Dilat.	Radio
CMW1	Oyo HS-1	Wilcoxon 731A	-90	TBD	TBD	Nanometrics HRD24	Dilat.	Radio

Table 4.2: Instrumentation of the HFN as of 06/30/2002. Every HFN downhole package consists of co-located geophones and accelerometers, with the exception of MPBO sites. 6 HFN sites also have dilatometers (Dilat.) and the 5 MPBO sites have tensor strainmeters (Tensor.) 12 NHFN sites have Quanterra data loggers with continuous telemetry to the BSL. The remaining sites are being upgraded to Quanterra data loggers. The 5 SHFN sites have Nanometrics data loggers with radio telemetry to the USGS. The orientation of the sensors (vertical - Z, horizontals - H1 and H2) are indicated where known or identified as "to be determined" (TBD).

the greater depth of the MPBO sensors, the locations of MPBO stations in regions of generally less industrial and other cultural noise sources, and possibly to the absence of powered sensors (i.e. accelerometers) in their borehole sensor packages.

One of the most pervasive problems at NHFN stations equipped with the new Q4120 data loggers is power line noise (60 Hz and its harmonics at 120, 180, and 240 Hz). This noise reduces the sensitivity of the MHH detectors. Whenever a NHFN station is visited, the engineer at the site and a seismologist at the BSL work together to expedite the testing process, especially when attempting to identify and correct ground-loop faults which generally induce significant 60, 120, 180, and 240 Hz seismic signal contamination due to stray power line signal pickup, generally inductively coupled and aggravated by the presence of ground loops.

Below is a synopsis of maintenance efforts performed over the past year for several NHFN stations that gives some idea of the ongoing maintenance and performance enhancing measures that we are continuing to implement.

NHFN Station Maintenance Synopsis

BBEB: Installed upgraded power system in July. Installed Q4120 data logger and started data acquisition on September 10, 2002. Replaced coaxial cable and connector between Cylink radio and antenna to fix problem with poor data flow.

BRIB: Vault flooded in December during heavy rains owing to failure of sump pump. A portable electric generator and sump pump were used to pump out the water. Wood platforms were installed to raise the batteries off of the floor so that they will not become submerged if the vault floods again. The Rule 2000 Sump pump, Sure Bail switch, associated wiring and battery were repaired in the lab and reinstalled in the vault.

CMSB: Replaced batteries with two new C & D Technologies UPS 12-310 batteries. Replaced Q4120 data logger and FRAD. Rodents had chewed on the data logger case but they did not penetrate the case. Replaced defective rodent repeller near the FRAD and installed a second repeller near the data logger. Replaced preamp when it was discovered that channel 4 was bad. Upgraded Q4120 with installation of Q730PWR board. Experienced some problems during year with clock quality owing to poor antenna sky visibility.

CRQB: Upgraded Q4120 data logger with installation of Q730PWR board. Disconnect DAT to fix multiple boot up messages and questionable EP counts problem when booting up the Q4120 data logger. The DAT drive is not used so this is not a problem.

HERB: Swapped in a new preamp to fix a channel gain problem. Spent some time troubleshooting problem with 60 Hz and its harmonics contaminating geophone channels and running a series of experiments and discovered

that the 120 Hz signal is a 100 kHz spike which repeats at a 120 Hz rate. Installed damping resistor when it was discovered to be missing. Also installed shunt capacitors to reduce the high frequency spike noise. Replaced power supply when it was discovered to have periods of imperfect regulation.

RFSB: Upgraded Q4120 data logger with installation of Q730PWR board and new software.

SMCB: Station was down from August 28 through October 29 owing to construction at Moore Hall which provided power and telemetry. Q4120 digitizers failed due to a blown fuse. While Q4120 was in lab for fuse replacement a Q730PWR board was added to give input power monitoring capability.

W02B: Installed hardware (data logger, etc.) in utility boxes bolted to the NW face of the pier, just above water level. Began data acquisition and telemetry on June 17th.

Geophone Calibrations

Comparisons of the inferred ground accelerations generated by local earthquakes, from co-sited HFN geophone and accelerometer pairs, shows that the waveforms generally are quite coherent in frequency and phase response but that their inferred ground accelerations differ significantly. At times the amplitudes differ by up to a factor of 2 while the times of the peak amplitudes are identical. This implies that the free period and damping of the geophones are well characterized and also that the generator constant is not accurate (assuming that the corresponding ground accelerations inferred from the accelerometers are accurate).

Generally speaking, the accelerometers, being an active device, are more accurate and also more stable than the geophones so it is reasonable to assume that the most likely reason for the difference is that the assumed generator constants for the geophones are not accurate. *Rodgers et al.* (1995) describe a way to absolutely calibrate the geophones in situ and to determine their generator constant, free period and fraction of critical damping. The only external parameter that is required is the value of the geophones inertial mass.

We have built a calibration test box which allows us to routinely perform the testing described by *Rodgers et al.* whenever site visits are made. The box drives the signal coil with a known current step and rapidly switches the signal coil between the current source and the data logger input. From this information, expected and actual sensor response characteristics can be compared and corrections applied. Also, changes in the sensor response over time can be evaluated so that adjustments can be made and pathologies arising in the sensors due to age can be identified. Once a geophone is absolutely calibrated, we can also check the response of the corresponding accelerometer.

We are now performing the initial calibration tests and response adjustments for all NHFN stations as sites are visited for routine maintenance. We also plan a scheduled re-tests of all sites to monitor for sensor responses changes through time.

3.2 Combined Catalog

We are building a HF-specific data archive from the existing waveform data that have been collected by the heterogeneous set of recording systems in operation along the Hayward fault (i.e. the NHFN, SHFN, NCSN, and BDSN continuous and triggered waveforms). Recently we have taken the NHFN triggers collected during operations between 1995.248 and 1998.365 (recorded on portable RefTek recorders) and origin times from the NCSN and BDSN catalogs for this time period and undertaken a massive association of event and trigger times. The purpose of the effort is to compile a relatively uniform catalog of seismic data to low magnitudes and extending back in time to the beginning of reliable HFN data collection. The process has reduced nearly a million individual time segments to 316 real events along the Hayward fault during the period—an increase in the number of events of a factor of about 2.5 to 3 over the NCSN catalog alone in the same area.

3.3 Event Detection

As noted in the Introduction, one of the purposes of the HFN is to lower the threshold of microearthquake detection. Towards this goal, we have been developing new algorithms: a pattern recognition approach to identify small events; a phase onset time detector with sub-sample timing resolution, and; a phase coherency method for single component identification of highly similar events.

Pattern Recognition

In order to improve the detection and analysis of small events (down to $M_L \sim -1.0$) some specialized algorithms are being developed. The Murdock-Hutt detection algorithms used by MultiSHEAR, which basically flags an event whenever the short-term average exceeds a longer-term average by some threshold ratio, is neither appropriate for nor capable of detecting the smallest seismic events. One solution is to use a pattern recognition approach to identify small events associated with the occurrence of an event which was flagged by the REDI system. Tests have indicated that the pattern recognition detection threshold is $M_L \sim -1.0$ for events occurring within ~ 10 km of a NHFN station. The basic idea is to use a quarter second of the initial P-wave waveform, say, as a master pattern to search for similar patterns that occur within \pm one day, say, of the master event. Experimentally, up to six small CMSB recorded events, at the $M_L \sim$

-1.0 threshold and occurring within \pm one day of a master pattern, have been identified.

The pattern recognition method is CPU intensive, however, and it will require a dedicated computer to handle the pattern recognition tasks. To expedite the auto-correlation processing of the master pattern, an integer arithmetic cross-correlation algorithm has been developed which speeds up the requisite processing by an order of magnitude.

Phase Onset Time Detection

The phase onset time detector makes use of the concept that the complex spectral phase data, over the bandwidth of interest (i.e., where the SNR is sufficiently high), will sum to a minimum at the onset of an impulsive P-wave. The algorithm searches for the minimum phase time via phase shifting in the complex frequency domain over the bandwidth where the SNR is above 30 dB, say, to identify the onset time of the seismic phase. The algorithm requires that the recorded waveforms be deconvolved to absolute ground displacement. This implicitly requires that any acausality in the anti-aliasing filtration chain, such as the FIR filters used in the BDSN Quanterra data loggers, be removed. The algorithm typically resolves P-wave onset times to one-fiftieth of the sample interval or better.

Phase Coherency

A spectral phase coherency algorithm was developed to facilitate high resolution quantification of the similarities and differences between highly similar Hayward fault events which occur months to years apart. The resolution of the complex spectral phase coherency methodology is an order of magnitude better than the cross correlation method which is commonly used to identify highly similar events with resolution of order a few meters. This method, originally developed using NHFN borehole data, is now being applied as well to data from another borehole network (the HRSN) to provide more rapid and objective identification of the large fraction (approx. 40%) of characteristically repeating microearthquakes that occur at Parkfield, CA.

3.4 New Installations

San Francisco-Oakland Bay Bridge

The infrastructure at seven stations along the San Francisco-Oakland Bay Bridge (SFAB, W02B, W05B, YBAB, E07B, E17B, and BBEB) was upgraded with the installation of weatherproof boxes, power, and telemetry in anticipation of installing Q4120 data loggers and telemetering the data back to Berkeley. BBEB was brought on-line in May of 2002, and W02B in June of 2003.

Land Sites

Agreements with Caltrans and St. Mary's college have been made to replace the post hole installation at St. Mary's college (SMCB) with a deep borehole installation. The hole is to be drilled by Caltrans as a hole of opportunity when the schedule of a Caltrans drilling crew has an opening. The site has been reviewed by UCB, Caltrans and St. Mary's college personnel, and we are now in the drilling queue. Depending on the geology at borehole depth, this site may either become a MPBO site (w/o accelerometers) or a standard land site installation including both geophones and accelerometers.

Caltrans has also provided funding for instrumentation of several other land sites which we will install as future Caltrans drill time becomes available. Currently we are considering sites for these additional holes-of-opportunity at Pt. Pinole, on Wildcat Mtn. in the north Bay.

Mini-PBO

The stations of the Mini-PBO project (Chapter 8) are equipped with borehole seismometers. As these stations have become operational, they augment HFN coverage (Figure 4.1). In the last year, SVIN and SBRN have added coverage to the north bay and east side of the south bay, respectively.

4. Acknowledgements

Thomas V. McEvelly, who passed away in February 2002, was instrumental in developing the Hayward Fault Network, and without his dedication and hard work the creation and continued operation of the NHFN would not have been possible.

Under Bob Nadeau's, Bob Uhrhammer's and Doug Dreger's general supervision, Rich Clymer, Wade Johnson, Doug Neuhauser, Bill Karavas, John Friday, and Dave Rapkin all contribute to the operation of the NHFN. Bob Nadeau, Bob Uhrhammer and Lind Gee contributed to the preparation of this chapter.

Partial support for the NHFN is provided by the USGS through the NEHRP external grant program. Expansion of the NHFN has been made possible through generous funding from Caltrans, with the assistance of Pat Hipley. Larry Hutchings of LLNL has been an important collaborator on the project.

5. References

Rogers, P.W., A.J. Martin, M.C. Robertson, M.M. Hsu, and D.B. Harris, Signal-Coil Calibration of Electromagnetic Seismometers, *Bull. Seism. Soc. Am.*, 85(3), 845-850, 1995.

Murdock, J., and C. Hutt, A new event detector designed for the Seismic Research Observatories, *USGS Open-File-Report 83-0785*, 39 pp., 1983.

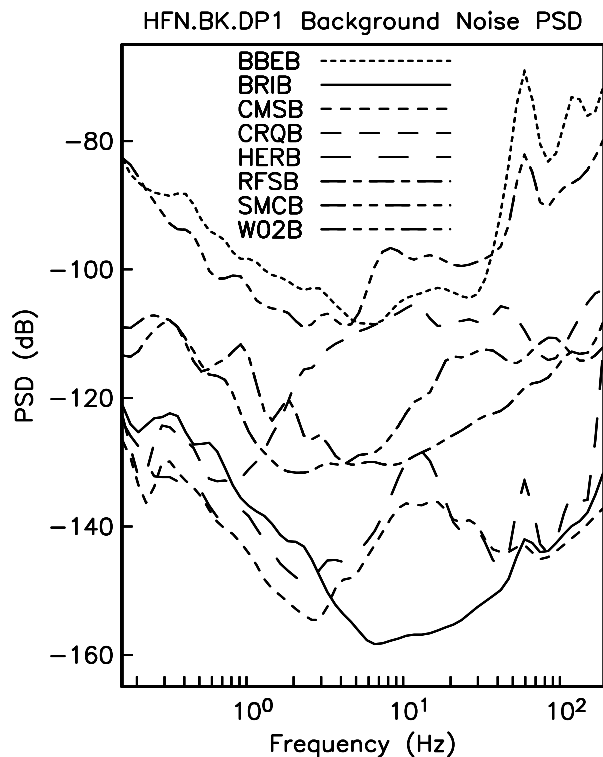


Figure 4.3: Plot showing the HFN.BK.DP1 background noise, PSD, for 8 of the NHFN stations. Plotted are the background low-noise PSD estimates. Ten minutes of .BK.DP1 data starting at 2003.225.0900 (2 AM PDT) were used in the analysis. Note that there is considerable variation in the general level and structure of the individual station background noise PSD estimates. Some of the stations show peaks at 60 Hz and its harmonics while others have a high average background level. The two bridge sites, BBEB and W02B are the noisiest while land site BRIB in Briones Regional Park (well away from the heavy cultural noise of the more populated region of the Bay Area) is the quietest. Two stations, CMSB and HERB show a peak in the 20-30 Hz range. The peak at CMSB is probably due to excitation of modes in the open bore hole and the peak at HERB is due to excitation of the local structure by the adjacent railway line and highways 4 and 80. The three stations in the middle of the group (RFSB, SMCB and CRQB) are responding to the local cultural noise. There are numerous ongoing experiments at the Richmond Field Station which are affecting the noise level at RFSB, CRQB is sited near a sewage treatment plant and the Carquinez bridge, and SMCB is currently only installed at post hole depth (3.5 m) on the St. Mary's campus.

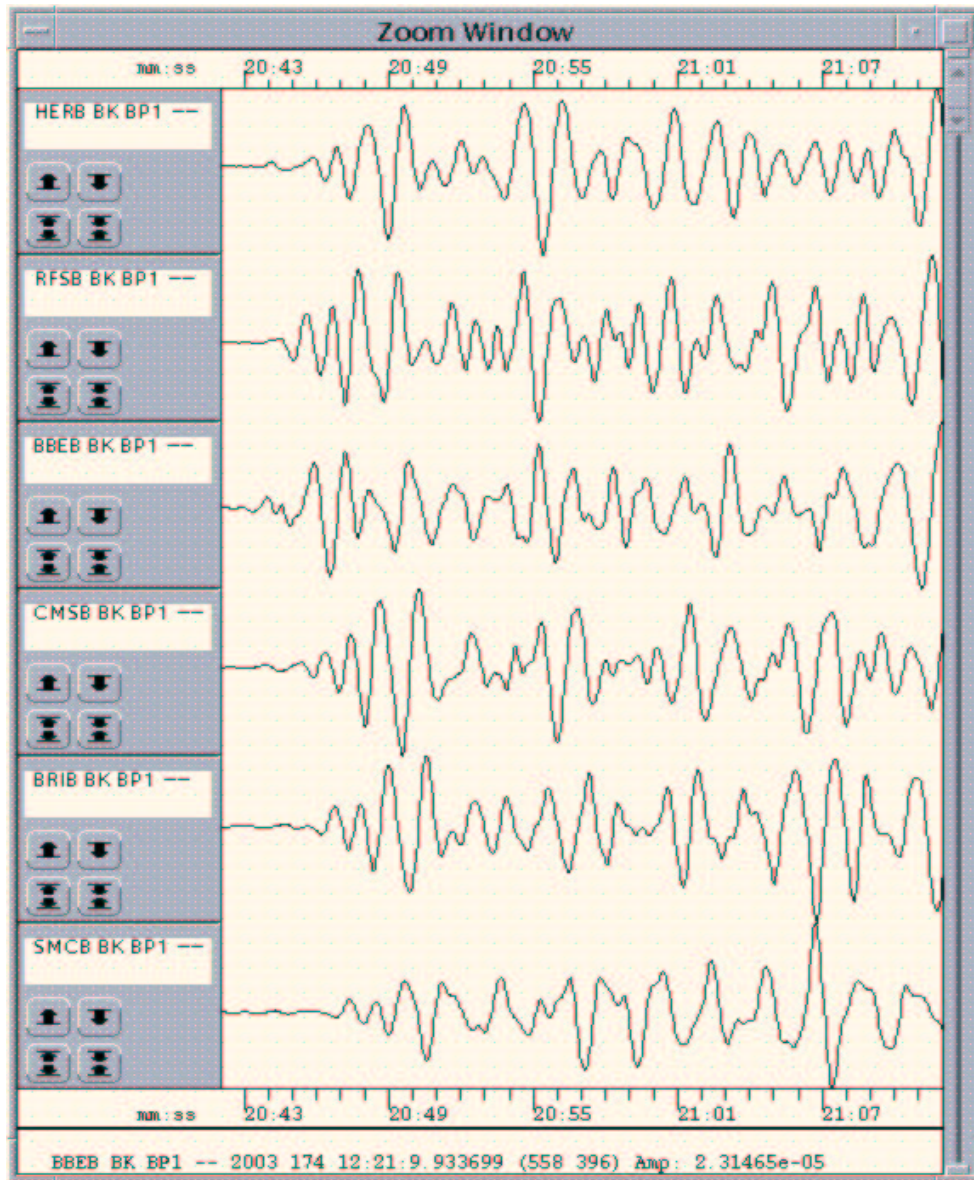


Figure 4.2: Displayed are 30 seconds of 0.5-2.0 Hz BP filtered ground velocity data for a M_w 6.9 deep focus teleseism which occurred 6/23/2003 at 12:12 UT at a depth of 685 km in the vicinity of the Rat Islands in the Aleutian Islands chain (51.44N,176.78E). The traces have been ordered by increasing distance (top to bottom). For reference, the great circle distance of the event from the NHFN is $\sim 44.2^\circ$ with an azimuth of $\sim 308^\circ$. The NHFN waveforms are relative scaled. Absolute scaling of the plot has indicated that the transfer function gain for station BBEB may be too low, making the inferred filtered ground velocity too large for a true comparison of the ground velocity. By periodically analyzing the network-wide response to deep focus teleseisms, whose arrivals are of near vertical plane wave incidence of uniform amplitude, anomalous station response (indicating potential problems in the network) such as that seen for BBEB are easily identifiable and can be further investigated to ensure accurate station operation. The same teleseism may be seen in Figure 5.2, recorded on the HRSN.

Chapter 5

Parkfield Borehole Network

1. Introduction

The operation of the High Resolution Seismic Network (HRSN) at Parkfield, California began in 1987, as part of the U.S. Geological Survey initiative known as the Parkfield Prediction Experiment (PPE) (*Bakun and Lindh, 1985*).

Figure 5.1 shows the location of the network, its relationship to the San Andreas fault, sites of significance from previous and ongoing research using the HRSN, relocated earthquake locations from 1987-1998.5, routine locations of seismicity since August 2002, and the epicenter of the 1966 M6 earthquake that motivated the PPE. The HRSN records exceptionally high-quality data, owing to its 13 closely spaced three-component borehole sensors (generally emplaced in the extremely low attenuation and background noise environment at 200 to 300 m depth (5.1)), its high-frequency wide bandwidth recordings (0-125 Hz), and its low magnitude detection threshold (recording events below magnitude -1.0).

Several aspects of the Parkfield region make it ideal for the study of small earthquakes and their relationship to tectonic processes. These include the fact that the network spans the expected nucleation region of a repeating magnitude 6 event and a significant portion of the transition from locked to creeping behavior on the San Andreas fault, the availability of three-dimensional P and S velocity models (*Michelini and McEvilly, 1991*), a seismicity catalogue that is complete to very low magnitudes and that includes at least half of the M6 seismic cycle, a well-defined and simple fault segment, a homogeneous mode of seismic energy release as indicated by the earthquake source mechanisms (over 90% right-lateral strike-slip), and the planned drilling zone and penetration and instrumentation site of the San Andreas Fault deep observatory at depth experiment (SAFOD) (see: <http://www.earthscope.org/safod/index.html> or <http://www.iris.iris.edu/HQ/EarthScope/EarthScope.saf.html>).

In a series of journal articles and Ph.D. theses, we have presented the cumulative, often unexpected, results of U.C. Berkeley's HRSN research efforts (see: www.seismo.berkeley.edu/seismo/faq/

[parkfield_bib.html](#)). They trace the evolution of a new and exciting picture of the San Andreas fault zone responding to its plate-boundary loading, and they are forcing new thinking on the dynamic processes and conditions within the fault zone at the sites of recurring small earthquakes.

2. HRSN Overview

2.1 1986 - 1998

The HRSN was installed in deep (200-300m) boreholes beginning in 1986. Sensors are 3-component geophones in a mutually orthogonal gimbaled package. This ensures that the sensor corresponding to channel DP1 is aligned vertically and that the others are aligned horizontally. In November 1987, the Varian well vertical array was installed and the first VSP survey was conducted, revealing clear S-wave anisotropy in the fault zone (*Daley and McEvilly, 1990*). During 1988, the original network was completed to a ten station 3-component 500 sps set of stations telemetered into a central detection/recording system operating in triggered mode and incorporating a deep (572 m) sensor in the Varian well string into the network. The Varian system was slaved in 1988, for about two years, to the Vibroseis control signals, allowing simultaneous recording of vibrator signals on both systems. For several years beginning in 1991, low-gain event recorders (from PASSCAL) were installed at several of the sites to extend the dynamic range to M_L about 4.5. The data acquisition system operated quite reliably until late 1996, when periods of unacceptably high down time developed. During this period as many as 7 of the remote, solar-powered telemetered stations were occasionally down simultaneously due to marginal solar generation capacity, old batteries, and recording system outages of a week or more were not uncommon. In July of 1998 the original data acquisition system failed permanently. This system was a modified VSP recorder acquired from LBNL, based on a 1980- vintage LSI-11 cpu and a 5 MByte removable Bernoulli system disk with a 9-track tape drive, configured to record both triggered microearthquake and Vibroseis data (dis-

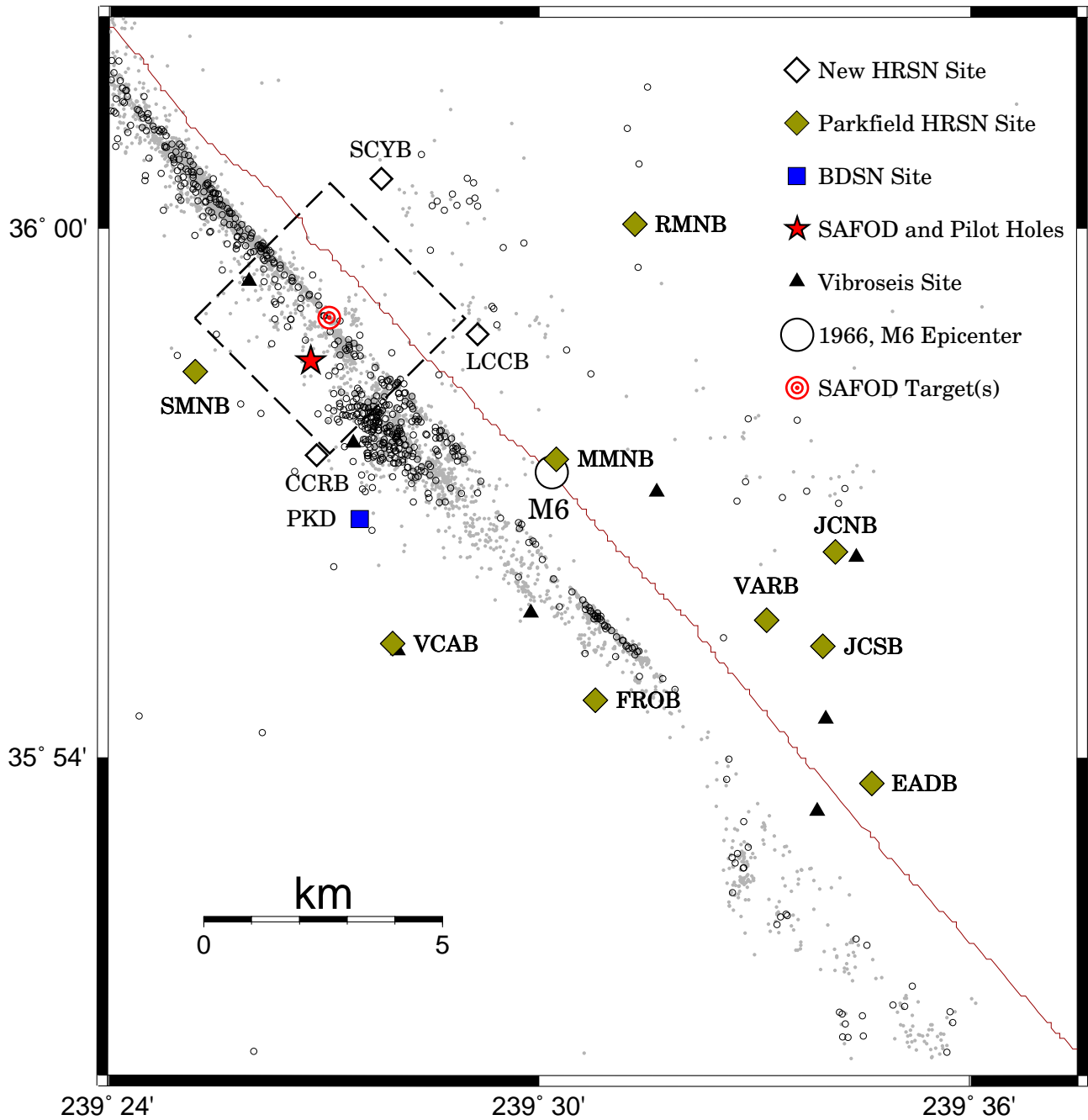


Figure 5.1: Map showing the San Andreas Fault trace, the location of the original 10 Parkfield HRSN stations (filled diamonds) and the 3 new sites installed to enhance coverage of the region containing the SAFOD facility (open diamonds), along with the BDSN station PKD (filled square). The locations of the 8 source points for the Vibroseis wave propagation monitoring experiment are represented by small black triangles. The epicenter of the 1966 M6 Parkfield main shock is located at the large open circle. The location of the pilot hole and SAFOD drill site is shown by the filled star, and the location of the 2 alternative M2 repeating earthquake targets (70 meters apart) are shown as concentric circles. Because of the SAFOD experiment, the 4 km by 4 km dashed box surrounding the SAFOD zone is a region of particular interest to BSL researchers. Routine locations of earthquakes recorded by the expanded and upgraded 13 station HRSN are shown as open black circles. Locations of events recorded by the earlier vintage 10 station HRSN, relocated using an advanced 3-D double-differencing algorithm applied to a cubic splines interpolated 3-D velocity model (*Michelini and McEvilly, 1991*), are shown as gray points. Station GHIB (Gold Hill, not shown) is located on the San Andreas Fault about 8 km to the Southeast of station EADB.

continued in 1994, *Karageorgi et al.*, 1997). The system was remote and completely autonomous, and data tapes were mailed about once a month to Berkeley for processing and analysis. The old system also had a one-sample timing uncertainty and a record length limitation because the tape write system recovery after event detection was longer than the length of the record, leaving the system off-line after record termination and until write recovery was completed.

2.2 1998 - 1999

In December of 1998, the original HRSN acquisition system was replaced by 10 stand-alone PASSCAL RefTek systems with continuous recording. To process these data, development of a major data handling procedure was required, in order to identify the microearthquakes down to $M = -1$, since continuous telemetry to the Berkeley Seismological Laboratory (BSL) and application of a central site detection scheme was not an option at that time.

In July, 1999 we had to reduce the network to four RefTeks at critical sites that would ensure continuity in monitoring at low magnitudes and the archive of characteristic events for studying the evolution of their recurrence intervals. Properties of the 10 original sites are summarized in Table 5.2.

2.3 Upgrade and SAFOD Expansion

Thanks to emergency funding from the USGS NEHRP, we have replaced the original 10-station system with a modern 24-bit acquisition system (Quanterra 730 4-channel digitizers, advanced software using flash disk technology, spread-spectrum telemetry, Sun Ultra 10/440 central processor at the in-field collection point, with 56K frame-relay connectivity to Berkeley). The new system is now online and recording data continuously at a central site located on the California Department of Forestry (CDF) fire station in Parkfield.

We have also added three new borehole stations at the NW end of the network as part of the SAFOD project, with NSF support, to improve resolution at the planned drilling target on the fault. Figure 5.1 illustrates the location of the proposed drill site (star), the new borehole sites, and locations of earthquakes recorded by the initial and the upgraded/expanded HRSN.

These three new stations use similar hardware to the main network, with the addition of an extra channel for electrical signals. Station descriptions and instrument properties are summarized in Tables 5.1 and 5.2. All HRSN Q730 data loggers employ FIR filters to extract data at 250 and 20 Hz (Table 5.3).

The remoteness of the drill site and new stations require an intermediate data collection point at Gastro Peak, with a microwave link to the CDF facility. The

Sensor	Channel	Rate (sps)	Mode	FIR
Geophone	DP?	250.0	T	Ca
Geophone	BP?	20.0	C	Ac

Table 5.3: Data streams currently being acquired at each HRSN site. Sensor type, channel name, sampling rate, sampling mode, and type of FIR filter are given. C indicates continuous; T triggered; Ac acausal; Ca causal. "?" indicates orthogonal vertical and 2 horizontal components.

HRSN stations use SLIP to transmit TCP and UDP data packets over bidirectional spread-spectrum radio links between the on-site data acquisition systems and the central recording system at the CDF. Six of the sites transmit directly to a router at the central recording site. The other seven sites transmit to a router at Gastro Peak, where the data are aggregated and transmitted to the central site over a 4 MBit/second digital 5.4 GHz microwave link. All HRSN data are recorded to disk at the CDF site. A modified version of the REDI real-time system detects events from the HRSN data, creates event files with waveforms from the HRSN and sends the event data in near real-time to UC Berkeley. Currently the continuous data is being migrated to DLT tape when local disk space fills up, and the tapes are mailed to the BSL for long-term storage. Efforts are being made to acquire funding to make this data Internet accessible to the research community through the NCEDC.

The upgraded system is compatible with the data flow and archiving common to all the elements of the BDSN/NHFN and the NCEDC, and is providing remote access and control of the system. It is also providing data with better timing accuracy and longer records, which are to eventually flow seamlessly into NCEDC. The new system also solves the problems of timing resolution, dynamic range, and missed detections, in addition to providing the added advantage of conventional data flow (the old system recorded SEG Y format).

3. 2002-2003 Activities

Over the past year, activities associated with the operation of the HRSN primarily involved three components: 1) routine operations and maintenance of the network, 2) enhancement of the network's performance for detection and recording of very low magnitude earthquakes, and 3) routine data processing and analysis.

3.1 Operations and Maintenance

In addition to the routine maintenance tasks required to keep the HRSN in operation, various refinements and adjustments to the networks infrastructure and opera-

Site	Net	Latitude	Longitude	Surf. (m)	Depth (m)	Date	Location
EADB	BP	35.89525	-120.42286	499	245	01/1988 -	Eade Ranch
FROB	BP	35.91078	-120.48722	542	284	01/1988 -	Froelich Ranch
GHIB	BP	35.83236	-120.34774	433	63	01/1988 -	Gold Hill
JCNB	BP	35.93911	-120.43083	559	224	01/1988 -	Joaquin Canyon North
JCSB	BP	35.92120	-120.43408	487	155	01/1988 -	Joaquin Canyon South
MMNB	BP	35.95654	-120.49586	731	221	01/1988 -	Middle Mountain
RMNB	BP	36.00086	-120.47772	1198	73	01/1988 -	Gastro Peak
SMNB	BP	35.97292	-120.58009	732	282	01/1988 -	Stockdale Mountain
VARB	BP	35.92614	-120.44707	511	572	01/1988 -	Varian Well
VCAB	BP	35.92177	-120.53424	790	200	01/1988 -	Vineyard Canyon
CCRB	BP	35.95716	-120.55161	601	251	05/2001 -	Cholame Creek
LCCB	BP	35.98006	-120.51423	637	252	08/2001 -	Little Cholame Creek
SCYB	BP	36.00942	-120.53661	947	252	08/2001 -	Stone Canyon

Table 5.1: Stations of the Parkfield HRSN. Each HRSN station is listed with its station code, network id, location, date of initial operation, and site description. The latitude and longitude (in degrees) are given in the WGS84 reference frame, the surface elevation (in meters) is relative to mean sea level, and the depth to the sensor (in meters) below the surface. Coordinates and station names for the 3 new sites are given at the bottom.

Site	Sensor	Z	H1	H2	RefTek 24	RefTek 72-06	Quanterra 730
EADB	Mark Products L22	-90	170	260	01/1988 - 12/1998	12/1998 - 07/1999	03/2001 -
FROB	Mark Products L22	-90	338	248	01/1988 - 12/1998	12/1998 - 07/1999	03/2001 -
GHIB	Mark Products L22	90	failed	unk	01/1988 - 12/1998	12/1998 - 07/1999	03/2001 -
JCNB	Mark Products L22	-90	0	270	01/1988 - 12/1998	12/1998 - 06/2001	03/2001 -
JCSB	Geospace HS1	90	300	210	01/1988 - 12/1998	12/1998 - 07/1999	03/2001 -
MMNB	Mark Products L22	-90	175	265	01/1988 - 12/1998	12/1998 - 06/2001	03/2001 -
RMNB	Mark Products L22	-90	310	40	01/1988 - 12/1998	12/1998 - 07/1999	03/2001 -
SMNB	Mark Products L22	-90	120	210	01/1988 - 12/1998	12/1998 - 06/2001	03/2001 -
VARB	Litton 1023	90	15	285	01/1988 - 12/1998	12/1998 - 07/1999	03/2001 -
VCAB	Mark Products L22	-90	200	290	01/1988 - 12/1998	12/1998 - 06/2001	03/2001 -
CCRB	Mark Products L22	-90	N45W	N45E	-	-	05/2001 -
LCCB	Mark Products L22	-90	N45W	N45E	-	-	08/2001 -
SCYB	Mark Products L22	-90	N45W	N45E	-	-	08/2001 -

Table 5.2: Instrumentation of the Parkfield HRSN. Most HRSN sites have L22 sensors and were originally digitized with a RefTek 24 system. After the failure of the WESCOMP recording system, PASSCAL RefTek recorders were installed. In July of 1999, 6 of the PASSCAL systems were returned to IRIS and 4 were left at critical sites. The upgraded network uses a Quanterra 730 4-channel system. For the three new stations (bottom) horizontal orientations are approximate (N45W and N45E) and will be determined more accurately in the near future.

tional parameters have been needed this year to correct for pathologies that continue to manifest themselves in the recently upgraded and expanded system.

A feature of the new system that has been particularly useful both for routine maintenance and for pathology identification has been the Internet connectivity of the central site processing computer and the station data loggers with the computer network at BSL. Through this connection, select data channels and on-site warning messages from the central site processor are sent directly to BSL for evaluation by project personnel. If, upon these evaluations, more detailed information on the HRSN's performance is required, it can also be directly accessed. Analysis of this remotely acquired information has been extremely useful for trouble shooting by allowing field personnel to schedule and plan the details of maintenance visits to Parkfield. The connectivity also allows certain data acquisition parameters to be modified remotely when needed, and commands can be sent to the central site computer and data loggers to modify or restart processes when necessary.

The network connectivity allows analysts at the BSL to routinely perform checks on the system health of the HRSN and its data quality. One example of a technique used by BSL analysts involves the use of teleseismic arrivals from deep focus earthquakes. Since seismic waves from such events impose a near simultaneous and vertically incident plane wave of relatively uniform amplitude on all HRSN stations, seismograms from these events can be used to assess relative station responses across the network and help identify pathologies in station polarities, individual component failures and other response characteristics.

Figure 5.2 shows an example of a recent teleseism recorded on the DP1 (vertical) channel across the network. Not shown are recordings from stations MMNB and VARB. The initial display of seismograms from this teleseism showed these station components to be responding abnormally at the time of the earthquake. Based on this teleseismic result other remotely acquired information was uploaded from the HRSN and it was determined that these components were indeed malfunctioning. Subsequent field visits were then scheduled and the necessary repairs made.

The network connectivity also allows remote monitoring of the background noise levels being recorded by the HRSN stations. For example shown in Figure 5.3 are power spectral density plots of background noise for vertical components of the 7 HRSN stations that are most critical for monitoring seismicity in the region containing SAFOD. The PSD analysis gives a rapid assessment of the HRSN seismometer responses across their wide bandwidth. By routinely generating these plots with data telemetered from Parkfield, changes in the seismometer responses, often indicating problems with the acquisition

system, can be easily identified, and corrective measures can then be planned and executed on a relatively short time-frame.

Triggered event data for the HRSN is also telemetered in near real time to the BSL, and this allows for rapid evaluation of the triggered data. This year we have implemented a semi-automated waveform and trigger review procedure using a graphical user interface (GUI). This procedure is now being used to review the triggered waveform data daily to discriminate between earthquake and non-earthquake events and to pick P and S phases of the local events. In the process, our analyst/field technician also makes note of obvious problems with station/component specific earthquake recording, and this malfunction information is used to identify maintenance needs for the HRSN.

3.2 Enhancing HRSN Performance

Over the past year significant efforts were made to identify and reduce noise problems arising from the new and expanded data acquisition system. Detection, monitoring, and high-resolution recording of earthquakes down to the smallest possible magnitudes with the highest possible signal-to-noise (especially in the region of the proposed SAFOD drilling) is a major objective of the HRSN data collection effort. Consequently, elimination of all sources of unnaturally occurring system noise is a primary goal. The minimization of data loss due to station outages and data-dropouts is also critical to this objective.

The sophisticated HRSN data acquisition involves integration of a number of distinct components at each station (i.e., sensor, preamp, solar panels, solar regulator, batteries, Freewave radio, antenna, lightning arresters, and associated cabling, connectors and grounds) and radio telemetry apparatus between the seismic stations, telemetry relay stations, and the central processing site on the CDF site in Parkfield.

This complex integration of station and communication components combined with a variety of associated concerns (e.g., ground loops, cable resistances, radio feedback into recording equipment at stations, radio interference between stations, marginal line of site paths, cloud cover and solar power, the integration of older (pre-upgrade) hardware components with new components, old component deterioration and failures, and malfunctioning and unexpected performance characteristics of newer components) all make identification of specific causes of network generated (i.e. artificial) noise difficult to identify.

Exhaustive and iterative testing of HRSN performance has identified two primary causes for observed artificial noise remaining in the system (i.e. solar regulator spiking and preamp self-noise generation). We have designed and have implemented or are in the process of implementing

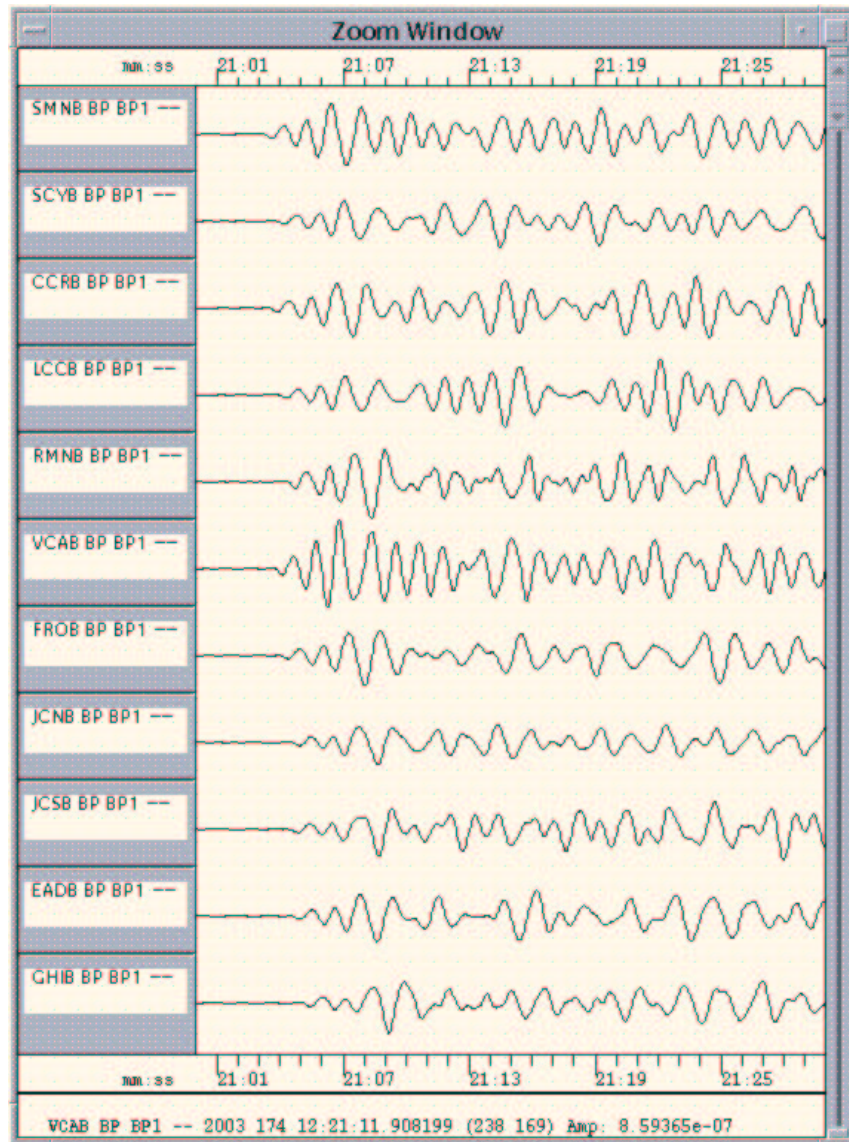


Figure 5.2: Displayed are 30 seconds of 0.5-2.0 Hz BP filtered vertical ground velocity data for a M_w 6.9 deep focus teleseism which occurred 6/23/2003 at 12:12 UT at a depth of 685 km in the vicinity of the Rat Islands in the Aleutian Islands chain (51.44N,176.78E). The traces have been ordered by increasing distance (top to bottom), their waveforms are absolute scaled to allow comparisons between the response functions between stations. The great circle distance to the HRSN is approximately 46.5 degrees with an azimuth of $\sim 310^\circ$. The recording of this teleseism on the Northern Hayward Fault Network is show in Figure 4.2.

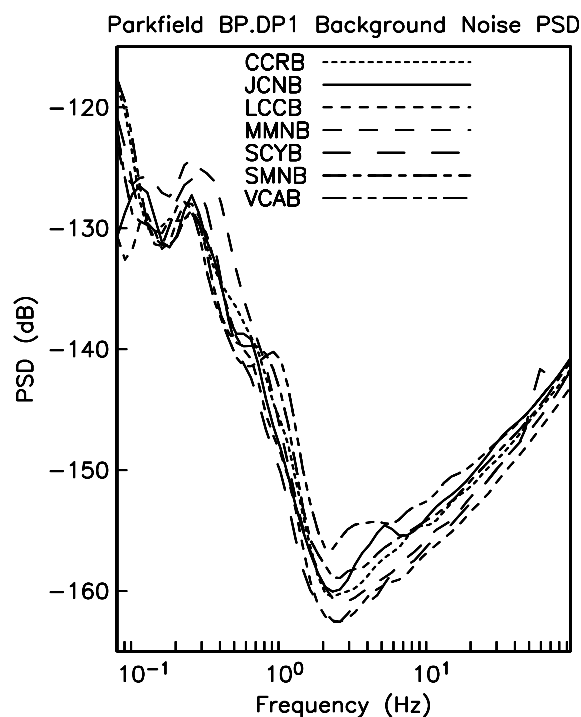


Figure 5.3: Background noise PSD plot for the seven continuously telemetered BP.DP1 data streams from Parkfield. The data are 20 minute samples starting at 2003.225.0900 (2 AM PDT). The plots show the background noise PSD as a function of frequency for the the highest available sampling rate (250 sps) vertical component data which are continuously telemetered to Berkeley. Note the relatively low PSD levels and the overall consistency for all the HRSN stations. By comparison, the PSD curves among the borehole Northern Hayward Fault Network (NHFN) land and bridge stations (Figure 4.3) are much more variable and show a generally higher background noise level. On the other hand, PSD curves for the MPBO stations of the NHFN are much more consistent with the HRSN PSD's (Figure 8.6). The differences among the various station PSD's can, in large part, be explained by the relative cultural noise levels at the various stations, by the depth of the borehole sensors, and by whether the boreholes remain open holes (noisier) or have been filled with cement. The 2 Hz minimum in the PSD plots for the HRSN sensor results from the 2 Hz sensors used at these sites. Below 2 Hz, noise levels rise rapidly and the peak at 3 sec (.3 Hz) is characteristic of teleseismic noise observed throughout California. In the 2 to 5 Hz range, VCAB and JCNB have historically shown higher background noise which is believed to result from excitation modes in the local structure. A small 60 Hz blip can be seen in the SCYB curve due to its close proximity to a power-line.

fixes for these problems. We are also continuing to improve the HRSN event detection sensitivity by refining the HRSN triggering scheme.

Solar Regulators

Regularly occurring spikes occurring during the daylight hours were observed in the continuous data streams and found to be due to the solar regulators. We have tested a variety of solar regulator designs and have identified the Prostar 30 as having the optimal cost-benefit. We have purchased and installed several of these devices at several of the HRSN sites with the ultimate goal of installing the Prostar's at all the HRSN stations as time and funding permit.

Pre-amplifier Noise

We found that a significant source of artificial noise was coming from the station pre-amplifiers. In the upgraded system, preamps from the older network were used. During integration of the older preamps with the increased dynamic range capabilities of the 24-bit Quanterra system, gain settings of the preamps were reduced from $\times 10,000$ to $\times 80$ in order to match signal sensitivity of the new system with the older one. While these lower preamp gain levels are still within the operational design of the preamps, they are no longer in their optimal range and a significant contribution of preamp's self-generated noise is present in the recorded seismograms. Initially, this was not expected to be a significant problem. However, we have subsequently found that even the small increase in preamp noise that results from the preamp gain reduction significantly impacts the sensitivity of the network for detecting and recording the smallest locatable events.

Figure 5.4 shows the preamp noise reduction effect observed on background noise signals at three vertical components of the HRSN when gains are raised from $\times 80$ to $\times 1,000$. Considerable signal hash is seen at gain levels of $\times 80$ (top waveform in each station pair), and significantly reduced when gains are increased to $\times 1,000$ (lower waveforms). Since we are also interested in recording large earthquakes on-scale, simply increasing gain levels on all stations is not the preferred solution, since doing so causes the recording system to saturate at much lower magnitudes. Instead we are attempting to redesign the preamps using modern components to reduce the noise levels at the lower gain levels. However our attempts at redesign have not yet yielded satisfactory results.

Since a primary objective of the HRSN is to monitor the evolving patterns of the numerous small earthquakes that occur at very low magnitudes, and since this objective also complements the scientific objectives of the recently funded SAFOD experiment, it is important to address the preamp noise problem in a timely manner. We have opted, therefore, to raise the gain levels for the

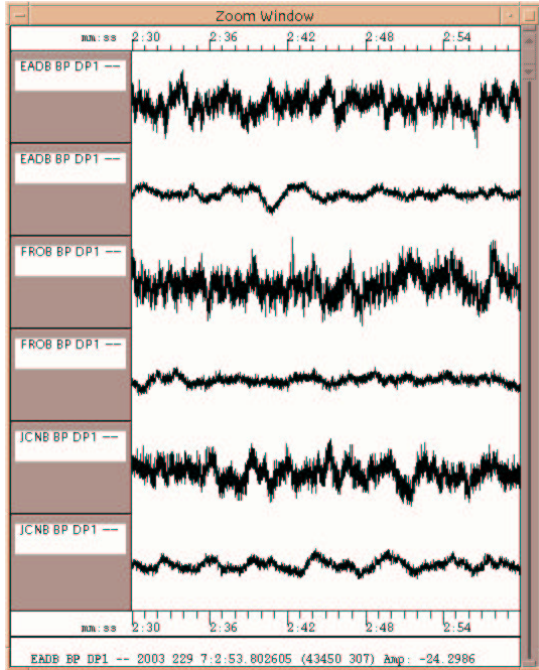


Figure 5.4: Preamp noise reduction test. Shown are 30 seconds of vertical background signal recorded at stations EADB, FROB and JCNE on day 229 of 2003 at 0700 UTC (top of station pairs, recorded at x80 gain and scaled up by 1000/80 for comparison to the x1000 preamp gain levels) and 0700 UTC on day 233 (bottom of station pairs, recorded at x1000 preamp gain). Note the substantial reduction in background noise, due primarily to the lower preamp generated noise at higher preamp gain.

near-term on all the station preamps from x80 to x1,000. These gain changes are currently (late August, 2003) being implemented, and we estimate that the number of small earthquakes we will detect will increase by a factor of 2 to 3. We will continue investigating preamp redesigns until a suitable alternative is found at which time we will install the new preamps and lower the preamp gain back to x80—allowing both the increased detection of small events and the on-scale recording of events up to about magnitude 4 to 4.5.

Triggering Refinement

Additional efforts underway to increase event detection sensitivity include: 1) development of a station specific filtering scheme for input into the triggering algorithm, 2) refinement of the multi-station trigger association algorithm to include subnet triggering, and 3) incorporation of the pilot hole array data into the network trigger-

ing scheme to capture the smallest events in the SAFOD drilling area.

3.3 Routine Data Analysis

Monitoring the evolution of microseismicity, particularly in the SAFOD drilling and target zone, is a primary objective of the HRSN project. In addition, the continued analysis of the HRSN data for determining detailed seismic structure, for the study of similar and characteristic microearthquake systematics, for estimation of deep fault slip rate evolution, and for various studies of fault zone and earthquake physics is also of great interest to seismologists. Before advanced studies of the Parkfield microseismicity can take place, however, initial processing, analysis and routine cataloging of the earthquake data must be done. An integral part of this process is quality control of the processed data, including a final check of the routine catalog results.

Initial Processing

At this time, continuous data streams on all 39 components are being recorded at 20 and 250 sps on disk on the local HRSN computer at the CDF facility and when the local disk space is full, the continuous data is migrated onto DLT tape. The 20 sps data are transmitted continuously to the BSL over the frame-relay linked and archived at the NCEDC. In addition, the vertical component channels for the 7 stations critical to resolving seismicity in the SAFOD area are also being transmitted continuously to the BSL at 250 sps over the frame relay-circuit for purposes of quality control and fine tuning the triggering algorithm for the detection of the smallest possible events around SAFOD.

Shortly after being recorded to disk, event triggers for the individual station data are determined and a multi-station trigger association routine then processes the station triggers and identifies potential earthquakes. For each potential earthquake trigger, 30 second waveform segments are then collected for all stations and components, assigned a unique event identifier (compatible with the NCEDC classification scheme) and saved as an event gather. Event gathers are then periodically telemetered to BSL and included directly into the NCEDC earthquake database (dbms) for analysis and processing.

An ongoing effort has been the development of a new earthquake triggering scheme, with the goal of routinely detecting SAFOD area events to magnitudes below -1.0. A first cut version of the new scheme has been implemented and is already detecting earthquakes at an increased rate—nearly 3 times the number of earthquakes detected before the upgrade.

In order to facilitate the processing and archiving of this large number of events (approx. 150 per month), BSL personnel have recently developed a Graphical User Interface (GUI). The GUI is integrated with the NCEDC

dbms and allows review of the waveforms from every triggered event. Initial analysis of the data using the GUI involves review of the waveforms and classification of the event as an earthquake or non-earthquake event. The GUI also allows the analyst to log potential network problems that become apparent from the seismograms. The HRSN analyst then classifies the event as a local, distant-local, regional, or teleseismic event and then systematically hand picks the P- and S-phases for the local and distant local events.

Picking of the numerous microearthquake events is no mean task. On average about 7 P-phases and 4 S-phases are picked for each event, putting the total number of annual phase picks for the HRSN data on the order of 19,000 to 20,000. We have experimented with algorithms that make initial auto-picks of the phase arrivals, but have so far found picking by hand to be an advantage since it forces the analyst to review each pick carefully while at the same time allowing him to assess the state of health of recording on each station-component in detail. In all our tests, repicked autopicks have also invariably resulted in catalog locations that are significantly more scattered and that have higher residuals than locations done with purely hand-picked data.

A peculiarity of processing very small earthquake data, is that multiple events commonly occur within a few seconds of one another (Figure 5.5). The close timing of these events does not allow the local triggering algorithm to recover from one event before another occurs. As a result, the central site processor often does not trigger uniquely for each event. In such cases only one, 30 sec waveform gather and one earthquake identifier will be created for all the events. These multiple earthquake records (MER) account for only 3 to 5% of the total seismicity recorded by the HRSN. However, there are times when this rate rises to over 10%. In order to assign each event in an MER a unique event identifier for the NCEDC dbms and to make picking and automated processing of these events more manageable an additional feature of the GUI was developed that allows the analyst to "clone" MER into separate gathers for each event.

Quality Control

Once false triggers have been removed and picks for the events completed, quality control on the picks is made to ensure that all picks have phase and weights assigned, that extraneous characters have been removed from the pick files, that double station-phase picks have not inadvertently been made, and that no repicks of the same event had been accidentally made during any cloning that was performed.

Initial locations are then performed and phase residuals analyzed in order to determine whether severe pick outliers must be removed or adjusted. Unstable location solutions based on events with few picks are also assessed

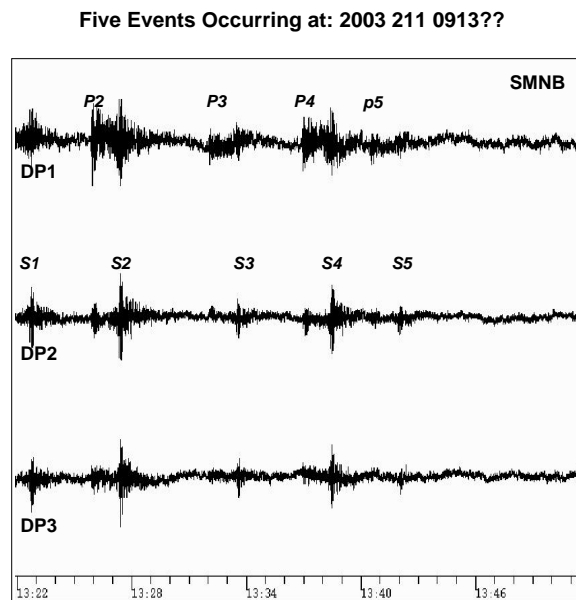


Figure 5.5: Five events occurring on the same MER. The P phase of the first event was not captured on this record. These five events occurred as part of a swarm of 47 small events recorded by the HRSN that occurred on day 211 of 2003. Of these 47 events, the NCSN catalog contains only 2. Events shown are all less than magnitude 0.

to see if the addition of marginal phases will improve the stability of the location determination.

After any required pick adjustments have been made, the events are then relocated, and combined with error information to allow ranking of the confidence of location quality.

These procedures have all been put in place and tested over the past year for the new HRSN configuration. Currently we have located 9 months of data recorded by the new HRSN (over 1300 events) and are staying current with ongoing seismicity and also moving backwards in time to pick and locate the earlier data collected since early 2001.

We now have enough data and are confident enough with the procedures to begin organizing the locations for formal inclusion into the NCEDC dbms and dissemination to the community. These efforts are now underway. We are also in the early stages of establishing a scalar seismic moment catalog for the new HRSN events that is also to be included in the NCEDC dbms.

Catalog Assessment

We continue to examine the ongoing earthquake data being collected by the HRSN in search of possible earthquake precursors. This includes quality control and evaluation of the routine earthquake catalog locations and analyses of the spatial and temporal distribution of the microseismicity in relation to the occurrence of larger earthquakes in the area and heightened alert levels declared as part of the Parkfield Prediction Experiment. Even before our planned enhancement of HRSN performance, the new central detection system that operates at the telemetry hub, along with real-time telemetry of selected high-sensitivity channels to Berkeley for monitoring, allows event detection below magnitude 0.0. As a result, the rate of earthquake detection by the HRSN exceeds that of the NCSN by about a factor of 3 in the 30 km stretch of the SAF centered at the location of the 1966 M6 Parkfield event (Figure 5.6). The additional rate of HRSN event detection significantly increases both the spatial and temporal coverage of the changing seismicity patterns and provide unique additional information on the earthquake pathology at very low magnitudes. With our planned noise reduction and triggering enhancement, we estimate the proportion of HRSN located events relative to the NCSN catalog to increase by an additional factor of 2. Differences between earthquake locations evident in Figure 5.6 are largely attributable to the more advanced 3-D P- and S- wave velocity model used in determining the HRSN locations and the more accurate hand-picked P- and S- phases made possible by the high sampling rate (250 sps) and horizontal component borehole recordings of the HRSN.

4. Acknowledgements

Thomas V. McEvelly, who passed away in February 2002, was the PI on the HRSN project for many years, and without his dedication and hard work the creation and continued operation of the HRSN would not have been possible. His contributions continue to be appreciated in the extreme and the fruits of his labor many-fold.

Under Bob Nadeau's and Doug Dreger's general supervision, Rich Clymer, Wade Johnson, Bob Uhrhammer, Doug Neuhauser, Don Lippert, Bill Karavas, John Friday, Pete Lombard, and Lane Johnson all contribute to the operation of the HRSN. Bob Nadeau prepared this chapter with the assistance of Bob Uhrhammer and Wade Johnson.

During the period of this report, the operation and maintenance of the HRSN and the processing and archiving of its data was supported in large part by the USGS, through the NEHRP External Grants Program (grants: 02HQGR0067 and 03HQGR0065). NSF also provided support for the expansion of the HRSN near the SAFOD drill site through grant EAR-9814605.

5. References

Bakun, W. H., and A. G. Lindh, The Parkfield, California, prediction experiment, *Earthq. Predict. Res.*, 3, 285-304, 1985.

Daley, T.M. and T.V. McEvelly, Shear wave anisotropy in the Parkfield Varian Well VSP, *Bull. Seism. Soc. Am.*, 80, 857-869, 1990.

Karageorgi, E., R. Clymer and T.V. McEvelly, Seismological studies at Parkfield. IV: Variations in controlled-source waveform parameters and their correlation with seismic activity, 1987-1994, *Bull. Seismol. Soc. Am.*, 87, 39-49, 1997.

Michelini, A. and T.V. McEvelly, Seismological studies at Parkfield: I. Simultaneous inversion for velocity structure and hypocenters using B-splines parameterization, *Bull. Seismol. Soc. Am.*, 81, 524-552, 1991.

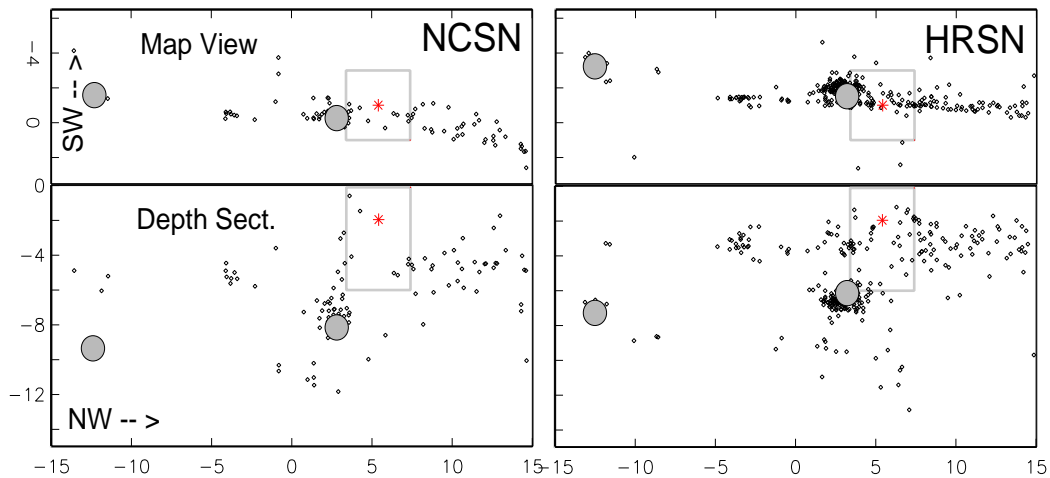


Figure 5.6: Comparison of NCSN and HRSN catalog locations for the period September through November of 2002. During this period, magnitude M3.8 and M4.2 earthquakes occurred at about -13 and $+3$ km NW, respectively (gray disks). The proposed SAFOD drilling target is shown as an asterisks and a 4×4 km gray box of 6km depth is shown surrounding the target (corresponding to the 4×4 km box in Figure 5.1). The region shown is centered on the hypocentral region of the 1966 Parkfield M6 earthquake that occurred at 0 km at about 9 km depth. The lower magnitude detection and greater rate of microearthquake detection by the HRSN provides increased spatial coverage and detail in the temporal pattern of the evolution of seismic activity in the region. Station coverage in the region is comparable for both networks, yet the more accurate S- phase picks possible on the horizontal HRSN component seismograms and the use of a 3-D P and S velocity model for hypocentral inversion provides a sharper picture of the fault zone structure. On average the current detection rate of locatable earthquakes by the HRSN is about 3 times that of the NCSN. Planned enhancements for the HRSN are expected to increase rate of locatable earthquakes by an additional factor of 2 to 3.

Chapter 6

Parkfield-Hollister Electromagnetic Monitoring Array

1. Introduction

The primary objective of the UC Berkeley electromagnetic (EM) monitoring array is to identify EM fields that might be associated with earthquakes. The array has consisted of up to three sites since 1995 at SAO, PKD, and PKD1, each of which measures three orthogonal components of the magnetic field and two orthogonal components of the electric field. Such an array is necessary in order to separate the fields of a local source (e.g., an earthquake signal) from the natural EM fields of the Earth. Our approach has been to determine the transfer function between fields at different sites for periods of normal background EM variations and then use this transfer function to predict fields between sites. Differences between the observed and predicted fields are used to search for anomalous local fields.

Analysis of the UCB array has shown that cultural noise from the San Francisco Bay Area (in particular BART) extends over surprisingly large areas, and that natural ionospheric sources may exhibit significant spatial complexity (Egbert et al., 2000). The fundamental MT assumption of spatially uniform sources is thus frequently violated in this area. These source complications are highly variable in time, reducing the effectiveness of a single remote site for EM noise cancellation. Multiple remote sites would allow significantly better cancellation of these more spatially complex EM noise fields, and would also reduce bias errors in the inter-station transfer function estimates. It was always the goal of the project to have three stations, but in 1999 the use permit at Haliburton Ranch was lost and PKD1 was removed just one month after PKD was installed. Analysis of data from this one month clearly demonstrates the value of three sites for improving the residual analysis, 2000 BSL Annual Report.

2. MT Overview

In 1995 we installed two well-characterized electric and magnetic field measuring systems at two sites along the San Andreas Fault which are part of the Berkeley Digital Seismic Network. Since then, magnetotelluric (MT) data have been continuously recorded at 40 Hz and 1 Hz and archived at the NCEDC (Table 6.1 and 6.2). At least one set of orthogonal electric dipoles measures the vector horizontal electric field, E , and three orthogonal magnetic sensors measure the vector magnetic field, B . These reference sites, now referred to as electromagnetic (EM) observatories, are co-located with seismographic sites so that the field data share the same time base, data acquisition, telemetry and archiving system as the seismometer outputs.

The MT observatories are located at Parkfield (PKD1, PKD) 300 km south of the San Francisco Bay Area and Hollister (SAO), halfway between San Francisco and Parkfield (Figure 6.1). In 1995, initial sites were established at PKD1 and SAO, separated by a distance of 150 km, and equipped with three induction coils and two 100 m electric dipoles. PKD1 was established as a temporary seismic site, and when a permanent site (PKD) was found, a third MT observatory was installed in 1999 with three induction coils, two 100 m electric dipoles, and two 200 m electric dipoles. PKD and PKD1 ran in parallel for one month in 1999, and then the MT observatory at PKD1 was closed.

Data at the MT sites are fed to Quanterra data loggers, shared with the collocated BDSN stations, synchronized in time by GPS and sent to the BSL via dedicated communication links.

3. 2002-2003 Activities

Over the past year new electrodes have been installed at the PKD site, and automated quality control software has been implemented. Any failures of the UCB MT array are now immediately detected so that corrective

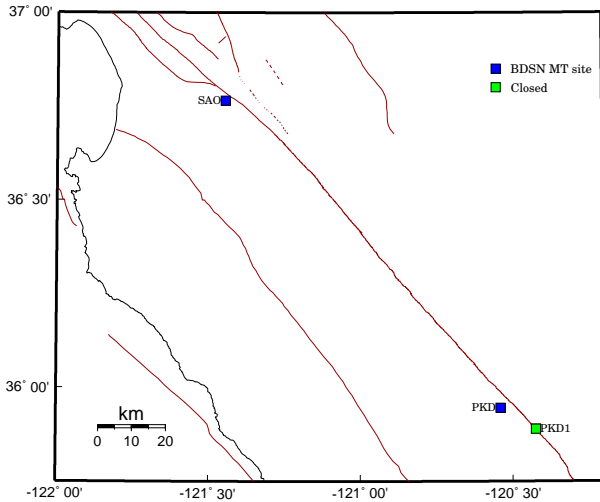


Figure 6.1: Map illustrating the location of operational (filled squares) and closed (grey squares) MT sites in central California.

action can be taken in a timely fashion. With these improvements in the system, nearly continuous high quality data have been collected.

This year time domain processing codes have been developed and tested on short segments of data. Karl Kappler is using a least squares Wiener filter, while Gary Egbert employs multivariate array transfer functions.

3.1 Station Maintenance

SAO

In January of this year the Q4120 datalogger was replaced. In February, the Hx coil was replaced.

PKD

Last September, lead-lead chloride electrodes from John Booker were installed in the 200 m dipoles. They require less maintenance than the copper-copper sulfate electrodes used in the 100 m dipoles. The addition of bentonite has significantly improved water retention in the electrode holes, increasing electrode longevity. In December the vertical coil was replaced, and in May and June 2003, the batteries powering the electric field pre-amplifiers were replaced.

Instrument Responses

Sierra Boyd ensures the transfer function information at the NCEDC is correct and current.

3.2 Data Quality Control

During this year, BSL staff worked in collaboration with Gary Egbert to install his software for automated

data processing. The software provides the capability of identifying problems and alerting staff. There is a daily printout of the signal to noise ratios (SNR) in dB for each channel of the array. Currently, SNR's below 10 dB are flagged for inspection or repair by the array operators.

4. Data Processing

An effort has been made to do residual analysis purely in the time domain. The data used are the MT measurements on all five channels sampled at 1Hz. Since the station mostly sees noise originating by large sheet currents in the ionosphere, and the distance between sites is only a few hundred km, the input EM signal at each station should be roughly the same. Thus, a transfer function (TF) between two sites should be approximately constant. The relationship between the two sites is determined at a time when no significant seismic activity (SSA) is occurring near the arrays. On a day when SSA is present at one site, we can examine the residuals for anomalous activity.

4.1 Residuals

In this section we use an impulse response operator (IRO) rather than a TF as we are working in the time domain. The current IRO is a Wiener filter computed using least squares. The operator is computed using a days worth of data (86400 observations). Before computing the operator, the data must be despiked. For this, an automated despiking algorithm has been employed. Time series data are scanned for anomalies which lie more than a user specified number of standard deviations from the sample mean (default is 10). When an outlier is observed, the corresponding channel at the other station is examined within a two minute window about the time of the outlier. If a similar event took place, the anomaly is considered signal. Otherwise it is considered anomalous noise and is replaced. Currently a two minute window about the spike is replaced with a linear fit. Substituting with an ARMA (AutoRegressive Moving Average) model prediction has also been used, but is not yet the standard.

After despiking, the data are detrended using a first order polynomial. Then the IRO is computed. To predict a given channel we use all five channels at the other site. Denoting the channel to be predicted as the time series $\{X_t\}$ we obtain the formula

$$X_t = \sum_{ch=1}^5 \Psi_{ch} * T_{ch} \quad (6.1)$$

where ch denotes that the sum is over each channel, and each channel has its own convolution operator. The * then denotes the convolution between the filter and T , the time series.

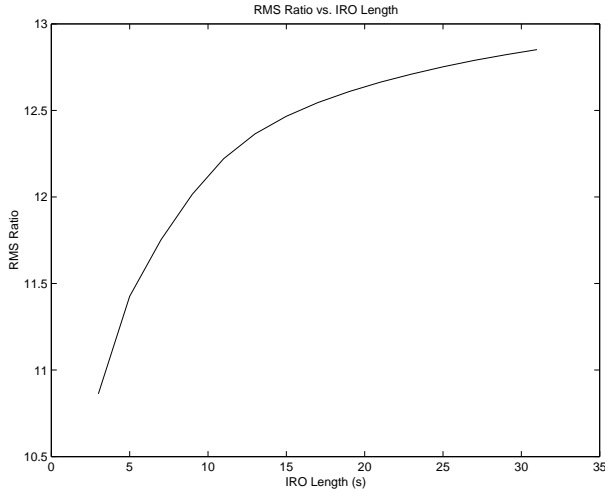


Figure 6.2: As the filter gets longer, the fit is better.

The length of the IRO can be any odd number. It has been observed that by using a longer IRO, predictions improve. With a long enough operator the least squares fit can be made arbitrarily fine ($\text{RMS}(\text{signal-fit}) \rightarrow 0$), but such a fine fit is also fitting noise unique to the data segment used to compute the IRO. We choose an IRO length which gives a fit roughly as good as it gives a prediction of future signal. The following chart (Figure 6.2) shows the ratio of the RMS signal to residuals as a function of IRO length.

Due to the computing power needed for this approach (inverting a matrix of dimension 5 times the filter length, and multiplying two matrices of dimension [number of seconds of data, 5xfilter length]), we can see that the number of calculations rises quadratically with filter length. For day long time segments (86400 rows) it is difficult to compute an IRO much longer than 35. An optimization can be performed for a given time segment length to determine the best IRO length. These may include a constrained least squares inversion using support vector machines, or ARMA approaches. For simply reducing one channel to residuals through modeling, invertible ARMA methods yield reduction as good or better. The disadvantage to this type of modeling, however, is that it is difficult to use in predicting one station from another. Furthermore, the method is expensive on computing power and can only model short segments, say of order one hour, with the current computing system and software.

Figure 6.3a shows the result of five 11-point Wiener filters applied to the five channels of Parkfield on day 228 in 1996. This day was chosen for its good signal to noise ratios in the raw data, and the fact that a M4.0 quake occurred one month later near the Parkfield array. The IRO was computed using this day's data, so this is

Sensor	Channel	Rate (sps)	Mode	FIR
Magnetic	VT?	0.1	C	Ac
Magnetic	LT?	1.0	C	Ac
Magnetic	BT?	40.0	C	Ac
Electric	VQ?	0.1	C	Ac
Electric	LQ?	1.0	C	Ac
Electric	BQ?	40.0	C	Ac

Table 6.2: Typical data streams acquired at each MT site, with channel name, sampling rate, sampling mode, and FIR filter type. C indicates continuous; T triggered; Ac acausal.

essentially a least squares fit. The edges are imperfect, but the fit is generally excellent. The RMS ratio is around 12.2; however, if we neglect the edges (5000 s to either side), the RMS is 14.

In Figure 6.3b, the day 228 filters are used for prediction of day 230. We can see that the shape of the fit is again excellent, but there are some long period effects, which leave the prediction higher than the signal in some places and lower than the signal in others.

In the raw data there have been some long period instrument related diurnal effects in the magnetic data. A high pass filter has been designed for this job. Care is required in filtering out the long period signals, as the MT precursors we are looking for could be low frequency.

4.2 The Future

The residual analysis in time domain is free of the frequency domain inherent errors. The Gibbs phenomenon and effects due to discrete modeling are non existent. The time domain residuals can be computed and scanned for anomalous activity. Bandpass filtering of the raw data will likely remove some of the prediction misfit. Also, cutting the data into smaller parcels (one-three hours) and detrending each of these segments individually may reduce some of the long period noise. High frequency noise also leads to misfits in data. Low pass filters need to be employed to decimate signal to about 0.03 Hz, as we are looking for signals with duration greater than half a minute. Cleaning out this high frequency noise will likely improve predictions. The code is in place to begin the filtering this fall. Experiments with other prediction methods (such as constrained LS and ARMA's mentioned earlier) will continue as well. The plan is to have an automated system which reads in data from the array, despikes, computes residuals, and then scans the residuals for RMS anomalies in place over the next 4 months.

5. Acknowledgements

Frank Morrison directs the MT program, and collaborates closely with Gary Egbert of Oregon State Univer-

sity and Steve Park of UC Riverside. Sierra Boyd, John Friday, Lind Gee, and Doug Neuhauser also contribute to the operation of the MT observatories. Karl Kappler, Sierra Boyd, Gary Egbert, and Lind Gee contributed to the preparation of this chapter.

Support for the MT array is provided by the USGS through the NEHRP external grants program and by the Plato Malozemoff Chair in Mineral Engineering held by Frank Morrison.

6. References

Egbert, G.D., M. Eisel, O.S. Boyd and H.F. Morrison, DC trains and Pc3s: Source effects in mid-latitude geomagnetic transfer functions, *Geophys. Res. Lett.*, 27, 25-28, 2000.

Egbert, G.D., Robust Multiple-Station Magnetotelluric Data Processing, *Geoph. J. Int.*, 130, 475-496, 1997.

Eisel, M., and G.D. Egbert, On the stability of magnetotelluric transfer function estimates and the reliability of their variances, *Geophys. J. Int.*, 144, 65-82, 2001.

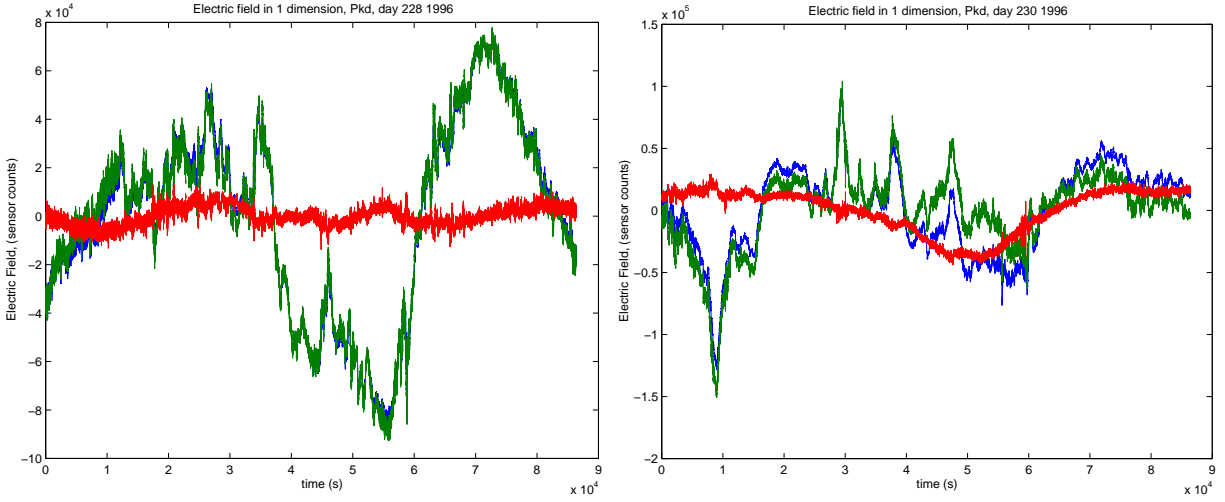


Figure 6.3: it a): A least squares fit (green) to the signal (blue), and the residuals (red), using an 11 point filter to the PKD data of day 228 in 1996. b): Signal(blue), prediction (green), and residual(red) from using the day 228 filters to predict day 230. Note the change in scale from figure a.

Site	Net	Latitude	Longitude	Elev (m)	Date	Location
PKD	BK	35.945171	-120.541603	583	1999/02/05 -	Bear Valley Ranch, Parkfield
PKD1	BK	35.8894	-120.426109	431.6	1995/06/06 - 1999/03/08	Haliburton House, Parkfield
SAO	BK	36.76403	-121.44722	317.2	1995/08/15 -	San Andreas Obs., Hollister

Table 6.1: Sites of MT observatories

Chapter 7

Bay Area Regional Deformation Network

1. Introduction

The Bay Area Regional Deformation (BARD) network of continuously operating Global Positioning System (GPS) receivers monitors crustal deformation in the San Francisco Bay area (“Bay Area”) and northern California (Murray *et al.*, 1998). It is a cooperative effort of the BSL, the USGS, and several other academic, commercial, and governmental institutions. Started by the USGS in 1991 with 2 stations spanning the Hayward fault (King *et al.*, 1995), BARD now includes 70 permanent stations (Figure 7.1). The principal goals of the BARD network are: 1) to determine the distribution of deformation in northern California across the wide Pacific–North America plate boundary from the Sierras to the Farallon Islands; 2) to estimate three-dimensional interseismic strain accumulation along the San Andreas fault (SAF) system in the Bay Area to assess seismic hazards; 3) to monitor hazardous faults and volcanoes for emergency response management; and 4) to provide infrastructure for geodetic data management and processing in northern California in support of related efforts within the surveying and other interested communities.

BARD currently includes 38 continuously operating stations in the Bay Area and northern California (Table 7.1), 14 near Parkfield along the central San Andreas fault, and 18 near the Long Valley caldera near Mammoth (Table 7.2). The BSL maintains 22 stations (including 2 with equipment provided by Lawrence Livermore National Laboratory (LLNL) and UC Santa Cruz). Other stations are maintained by the USGS (Menlo Park and Cascade Volcano Observatory), LLNL, Stanford University, UC Davis, UC Santa Cruz, and East Bay Municipal Utilities District, the City of Modesto, the National Geodetic Survey, Thales, Inc., and the Jet Propulsion Laboratory. Many of these stations are part of larger networks devoted to real-time navigation, orbit determination, and crustal deformation.

Between 1993 and 2001, the BSL acquired 29 Ashtech Z-12 and Micro-Z receivers from a variety of funding sources, including from federal (NSF and USGS), state (CLC), and private (EPRI) agencies. The network en-

hances continuous strain measurements in the Bay Area and includes several profiles between the Farallon Islands and the Sierra Nevada in order to better characterize the larger scale deformation field in northern California (Figure 7.1). Five more of the BSL receivers will be installed next year, 2 along the southern Hayward fault, and 3 as part of the NSF-funded Mini-PBO project establishing collocated GPS, and borehole strainmeter and seismometer observatories in the Bay Area (see Chapter 8).

The number of continuous GPS stations in northern California will dramatically increase over the next 5 years, with over 250 new site installations planned as part of the Plate Boundary Observatory (PBO) component of the NSF-funded Earthscope project. The BARD network will form the initial core of the northern California array, and the BSL recently received NSF funding to maintain 40 stations for an 18-month period. During this period, BARD and the other regional networks, such as SCIGN, BARGEN, and PANGA, will be developing plans to fold operation and maintenance of portions the existing networks into the PBO array at the end of 5 years. We are working closely with UNAVCO, Inc., who has primary responsibility for implementation of PBO, to facilitate this transition and are acting in an advisory role on siting issues for the new installations.

Today, raw and Rinex data files from the BSL stations and the other stations run by BARD collaborators are archived at the BSL/USGS Northern California Earthquake Data Center data archive maintained at the BSL (Romanowicz *et al.*, 1994). The data are checked to verify their integrity, quality, completeness, and conformance to the RINEX standard, and are then made accessible, usually within 2 hours of collection, to all BARD participants and other members of the GPS community through Internet, both by anonymous FTP and by the World Wide Web (<http://quake.geo.berkeley.edu/bard/>).

Many of the BARD sites are classified as CORS stations by the NGS, which are used as reference stations by the surveying community. We coordinate efforts with surveying community at meetings of the Northern California GPS Users Group and the California Spatial Reference Center, and are currently developing plans to use the

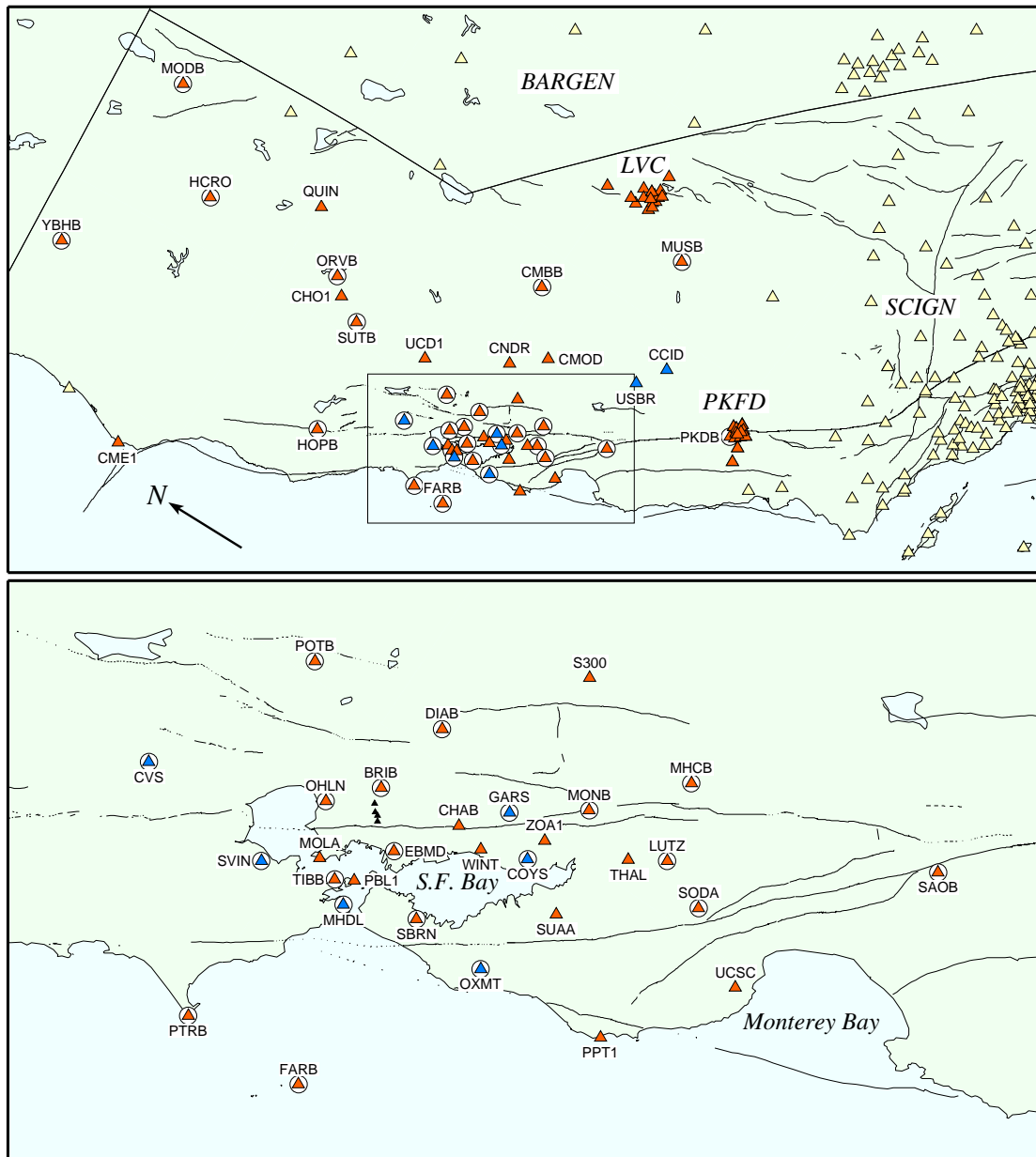


Figure 7.1: Operational (red) and planned (blue) BARD stations in northern California (top) and in the San Francisco Bay area (bottom). In the oblique Mercator projection expected Pacific–North America relative plate motion is parallel to the horizontal. Circled stations use continuous real-time telemetry. The 18 station Long Valley Caldera (LVC) network and 15 station Parkfield (PKFD) networks are also part of BARD. The small black triangles near BRIB are the experimental L1 stations. Mini-PBO stations are OHLN and SBRN (existing), and MHDL, OXMT, and SVIN (planned), all located along the northern Hayward and San Andreas fault. We plan to install 3 other stations at CVS, GARS, and COYS. The 2 Central Valley sites (USBR and CCID) are being installed in cooperation with the CSRC. Other nearby networks (open triangles) include: Basin and Range (BARGEN), and Southern California Integrated GPS Network (SCIGN).

Code	Latitude	Longitude	Start	Receiver	Maint.	Telem.	Location
BRIB	37.91940	-122.15255	1993.58	A-Z12	BSL	FR	Briones Reservation, Orinda
CMBB	38.03418	-120.38604	1993.92	A-Z12	BSL	FR	Columbia College, Columbia
DIAB	37.87858	-121.91563	1998.33	A-Z12	BSL	FR	Mt. Diablo
FARB	37.69721	-123.00076	1994.00	A-Z12	BSL	R-FR/R	Farallon Island
HOPB	38.99518	-123.07472	1995.58	A-Z12	BSL	FR	Hopland Field Station, Hopland
LUTZ	37.28685	-121.86522	1996.33	A-Z12	BSL	FR	SCC Comm., Santa Clara
MHCB	37.34153	-121.64258	1996.33	A-Z12	BSL	FR	Lick Obs., Mt. Hamilton
MODB	41.90233	-120.30283	1999.83	A-Z12	BSL	NSN	Modoc Plateau
MOLA	37.94657	-122.41992	1993.75	T-SSE	BSL		Pt. Molate, Richmond
MONB	37.49892	-121.87131	1998.50	A-Z12	BSL	FR	Monument Peak, Milpitas
MUSB	37.16994	-119.30935	1997.83	A-Z12	BSL	R-Mi-FR	Musick Mt.
OHLN	38.00742	-122.27371	2001.83	A-uZ	BSL	FR	Ohlone Park, Hercules
ORVB	39.55463	-121.50029	1996.83	A-Z12	BSL	FR	Oroville
PKDB	35.94524	-120.54155	1996.67	A-Z12	BSL	FR	Bear Valley Ranch, Parkfield
POTB	38.20258	-121.95560	1998.92	A-Z12	BSL	FR	Potrero Hill, Fairfield
PTRB	37.99640	-123.01490	1998.58	A-Z12	BSL	R-FR	Point Reyes Lighthouse
SAOB	36.76530	-121.44718	1997.58	A-Z12	BSL	FR	San Andreas Obs., Hollister
SBRN	37.68622	-122.41044	2003.18	A-uZ	BSL	FR	San Bruno Mt., Brisbane
SODB	37.16640	-121.92552	1996.33	A-Z12	BSL	R-FR	Soda Springs, Los Gatos
SUTB	39.20584	-121.82060	1997.33	A-Z12	BSL	R-FR	Sutter Buttes
TIBB	37.89087	-122.44760	1994.42	A-Z12	BSL	R	Tiburon
YBHB	41.73166	-122.71073	1996.75	A-Z12	BSL	FR	Yreka Blue Horn Mine, Yreka
CHAB	37.72412	-122.11931	1992.00	A-Z12	USGS		Chabot, San Leandro
WINT	37.65264	-122.14056	1992.00	A-Z12	USGS		Winton, Hayward
EBMD	37.81501	-122.28380	1999.18	T-SSi	EBMUD		EBMUD, Oakland
QUIN	39.97455	-120.94443	1992.68	Rogue	JPL		Quincy
S300	37.66642	-121.55815	1998.48	T-SSi	LLNL		Site 300, Livermore
HCRO	40.81563	-121.46915	2003.50	T-SSi	HCRO		Hat Creek Radio Obs.
CHO1	39.43264	-121.66496	1999.50	A-Z12	NGS		Chico
CME1	40.44177	-124.39633	1995.74	A-Z12	NGS		Cape Mendocino
CMOD	37.64130	-121.99997	2000.76	T-SSi	City		Modesto
CNDR	37.89641	-121.27849	1999.27	A-Z12	NGS		Condor, Stockton
PBL1	37.85306	-122.41944	1995.50	A-Z12	NGS		Point Blunt, Angel Island
PPT1	37.18167	-122.39333	1996.00	A-Z12	NGS		Pigeon Point
SUAA	37.42691	-122.17328	1994.30	A-Z12	SU		Stanford University
THAL	37.35149	-121.93549	2003.00	A-uZ	Thales		Thales, Inc., Santa Clara
UCD1	38.53624	-121.75123	1996.38	T-SSi	UCD		UC Davis
UCSC	36.99279	-122.05219	2000.31	T-SSi	UCSC		UC Santa Cruz
ZOA1	37.54305	-122.01594	2002.50	Novatel	FAA		Fremont

Table 7.1: Currently operating stations of the BARD GPS network maintained by the BSL or by other agencies except in the Parkfield and Long Valley caldera regions. Other agencies include: EBMUD = East Bay Mun. Util. Dist., UCD = UC Davis, SU = Stanford Univ., UCSC = UC Santa Cruz, City = City of Modesto (see also Table 1.1). Receivers: A = Ashtech, T = Trimble. See Table 3.2 for telemetry codes and for BSL sites collocated with seismic stations. Data from other agencies retrieved or pushed by FTP or from the Web.

existing infrastructure at the NCEDC to provide a hub for a high-frequency real-time surveying network in the Bay Area. Data and ancillary information about BARD stations are also made compatible with standards set by the International GPS Service (IGS), which administers the global tracking network used to estimate precise orbits and has been instrumental in coordinating the efforts

of other regional tracking networks. The NCEDC also retrieves data from other GPS archives, such as at SIO, JPL, and NGS, in order to provide a complete archive of all high-precision continuous GPS measurements collected in northern California.

Code	Latitude	Longitude	Start	Receiver	Maint.	Location
CAND	35.93935	-120.43370	1999.33	A-Z12	USGS	Cann, Parkfield
CARH	35.88838	-120.43082	2001.58	A-Z12	USGS	Carr Hill 2, Parkfield
CARR	35.88835	-120.43084	1989.00-2003.31	A-Z12	JPL	Carr Hill, Parkfield
CRBT	35.79161	-120.75075	2001.67	A-Z12	USGS	Camp Roberts, Parkfield
HOGS	35.86671	-120.47949	2001.50	A-Z12	USGS	Hogs, Parkfield
HUNT	35.88081	-120.40238	2001.58	A-Z12	USGS	Hunt, Parkfield
LAND	35.89979	-120.47328	1999.33	A-Z12	USGS	Lang, Parkfield
LOWS	35.82871	-120.59428	2001.58	A-Z12	USGS	Lowes, Parkfield
MASW	35.83260	-120.44306	2001.58	A-Z12	USGS	Mason West, Parkfield
MIDA	35.92191	-120.45883	1999.75	A-Z12	USGS	Mida, Parkfield
MNMC	35.96947	-120.43405	2001.58	A-Z12	USGS	Mine Mt., Parkfield
POMM	35.91991	-120.47843	1999.75	A-Z12	USGS	Pomm, Parkfield
RNCH	35.89999	-120.52482	2001.58	A-Z12	USGS	Ranchita, Parkfield
TBLP	35.91741	-120.36034	2001.67	A-Z12	USGS	Table, Parkfield
BALD	37.78330	-118.90130	1999.67	A-ZFX	CVO	Bald Mt., LVC
CA99	37.64460	-118.89670	1999.67	A-ZFX	CVO	Casa 1999, LVC
CASA	37.64464	-118.89666	1993.00	Rogue	JPL	Casa Diablo, LVC
DDMN	37.74430	-118.98120	1999.67	A-ZFX	CVO	Deadman Creek, LVC
DECH	38.05150	-119.09060	2001.58	A-ZFX	CVO	Dechambeau Ranch, LVC
HOTK	37.65860	-118.82130	2001.67	A-Z12	CVO	Hot Creek, LVC
JNPR	37.77170	-119.08470	1997.81	A-Z12	USGS	Juniper, LVC
KNOL	37.65912	-118.97917	1998.58	A-ZFX	CVO	Knolls, LVC
KRAC	37.71330	-118.88050	2001.67	A-Z12	CVO	Krakatoa-USGS, LVC
KRAK	37.71313	-118.88114	1994.73	Rogue	JPL	Krakatoa, LVC
LINC	37.63719	-119.01729	1998.67	A-Z12	CVO	Lincoln, LVC
MINS	37.65376	-119.06090	1995.92	A-Z12	USGS	Minaret Summit, LVC
MWTP	37.64052	-118.94473	1998.58	A-ZFX	CVO	Mammoth Water Treat Plant, LVC
PMTN	37.83130	-119.05690	1999.67	A-Z12	CVO	Panorama Mt., LVC
RDOM	37.67707	-118.89794	1998.58	A-ZFX	CVO	Resurgent Dome, LVC
SAWC	37.68990	-118.95310	2000.65	A-ZFX	CVO	Saw, LVC
TILC	37.61890	-118.86280	2000.65	A-Z12	CVO	Tilla, LVC
WATC	37.66440	-118.65390	2001.67	A-Z12	CVO	Waterson, LVC

Table 7.2: Currently operating stations of the BARD GPS network maintained by other agencies in the Parkfield and Long Valley caldera regions. Other agencies include: CVO = USGS Cascade Volcano Observatory (see also Table 1.1). Receivers: A = Ashtech. Data from other agencies retrieved or pushed by FTP or from the Web.

2. 2002-2003 Activities

The typical configuration of a BSL continuous GPS station installation has been described in detail in previous annual reports. We here provide a brief description and highlight some of the recent changes. During July 2002–June 2003, we performed maintenance on existing BARD stations, installed a new station, assisted collaborators with the installation of two new stations, and prepared for new stations near the Hayward fault, on the San Francisco peninsula, and north Bay area regions.

2.1 BARD Stations

Each BSL BARD station uses a low-multipath choking antenna, most of which are mounted to a reinforced concrete pillar approximately 0.5–1.0 meter above local

ground level. The reinforcing steel bars of the pillar are drilled and cemented into rock outcrop to improve long-term monument stability. A low-loss antenna cable is used to minimize signal degradation on the longer cable setups that normally would require signal amplification. Low-voltage cutoff devices are installed to improve receiver performance following power outages. Most use Ashtech Z-12 receivers programmed to record data once every 30 seconds, observing up to 12 satellites simultaneously at elevations down to the horizon. The antennas are equipped with SCIGN antenna adapters and hemispherical domes, designed to provide security and protection from weather and other natural phenomenon, and to minimize differential radio propagation delays.

Data from most BSL-maintained stations are collected at 30-second intervals and transmitted continuously over

serial connections (Table 7.1). Station TIBB uses a direct radio link to Berkeley, and MODB uses VSAT satellite telemetry. Nineteen stations use frame relay technology, either alone or in combination with radio telemetry. Thirteen GPS stations are collocated with broadband seismometers and Quanterra data collectors (Table 3.2). With the support of IRIS we developed software that converts continuous GPS data to MiniSEED opaque blockettes that are stored and retrieved from the Quanterra data loggers (*Perin et al.*, 1998), providing more robust data recovery from onsite disks following telemetry outages.

Data from DIAB and MONB in the Bay Area, and 13 stations in the Parkfield regional (all but PKDB), are now being collected at 1 second intervals. Collecting at such high-frequency (for GPS) allows dynamic displacements due to large earthquakes to be better measured, such as was demonstrated by several studies following the 2002 Denali fault earthquake. However, this 30-fold increase in data can be limited by telemetry bandwidth issues. Data from the Parkfield stations are collected on an onsite computer, written to removable disk once per month, and sent to SOPAC for long-term archiving (decimated 30-sec data is acquired daily via the BSL frame relay circuit). In the Bay Area, we have converted the two stations that have sufficient bandwidth and are not collocated with seismic instrumentation. We are currently assessing bandwidth issues at other stations and are planning to convert to 1-second sampling where possible, such as the Mini-PBO stations, in the next year.

The BSL acquired 7 Ashtech MicroZ-CGRS (uZ) receivers with NSF funding for the Mini-PBO project. These receivers, designed for continuous station applications, use less power (5.6 W) than the Z-12 receivers due to the lack of an interactive screen, provide better remote receiver control, and can support serial telemetry in both native raw format and the receiver independent BINEX format. We installed a uZ at SBRN and replaced the Z-12 at OHLN with a uZ in May 2003 after the clock chip on Z-12 at the site began to malfunction. We are currently considering switching to the more compact BINEX format where possible, as this will reduce some of the bandwidth limitations and allow us to convert more stations to 1-second sampling.

The BSL also acquired several Wi-Lan VIP 110-24 VINES ethernet bridge radios. These 2.4 GHz spread spectrum radios use a tree structure to create a distributed ethernet backbone with speeds up to 11 Mbps. Each system uses a directional antenna to talk to its “parent” in the tree, and an omni-directional antenna to talk to its children, if multiple, or a directional antenna if it has only 1 child. These radios offer several advantages over the Freewave radios used at other sites, including TCP/IP ethernet control, higher bandwidth, and greater flexibility for setting up networks. We installed a set of

Wi-Lan radios at the SVIN Mini-PBO station to transmit data from the site to the frame relay circuit, and are assisting EBMUD in converting their continuous station to real-time telemetry using Wi-Lan radios.

2.2 Station Maintenance

In February 2003, telemetry flow of GPS data stopped at MUSB. Access to the site was initially limited by the winter snowpack, and then by the need to coordinate the visit with Southern California Edison engineers. During a visit to the site in August 2003 continuity tests revealed that the hardline antenna cable had apparently failed. This 70 m cable may have been damaged by repeated water freezing in the PVC conduit that houses it. We intend to replace the antenna cable and improve the drainage of the conduit in September 2003.

As part of the Plate Boundary Deformation project (Chapter 8), nine new continuous GPS sites were installed in the Parkfield area (see Table 7.2) in Summer 2001 by the USGS and SIO. These sites span about 25 km on either side of the San Andreas fault and are designed to link the BARD network in central and northern California to the SCIGN network in southern California. As part of this upgrade, the new station CARH was installed at Carr Hill near the original CARR station, which had been running since 1989. After allowing both stations to run side-by-side for nearly 2 years, CARR was turned off in April 2003. In February 2003, the NCEDC assumed responsibility from the USGS Pasadena for the telemetry download of these stations over their existing frame relay circuit at Parkfield. We installed an onsite LINUX computer that controlled the sequential download of data. In June 2003, the stations were upgraded to real-time streaming using Wi-Lan radios by SIO and the USGS.

2.3 New Installations

Throughout the year, we have continued installations for the NSF-funded mini-PBO project establishing collocated GPS, and borehole strainmeter and seismometer observatories in the Bay Area. Completion of these sites have been hampered by problems with the original permitting at Ox Mt and Marin Headlands, and by the need to redesign the GPS antenna mount. The GPS system at the Mini-PBO site SBRN was installed in early March 2003. Two major changes were made since the installation of the first Mini-PBO site at OHLN. We increased the diameter of the upper part of the steel shroud, which protects the borehole casing, from 10 to 14 inches to ensure that the casing remains decoupled from the surface. We also used a new borehole adapter for the GPS mount that was machined from two stainless steel flanges. Should borehole access be needed, this adapter allows a very high level of horizontal accuracy when reinstalling the antenna. These GPS mounts will be installed at the

remaining 3 sites in Fall 2003 after rainfall lessens the fire hazards posed by the required welding of the lower flange onto the casing. For more details about the Mini-PBO station installations, see Chapter 8).

We assisted Hat Creek Radio Observatory (HCRO), located in northeastern California near Mt Lassen (Figure 7.1), in designing and installing a continuous GPS station. The HCRO is installing the new Allen Telescope Array (ATA), which will consist of approximately 350 6.1-meter radio telescope dishes arrayed at the site, for both astrophysical and Search for Extraterrestrial Intelligence (SETI) studies. We previously assisted UC Berkeley astrophysicists in conducting an RTK survey of the HCRO site to determine the optimal locations for the 350 dishes using Trimble RTK equipment purchased for the project. After completion of the RTK survey, the base receiver was converted into the continuous station. The site is set amidst and underlain by extensive lava fields. After extensive reconnaissance of the site, we chose a monument location that is close to the main laboratory buildings, unlikely to be affected by future ATA dish placement, and on a reasonably stable lava flow. In June 2003, we assisted with the construction of a 12"-diameter concrete pier that is anchored to the lava flow outcrop. The Trimble Zephyr antenna was attached using a SCIGN adapter. We are currently establishing data acquisition procedures with the HCRO to archive the data at the NCEDC.

We also assisted Thales, Inc. (formerly Ashtech, Inc.) to establish a continuous GPS station on the roof of their Santa Clara office building. The choking antenna is attached to a metal pin that was drilled and cemented into a corner of the roof's concrete parapet. Data is currently acquired daily by FTP from a server located at Thales, and we are investigating methods to acquire the data more rapidly using some of the TCP/IP capabilities of the recently developed Ashtech iCGRS receiver. Other agencies have also installed new continuous stations in the Bay Area, including an FAA site in Fremont (ZOA1) that will be used for Wide Area Augmentation System (WAAS) navigation control.

2.4 L1-System Profile

The BSL staff is evaluating the performance of the UNAVCO-designed L1 system in an urban setting. This single-frequency receiver is relatively inexpensive but is less accurate than dual-frequency receiver systems that can completely eliminate first-order ionospheric effects. Hence we expect the L1 system to be most useful for short baseline measurements where ionospheric effects tend to cancel due to similar propagation paths. The systems are self-contained, using solar power and integrated radio modems.

In April 2002, we installed 4 sites in a 10-km profile extending normal to the Hayward fault between the UC Berkeley campus and BARD station BRIB (Figure 7.2).

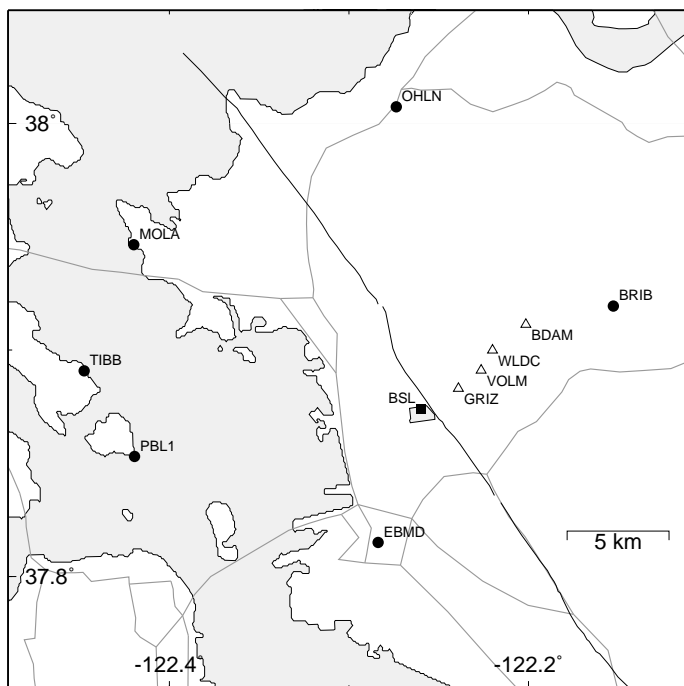


Figure 7.2: Location of L1-system (open triangles) and BARD (closed circles) stations. BSL, just southwest of the Hayward fault, is the location of the Berkeley Seismological Laboratory, where data from the 4 L1-system receivers northeast of the Hayward are telemetered.

Due to the topography of the East Bay hills, each site acts as a repeater for other sites. Data from WLDC passes through all the other stations, with its relay path being (in order) BDAM, VOLM, GRIZ, a repeater on the UC Berkeley Space Sciences Building, and then finally the master radio on the roof of McCone Hall where the BSL is located on campus. This profile, complemented by BRIB and EBMD to the west of the fault, will be most sensitive to variations in locking at 2–8 km depth. We expect that these systems will provide useful constraints on relative displacements near the Hayward fault in 3–5 years, and should help to resolve variations in creeping and locked portions of the fault (e.g., Bürgmann *et al.*, 2000).

Between April 2002 and January 2003, the L1 system operated reasonably well, although problems with faulty batteries solar power regulators caused some loss of data. The Freewave radio at the repeater site SPSC was replaced with an Intuicom system. The original radio was sent in for routine maintenance and was found to have a frequency crystal that was beyond its normal operating range. In mid-January 2003, the solar panel at GRIZ was stolen, which resulted in damage to the cables located outside of the protective metal enclosure. The replacement solar panel was installed in a steel channel frame

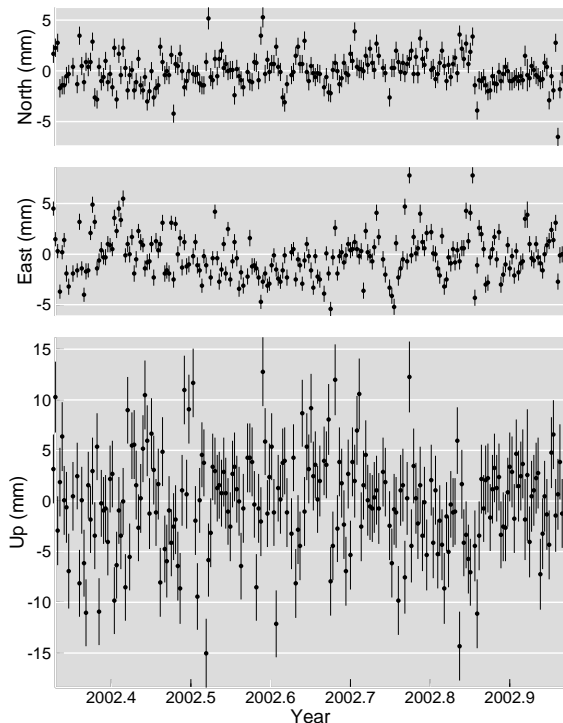


Figure 7.3: Daily estimates of the north, east, and vertical components of the BRIB to BDAM 3-km baseline. Daily repeatabilities are about 1, 2, and 5 mm, respectively.

welded to the vertical steel post that forms the monument base. A 0.5" -thick Plexiglas layer was inserted to protect the surface of the solar panel. Acquisition of all data failed not long after this repair. Initial tests suggested a problem at the repeater site SPSC, but subsequent efforts failed to resolve the problem. In August 2003 we isolated the problem to bad cable connections at the GRIZ sites and re-established operations of the network.

We are processing the data using the GAMIT/GLOBK analysis package, which required modifications to handle L1-only observations. We corrected software provided by UNAVCO to synchronize the phase, pseudorange, and clock offset observables, which allows the data to be cleaned in an automatic fashion. Preliminary results suggest that repeatabilities of 1–2 mm in daily horizontal relative positions and 5 mm in the vertical on the shortest (several km) baselines can be achieved (Figure 7.3), but these degrade to 3–4 mm on the longer (10 km) baselines. We are investigating ways to simultaneously process the dual-frequency data from nearby BARD stations (e.g., BRIB, OHLN), with the single-frequency L1

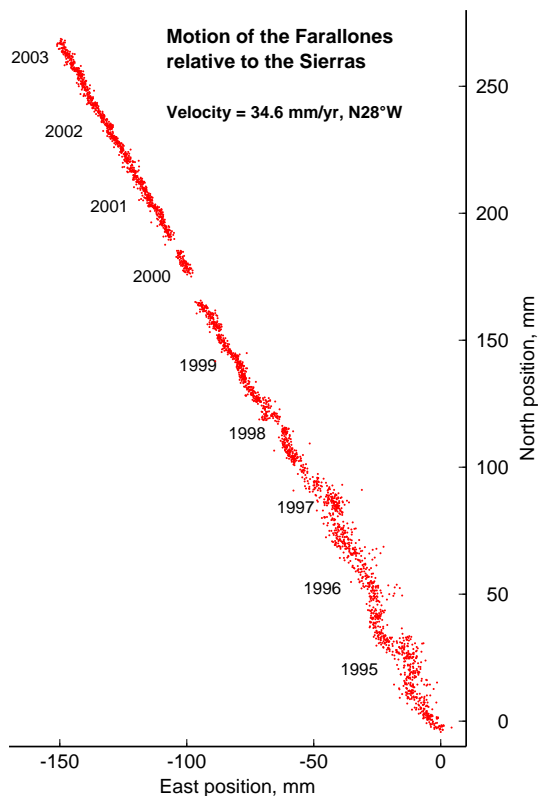


Figure 7.4: Daily position of FARB on the Farallon Islands west of San Francisco relative to CMBB at Columbia College in the Sierran foothills. The greater scatter in the 1994–1998 interval is due primarily to reference frame effects resulting from the weaker fiducial network available at that time.

data to improve these results. Currently data from second frequency on the BARD stations is not used, which degrades the definition of the local reference frame and repeatability of the baselines.

3. Data Analysis and Results

We use the GAMIT/GLOBK software developed at MIT and SIO to process data from the BARD and other nearby continuous GPS networks. We have recently modified our processing strategies to take better advantage of recent enhancements to the GAMIT software and automated scripts. These improvements include better accounting of ocean-tide effects, estimating gradients in atmospheric variations, and applying elevation-dependent weighting to the data observables. We process data from more than 70 stations within hours of the completion of the day using rapid or predicted orbits and are reprocessing older data from the present to 1991 using improved orbits, which we expect to be completed by Fall 2003. Data from 5 primary IGS fiducial sites located in North

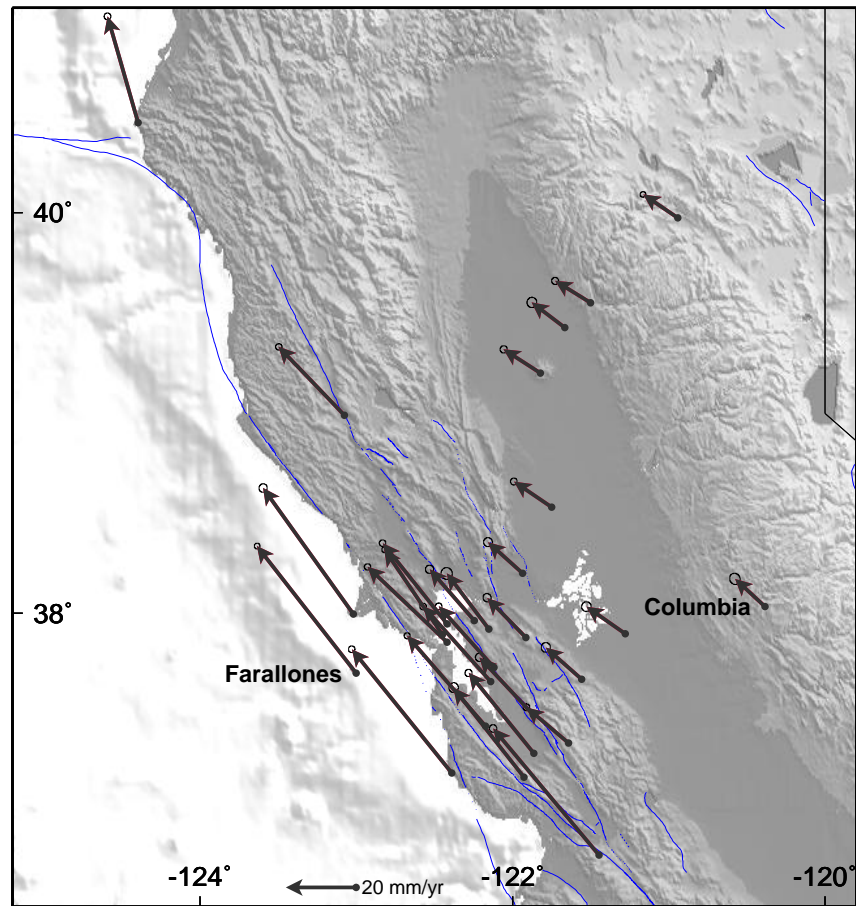


Figure 7.5: Velocities relative to stable North America for the BARD stations derived from 1993–2003 data. Ellipses show 95% confidence regions, assuming white noise only. The 35 mm/yr motion between Columbia and the Farallones is primarily due to shear across the San Andreas fault system.

America and Hawaii are included in the solutions to help define a global reference frame. For long-term velocity estimates, we combine these solutions with global and regional solutions provided by SOPAC to better define a stable North America reference frame.

The estimated relative baseline determinations typically have 2–4 mm long-term scatter in the horizontal components (Figure 7.4) and the 10–20 mm scatter in the vertical. Average velocities for the longest running BARD stations during 1993–2003 are shown in Figure 7.5, with 95% confidence regions assuming only white noise. The velocities are relative to stable North America, as defined by the IGS and CORS fiducial stations. Together with students in the department who are now using the GAMIT software to process survey-mode data in the San Francisco Bay area, we are working to com-

bine the survey-mode and continuous GPS solutions into a self-consistent velocity field for northern California.

Most of the Sierra Nevada sites (CMBB, QUIN, and ORVB), as well as SUTB in the Central Valley, show little relative motion, indicating that the northern Sierra Nevada–Central Valley is tectonically stable. The motion of these sites relative to North America differs from the inferred motion of the western Basin and Range Province, suggesting 3 mm/yr right-lateral shear across the Walker Lane–Mt. Shasta seismicity trend. Deformation along the coast in central California is dominated by the active SAF system, which accommodates about 35 mm/yr of right-lateral shear. The Farallon Island site (FARB) off the coast of San Francisco is moving at nearly the rate predicted by the NUVEL-1A Pacific–North America Euler pole. Two-dimensional modeling

of the observed fault-parallel strain accumulation (*Murray and Segall, 2001*) predicts deep slip rates for the San Andreas, Hayward, and Calaveras/Concord faults are 19.3 ± 1.8 , 11.3 ± 1.9 , and 7.4 ± 1.6 mm/yr, respectively, in good agreement with estimated geologic rates (17 ± 4 , 9 ± 2 , and 5 ± 3 mm/yr, respectively). Most of the 46 mm/yr of relative motion is accommodated within a 100-wide zone centered on the SAF system and a broader zone in the Basin and Range Province in Nevada.

4. Real-Time Processing

We are developing real-time analysis techniques that will enable rapid determinations (within minutes) of deformation following major earthquakes to complement seismological information. We use GAMIT/GLOBK processing techniques to estimate independent hourly solutions at the several cm-level horizontal precision and during the past year established an extension of the REDI system where estimates of postseismic positions are attempted when 10 minutes of data become available following an earthquake (*Murray et al., 2002*).

We currently process 1 hour data batches available within 20 minutes of measurement from more than 20 continuously telemetered BSL and other stations providing hourly data. The hourly solutions have higher scatter than the 24-hour solutions (3–10 mm in the horizontal and 10–30 mm in the vertical), but our simulations suggest that displacements 3–5 times these levels should be reliably detected, and that the current network should be able to resolve the finite dimensions and slip magnitude of a M7 earthquake on the Hayward fault. Due to the poor ability of GAMIT to resolve ambiguities from short data spans, estimates of coseismic displacements within minutes of an event have high (decimeter-level) uncertainty. We are testing a relatively new component of GAMIT that uses Kalman filtering techniques and improved ambiguity resolution methods to provide higher-precision kinematic positions. This method works well for networks with small interstation distances (e.g., near the 1999 Hector Mine earthquake), which aids ambiguity resolution, but has less success on more widely spaced networks, such as the continuous GPS stations in the vicinity of the 2002 Denali earthquake. The August 1998 M=5.1 San Juan Bautista earthquake (*Uhrhammer et al., 1999*) is the only event to have produced a detectable earthquake displacement signal (of 4 mm) at a BARD GPS receiver.

5. Acknowledgements

Mark Murray oversees the BARD program. André Basset, Bill Karavas, John Friday, Dave Rapkin, and Doug Neuhauser contribute to the operation of the BARD and L1 networks. Mark Murray and André Basset

contributed to the preparation of this chapter.

6. References

- Bürgmann, R., D. Schmidt, R.M. Nadeau, M. d’Alessio, E. Fielding, D. Manaker, T. V. McEvelly, and M. H. Murray, Earthquake potential along the northern Hayward fault, California, *Science*, *289*, 1178–1182, 2000.
- King, N. E., J. L. Svarc, E. B. Fogleman, W. K. Gross, K. W. Clark, G. D. Hamilton, C. H. Stiffler, and J. M. Sutton, Continuous GPS observations across the Hayward fault, California, 1991–1994, *J. Geophys. Res.*, *100*, 20,271–20,283, 1995.
- Murray, M. H., and P. Segall, Continuous GPS measurement of Pacific–North America plate boundary deformation in northern California and Nevada, *Geophys. Res. Lett.*, *28*, 4315–4318, 2001.
- Murray, M. H., R. Bürgmann, W. H. Prescott, B. Romanowicz, S. Schwartz, P. Segall, and E. Silver, The Bay Area Regional Deformation (BARD) permanent GPS network in northern California, *EOS Trans. AGU*, *79(45)*, Fall Meeting Suppl., F206, 1998.
- Murray, M., Neuhauser D., Gee, L., Dreger, D., Basset, A., and Romanowicz, B., Combining real-time seismic and geodetic data to improve rapid earthquake information, *EOS. Trans. AGU*, *83(47)*, G52A-0957, 2002.
- Perin, B. J., C. M. Meertens, D. S. Neuhauser, D. R. Baxter, M. H. Murray, and R. Butler, Institutional collaborations for joint seismic and GPS measurements, *Seismol. Res. Lett.*, *69*, 159, 1998.
- Romanowicz, B., B. Bogaert, D. Neuhauser, and D. Oppenheimer, Accessing northern California earthquake data via Internet, *EOS Trans. AGU*, *75*, 257–260, 1994.
- Uhrhammer, R., L. S. Gee, M. Murray, D. Dreger, and B. Romanowicz, The M_w 5.1 San Juan Bautista, California earthquake of 12 August 1998, *Seismol. Res. Lett.*, *70*, 10–18, 1999.

Chapter 8

Plate Boundary Deformation Project

1. Introduction

The Integrated Instrumentation Program for Broadband Observations of Plate Boundary Deformation, commonly referred to as “Mini-PBO”, is a joint project of the BSL, the Department of Terrestrial Magnetism at Carnegie Institution of Washington (CIW), the IGPP at UC San Diego (UCSD), and the U.S. Geological Survey (USGS) at Menlo Park, Calif. It augments existing infrastructure in central California to form an integrated pilot system of instrumentation for the study of plate boundary deformation, with special emphasis on its relation to earthquakes. This project is partially funded through the EAR NSF/IF program with matching funds from the participating institutions and the Southern California Integrated Geodetic Network (SCIGN).

Because the time scales for plate boundary deformation range over at least 8 orders of magnitude, from seconds to decades, no single technique is adequate. We have initiated an integrated approach that makes use of three complementary and mature geodetic technologies: continuous GPS, borehole tensor strainmeters, and interferometric synthetic aperture radar (InSAR), to characterize broadband surface deformation. Also, ultrasensitive borehole seismometers monitor microearthquake activity related to subsurface deformation.

The project has three components: 1) the installation of broadband deformation stations in the San Francisco Bay area; 2) the installation of GPS stations in the Parkfield region; and 3) support for skeletal operations of a 5-m X-band SAR downlink facility in San Diego to collect and archive radar data, and develop an online SAR database for WInSAR users. The BSL has participated in the first two of these components. Additional details about the Parkfield GPS stations, installed in 2001 to link the BARD network in central and northern California to the SCIGN network in southern California and currently operating in real-time streaming mode with instantaneous position analysis, are provided in the BARD chapter of this report. The remainder of this chapter describes San Francisco Bay area broadband deformation station component of this project.

The broadband deformation stations augment existing instrumentation along the Hayward and San Andreas faults in the San Francisco Bay area (Figure 8.1). During July 2001 to August 2002, five boreholes were drilled and equipped with tensor strainmeters and 3-component L22 (velocity) seismometers (Table 8.1). The strainmeters were recently developed by CIW and use 3 sensing volumes placed in an annulus with 120 degree angular separation, which allows the 3-component horizontal strain tensor to be determined. All of the stations include pore pressure sensors and 2-component tiltmeters. Three of the stations now are equipped with Quanterra recording systems that provide 100-Hz seismic and strainmeter data, and two of the stations now include a GPS receiver. The GPS antennas at these stations are mounted at the top of the borehole casings in an experimental approach to achieve stable compact monuments. The GPS stations complement existing Bay Area stations of the BARD continuous network.

The 30-second GPS, and 100-Hz strainmeter and seismometer data is acquired on Quanterra data loggers and continuously telemetered by frame relay to the BSL. Low frequency (600 second) data (including strainmeters, for redundancy) is telemetered using the GOES system to the USGS. All data is available to the community through the Northern California Earthquake Data Center (NCEDC) in SEED format, using procedures developed by the BSL and USGS to archive similar data from 139 sites of the USGS ultra-low-frequency (UL) geophysical network, including data from strainmeters, tiltmeters, creep meters, magnetometers, and water well levels.

2. New Site Installations

During the period July 2002–June 2003, the BSL and USGS began the installation of the broadband deformation stations at Marin Headlands (MHDL) in the Golden Gate National Recreation Area near Pt. Reyes, and at St. Vincent’s School for Boys (SVIN) near San Rafael. Additional equipment installation and maintenance was performed at the first three stations, including the installation of tiltmeters at all stations, and the GPS monu-

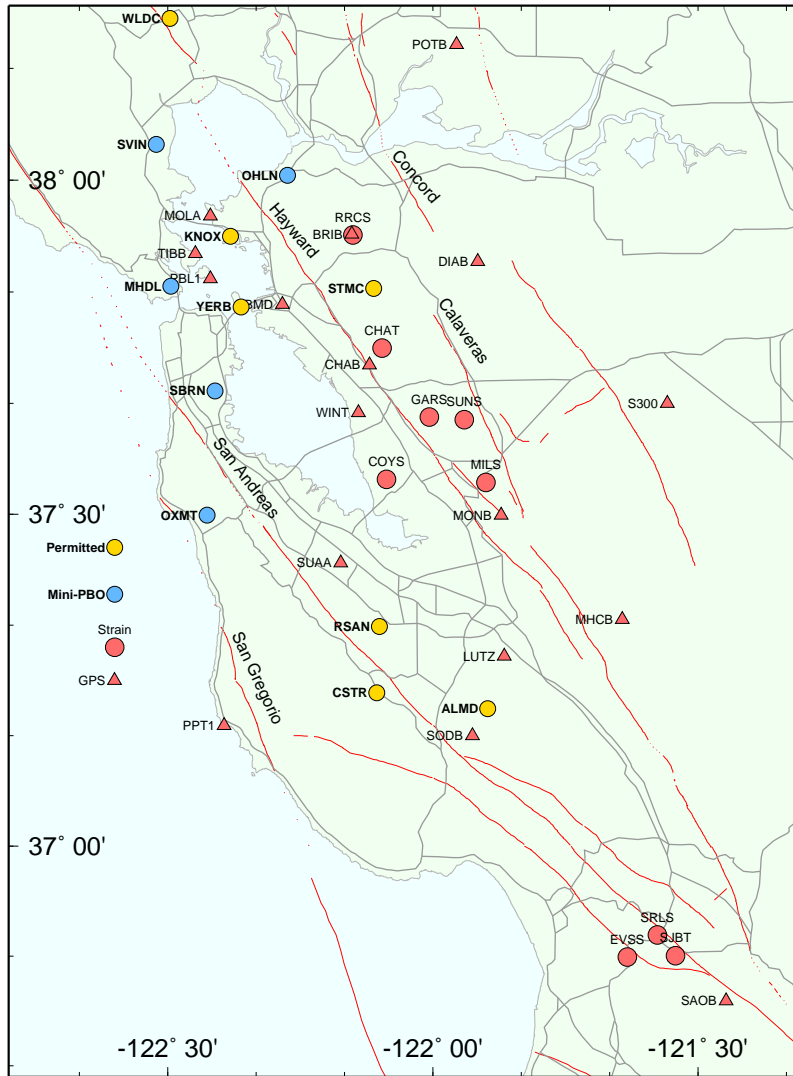


Figure 8.1: Location of existing (red), in preparation (yellow), and pending (blue) Mini-PBO sites in the San Francisco Bay area. Shown also (red) are currently operating strainmeter (circles) and BARD (triangles) stations. Blue triangles are other pending BARD stations. Black triangles are L1-system profile sites near the Hayward fault and the UC Berkeley campus.

Code	Latitude	Longitude	Installed	Strainmeter depth (ft)	Seismometer depth (ft)	Location
OHLN	38.00742	-122.27371	2001/07/16	670.5	645.5	Ohlone Park, Hercules
SBRN	37.68562	-122.41127	2001/08/06	551.5	530.0	San Bruno Mtn. SP, Brisbane
OXMT	37.49795	-122.42488	2002/02/06	662.7	637.3	Ox Mtn., Half Moon Bay
MHDL	37.84227	-122.49374	2002/08/06	520.6	489.2	Golden Gate NRA, Sausalito
SVIN	38.03325	-122.52638	2002/08/29	527.0	500.0	St. Vincent CYO School, San Rafael
SMCB	37.83881	-122.11159				St. Mary's College, Moraga
WDCB	38.24088	-122.49628				Wildcat Mt., Sears Pt.

Table 8.1: Currently operating and planned stations of the Mini-PBO network. Strainmeter installation date is given. Depth to tensor strainmeter and 3-component seismometers in feet.

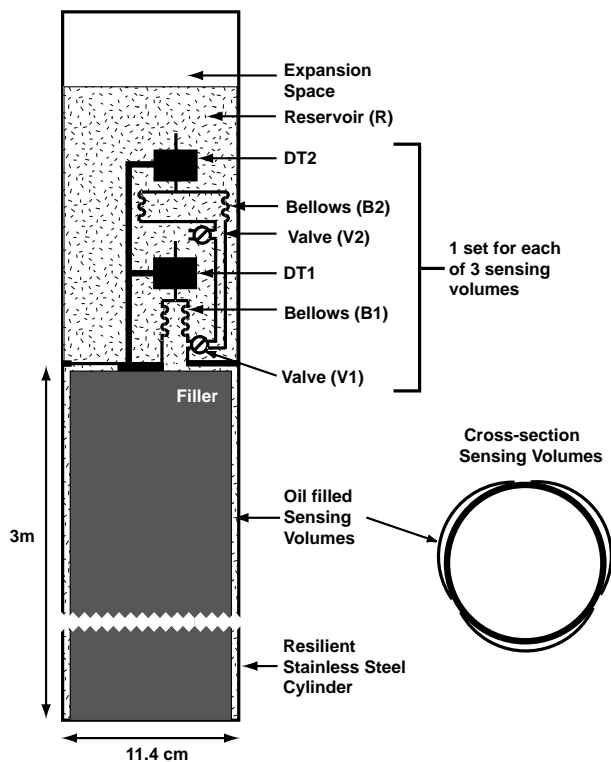


Figure 8.2: Tensor strainmeter diagram. These instruments are a modification of the Sacks- Evertson dilatometers that use a hydraulic sensing technique to achieve a volume strain sensitivity of 10^{*-12} with constant frequency response from 0 to more than 10 Hz and a dynamic range of about 130 dB. The design incorporates a second bellows- DT- valve sub- system which provides extended dynamic range, complete preservation of baseline during required instrumental resets, and redundant sensing electronics. Figure courtesy A. Linde (USGS).

ment and receiver at San Bruno (SBRN).

The BSL directly supervised the drilling operations at St. Vincents during the August 2002. The boreholes were drilled by the USGS Water Resources Division using a relatively new rig that experienced numerous problems (hydraulics, stuck bits, etc.), which delayed the drilling considerably at several of the sites and significantly increased the costs of the project. At St. Vincents, the first hole had to be abandoned after some tungsten grinding buttons from a defective bit dislodged and could not be retrieved from the bottom of the hole. Hammer drilling through the very hard graywacke encountered throughout the hole also proved difficult due to the lack of proper stabilization on the drill string. Rotary drilling, although relatively slow, enabled penetration to 528' in the limited time available. A video log showed a promising region devoid of open fractures near the bottom of the hole where the strainmeter and seismometer packages were installed

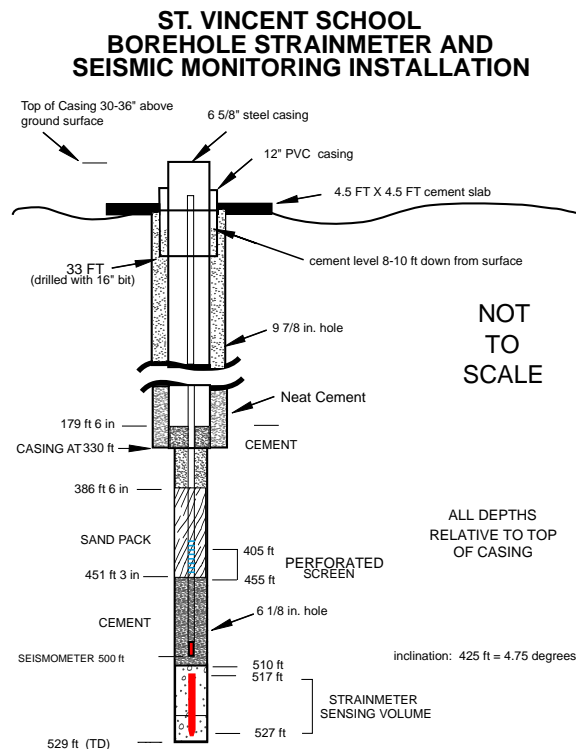


Figure 8.3: The Mini-PBO borehole configuration at St. Vincents, showing the emplacement of the strainmeter and seismometer instruments downhole. The GPS receiver is mounted on the top. Figure courtesy B. Mueller (USGS).

without any further difficulties.

The USGS supervised the drilling at the Marin Headlands (MHDL) site. The drilling in October 2001 encountered hard greenstone with some fractures and clay layers between 410-608' and red and green chert below to 659'. Coring at around 545' was slow and poorly recovered. A video log of the hole showed several promising strainmeter installation regions at 500-550' depths. However, containment of high volumes of artesianing fluids from the well became increasing problematic. The hole was cased to 278', sand filled on the bottom, and cemented and plugged at the top in mid-October. In August 2002, the cement and sand were rapidly drilled out, without any artesianing problems, allowing the strainmeter and seismometer packages to be successfully installed.

Figure 8.3 shows the typical configuration of the borehole instrument installation. A 6.625" steel casing was cemented into a 10.75" hole to 500-650' depth to prevent the upper, most unconsolidated materials from collapsing into the hole. Below this depth a 6" uncased hole was drilled to the target region for the strainmeter and seismometer packages. Coring, in order to identify the region with the most competent rock for the strainmeter, was

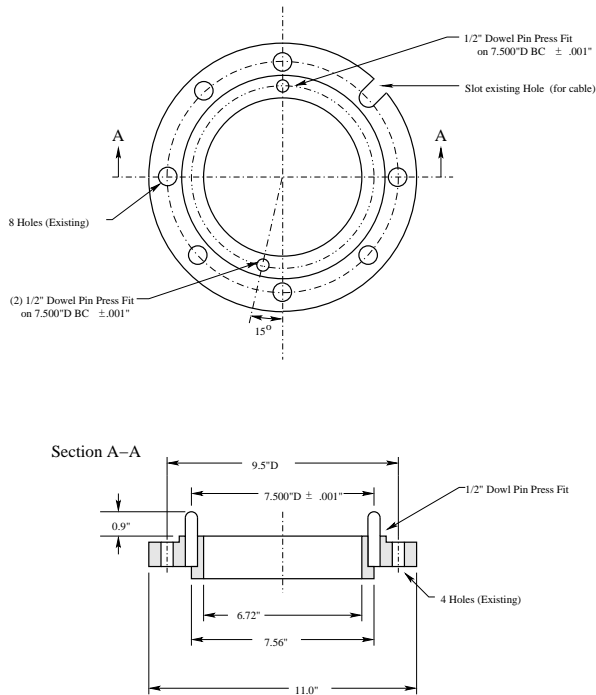


Figure 8.4: Design of the bottom flange of GPS antenna mount, which is welded to the top of the casing.

attempted with only moderate success at a few of the holes and was not attempted at St. Vincents. We found that video logs provided a reasonable substitute. The target region of each hole was filled with a non-shrink grout into which the strainmeter was lowered, allowing the grout to completely fill the inner cavity of the strainmeter within the annulus formed by the sensing volumes to ensure good coupling to the surrounding rock.

The 3-component seismometer package was then lowered to just above the strainmeter, on a 2" PVC pipe, and neat cement was used to fill the hole and PVC pipe to entirely enclose the package. The pipe above this depth was left open for later installation of the pore pressure sensor. To allow water to circulate into the pipe from the surrounding rock for the pore pressure measurements, the the steel casing was perforated, a sand/gravel pack was emplaced, and a PVC screen was used at this depth. At each hole, the casing was then cemented inside to about 200', and outside to about 20' depth. A 12" PVC conductor casing was cemented on the outside from the surface to 20' to stabilize the hole for drilling and to provide an environmental health seal for shallow groundwater flow. The annulus between the 12" conductor casing and the 6.625" steel casing was cemented to about 10' depth and above was left decoupled from the upper surface to help minimize monument instability for the GPS antenna mounted on top of the steel casing.



Figure 8.5: GPS antenna mount. The bottom flange is welded to the top of the borehole casing. The upper flange can be removed and replaced with sub-0.1 mm repeatability to provide access to the interior of the casing.

Due to the unexpectedly high costs of drilling, only 5 boreholes could be completed under the NSF/IF grant, although additional instrumentation was purchased in anticipation of acquiring more sites. Caltrans intends to drill boreholes at several locations for the HFN project in the coming year that might be suitable for Mini-PBO installations, depending on the quality of the rock encountered at about 600' depth. Two of the already permitted potential sites, St. Mary's College (SMCB) and Wildcat Mt. (WDCB) (Figure 8.1 and Table 8.1), would nicely complement existing instrumentation, providing additional monitoring of the northern Hayward fault and initiating monitoring of the southern Rodgers Creek fault north of San Pablo Bay.

The BSL is supervising GPS, power, frame relay telemetry, and Quanterra 4120 datalogger installation at all the broadband deformation stations. Power, telemetry, and dataloggers are currently installed at OHLN, SBRN, and SVIN. The frame relay circuit at OXMT is also installed, but the power hookup has been delayed due to permitting complications that should be resolved in Fall 2003. Permitting complications have also delayed the establishment of power and telemetry at MHDL. Our original plans and permitting to use phone line connections became prohibitively expensive, so we are currently seeking permits to establish radio telemetry from the site either to a nearby telephone pole where a frame relay cir-

cuit can be installed or from the site directly to the BSL via a radio repeater on the ridge above the station. The USGS has installed solar panels at OXMT and MHDL to collect the low-frequency strainmeter data prior to establishing DC power at the sites. Telemetry at SVIN was established in June 2003 using Wi-LAN radios, a new type of radio that the BSL is currently beginning to adopt. These radios act as ethernet bridges, providing superior access to console control on the Quanterras. The radios can also provide a spanning tree network structure for a regional wireless network, which allows greater flexibility for future network installations.

The BSL is developing an experimental GPS mount for the top of the borehole casings to create a stable, compact monument (Figure 8.4). The antennas, using standard SCIGN adapters and domes for protection, are attached to the top of the 6-inch metal casing, which will be mechanically isolated from the upper few meters of the ground. The casing below this level is cemented fully to the surrounding rock. Our original mount design used at OHLN, which consists of a metal pipe symmetrically centered with respect to the casing that is welded to a cross beam and bolted inside the top of the casing, was found to have too much play in the area where the bolts are attached to ensure long-term stability of the monument.

We therefore redesigned the mount to minimize such non-tectonic motions. The current GPS mount design (Figures 8.4 and 8.5) consists of two 11- inch diameter stainless steel flanges. The lower slip- and- weld type flange is welded onto the top of the 6 5/ 8"- inch borehole casing providing a level surface for the second flange . The upper blind-type flange, to which the 1 1/ 4" stainless steel pipe used to connect to the SCIGN DC3 adaptor is attached, is bolted to the lower flange using four 3/ 4" by 3" stainless steel bolts. Two half- inch stainless steel dowels are press fit with high location precision (radius 7.500" +/- 0.001") into the lower flange. Two matching holes are machined into the upper flange with a high location precision (radius 7.500" +/- 0.001") and hole diameter precision (between +0.005" and -0.000"). One of the dowels is offset to insure unique directional alignment. This mount was installed at SBRN in March 2003, and we are preparing to install this mount at the other broadband deformation stations in Fall 2003, after rainfall lessens the fire hazards that result from the welding.

Analysis of GPS observations at OHLN and SBRN shows that the short-term daily repeatabilities in the horizontal components are about 0.5-1 mm. These values are similar to those obtained with more typical monuments, such as concrete piers or braced monuments, but it is too early to assess the long-term stability of the borehole casing monument, which might also be affected by annual thermal expansion effects on the casing.

Two-component tiltmeters were installed at all the stations by the USGS in Spring 2003. Data from these sensors are recorded at 10-minute intervals and telemetered using the GOES system. Pore pressure sensors are also installed at all the stations and data are recorded at 1 Hz on the Quanterra dataloggers, except at Marin Headlands, where 10-minute interval data are also recorded on the Zeno datalogger. After the server for the pore pressure channels was initiated in Spring 2003, the Quanterra data loggers have occasionally encountered memory overwrite problems that cause them to cease operating. We believe the problem is due to the server, which Quanterra is currently investigating. We currently are running the pore pressure sensors on a trial basis on the system at Ohlone, which seems to behave more robustly than the system at San Bruno.

We are addressing minor problems at several of the stations. Highly correlated low-amplitude noise is contaminating the seismic and strain channels at the recently installed SVIN station. We are still in the process of investigating the source of this noise, which we believe is due to deficiencies in the power grid at the maintenance yard at the school where the data loggers are housed. The vertical seismic channel at OHLN also shows poor long-period characteristics compared to the other channels, and recently displayed a non-linear response to a local earthquake. The source of this problem is probably in the Quanterra electronics, which we intend to swap out in the near future. The USGS and CIW are also investigating anomalies in the strainmeter channels, including unusual steps in the SBRN instrument and a poor long-period response of one of the channels at OXMT, both of which are probably due to electrical grounding problems.

3. Broadband Deformation Data

We are in the initial stages of assessing the data quality of the broadband deformation instrumentation. The borehole seismic packages provide good signal to noise characteristics compared to the NHFN stations due to their relatively deep installation. The systems have the best signal to noise near their 2-Hz characteristic frequency, but typical microseismic noise around 0.1 Hz is not evident (Figure 8.6). It is possible that the microseismic noise could be resolved if the systems included a pre-amplifier. We are planning to test this at OXMT and MHDL when the power and telemetry issues at those sites are resolved. These stations currently sample at 100-Hz, so they miss some of the seismic energy at high frequencies that are observed on the 500-Hz Parkfield borehole stations.

The newly designed tensor strainmeters appear to faithfully record strain signals over a broad frequency range. During the 2 years that the strainmeter at OHLN has been providing high-frequency data, the strain has

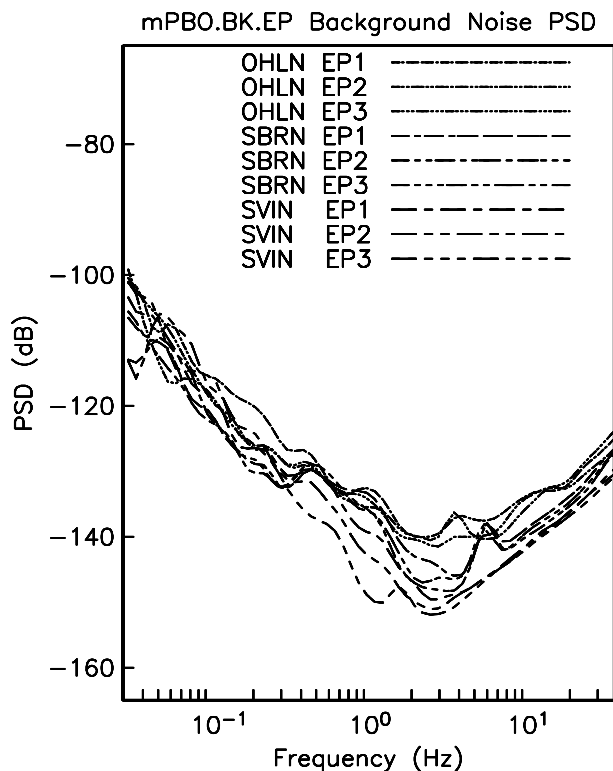


Figure 8.6: Background noise measured by the borehole seismic packages at OHLN, SBRN, and SVIN. Component 1 is vertical. The systems have the best signal to noise ratio near their 2-Hz characteristic frequency. Typical microseismic noise around 0.1 Hz is not evident.

a long-term exponential signal (Figure 8.7). This large signal is most likely due to cement hardening effects and re-equilibration of stresses in the surrounding rock in response to the sudden appearance of the borehole. These effects can last for many years and are the principal reason that borehole strainmeters can not reliably measure strain at periods greater than a few months. We are currently developing techniques to automatically clean the outliers and step offsets (due usually to valve resetting operations) seen in the raw data.

At periods around 1 day, tidally induced strains are the dominant strain signal, about 3 orders of magnitude smaller than the long-term exponential signal (Figure 8.8). Since the response of the strainmeter volumes is difficult to estimate independently, theoretically predicted Earth tides are typically used to calibrate the strainmeters. Figure 8.8 shows the approximate microstrain of the OHLN strainmeter over a several month period interval, and some of the steps required to clean the data, including removing the tides and atmospheric pressure effects. The remaining signal is highly correlated with rainfall, indicating the extent that hydrologic events can affect strain.

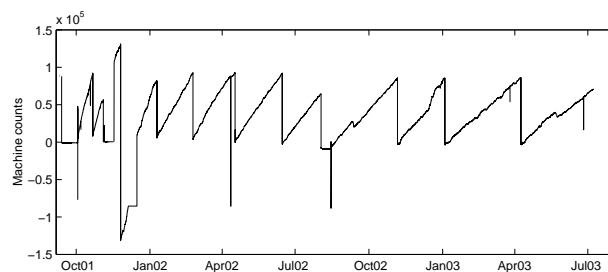


Figure 8.7: Two-year raw data time series from OHLN tensor strainmeter (component 1, flagged bad data removed) showing outliers, valve resetting offsets, and instrumental effects, such as faulty electronics in the strainmeter during the flat section in August 2002. Between the vertical offsets, the slope becomes less steep with time and shows the long-term exponentially decaying strain signal caused by grout curing and re-equilibration of stresses in the surrounding rock following the introduction of the borehole. This non-tectonic signal limits the ability of these strainmeters to reliably measure tectonic strain at periods greater than a few months.

At higher frequencies, strains due to seismic events are also evident. Figure 8.9 shows borehole strain measurements with clear seismic phases at OHLN for the M7.9 Denali Fault, Alaska earthquake on November 3, 2002. This figure also shows measurements of pore pressure, which responds to variations in volumetric strain although not necessarily in a linear fashion. Thus pore pressure provides both an independent check on the strainmeter observations and complementary information about the surrounding rock that will aid in determining the true tectonic strains. We are beginning to examine the strain data for other types of transient behavior, such as episodic creep or slow earthquake displacements.

4. Acknowledgements

This project is sponsored by the National Science Foundation under the Major Research Instrumentation (MRI) program with matching funds from the participating institutions and the Southern California Earthquake Center (SCEC).

Under Mark Murray's supervision, André Basset, Bill Karavas, John Friday, Dave Rapkin, Doug Neuhauser, Tom McEvelly, Wade Johnson, and Rich Clymer have contributed to the development of the BSL component of the Mini-PBO project. Several USGS colleagues, especially Malcolm Johnston, Bob Mueller, and Doug Myren, played critical roles in the drilling and instrument installation phases. Mark Murray and Barbara Romanowicz contributed to the preparation of this chapter.

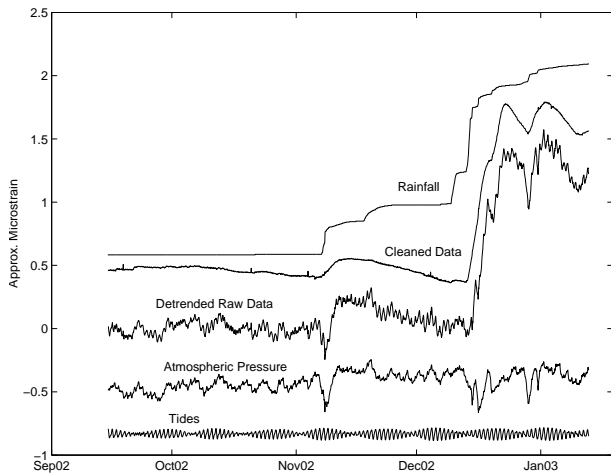


Figure 8.8: Four-month subset of OHLN data, detrended to flatten the first 50 days (middle trace), separated using BAYTAP-G (Tamura et al., 1991) into tidal, atmospheric pressure, and "cleaned" data components (with arbitrary vertical offsets). The atmospheric pressure time series measured at the site was also used for this decomposition. Approximate microstrain values are based on peak-to-peak tidal amplitude. The remaining large strain signals in the cleaned data are highly correlated with rainfall measured at an instrument located about 5 km from the site (40 cm total cumulative rainfall during this interval), and therefore are probably not geophysically interesting.

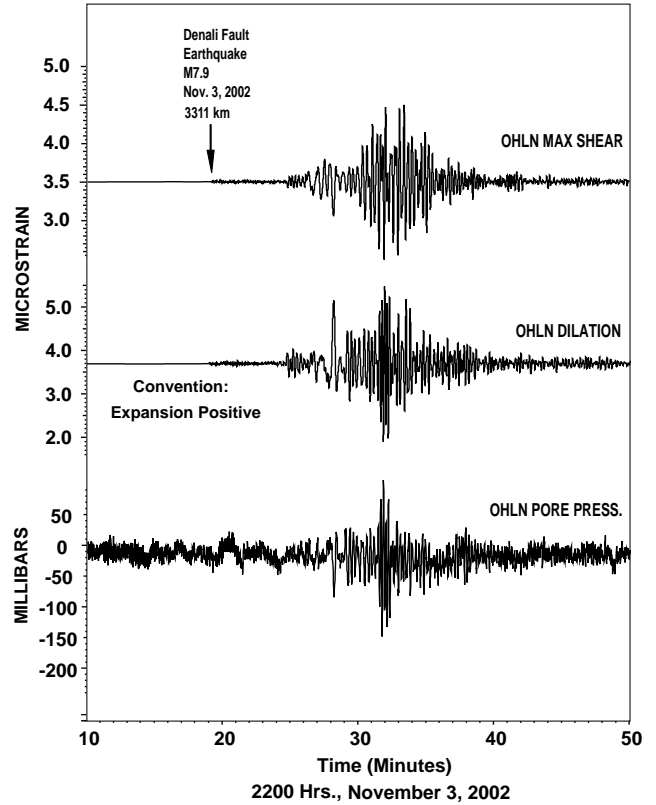


Figure 8.9: Borehole tensor strain and pore pressure monitor measurements of earthquake dynamic strains from the M7.9 Denali Fault, Alaska earthquake on November 3, 2002 observed at the Mini-PBO station OHLN. The strainmeter data have been converted to dilation and shear components based on preliminary calibrations of the sensors. Courtesy M. Johnston.

Chapter 9

Data Acquisition and Quality Control

1. Introduction

Stations from nearly all networks operated by the BSL transmit data continuously to the BSL facilities on the UC Berkeley campus for analysis and archive. In this chapter, we describe activities and facilities which cross-cut the individual networks described in Chapters 3 - 8, including the facilities in McCone Hall, procedures for data acquisition and quality control, sensor testing capabilities and procedures, and a collaborative experiment in early warning.

While some of these activities are continuous from year to year, we have identified changes or activities which are specific to 2002-2003.

2. McCone Hall Facilities

The routine data acquisition, processing, and archiving activities of the BSL are carried out in McCone Hall. The BSL facilities in McCone are designed to provide air conditioning, 100-bit switched network, and reliable power with UPS and generator.

Because of the mission-critical nature of the automated earthquake processing, most computer systems operated by the BSL run on circuits with both UPS and generator power. Air conditioning is provided through both "building air" and a separate room AC unit.

2.1 Power

Over the years, the BSL has experienced problems with the McCone generator system, including a failure in 1999 due to a combination of a weakened power system and a leak in the water pump. In last year's Annual Report, we described the failure of the McCone and Byerly generators in the March 7, 2002 campus-wide power outage.

While the failure of the generator at Byerly Vault was traced to PPCS human error (the generator had been left in a mode where it would not automatically start when power was lost), the failure of the McCone generator was due to poor maintenance. Similar to the situation in 1999, it failed due to problems in the power system combined with a leak in the water pump.

Last fall, BSL staff met with Eric Haemer, Sara Shirazi, and several others from PPCS to discuss maintenance and routine load testing of the McCone generator. As a result, the McCone generator is scheduled for quarterly load tests and bi-monthly run tests.

These quarterly load tests have proven extremely valuable. In January 31st, 2003 test, the generator failed. The failure was due to a problem with the thermostat (since replaced), but the test also revealed that the BSL is drawing more AC power than desirable from the generator, largely from the growth of the computing facilities.

In order to reduce the load on generator and UPS, BSL staff were forced to remove computer systems to building power. Mission-critical systems (communications, data acquisition, data processing, and archiving) were kept on the generator and UPS circuits, which research-specific systems were migrated to building power. To accomplish this, building power circuits were added to the computer server room (the room had originally been designed with only generator and generator/UPS circuits).

This change has meant that BSL researchers have had to address the impact on their programs with long run-times. Without UPS power, the servers and workstations will immediately shut off during a power failure, causing all active programs to terminate. BSL researchers have been asked to build or modify their programs to save incremental results to disk, in order to minimize the loss of work.

2.2 Air Conditioning

In parallel with power problems, the BSL has faced cooling problems in room 237 in the past year. As with power, the growth of the computing systems in the past year has led to an increased heat load. This came to a crisis during the fall of 2002, with peak temperatures in the computer room exceeded 85deg when the AC unit failed. After consideration of several options, the BSL decided to add an additional AC unit to room 237. The new unit (which is not supported by UPS/generator power) has helped keep systems running this spring and summer, although the real test will be this fall.

BDSN and REDI Telemetry and Data Flow

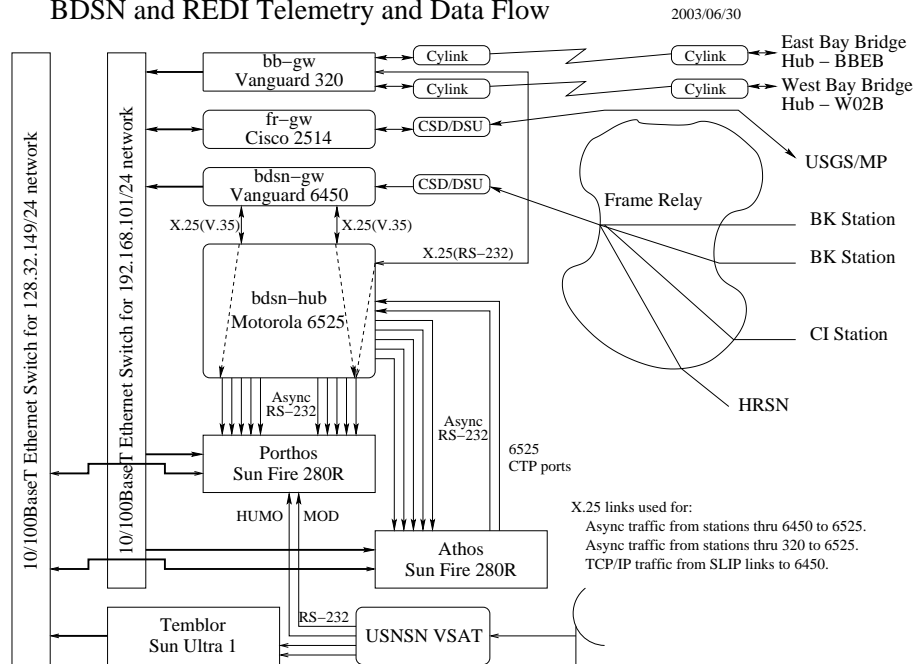


Figure 9.1: Data flow from the BDSN, NHFN, MPBO, HRSN, and BARD network into the BSL central processing facility.

In addition, the BSL staff set up a temperature monitoring system for room 237. For several years, we have relied on a temperature sensor within one of our disk drives to notify us of excessive heat. In the last year, we purchased two temperature probes and a simple digitizing system that allows us to monitor temperature in several locations within the room. Complementing our pager notification, we can now monitor the temperature through real-time graphs accessible through the BSL Web site.

2.3 New Facilities

The BSL is actively working with the campus to relocate the critical operations of data acquisition, processing, archiving, and distribution to a more robust facility. With assistance from the Office of the Vice Chancellor for Research, the BSL has been granted space in a building currently under construction. The building is designed to current codes and has been given special attention for post-earthquake operations. Anticipated occupancy is in FY 2004-2005.

3. Data Acquisition

Central-site data acquisition for the BDSN/NHFN/MPBO is performed by two computer systems located at the BSL (Figure 9.1). These acquisition systems are also used for the Parkfield-Hollister electromagnetic array and for the BARD network. A

third system is used primarily as data exchange system with the USNSN receives a feed from CMB, HUMO, MOD, SAO, and WDC from the the NSN VSAT. This system transmits data to the USNSN from HOPS, CMB, SAO, WDC, and YBH. Data acquisition for the HRSN follows a more complicated path, as described in Chapter 5.

Data acquisition and communication with the Quanterra data loggers depends both on the software on the recording systems and at the central site.

3.1 Comserv

The BSL uses the `comserv` program for central data acquisition, which was developed by Quanterra. The `comserv` program receives data from a remote Quanterra data logger, and redistributes the data to one or more `comserv` client programs. The `comserv` clients used by REDI include `dataLog`, which writes the data to disk files for archival purposes, `cdafill`, which writes the data to the shared memory region for REDI analysis, and other programs such as the seismic alarm process, the DAC480 system, and the feed for the Memento Mori Web page (Figure 9.2).

The two computers that perform data acquisition also serve as REDI processing systems. In order to facilitate REDI processing, each system maintains a shared memory region that contains the most recent 30 minutes of data for each channel used by the REDI analysis sys-

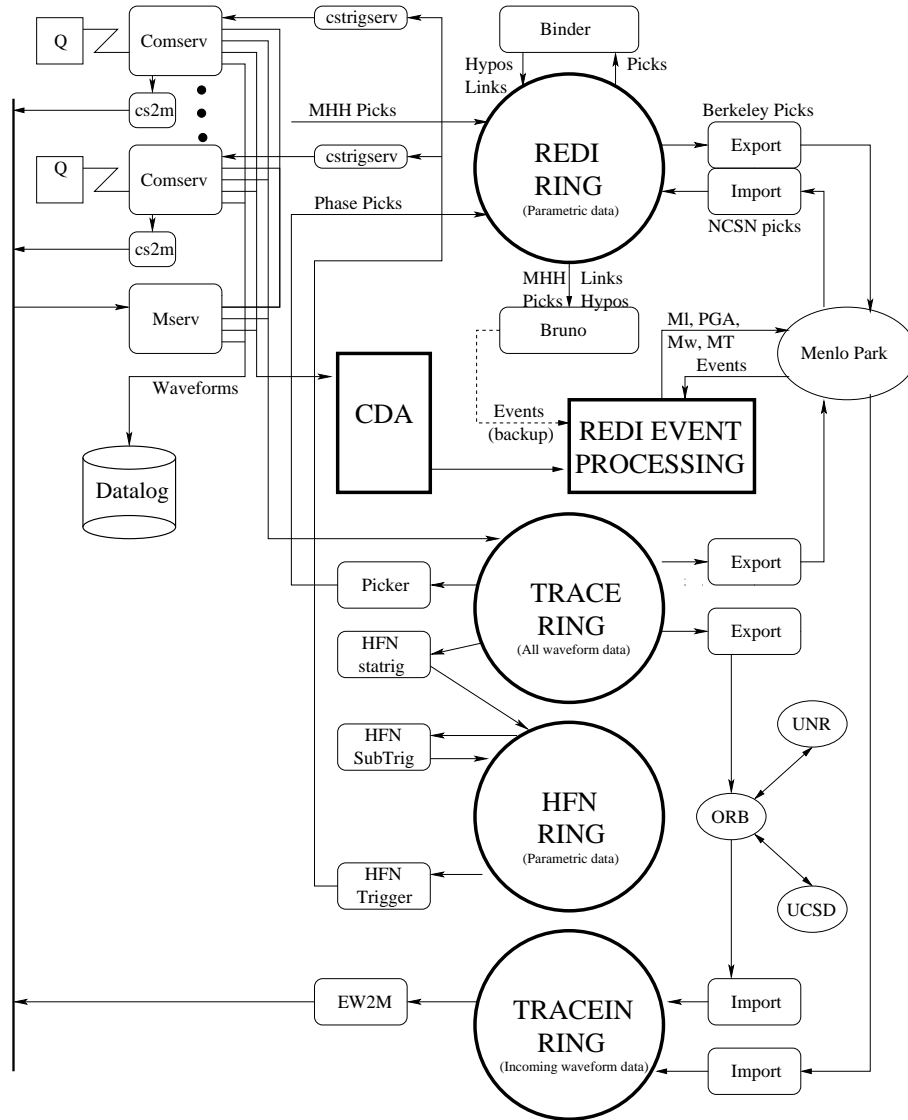


Figure 9.2: Dataflow in the REDI processing environment, showing waveform data coming in from the Quanterra data loggers (Q) into `comserv`. From `comserv`, data are logged to disk (via `datalog`), distributed to other computers (`mserv`), fed into the CDA for REDI processing, and spooled into a trace ring for export.

tem. All REDI analysis routines first attempt to use data in the shared memory region, and will only revert to retrieving data from disk files if the requested data is unavailable in the shared memory region.

Most stations transmit data to only one or the other of the two REDI systems. The `comserv` client program `cs2m` receives data from a `comserv` and multicasts the data over a private ethernet. The program `mcast`, a modified version of Quanterra's `comserv` program, receives the multicast data from `cs2m`, and provides a `comserv`-like interface to local `comserv` clients. This allows each REDI system to have a `comserv` server for every station.

We have extended the multicasting approach to handle data received from other networks such as the NCSN and UNR. These data are received by Earthworm data exchange programs, and are then converted to MiniSEED and multicast in the same manner as the BSL data. We use `mserv` on both REDI computers to receive the multicast data, and handle it in an identical fashion to the BSL MiniSEED data.

3.2 FIR Filter Changes

At 5:00 PM PST June 30th (July 1, 00:00 UTC), 2003, the BDSN and MiniPBO Q4120 Quanterras were recon-

figured and rebooted to change the FIR filter for the 100 Hz channels from acausal to causal. The affected stations are: BDM, CVS, FARB, HUMO, OHLN, PACP, POTR, SBRN, and WENL. The new BDSN Q4120 station MNRC was upgraded on the 29th, since it is a new station and continuous telemetry has not yet been installed.

This change means that all Q4120/Q730 dataloggers operated by the BSL will use causal filters for sampling rates of 100 Hz and higher (the HRSN and NHFN have traditionally used causal filters for the higher sampling rates). Lower data rates will continue to use the acausal filters. This change does NOT apply to the BDSN sites with Q680/980 dataloggers, as the FIR filters are set in firmware and are not readily changed.

This change is motivated by the desire to improve phase picking on the 100 Hz channels. A detailed comparison of casual and acausal FIR filters and their effect on the data is available by Bob Uhrhammer and Bob Nadeau is available at http://quake.geo.berkeley.edu/bdsn/FIR_FILTRATION.pdf.

4. Seismic Noise Analysis

BSL seismic data are routinely monitored for state-of-health. An automated analysis is computed weekly to characterize the seismic noise level recorded by each broadband seismometer. The estimation of the Power Spectral Density (PSD) of the ground motion recorded at a seismic station, provides an objective measure of background seismic noise characteristics over a wide range of frequencies. When used routinely, the PSD algorithm also provides an objective measure of seasonal and secular variation in the noise characteristics and aids in the early diagnoses of instrumental problems. A PSD estimation algorithm was developed in the early 1990's at the BSL for characterizing the background seismic noise and as a tool for quality control. As presently implemented, the algorithm sends the results via email to the engineering and some research staff members and generates a bargraph output which compares all the BDSN broadband stations by components. A summary of the results for 2002-2003 is displayed in Figure 3.3.

Three years ago, we expanded our use of the weekly PSD results to monitor trends in the noise level at each station. In addition to the weekly bar graph, additional figures showing the analysis for the current year are produced. These cumulative PSD plots are generated for each station and show the noise level in 5 frequency bands for the broadband channels. These cumulative plots make it easier to spot certain problems, such as failure of a sensor. In addition to the station-based plots, a summary plot for each channel is produced, comparing all stations. These figures are presented as part of a noise analysis of the BDSN on the WWW at <http://www.seismo.berkeley.edu/seismo/bdsn/psd/>.

The PSD algorithm has been documented in previous annual reports.

5. Sensor Testing Facility

The BSL has set up an instrumentation test facility in the Byerly Seismographic Vault in order to systematically determine and to compare the characteristics of up to eight sensors at a time. The test equipment consists of an eight-channel Quanterra Q4120 high-resolution data logger and a custom interconnect panel that provides isolated power and preamplification when required to facilitate the connection and routing of signals from the sensors to the data logger with shielded signal lines. Upon acquisition of the 100 samples-per-second (sps) data from the instruments under test, PSD analysis and spectral phase coherency analysis are used to characterize and compare the performance of each sensor. Tilt tests and seismic signals with a sufficient signal level above the background seismic noise are also used to verify the absolute calibration of the sensors. A simple vertical shake table is used to access the linearity of a seismic sensor.

The sensor testing facility of the BSL is described in detail in the 2001-2002 Annual Report.



Figure 9.3: Photo of the three Guralp CMG-1TD OBS units (serial numbers T1046, T1047 and T1055 seismometers) in the Byerly Vault (BKS). Shown are the various circuit boards on the sides and the top of the sensor package. Three of the nine batteries used by the leveling system are on the left side, the system clock is on the circuit board on the front, the power board is on the right, and the 24-bit digitizer is on the top of each seismometer. The seismometers are in the mu metal shielded container mounted on leveling gimbals in the center.

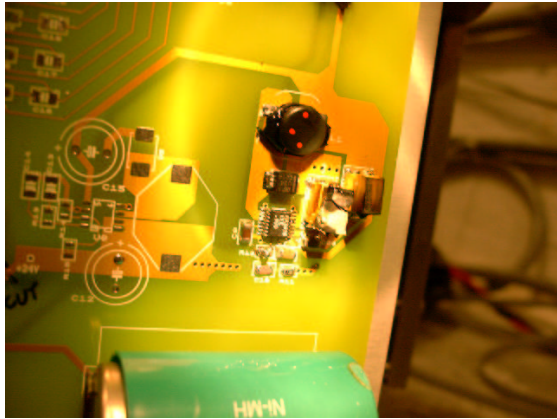


Figure 9.4: Closeup of the portion of the power board containing the failed capacitor (just to the right of center).

6. Sensor Testing in 2002-2003

6.1 CMG-1T Ocean Bottom Seismometers

Prior to the scheduled deployment of three CMG-1TD OBS sensor packages (Figure 9.3) on the ocean floor off of Washington State, beginning in the summer of 2003, we did extensive testing to verify the operation of the seismometers and the wide range leveling system, to verify the calibration of the seismometer and to characterize the background noise PSD performance of the seismometers. The following paragraphs provide a synopsis of the various problems we encountered when testing the three OBS systems. These problems significantly delayed the testing of the sensors and the lab personnel consequently spent more time on this project than was initially anticipated.

The testing of the OBS system in the Byerly Seismographic Vault (BKS) started on January 14, 2003 with the arrival, unpacking and installation of the three CMG-1TD seismometers (serial numbers T1046, T1047 and T1055) on the seismic pier in the Byerly Seismographic Vault (BKS). We installed a V200 FRAD in order to have sufficient serial ports to telemeter data the three sensors under test back to the lab. The next day we installed four 12 volt batteries (UPS12-310 type) to provide separate power for each of the three OBS systems and to the GPS clock. When we powered up T1047, a capacitor on the power input board caught fire and burned up with a spectacular flash and smoke within a second of applying power (see Figure 9.4). We confirmed that the power polarity was correct and we suspected that the polarized power capacitor was installed backwards. T1046 powered up without problems and responded to commands. T1055 was left unpowered pending inspection by Digital Technology Associates (DTA) (the US distributor for



Figure 9.5: Custom made titanium pressure spheres which are designed for deployment at depths of up to 3.5 km. The hemispheres were made using an injection molding process. There are two access ports drilled into the flat top of each sphere, one for the penetrator containing the wiring cable and one for purging with argon gas (and for relieving any pressure differences so that the hemispheres can be separated). The handle on top is designed for the Remote Operated Vehicle (ROV) which deploys the sphere on the sea floor.

Guralp). DTA replaced the defective power board on T1047 we tested the unit and found it to be within specifications. The three GPS clock modules associated, one for each OBS system, were tested one at a time on the front of the BKS vault. All three GPS clocks tested good so we installed one of the clocks on top of the entrance to the vault and ran cabling back to provide time to the three OBS sensors. DTA replaced the defective power board on T1047 we tested the unit and found it to be within specifications. Plastic bags were placed over the OBS units to keep dust and breezes off of the exposed sensors and electronics.

We encountered problems in telemetering data back to the lab so we set up a laptop with the SCREAM software provided by Guralp to locally log data from the sensors and troubleshoot the systems. We encountered no errors that would indicate telemetry problems when logging the data locally. When the three OBS's recorded a local earthquake, we discovered that horizontals on T1047 have half gain and inverted polarity. This was raw data so software and transfer functions errors are excluded. We found that the onboard rechargeable batteries on T1047 and T1055 were not charged enough to lock the seismometers. We moved the good power board from T1046 in order to lock the T1047 and T1055 seismometers. All three power boards were then removed and sent back to Guralp for repair with an expected turnaround time of three weeks.

On March 24th the "improved" power boards were in-

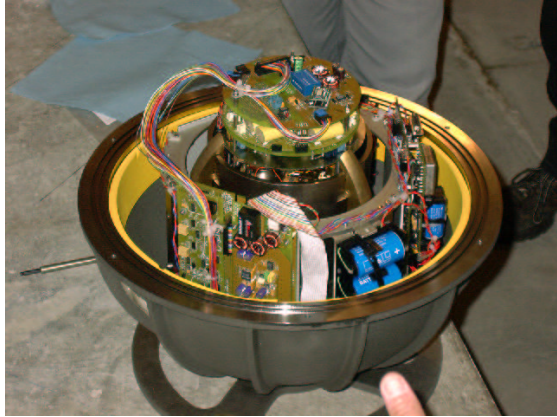


Figure 9.6: Closeup of the OBS installed in the lower hemisphere of the pressure vessel. Shown are the various circuit boards on the sides and the top of the sensor package. The thumb is pointing towards the rechargeable batteries which are used to supply the extra current required by the two high torque motors used in the leveling system. On the right side of the sensor is the circuit board containing the internal clock. On the left front is the I/O circuit board and on top is the 24-bit digitizer. The seismometers are in the mu metal shielded container mounted on leveling bowl. Also visible around the inside of the hemisphere, and just below the flange, is the high density foam insulation.

stalled on the three OBS units and the revised firmware was successfully uploaded to the onboard digitizers. During the initial simultaneous testing of all three OBS sensors, we found that the power management has improved and seems to work properly and also that the traces from all three sensors, as recorded on a local laptop computer, looked coherent in amplitude and phase. We then connected the three OBS units to the telemetry link back to the lab for further testing. The azimuth command was tested on T1055 by locking the sensors, rotating it 90 degrees counter clockwise and then using the azimuth command to reconfigure for NS/EW orientation. However, we found that T1055 would not re-level. Subsequently T1946 was removed for testing and evaluation by DTA. T1046 had some gaps in the telemetered data so we swapped its telemetry to a different serial port on the FRAD to see if a good OBS system produces data gaps through the same serial port.

On April 18th, T1046 was returned from Guralp and reinstalled in the BKS vault. Over the next couple of weeks, the OBS sensors were sequentially tested with local recording on the laptop computer. All three OBS units are operating nominally within specifications and we await the arrival of the titanium pressure vessels from MBARI to complete the testing.

On June 20th, the MBARI crew arrived with the pres-

sure vessels (Figure 9.5) and we spent most of the day installing the OBS units within the pressure vessels (Figure 9.6). The MBARI crew had installed ~ 0.5 inch thick high density foam insulation in the upper titanium hemisphere and ~ 4 inches into the lower hemisphere to inhibit convection within the enclosed pressure vessel. Additionally, each pressure vessel was purged with argon gas to further inhibit convection within the titanium pressure vessels. T1046 and T1055 were reconnected to the telemetry back to the lab and T1047 was taken to MBARI for testing in their cold room to determine whether or not the internal clock on the OBS unit met the factory specifications when operated at 4 degrees Celsius (the nominal temperature of the water on the ocean floor).

Subsequent testing indicated that T1055 had a high Z-component noise level and we suspected that it had drifted off center. We successfully recentered both OBS units via the laptop computer. T1046 was now operating nominally within specifications but T1055 remains noisy (Figure 9.7) so it will require further testing. The OBS units we picked up by the MBARI crew for transporting to the University of Washington on July 15th.

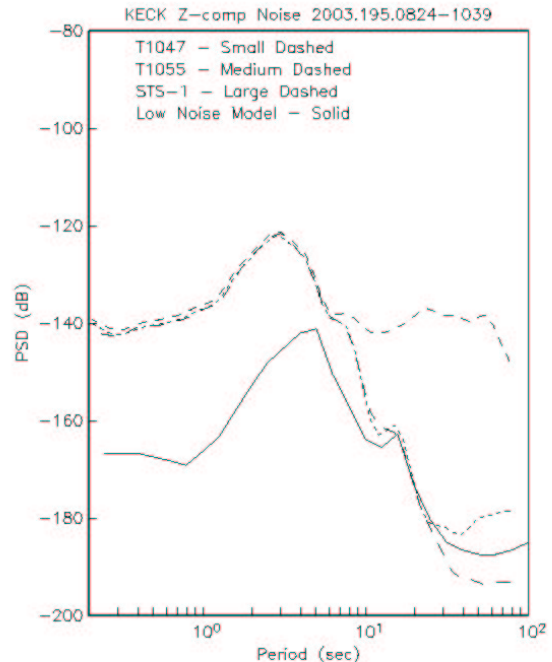


Figure 9.7: Power Spectral Density (PSD) plot of the background and instrumental noise levels in dB as a function of period. Shown are the PSD's for T1047 and T1055. The PSD for the co-sited STS-1 Z and the low seismic noise model are shown for reference. Note that the PSD for T1055 is excessively noisy at periods longer than ~ 10 seconds.

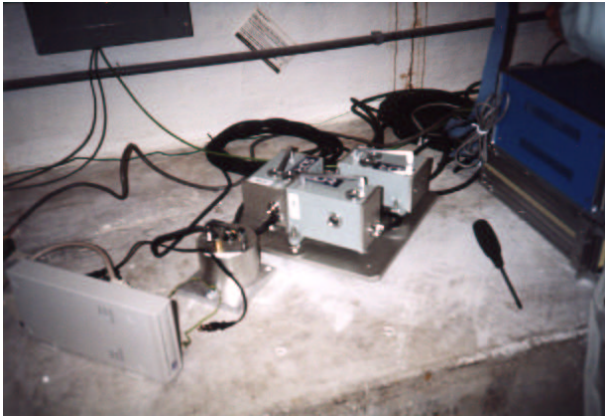


Figure 9.8: UrEDAS sensors installed at BKS site. The dedicated PC-based processing system (not shown here) is located in an adjacent room.

7. UrEDAS Project

The established joint notification system in Northern California provides accurate and reliable determination of earthquake parameters, but there is a time delay between the occurrence of an event and the determination of its size. In an emergency, this time delay prevents actions which could mitigate damage from strong ground shaking. In an effort to develop such capability with the BDSN, we started an experiment collocating a set of UrEDAS (Urgent Earthquake Detection and Alarm System; see *Nakamura, 1996*), an integrated real-time earthquake warning system, with the BDSN site BKS in 2001. Previous annual reports have described the UrEDAS system and its installation in Byerly Vault. Here we provide an update.

7.1 Collocating Experiment

The initial system installation at BKS was completed with the event detection and notification in February 2001 and was upgraded to transmit waveform data to the BSL in July 2001. The SDR crew visited the site in July 2002 to check on the equipment and to revise the values of the parameters used by the UrEDAS algorithms. They again visited the site in July 2003 to upgrade the software and revise the values of the processing parameters that determine the seismic wave apparent azimuth and dip. Figure 9.8 shows the UrEDAS sensors and Figure 9.9 shows an illustration of the UrEDAS network configuration.

7.2 Rapid Event Detection

In the UrEDAS system the event detection velocity threshold is pre-set; the epicentral azimuth is estimated from the direction of the initial motion projected on the

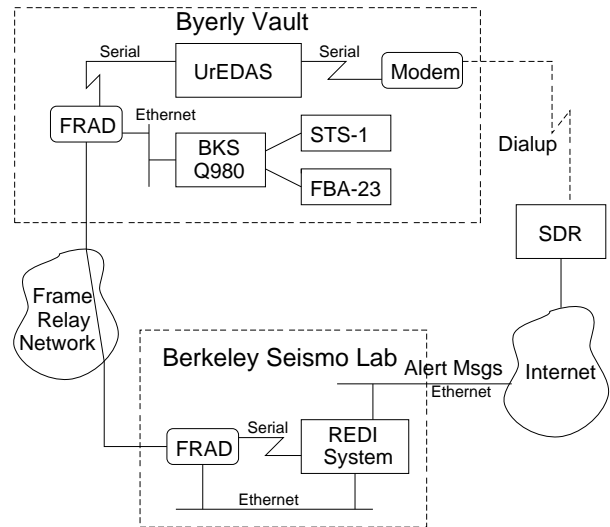


Figure 9.9: Schematic illustration of the UrEDAS collocation experiment with a Streckeisen STS-1 broadband instrument and a Kinemetrics FBA-23 strong motion accelerometer with a Quanterra Q980 data logger at BKS.

horizontal plane; and the preliminary estimate of the distance and magnitude is based on the frequency content and amplitudes of P-wave first motions (~ 3 sec). An alarm can be issued if a hazardous earthquake is detected by P-waves (Version 1 E-mail). If an S-wave arrival is detected, the preliminary estimate is revised (Version 2 E-mail)

The epicentral distance (R) is estimated using the relation $\log R = a \cdot \log A + b \cdot \log T + c$ where A is the amplitude of the initial P-wave motion (in mkin), T its prominent period, and a, b , and c are constant. The magnitude is estimated from the prominent period (T) of the initial P-wave motion using the relation $M = 3.2 \cdot \log T + 5.26$. We do not suppose that these relations apply universally but are testing them empirically. A UrEDAS waveform example is shown in Figure 9.10 and an expanded view of the P-wave is shown in Figure 9.11. The azimuth determination shows systematic biases, most likely due to the nearby Hayward fault where the impedance can change by $\sim 40\%$ across the fault zone. The erroneous location estimates can be also attributed to the propagation path effects through the faults, the near-site structural heterogeneity and/or noise level. If the azimuth estimate becomes reliable, the combined information from two stations could also make a reasonable estimate of an epicentral distance.

The estimated magnitudes of small local events in the epicentral distance between 20 and 200 km were within the range expected from other experiments. Magnitudes of the smaller events ($M < 2.5$) tend to be overestimated, and those of events at farther distances ($R > 200$ km)

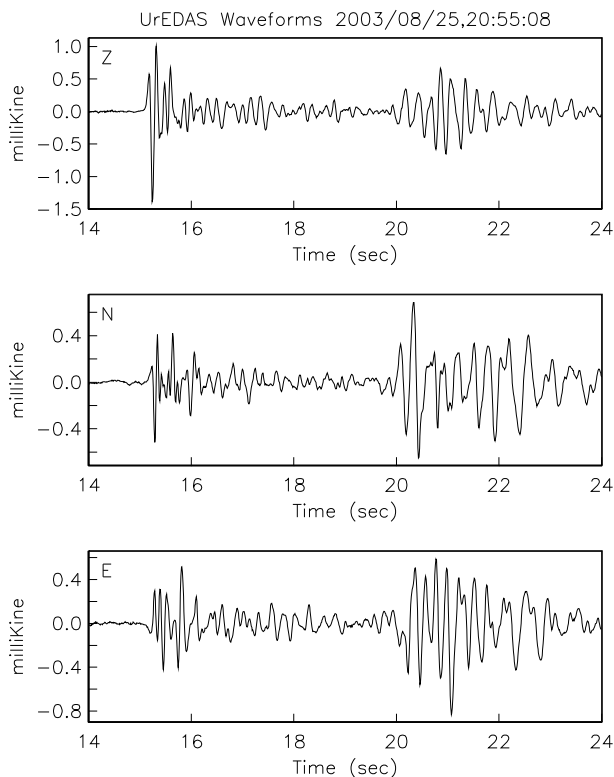


Figure 9.10: UrEDAS waveforms from a M 2.3 earthquake which occurred 32.2 km SE (123deg azimuth) from Berkeley and 8 km NNW of Pleasanton, CA. The vertical scales are in milliKine (1 Kine is 1 cm/sec).

are underestimated. See the previous Annual Report for more detail.

Since the installation of the UrEDAS system in February 2001, there have been 575 UrEDAS paged events ($1.3 \leq M \leq 8.1$) and 387 of these had corresponding NCSN events (within a 500 km radius and with a theoretical P-wave onset time at BKS within 20 seconds of the UrEDAS detection time). The 188 uncorrelated UrEDAS events are a mix of teleseisms (which UrEDAS has a tendency to mislocate as local events), some small local events near Berkeley, and a few random noise triggers. The UrEDAS performance was evaluated by comparing the event parameters with those recorded in the ANSS composite catalog. The event detection performance was satisfactory, although UrEDAS is designed to detect primarily local events ($R \leq 200$ km) and it does not have the ability to distinguish between teleseismic and local events at present.

We have done some preliminary comparison of the waveform data recorded by the BKS broadband instrument with those recorded by the UrEDAS. Because of the complexities of seismic structure, nonlinearities involved in the propagation of the complex faults areas,

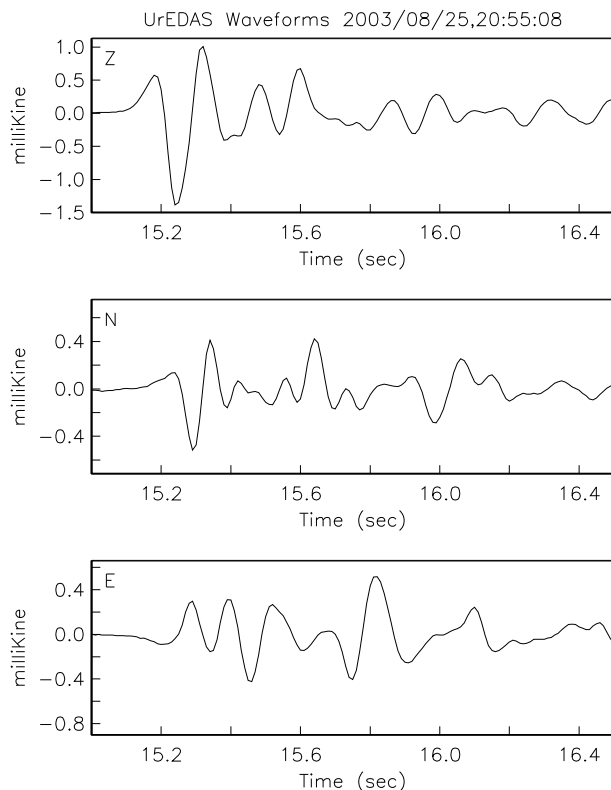


Figure 9.11: Expanded view of Figure 9.10 showing the first few seconds of the P-wave. Note that the P-wave particle motion is linear for the approximately the first cycle and then it predominantly elliptical owing to the near-receiver structural complexity of the crust and the proximity to the Hayward fault zone.

this problem does not lend itself to easy analysis without systematic and more advanced analyses and calibrations. We focus on improving the algorithm to rapidly evaluate preliminary earthquake source parameters, i.e., magnitude and location.

7.3 Discussion

To date UrEDAS readily detects the occurrence of local/regional events from the P-wave signal. It also does a fair job of determining the source distance out to 160 km or so but the azimuth determination is basically unusable. UrEDAS also has biased magnitude estimates. The UrEDAS algorithm assumes a one-dimensional velocity model with straight line propagation paths and a three-dimensional model of the crustal structure will likely be required to significantly improve the azimuthal estimates. Also, the magnitude estimation algorithm needs further tuning. During their July, 2003 visit, the UrEDAS engineers updated some of the UrEDAS algorithms parameter values. In particular, they shortened the time interval that is used to estimate the azimuth from the P-wave

waveform.

Assuming that the primary goal is to determine the event location and size as rapidly as possible, the fastest approach will prove to be a hybrid approach where the remote stations determine the azimuth and ramp growth rate and associated uncertainties and the central site uses a fuzzy logic algorithm to determine the location and size of the event. The primary advantage of this hybrid method is that the ramp growth rate can be reliably determined before the S-wave arrives. In the limiting case, and with a sufficiently high station density, one could even go so far as to determine and report from the remote sites using only the broadband P-wave impulse, the associated azimuth and apparent angle of incidence (along with estimates of their resolution). The central site could then coalesce the data into a viable and rapid event report.

The critical issue for a successful installation of a UrEDAS type system in the BDSN is the calibration of specific site effects at individual stations. A joint use of the single station detection system with the current northern California earthquake notification system would significantly increase the capability of real-time earthquake warning system.

8. Acknowledgements

Doug Neuhauser, Bob Uhrhammer, Lind Gee, Pete Lombard, and Rick McKenzie are involved in the data acquisition and quality control of BDSN/NHFN/MBPO data.

Development of the sensor test facility and analysis system was a collaborative effort of Bob Uhrhammer, Tom McEvelly, John Friday, and Bill Karavas. IRIS and DTRA provided, in part, funding and/or incentive to set up and operate the facility and we thank them for their support.

Bob Uhrhammer led the testing and problem solving effort of the KECK sensors, with help from John Friday, Doug Neuhauser, and Bill Karavas.

Bob Uhrhammer and Bob Nadeau evaluated the impact of the FIR filters on the BDSN data.

Fumiko Tajima initiated the collaboration with SDR on testing the UrEDAS system, which is now coordinated by Bob Uhrhammer. Doug Neuhauser, Bill Karavas, John Friday, and Dave Rapkin helped with installation and maintenance. We thank Yutaka Nakamura and his colleagues at SDR for providing us with the installation of UrEDAS system and information on the accumulated data by this system.

Bob Uhrhammer, Lind Gee, and Doug Neuhauser contributed to the preparation of this chapter.

9. References

Nakamura, Y. and A. Saito, Train stopping system for the Tohoku Shinkansen (in Japanese), *Proc. of Semianual meeting of the Seismological Society of Japan*, 82, 244, 1982.

Nakamura, Y., Real-time information systems for seismic hazards mitigation UrEDAS, HERAS, and PIC, *Quarterly Report of Railway Technical Research Institute*, 37, 112-127, 1996.

Scherbaum, Frank. Of Poles and Zeros: Fundamentals in Digital Seismology, Volume 15 of Modern Approaches in Geophysics, G. Nolet, Managing Editor, Kluwer Academic Press, Dordrecht, xi + 257 pp., 1996.

Tapley, W. C. and J. E. Tull, SAC - Seismic Analysis Code: Users Manual, *Lawrence Livermore National Laboratory*, Revision 4, 388 pp., March 20, 1992.

Chapter 10

Northern California Earthquake Monitoring

1. Introduction

Analysis of the data produced by BSL networks begins as the waveforms are acquired by computers at UC Berkeley, and ranges from automatic processing for earthquake response to analyst review for earthquake catalogs and quality control.

Over the last 10 years, the BSL has invested in the development of the hardware and software necessary for an automated earthquake notification system (*Gee et al.*, 2003; *Gee et al.*, 1996). The Rapid Earthquake Data Integration (REDI) project is a research program at the BSL for the rapid determination of earthquake parameters with three major objectives: to provide near real-time locations and magnitudes of northern and central California earthquakes; to provide estimates of the rupture characteristics and the distribution of ground shaking following significant earthquakes, and to develop better tools for the rapid assessment of damage and estimation of loss. A long-term goal of the project is the development of a system to warn of imminent ground shaking in the seconds after an earthquake has initiated but before strong motions begin at sites that may be damaged.

In 1996, the BSL and USGS began collaboration on a joint notification system for northern and central California earthquakes. The current system merges the programs in Menlo Park and Berkeley into a single earthquake notification system, combining data from the NCSN and the BDSN.

Today, the BSL and USGS system forms the Northern California Management Center (NCMC) of the California Integrated Seismic Network (Chapter 2).

2. Northern California Management Center

The details of the Northern California processing system and the REDI project have been described in past annual reports. In this section, we will describe how the

Northern California Management Center fits within the CISN system, detail recent developments, and discuss plans for the future development.

Figure 10.1 illustrates the NCMC as part of the the CISN communications ring. The NCMC is a distributed center, with elements in Berkeley and Menlo Park. The 35 mile separation between these two centers is in sharp contrast to the Southern California Management Center, where the USGS Pasadena is located across the street from the Caltech Seismological Laboratory. As described in Chapter 2, the CISN partners are connected by a dedicated T1 communications link, with the capability of falling back to the Internet. In addition to the CISN ring, the BSL and the USGS Menlo Park have a second dedicated communication link to provide bandwidth for shipping waveform data and other information between their processing systems.

Figure 10.2 provides more detail on the current system at the NCMC. At present, two Earthworm-Earlybird systems in Menlo Park feed two "standard" REDI processing systems at UC Berkeley. One of these systems is the production or paging system; the other is set up as a hot backup. The second system is frequently used to test new software developments before migrating them to the production environment. The Earthworm-Earlybird-REDI systems perform the standard detection, location, estimation of M_d , M_L , and M_w , as well as processing of ground motion data. The computation of ShakeMaps is also performed on two systems, one in Menlo Park and one in Berkeley, as described below. An additional system performs finite-fault processing and the computation of higher level ShakeMaps.

The dense network and Earthworm-Earlybird processing environment of the NCSN provides rapid and accurate earthquake locations, low magnitude detection thresholds, and first-motion mechanisms for smaller quakes. The high dynamic range data loggers, digital telemetry, and broadband and strong-motion sensors of the BDSN and REDI analysis software provide reliable magnitude determination, moment tensor estima-

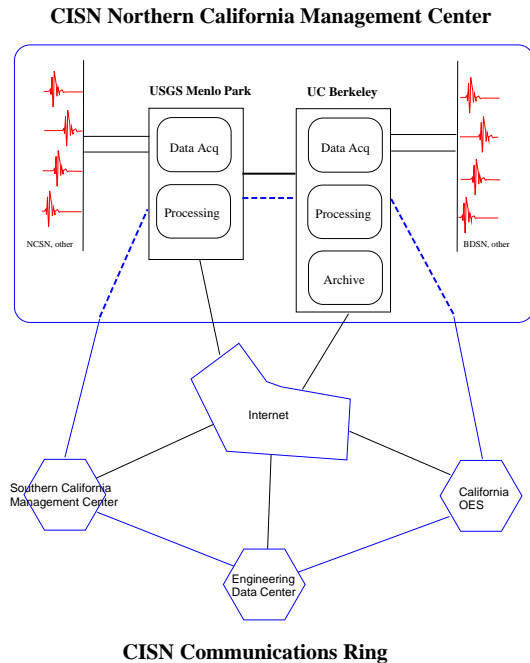


Figure 10.1: Schematic diagram illustrating the connectivity between the real-time processing systems at the USGS Menlo Park and UC Berkeley, forming the northern California Management Center, and with other elements of the CISON.

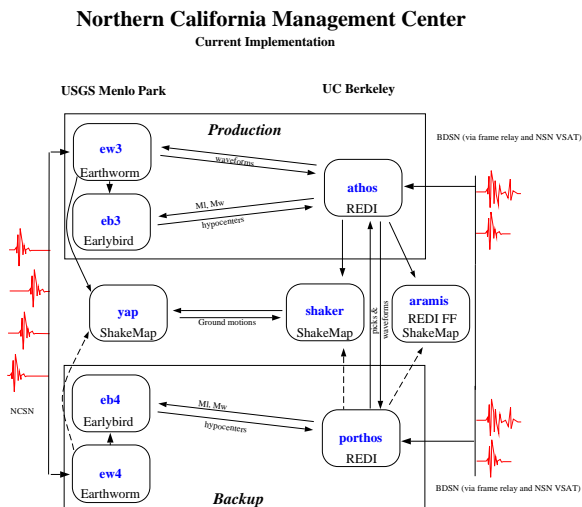


Figure 10.2: Detailed view of the current Northern California processing system, showing the two Earthworm-Earlybird-REDI systems, the two ShakeMap systems, and the finite-fault system.

tion, peak ground motions, and source rupture characteristics. Robust preliminary hypocenters are available about 25 seconds after the origin time, while preliminary coda magnitudes follow within 2-4 minutes. Estimates of local magnitude are generally available 30-120 seconds later, and other parameters, such as the peak ground acceleration and moment magnitude, follow within 1-4 minutes (Figure 10.3).

Earthquake information from the joint notification system is distributed by pager/cellphone, e-mail, and the WWW. The first two mechanisms "push" the information to recipients, while the current Web interface requires interested parties to actively seek the information. Consequently, paging and, to a lesser extent, e-mail are the preferred methods for emergency response notification. The *recenteqs* site has enjoyed enormous popularity since its introduction and provides a valuable resource for information whose bandwidth exceeds the limits of wireless systems and for access to information which is useful not only in the seconds immediately after an earthquake, but in the following hours and days as well.

3. 2002-2003 Activities

3.1 ShakeMap

The BSL and USGS/Menlo Park staff met in August 2002 to discuss how to improve the robustness of ShakeMap operation in northern California. At that time, ShakeMaps in northern California depended on the operation of a single computer, located in Menlo Park. This was in contrast to other earthquake monitoring operations, where 2 parallel systems provide back-up capability should a computer fail. The BSL and USGS Menlo Park agreed to bring up a second ShakeMap system at UC Berkeley, which will be twin or clone of the Menlo Park system.

The implementation of the second ShakeMap system was completed in early 2003, using one of the new CISON processing computers. Both ShakeMap systems are driven off the "production" monitoring system and both are configured to allow distribution of ShakeMaps to the Web and to recipients such as OES. At any one time, however, only one system distributes information.

In parallel, Pete Lombard at the BSL was trained to review ShakeMaps following an earthquake. Since early in 2003, the BSL has been trading the responsibility of ShakeMap production. The key to making a ShakeMap machine take over the production duty is to copy the earthquake database file from the former production machine to the new production machine. In that way, both machines can produce consistent ShakeMap archive lists.

The BSL has started work on a system to help with review of ShakeMaps. By modifying the program *grind*, we now write logs of the PGA and PGV values from station data, the regression curve, and the limits used by

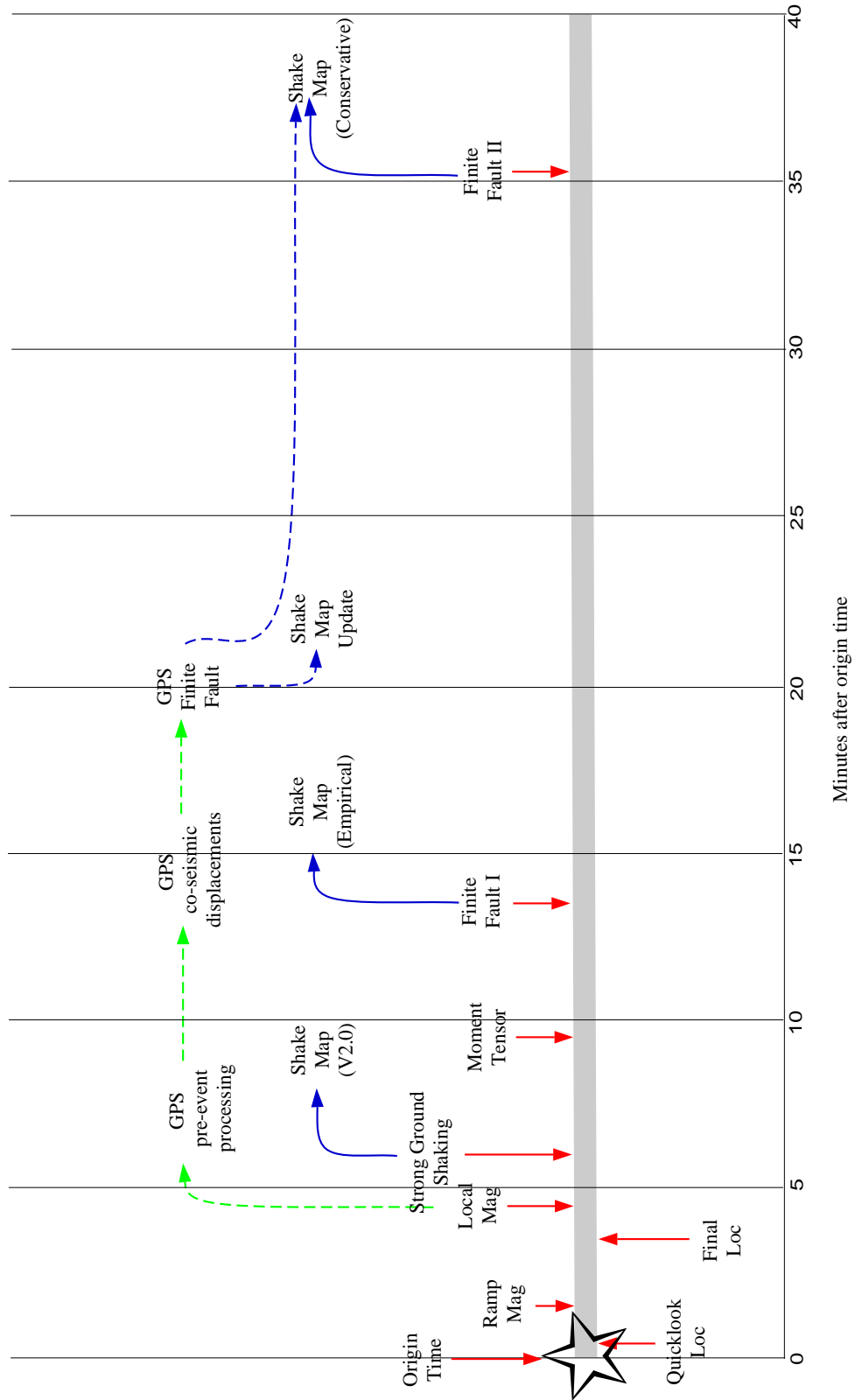


Figure 10.3: Illustration of the current (solid lines) and planned/proposed (dotted lines) development of real-time processing in northern California. The Finite Fault I and II are fully implemented within the REDI system at UC Berkeley and are integrated with ShakeMap. The resulting maps are still being evaluated and are not currently available to the public.

`grind` to flag outlier stations. This data is then plotted on amplitude vs. distance log-log plots. While this simple plot loses the spatial information available from a map view, it accurately reflects the process that `grind` uses for flagging stations. And the outlying data are more apparent on the x-y plots. For now, our plotting is done by a crude script running `gnuplot`. We intend at least to change this to use `GMT` for plotting. And we imagine that some day a pair of "clickable" plots could be presented on an internal Web server for use by ShakeMap reviewers.

3.2 M_w

The REDI system has routinely produced automatic estimates of moment magnitude (M_w) for many years. However, these estimates have not routinely used as the "official" magnitude, due in part to questions about the reliability of the automatic solutions. However, in response to the 05/14/2002 Gilroy earthquake (M_w 4.9, M_L 5.1) and the complications created by the publication of multiple magnitudes, the BSL and USGS Menlo Park have agreed to use automatically determined moment magnitudes, when available, to supplement estimates of local magnitude (M_L). This work was completed in the last year and M_w is now routinely reported when the solution is "good enough".

When is a solution "good enough"? This question has been under review in the last year - both to ensure reliable reporting of M_w in northern California and as part of the CISEN-effort to establish rules for a magnitude hierarchy. Figures 10.4 & 10.5 illustrate a dataset compiled since the most recent modification of the moment tensor software. The dataset indicates that the estimate M_w from the complete waveform inversion is quite robust for when a variance reduction of 40% or higher is obtained. In general, earthquakes of M4.5 and higher almost always achieve that level of variance reduction. Under the current rules, the Northern California Management Center always reports M_w if the variance reduction is 40% or better.

We have also looked at comparisons between our regional estimate of M_w and the moment magnitudes determined by Harvard as part of the Centroid Moment Tensor project. Figure 10.6 illustrates the regional M_w compared with the CMT M_w , along with comparisons between the NEIC estimates of M_w , m_b , M_s and the CMT M_w . This dataset spans approximately 60 events in the western US and good agreement between the regional and global methods is observed, although there appears to be a systematic difference in the estimates of approximately 0.08 - 0.09 magnitude units, with the CMT estimate being higher.

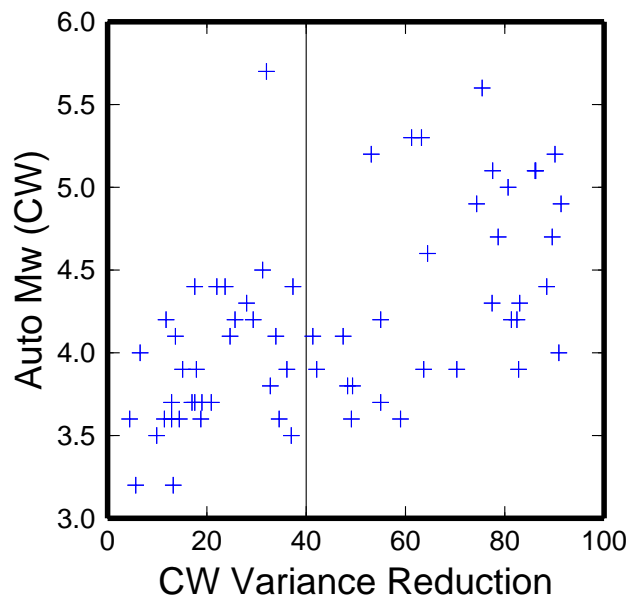


Figure 10.5: Results from the last year of complete waveform moment tensor inversions in the REDI system, with a few older events. With one exception, all events of M4.5 and higher achieved a variance reduction of 40%; approximately one third of the smaller events achieved the same level.

3.3 Version Numbers/Quake Data Delivery System

In the last year, the BSL and the USGS Menlo Park completed the software modifications necessary to track version numbers in the processing system. Version numbers are important for identifying the latest (and therefore hopefully the best) hypocenter and magnitude for an earthquake. Because both Menlo Park and Berkeley can be a source of earthquake information, it was critical to design a common versioning system. The modifications enabled the BSL to begin contributing solutions to QDDS, increasing the robustness of data distribution in northern California. At the present time, the USGS Menlo Park distributes solutions to 2 of the 3 QDDS hubs and the BSL distributes solutions to 2 of the 3 hubs (that is, 2 hubs receive notices from either the USGS or the BSL and 1 hub receives notices from both). This implementation should allow information to be distributed in the case of Internet shutdown of the Department of Interior (as occurred in December 2001 - see <http://www.cisn.org/news/doi.html>).

3.4 Database Implementation

During the past year, the BSL completed modifications to implement a database within real-time system. At this point, the database is used as a storage system,

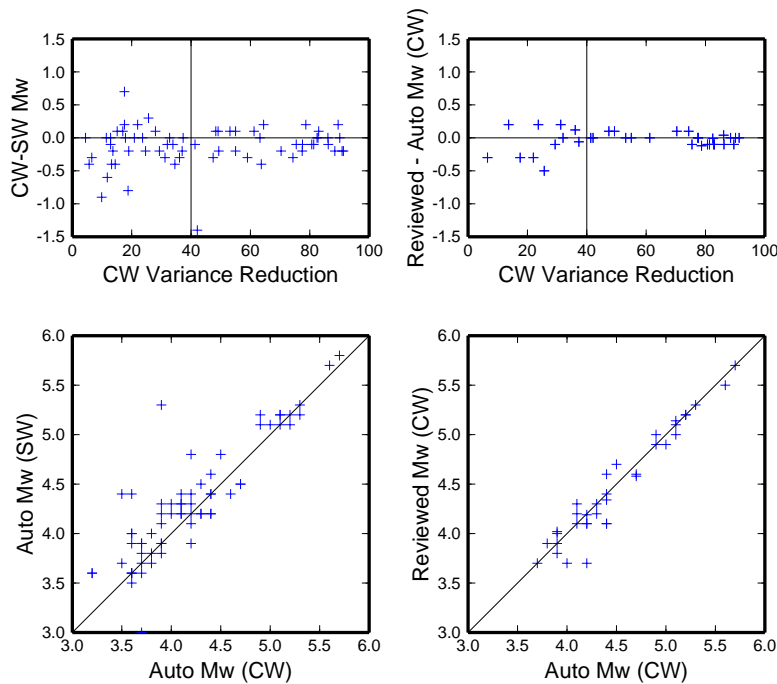


Figure 10.4: Left: Comparison of the two regional estimates of moment magnitude – the complete waveform (CW) and the surface wave (SW) methods – from the last year of REDI results and a few older events rerun through the system. As observed in *Pasyanos et al., 1996*, the estimates of moment from the surface wave inversion are larger than the complete waveform inversion. Right: Comparison of the estimates of M_w from automatic and reviewed complete waveform solutions.

supplementing the flat files that have been the basis of the REDI system. The modified software has now been installed on both REDI platforms.

3.5 System Development

As part of ongoing efforts to improve the monitoring systems in northern California, the BSL and the USGS Menlo Park have begun to plan for the next generation of the northern California joint notification system.

Figure 10.2 illustrates the current organization of the two systems. As described above, an Earthworm/Earlybird component is tied to a REDI component and the pair form a single "joint notification system". Although this approach has functioned reasonably well over the last 7 years, there are a number of potential problems associated with the separation of critical system elements by 30 miles of San Francisco Bay.

Recognizing this, we intend to redesign the Northern California operations so that a single independent system operates at the USGS and at UC Berkeley. Figure 10.7 illustrates the planned configuration. In FY01/02, our discussions proceeded to the stage of establishing specifications and determining the details required for design. However, in the last year, most of the development effort focused on CISN activities and specific plans for the

"next generation" Northern California system were put on hold. This enforced wait provided the opportunity for some ideas to mature and the current plans for the NCMC are somewhat different from those envisioned in 2001.

The current design draws strongly on the experience in Southern California for the development of TriNet. In the last year, BSL staff, particularly Pete Lombard, have become extremely familiar with portions of the TriNet software. We have begun to adapt the software for Northern California, making adjustments and modifications along the way.

We anticipate that the next generation of Northern California Management Center system will include many elements from the TriNet software. Certain components, such as the dependence on third part software for communication among processing modules, will be modified and an alternative distribution system utilized.

4. Routine Earthquake Analysis

On a daily basis, the BSL continues to locate and determine the magnitude of earthquakes in northern California and adjacent regions. As a general rule, events are analyzed if their magnitude is greater than 2.8 in the Central Coast ranges, greater than 3.0 in all of northern Califor-

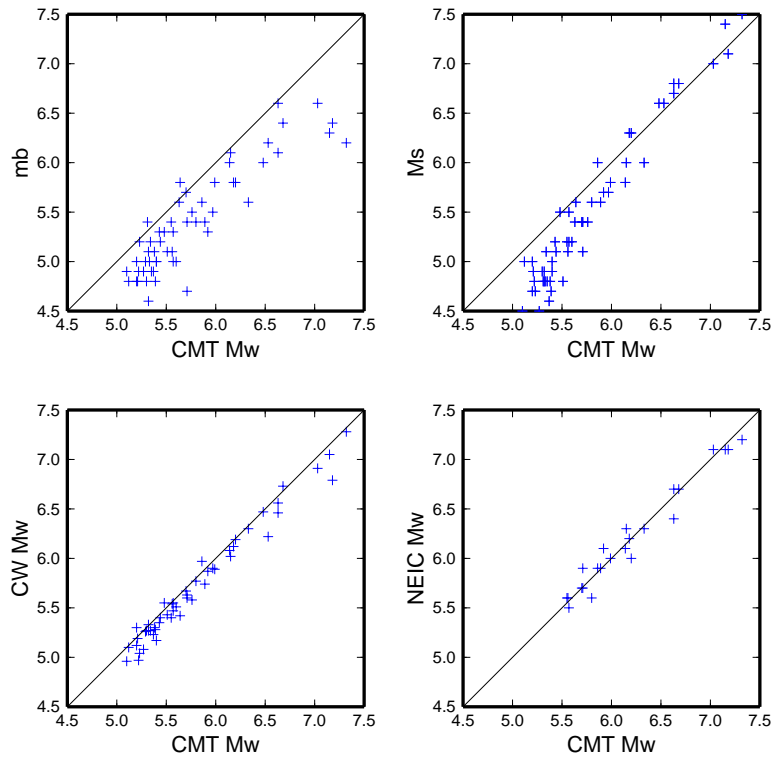


Figure 10.6: Comparison of several magnitudes with the M_w estimates determined from the Harvard Centroid Moment Tensor project. Lower left: Regional M_w from the reviewed solutions of the BSL; lower right: Global M_w from NEIC; upper left: m_b from NEIC; upper right: M_s from NEIC.

Northern California Earthquake Notification System

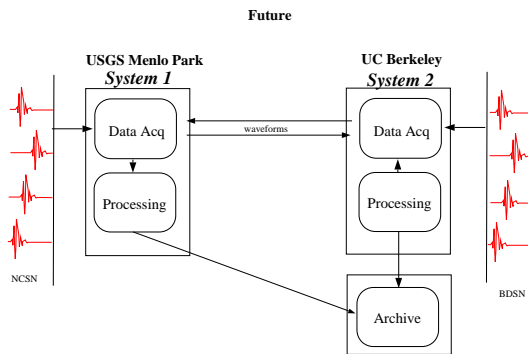


Figure 10.7: Future design of the Northern California Earthquake Notification System. In contrast with the current situation (Figure 10.2), the system is being redesigned to integrate the Earthworm/Earlybird/REDI software into a single package. Parallel systems will be run at the Berkeley and Menlo Park facilities of the Northern California Operations Center.

nia, or greater than 3.8 in the bordering regions. Traditionally, these events were located using hand-picked arrival times from the BDSN stations in conjunction with P-arrival times from the NCSN using the program st-relp. Over the past several years, the BSL has made a transition in the daily analysis to take advantage of the automatic processing system. As part of this transition, events which have been processed by the automatic system are not generally relocated, although phase arrivals are still hand-picked and the synthetic Wood-Anderson readings are checked. Instead, analysts are focusing on the determination of additional parameters, such as the seismic moment tensor, phase azimuth, and measures of strong ground shaking.

From July 2002 through June 2003, BSL analysts reviewed nearly 150 earthquakes in northern California and adjoining areas, ranging from M2.2 to 6.2. Reviewed moment tensor solutions were obtained for 24 events (through 6/30/2002). Figure 10.8 and Table 10.1 displays the earthquakes located in the BSL catalog and the moment tensor solutions.

4.1 Special Events

In late November, a small swarm of earthquakes occurred near the Calaveras fault in San Ramon. The

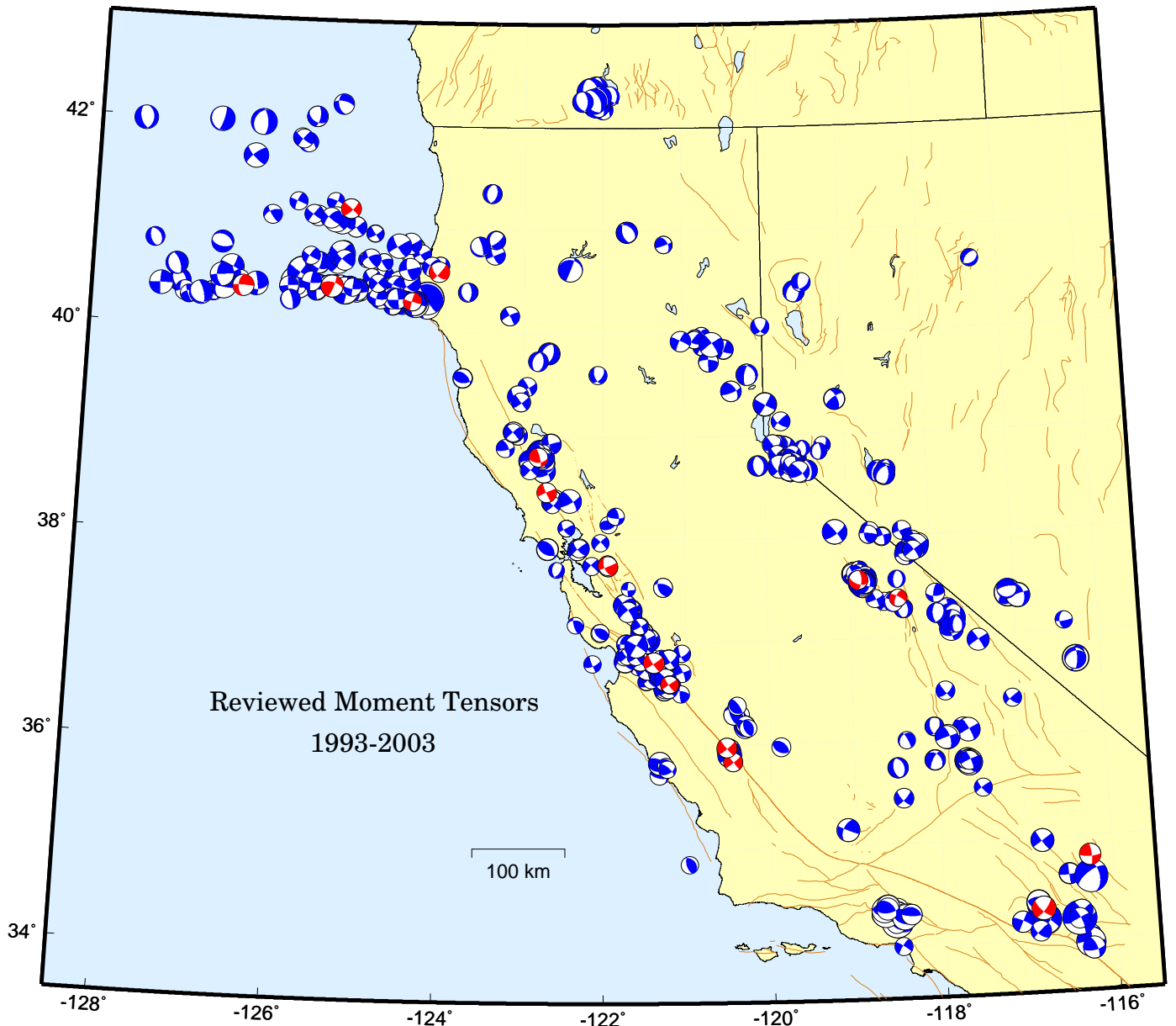


Figure 10.8: Map comparing the reviewed moment tensor solutions determined by the BSL in the last 10 years (blue) and those from the last fiscal year (red).

largest event was a M_w 3.9 and with 4 events over $M3.5$. The pre-Thanksgiving events were felt over a large area - the Community Internet Intensity Map reports approximately 2400 responses for the $M3.9$. The Northern California Management Center put together an Internet report on the sequence and posted it on the CISN Web page: <http://www.cisn.org/special/evt.02.11.24/> In early February, a small swarm of earthquakes occurred near the Calaveras fault in Dublin. The largest event in this sequence was an M_L 4.2, with 3 events of $M3.5$. In contrast to the events in November, these events occurred sub parallel to the Calaveras fault (Figure 10.9). As in November, these events were felt over a broad area, al-

though no damage was reported.

4.2 Teleseisms

In addition to the routine analysis of local and regional earthquakes, the BSL also processes teleseismic earthquakes. Taking advantage of the ANSS catalog, analysts review teleseisms of magnitude 5.8 and higher. All events of magnitude 6 and higher are read on the quietest BDSN station, while events of magnitude 6.5 and higher are read on the quietest station and BKS. Earthquakes of magnitude 7 and higher are read on all BDSN stations.

The locations and magnitude determined by the BSL are cataloged on the NCEDC. The phase and amplitude

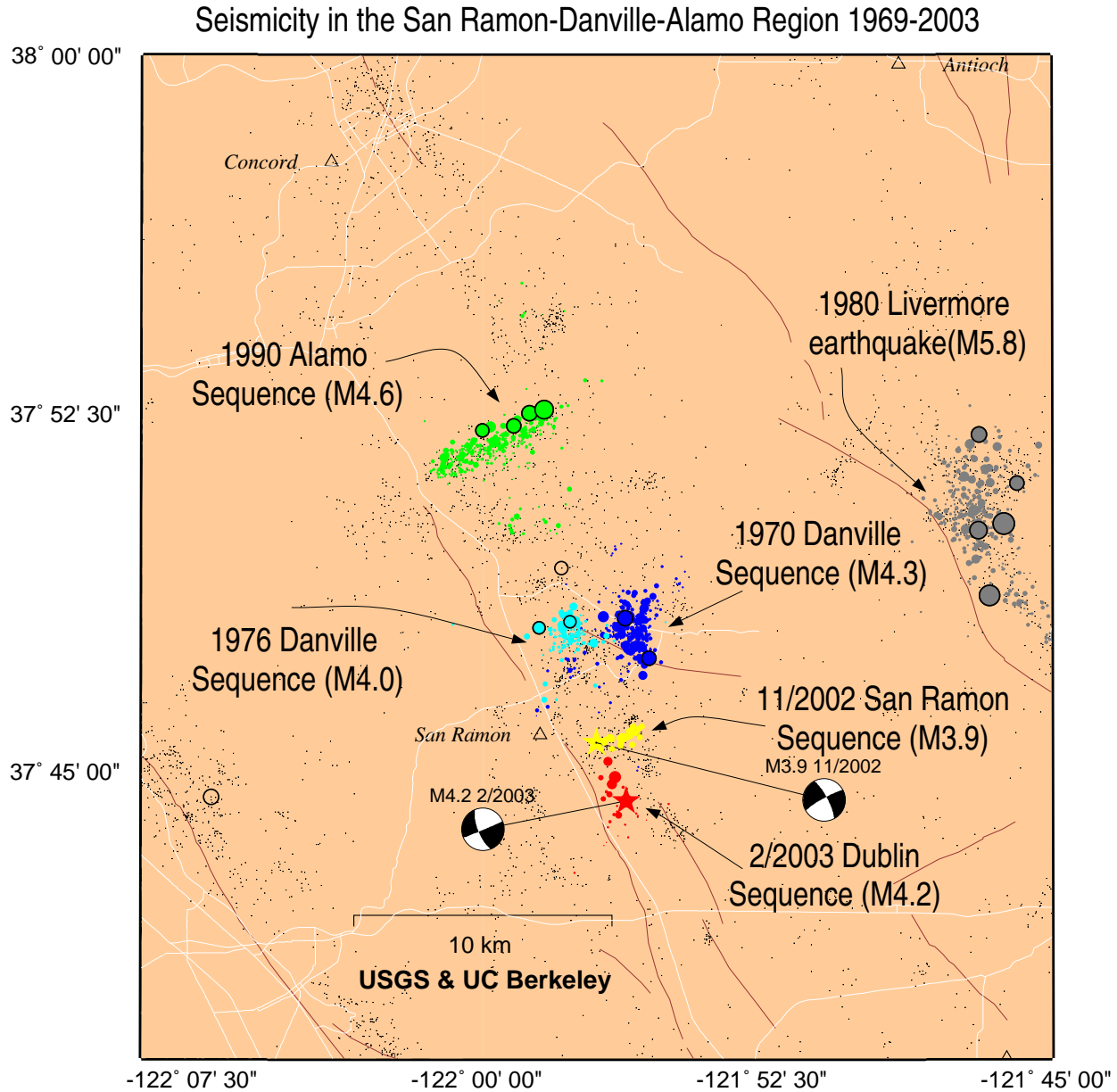


Figure 10.9: This map illustrates the Feb 2003 Dublin and Nov 2002 San Ramon swarms in the context of historical seismicity. Earthquakes from the USGS catalog 1970-2003 are plotted, with events of $M_L \geq 4.0$ plotted with large circles. Events associated with various sequences are plotted in color: 1970 Danville (blue), 1976 Danville (turquoise), 1980 Livermore (grey), and 1990 Alamo (green). Events from the 2002 swarm are plotted in yellow and the events from 2003 are plotted in red.

data are provided to the NEIC, along with the locations and magnitudes, as contributions to the global catalogs, such as that of the ISC.

5. Acknowledgements

Lind Gee leads the development of the REDI system and directs the routine analysis. Peter Lombard and Doug Neuhauser contribute to the development of software. Rick McKenzie, Doug Dreger, and Dennise Templeton contribute to the routine analysis. Lind Gee, Doug

Location	Date	Time	Lat.	Lon.	MT Dep.	M_L	M_w	M_o	Str.	Dip	Rake
Bishop	07/15/2002	20:18:17.0	37.385	-118.407	14.0	4.1	3.7	3.50e21	300	76	-154
Parkfield	09/06/2002	07:28:22.0	35.834	-120.450	14.0	4.0	4.0	9.79e21	321	88	175
San Benito	09/25/2002	07:08:46.0	36.592	-121.199	11.0	3.9	3.8	6.70e21	134	87	176
Pinnacles	09/28/2002	16:07:47.0	36.595	-121.200	14.0	3.7	3.7	4.49e21	146	81	177
Ludlow	10/29/2002	14:16:53.0	34.807	-116.267	8.0	4.9	4.6	7.84e22	356	79	167
Parkfield	11/12/2002	16:48:25.0	35.972	-120.522	11.0	4.2	4.1	1.80e22	141	87	-173
Punta Gorda	11/21/2002	13:17:39.0	40.295	-124.420	11.0	3.5	3.9	8.65e21	104	88	173
San Ramon	11/24/2002	14:54:23.0	37.760	-121.950	8.0	3.9	3.9	7.75e21	242	84	-13
Hollister	01/07/2003	22:29:27.0	36.806	-121.389	11.0	4.7	4.3	3.71e22	147	80	-174
Petrolia	01/08/2003	05:41:43.0	40.422	-125.445	8.0	4.2	4.7	1.12e23	20	79	31
Dublin	02/02/2003	16:22:52.0	37.746	-121.943	14.0	3.6	3.7	4.46e21	259	81	14
Dublin	02/02/2003	18:22:58.0	37.740	-121.937	14.0	4.2	4.1	1.36e22	67	88	-19
Dublin	02/02/2003	18:47:39.0	37.748	-121.942	11.0	4.0	4.1	1.36e22	67	87	-34
Arcata	02/18/2003	14:44:24.0	41.179	-125.237	11.0	3.7	4.2	2.39e22	44	75	3
Big Bear City	02/22/2003	12:19:10.0	34.310	-116.848	5.0	5.4	5.0	3.20e23	40	75	-20
Mammoth Lakes	03/08/2003	15:35:02.0	37.572	-118.885	5.0	4.3	4.1	1.36e22	2	62	-39
Hydesville	04/22/2003	10:46:09.0	40.588	-124.086	27.0	3.9	4.4	3.76e22	40	84	-33
Geysers	05/20/2003	16:50:42.0	38.800	-122.804	5.0	3.6	4.0	1.31e22	346	79	136
Santa Rosa	05/25/2003	00:09:33.0	38.460	-122.700	8.0	4.3	4.2	1.96e22	245	86	4
Petrolia	06/26/2003	03:39:35.4	40.395	-126.574	14.0	4.1	4.6	8.22e22	272	87	-142

Table 10.1: Moment tensor solutions for significant events from July 1, 2001 to June 30, 2002 using the complete waveform fitting method. Epicentral information from the UC Berkeley/USGS Northern California Earthquake Data Center. Moment is in dyne-cm and depth is in km.

Neuhauser, and Dennise Templeton contributed to the writing of this chapter.

Partial support for the develop of the REDI system is provided by the USGS.

6. References

Gee, L., D. Neuhauser, D. Dreger, M. Pasyanos, R. Uhrhammer, and B. Romanowicz, The Rapid Earthquake Data Integration Project, *Handbook of Earthquake and Engineering Seismology*, IASPEI, 1261-1273, 2003.

Gee, L., D. Neuhauser, D. Dreger, M. Pasyanos, B. Romanowicz, and R. Uhrhammer, The Rapid Earthquake Data Integration System, *Bull. Seis. Soc. Am.*, 86, 936-945, 1996.

Pasyanos, M., D. Dreger, and B. Romanowicz, Toward real-time estimation of regional moment tensors, *Bull. Seis. Soc. Am.*, 86, 1255-1269, 1996.

Chapter 11

Northern California Earthquake Data Center

1. Introduction

The Northern California Earthquake Data Center, a joint project of the Berkeley Seismological Laboratory and the U.S. Geological Survey at Menlo Park, serves as an "on-line" archive for various types of digital data relating to earthquakes in central and northern California. The NCEDC is located at the Berkeley Seismological Laboratory, and has been accessible to users via the Internet since mid-1992.

The primary goal of the NCEDC is to provide a stable and permanent archival and distribution center of digital geophysical data for northern and central California such as seismic waveforms, electromagnetic data, GPS data, and earthquake parametric data. The principal networks contributing seismic data to the data center are the Berkeley Digital Seismic Network (BDSN) operated by the Seismological Laboratory, the Northern California Seismic Network (NCSN) operated by the USGS, and the Bay Area Regional Deformation (BARD) GPS network. The collection of NCSN digital waveforms date from 1984 to the present, the BDSN digital waveforms date from 1987 to the present, and the BARD GPS data date from 1993 to the present.

The NCEDC continues to use the World Wide Web as a principal interface for users to request, search, and receive data from the NCEDC. The NCEDC has implemented a number of useful and original mechanisms of data search and retrieval using the World Wide Web, which are available to anyone on the Internet. All of the documentation about the NCEDC, including the research users' guide, is available via the Web. Users can perform catalog searches and retrieve hypocentral information and phase readings from the various earthquake catalogs at the NCEDC via easy-to-use forms on the Web. In addition, users can peruse the index of available broadband data at the NCEDC, and can request and retrieve broadband data in standard SEED format via the Web. Access to all datasets is available via research accounts at the NCEDC. The NCEDC's Web address is

<http://quake.geo.berkeley.edu/>

2. NCEDC Overview

The NCEDC is located within the computing facilities at the Berkeley Seismological Laboratory in McCone Hall. The BSL facility provides the NCEDC with air conditioning, 100 bit switched network, and reliable power from a UPS with generator backup.

The current NCEDC facilities consist of a Sun Ultra 450 computer, a 2.5 TByte capacity DISC 517 slot jukebox with four 5.2 GByte MO drives and 5.2 GB MO media, a 15-slot AIT tape jukebox which holds 25 GBytes per tape, and the SAM-FS hierarchical storage management (HSM) software, and 4.6 TB of online disk storage. A dual processor Sun Ultra 60 provides Web services and research account access to the NCEDC.

The hardware and software system can be configured to automatically create multiple copies of each data file. The NCEDC uses this feature to create an online copy of each data file on MO media, and another copy on AIT tape which is stored offline. As of 2003, all data is stored on magnetic disk, with backup copies on MO and tape media.

3. 2002-2003 Activities

By its nature, data archiving is an ongoing activity. In 2002-2003, the NCEDC continued to expand its data holdings and enhance access to the data. Projects and activities of particular note include:

- Establishment of a continuous archive for NCSN broadband data
- Significant progress on populating NCSN hardware information, instrument response, and waveform inventory in the NCEDC database

- Development and implementation of *IRIS FIS-SURES* services as a data distribution method for data from the NCEDC
- Improvement and implementation of *STP* at the NCEDC
- Conversion of the remaining 16-bit BDSN data to MiniSEED
- Development of new Web pages
- Migration of all waveform data from near-online storage to online storage

These activities and projects are described in detail below.

4. Data Collections

The bulk of the data at the NCEDC consist of waveform and GPS data from northern California. Figure 11.1 shows the relative proportion of each data set at the NCEDC. The total size of the datasets archived at the NCEDC is shown in Table 11.1. Figure 11.2 shows the geographic distribution of data archived by the NCEDC.

4.1 BDSN/NHFN/MPBO Seismic Data

The archival of current BDSN (Chapter 3), NHFN (Chapter 4), and Mini-PBO (Chapter 8) (all stations using the network code BK) seismic data is an ongoing task. These data are telemetered from more than 30 seismic data loggers in real-time to the BSL, where they are written to disk files. Each day, an extraction process creates a daily archive by retrieving all continuous and event-triggered data for the previous day. The daily archive is run through quality control procedures to correct any timing errors, triggered data is reselected based on the REDI, NCSN, and BSL earthquake catalogs, and the resulting daily collection of data is archived at the NCEDC.

All of the data acquired from the BDSN/NHFN/MPBO Quanterra data loggers are archived at the NCEDC. The NCEDC has made an effort to archive older digital data, and the 16-bit BDSN digital broadband data from 1987-1991 have been converted to MiniSEED and are now online. In late June 2002, the NCEDC initiated a project to convert the remaining 16-bit BDSN data (MHC, SAO, and PKD1) from late 1991 through mid-1992 to MiniSEED. An undergraduate student was hired to read the old tapes and to work on the conversion. All remaining 20 Hz 16 bit BDSN data has been converted to MiniSEED, and we are working on the decimation procedures to create the 1 Hz data channels. Data acquired by portable 24-bit RefTek recorders before the installation of Quanterra

data loggers at NHFN sites has not yet been converted to MiniSEED and archived.

4.2 NCSN/SHFN Seismic Data

NCSN and SHFN waveform data are sent to the NCEDC via the Internet. The NCSN event waveform files are automatically transferred from the Menlo Park to the NCEDC as part of the routine analysis procedure by the USGS, and are automatically verified and archived by the NCEDC.

A few corrupt NCSN event files were discovered at the NCEDC several years ago, and were eventually traced down to suspected flaws in the 12-inch WORM media and/or firmware problems on the Sony WDA-600 series jukeboxes used by the NCEDC. When we transcribed the data from the 12-inch WORM media to the current 5.25 inch magneto-optical media, we verified that all files were transcribed accurately. In 2000-2001, using software developed at the NCEDC to detect possibly corrupt NCSN files, we identified 4704 possibly corrupted NCSN waveform event files. We re-read the original NCSN tapes for all of these events, discovered that only 71 of the files were actually corrupt, and replaced the corrupted event waveform files.

The NCEDC maintains a list of teleseismic events recorded by the NCSN, which is updated automatically whenever a new NCSN event file is received at the NCEDC, since these events do not appear in the NCSN catalog.

The NCSN installed 9 continuously telemetered digital broadband stations in northwest California and southwest Oregon in support of the USGS/NOAA Consolidated Reporting of EarthquakeS and Tsunamis (CREST) system, and 2 continuously telemetered digital broadband stations in the Mammoth region. The NCEDC established procedures to create an archive of continuous data from these stations, in addition to the event waveform files. These data initially included channels at 50 and 100 Hz, but now are all 100 Hz sampling. The NCEDC hoped to generate an archive of 20 Hz data (for consistency with the BDSN data) from these 100 Hz waveforms, but incomplete continuous data due to telemetry problems between the stations and the USGS Menlo Park data collection center has made this difficult. At this point, the NCEDC is archiving the 100 Hz data without decimation.

4.3 Parkfield HRSN Data

Event seismograms from the Parkfield High Resolution Seismic Network (HRSN) from 1987 through June 1998 are available in their raw SEG-Y format via NCEDC research accounts. A number of events have faulty timing due to the lack or failure of a precision time source for the network. Due to funding limitations, there is currently no ongoing work to correct the timing problems

Volume of Data archived at the NCEDC

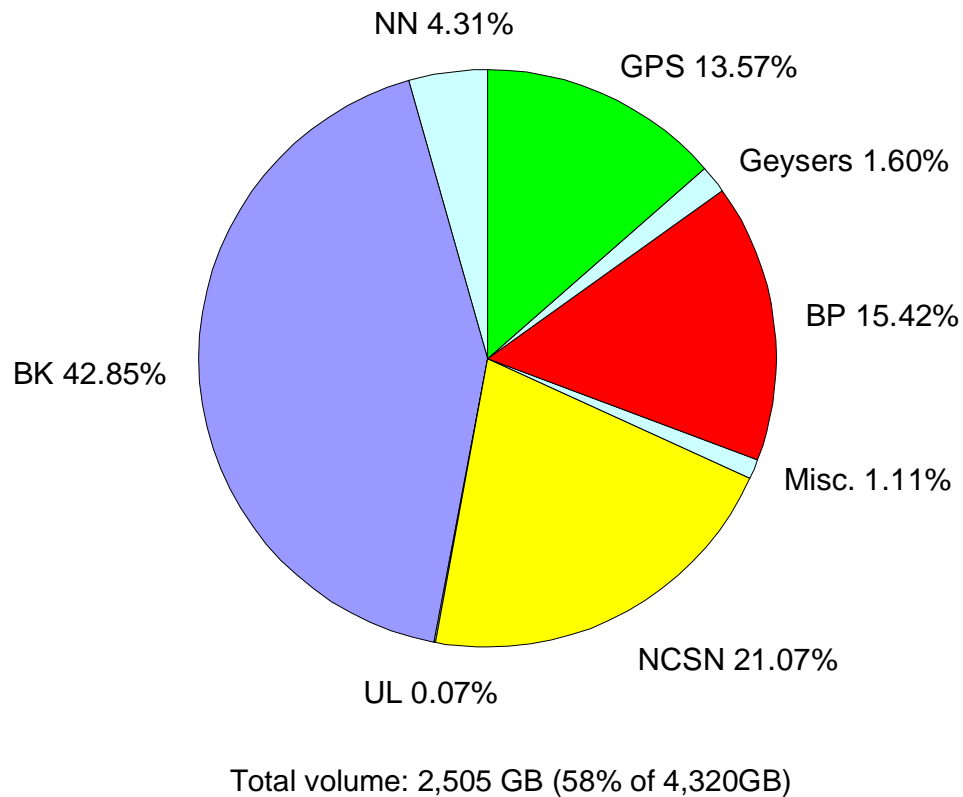


Figure 11.1: Chart showing the relative proportion of each data set at the NCEDC.

Data Type	MBytes
BDSN/NHFN/MPBO (broadband, electric field, magnetic field, strain) waveforms	1,073,842
NCSN seismograms	527,935
Parkfield HRSN seismograms	386,471
BARD GPS (RINEX and raw data)	339,970
UNR Nevada seismograms	107,887
Calpine/Unocal Geysers region seismograms	39,999
USGS Low frequency geophysical waveforms	18,585
Misc data	27,846
Total size of archived data	2,505,810

Table 11.1: Volume of Data Archived at the NCEDC by network

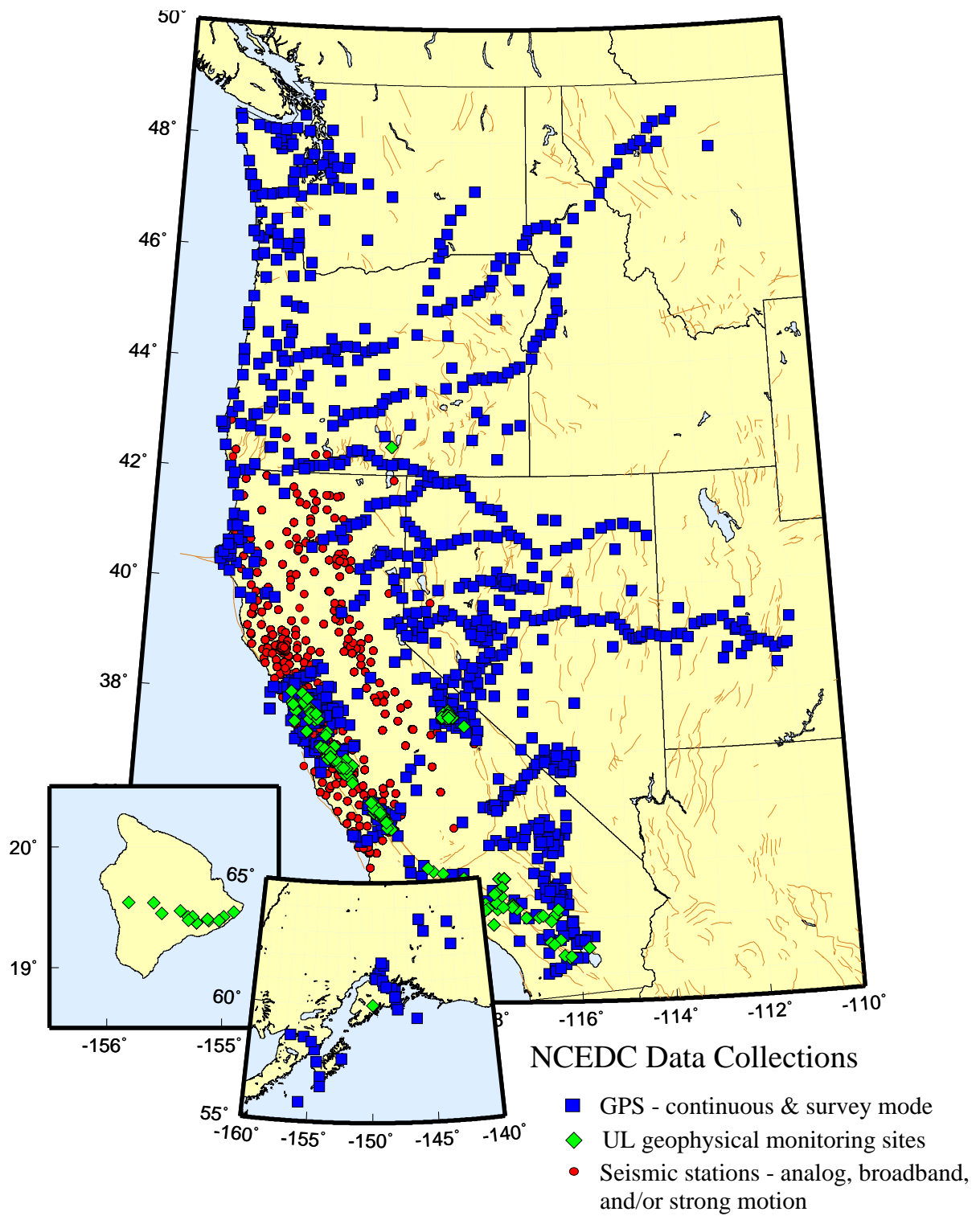


Figure 11.2: Map showing the location of stations whose data are archived at the NCEDC. Circles are seismic sites; squares are GPS sites, and diamonds are the locations of USGS Low-frequency experiments.

BK Data Availability

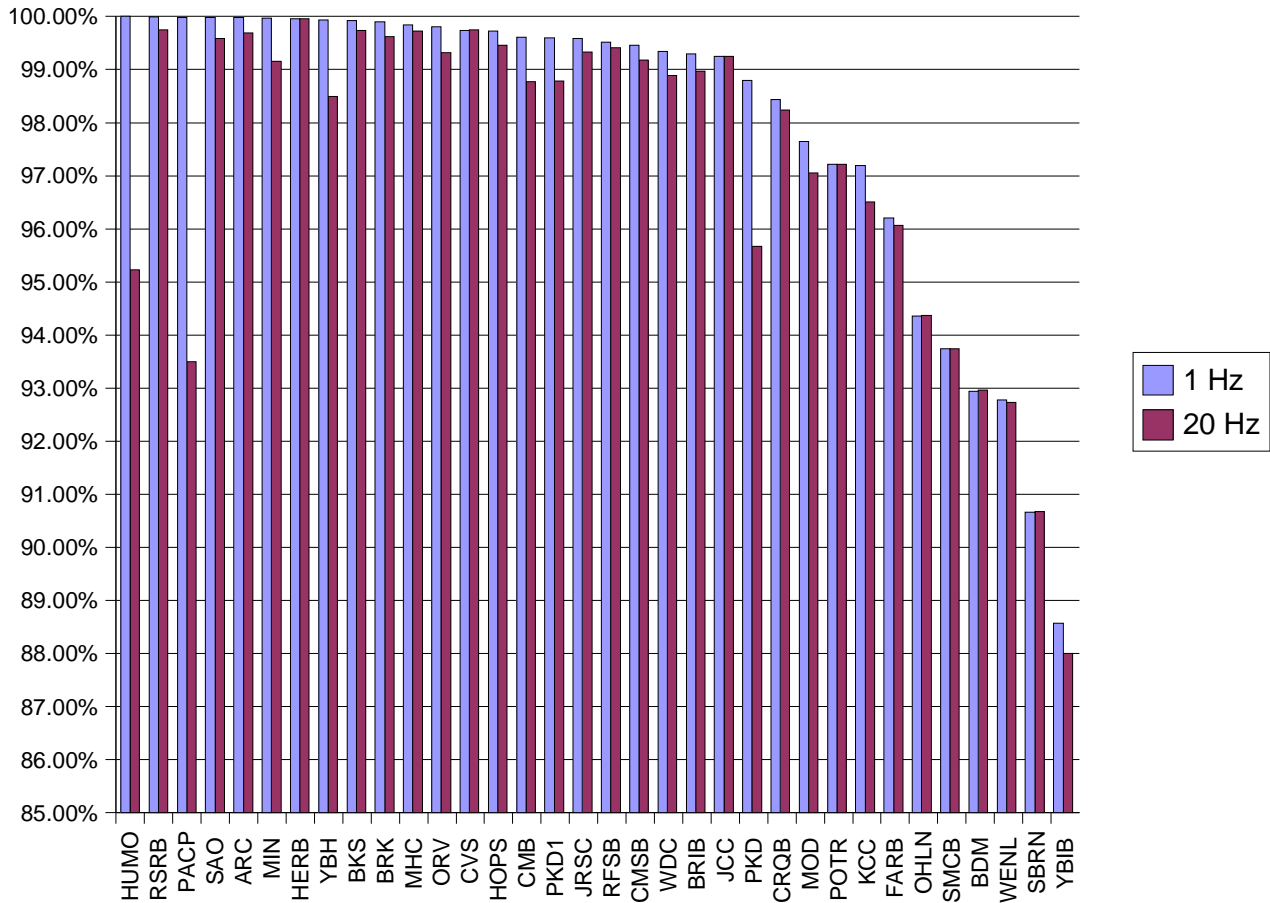


Figure 11.3: Chart showing the availability of BDSN/NHFN/MPBO data at the NCEDC for the 1 Hz and 20 Hz channels from 01/01/1996 - 06/30/2002. The "uptime" of these networks is better than 95% at nearly all stations. Exceptions are BDM (damaged by a lightning strike in May 2000), FARB (power problems when the USFWS generator failed in 1998), MOD (which suffered some delays during installation), WENL (flooded during the winter of 1997), YBIB (damaged during a lightning strike in 1997 and without AC power for the past 4 years), and SBRN and OHLN (which experienced software problems related to data acquisition from a digital pore pressure sensor). In general, a difference between the 1 and 20 Hz data is indicative of significant telemetry problems. Following a major telemetry outage, BSL staff will recover 1 Hz continuous data but only event data for the 20 Hz channels.

in the older events or to create MiniSEED volumes for these events. However, a preliminary catalog for a significant number of these events has been constructed, and the catalog is available via the Web at the NCEDC.

As described in Chapter 5, the original HRSN acquisition system died in late 1998, and an interim system of portable RefTek recorders were installed at some of the sites. Data from this interim system are not currently available online.

In 2000 and 2001, 3 new borehole sites were installed, and the network was upgraded to operate with Quanterra Q730 data loggers and digital telemetry. The upgraded acquisition system detects events using the HRSN stations and extracts waveforms from both the HRSN and the PASO stations. The event waveform files are automatically transferred to the NCEDC, where they are made available to the research community via anonymous FTP until they are reviewed and permanently archived. During the deployment of the temporary PASSCAL network (PASO) Parkfield during in 2000-2003 with the IRIS broadband array telemetry, the HRSN collected event data from both the HRSN and PASO array and provided this integrated data set to researchers in near-real-time.

The HRSN 20 Hz (BP) and state-of-health channels are being archived continuously at the NCEDC. As an interim measure, the NCEDC also archived continuous data from the 250 Hz (DP) channels through mid 2002 in order to help researchers retrieve events that were not detected during the network upgrade.

4.4 UNR Broadband Data

The University of Reno in Nevada (UNR) operates several broadband stations in western Nevada and eastern California that are important for northern California earthquake processing and analysis. Starting in August 2000, the NCEDC has been receiving and archiving continuous broadband data from four UNR stations. The data are transmitted in real-time from UNR to UC Berkeley, where it is made available for real-time earthquake processing and for archiving.

In a situation similar to that of the broadband waveforms from the NCSN, the NCEDC originally planned to create an archive of 20 Hz data from the 100 Hz data. However, frequent gaps in the data complicate the development of a robust decimation process. At this time, the UNR broadband waveforms are being archived at 100 Hz.

4.5 Electro-Magnetic Data

The NCEDC continues to archive and process electric and magnetic field data acquired from data loggers at two sites (SAO and PKD). At PKD and SAO, 3 components of magnetic field and 2 or 4 components of electric field are digitized and telemetered in real-time along with

seismic data to the Seismological Laboratory, where they are processed and archived at the NCEDC in a similar fashion to the seismic data (Chapter 6). The system generates continuous data channels at 40 Hz, 1 Hz, and .1 Hz for each component of data. All of these data are archived and remain available online at the NCEDC. Using programs developed by Dr. Martin Fullerkrug at the Stanford University STAR Laboratory (now at the Institute for Meteorology and Geophysics at the University of Frankfurt), the NCEDC is computing and archiving magnetic activity and Schumann resonance analysis using the 40 Hz data from this dataset. The magnetic activity and Schumann resonance data can be accessed from the Web.

In addition to the electromagnetic data from PKD and SAO, the NCEDC archives data from a low-frequency, long-baseline electric field project operated by Dr. Steve Park of UC Riverside at site PKD2. This experiment (which is separate from the equipment at PKD1 described in Chapter 6), uses an 8-channel Quanterra data logger to record the data, which are transmitted to the BSL using the same circuit as the BDSN seismic data. These data is acquired and archived in an identical manner to the other electric field data at the NCEDC.

4.6 GPS Data

The NCEDC archives GPS data from the BARD (Bay Area Regional Deformation) network of continuously monitored GPS receivers in northern California (Chapter 7). The NCEDC GPS archive now includes 77 continuous sites in northern California. There are approximately 70 core BARD sites owned and operated by UC Berkeley, USGS (Menlo Park and Cascade Volcano Observatory), LLNL, UC Davis, UC Santa Cruz, Trimble Navigation, and Stanford. Data are also archived from sites operated by other agencies including East Bay Municipal Utilities District, the City of Modesto, the National Geodetic Survey, and the Jet Propulsion Laboratory.

The NCEDC also archives non-continuous survey GPS data. The NCEDC is the principal archive for the survey GPS data collected by the USGS Menlo Park for northern California and other locations. Significant quality control efforts were implemented by the NCEDC to ensure that the raw data, scanned site log sheets, and RINEX data are archived for each survey. All of the USGS MP GPS data has been transferred to the NCEDC and virtually all of the data from 1992 to the present has been archived and is available for distribution.

4.7 Calpine/Unocal Geysers Seismic Data

The Calpine Corporation currently operates a microseismic monitoring network in the Geysers regions of northern California. Prior to 1999 this network was operated by Unocal. Through various agreements with both

Unocal and Calpine, the companies have release triggered event waveform data from 1989 to through 2000 along with and preliminary event catalogs for the same time period for archiving and distribution through the NCEDC. This dataset represents over 296,000 events that were recorded by Calpine/Unocal Geysers network, and are available via research accounts at the NCEDC.

4.8 USGS Low Frequency Data

Over the last 26 years, the USGS at Menlo Park, in collaboration with other principal investigators, has collected an extensive low-frequency geophysical data set that contains over 1300 channels of tilt, tensor strain, dilatational strain, creep, magnetic field, water level, and auxiliary channels such as temperature, pore pressure, rain and snow accumulation, and wind speed. In collaboration with the USGS, we assembled the requisite information for the hardware representation of the stations and the instrument responses for many channels of this diverse dataset, and developed the required programs to populate and update the hardware database and generate the instrument responses. We developed the programs and procedures to automate the process of importing the raw waveform data and convert it to MiniSEED format.

We have currently archived timeseries data from 887 data channels from 167 sites, and have instrument response information for 542 channels at 139 sites. The waveform archive is updated on a daily basis with data from 350 currently operating data channels. We will augment the raw data archive as additional instrument response information is assembled for the channels, and will work with the USGS to clearly define the attributes of the "processed" data channels.

4.9 Earthquake Catalogs

Northern California

Currently both the USGS and BSL construct and maintain earthquake catalogs for northern and central California. The "official" UC Berkeley earthquake catalog begins in 1910, and the USGS "official" catalog begins in 1966. Both of these catalogs are archived and available through the NCEDC, but the existence of 2 catalogs has caused confusion among both researchers and the public. The BSL and the USGS have spent considerable effort over the past years to define procedures for merging the data from the two catalogs into a single northern and central California earthquake catalog in order to present a unified view of northern California seismicity. The differences in time period, variations in data availability, and mismatches in regions of coverage all complicate the task.

Worldwide

The NCEDC, in conjunction with the Council of the National Seismic System (CNSS), produced and distributed a world-wide composite catalog of earthquakes based on the catalogs of the national and various U.S. regional networks for several years. Each network updates their earthquake catalog on a daily basis at the NCEDC, and the NCEDC constructs a composite world-wide earthquake catalog by combining the data, removing duplicate entries that may occur from multiple networks recording an event, and giving priority to the data from each network's *authoritative region*. The catalog, which includes data from 14 regional and national networks, is searchable using a Web interface at the NCEDC. The catalog is also freely available to anyone via FTP over the Internet.

With the demise of the CNSS and the development of the ANSS, the NCEDC was asked to update the Web pages to present the composite catalog as a product of the ANSS. This conversion was completed in the fall of 2002.

5. Data Quality Control

The NCEDC developed a GUI-based state-driven system *CalQC* to facilitate the quality control processing that is applied to the BK, NC broadband, NN, and BP data sets.

The quality control procedures for these datasets include the following tasks:

- data extraction of a full day of data,
- quick check program to summarize the quality and stability of the stations' clock,
- checks for missing data along with procedures to retrieve data from the stations and incorporate it into the day of data,
- optional creation of multi-day timeseries plots for state-of-health data channels,
- optional timing corrections for data,
- optional extraction of event-based waveforms from continuous data channels,
- optional repacking of MiniSEED data,
- creating waveform inventory entries in the NCEDC database,
- publishing the data for remote access on the NCEDC.

CalQC uses previously developed programs to perform each function, but it provides a graphical point-and-click interface to automate these procedures, and to provide the analyst with a record of when each process was started, whether it executed correctly, and whether the analyst has indicated that a step has been completed. *CalQC* is used to process all data from the BK network, and all continuous data from the NN, NC, and BP networks that is archived by the NCEDC.

6. Database Development

Most of the parametric data archived at the NCEDC, such as earthquake catalogs, phase and amplitude readings, waveform inventory, and instrument responses have been stored in flat text files. Flat files are easily stored and viewed, but are not efficiently searched. Over the last year, the NCEDC, in collaboration with the Southern California Earthquake Data Center (SCEDC) and the California Integrated Seismic Network (CISN), has continued development of database schemas to store the parametric data from the joint earthquake catalog, station history, complete instrument response for all data channels, and waveform inventory.

The parametric schema supports tables and associations for the joint earthquake catalog. It allows for multiple hypocenters per event, multiple magnitudes per hypocenter, and association of phases and amplitudes with multiple versions of hypocenters and magnitudes respectively. The instrument response schema represents full multi-stage instrument responses (including filter coefficients) for the broadband data loggers. The hardware tracking schema will represent the interconnection of instruments, amplifiers, filters, and data loggers over time. This schema will be used to store the joint northern California earthquake catalog and the ANSS composite catalog.

The entire description for the BDSN/NHFN/MPBO, HRSN, and USGS Low Frequency Geophysical networks and data archive has been entered into the hardware tracking, SEED instrument response, and waveform tables. Using programs developed to perform queries of waveform inventory and instrument responses, the NCEDC can now generate full SEED volumes for these network based on information from the database and the waveforms on the mass storage system.

During 2002-2003, the NCEDC and NCSN jointly developed a system consisting of an extensive spreadsheet that contains per-channel information that describes the hardware of each NCSN data channel and provides each channel with a SEED-compliant channel name. This spreadsheet, combined with a limited number of files that describe the central-site analog digitizer, FIR decimation filters, and general characteristics of digital acquisition systems, allow the NCSN to assemble its station

history in a format that the NCEDC can use to populate the hardware tracking and instrument response database tables for the NCSN. As of June 2003, the NCEDC has the preliminary response for approximately 75 percent of the NCSN network. However, significant work must still be done to complete and verify the NCSN instrument responses.

The second part of this project is the conversion of the NCSN waveforms from their native CUSP format into MiniSEED, the standard NCEDC waveform format. This process must deal with multiple problems such as ambiguous or erroneously labeled CUSP data channel, sensor that were recorded on multiple data channels, and ensuring that each distinct data channel is mapped to a distinct SEED channel name. The NCEDC developed programs to use the time-dependent NCSN instrument response spreadsheet and NCSN-supplied name channel name transformation rules to determine the SEED channel naming, and to provide feedback to the NCSN on channel naming problems. When the channel transformation rules have stabilized, the NCEDC will perform a bulk conversion of all historic NCSN waveforms to MiniSEED format.

The second stage of development will include the NCSN waveform inventory and later the NCSN instrument response data as they are made available. We distributed all of our programs and procedures to populate the hardware tracking and instrument response tables to the SCEDC in order to help them populate their database.

During 2002-2003, the BSL has been processing events detected by the HRSN (BP) network. The waveform data and event parameters (picks and hypocenters) are stored in separate HRSN database tables, and will be merged with events from the NCSN when the NCSN catalog is migrated to the database.

Additional details on the joint catalog effort and database schema development may be found at <http://quake.geo.berkeley.edu/db>

7. Data Access & Distribution

The various earthquake catalogs, phase, and earthquake mechanism can be searched using NCEDC Web interfaces that allow users to select the catalog, attributes such as geographical region, time and magnitude. The GPS data is available to all users via anonymous FTP. Research accounts are available to any qualified researcher who needs access to the other datasets that currently are not available via the Web.

7.1 SeismiQuery

During 2000 and 2001, the NCEDC has developed a generalized database query system to support the development of portable database query applications among

data centers with different internal database schemas. The initial goal was to modify the IRIS SeismiQuery Web interface program to make installation easier at the NCEDC and other data centers, as well as to introduce a new query language that would be schema independent.

In order to support SeismiQuery and other future database query applications, we defined a set of Generic Data Views (GDV) for the database that encompassed the basic objects that we expect most data centers to support. We introduced a new language we call MSQL (Meta SeismiQuery Language), which is based on generic SQL, and uses the GDV's for its core schema. MSQL queries are converted to Data Center specific SQL queries by the parsing program MSQL2SQL. This parser stores the MSQL parsing tree in a data structure and API's were implemented to browse and modify elements in the parsing tree. These API's are the only data center or database specific source codes. We finally modified the SeismiQuery Web interface to uniformly generate MSQL requests and to process these requests in a consistent fashion.

We have installed SeismiQuery at the NCEDC, where it provides a common interface for querying attributes and available data for SEED format data, and have provided both IRIS and the SCEC Data Center with our modified version of SeismiQuery. We envision using this approach to support other database query programs in the future.

7.2 NetDC

In a collaborative project with the IRIS DMC and other worldwide data centers, the NCEDC helped develop and implement NetDC, a protocol which will provide a seamless user interface to multiple data centers for geophysical network and station inventory, instrument responses, and data retrieval requests. The NetDC builds upon the foundation and concepts of the IRIS BREQ_FAST data request system. The NetDC system was put into production in January 2000, and is currently operational at three data centers worldwide – the NCEDC, IRIS DMC, and Geoscope. The NetDC system receives user requests via email, automatically routes the appropriate portion of the requests to the appropriate data center, optionally aggregates the responses from the various data centers, and delivers the data (or FTP pointers to the data) to the users via email.

The NCEDC hosts a Web page that allows users to easily query the NCEDC waveform inventory, generate and submit NetDC requests to the NCEDC. The NCEDC currently supports both the BREQ_FAST and NetDC request formats. As part of our collaboration with SCEDC, the NCEDC provided its BREQ_FAST interface code to SCEDC, have worked closely with them to implement BREQ_FAST requests at the SCEDC.

7.3 STP

Last year, the NCEDC wrote a collaborative proposal with the SCEDC to the Southern California Earthquake Center, with the goal of unifying data access between the two data centers. As part of this project, the NCEDC and SCEDC are working to support a common set of 3 tools for accessing waveform and parametric data: SeismiQuery, NetDC, and STP.

The Seismogram Transfer Program or STP is a GUI-based client-server program, developed at the SCEDC. Access to STP is either through a simple direct interface that is available for Sun or Linux platforms or through a Web interface. With the direct interface, the data are placed directly on a users' computer in several possible formats, with the byte-swap conversion performed automatically. With the Web interface, the selected and converted data are retrieved with a single FTP command. The STP interface also allows rapid access to parametric data such as hypocenters and phases.

The NCEDC has started implementing STP, working with the SCEDC on extensions and needed additions. We are adding support for the full SEED channel identifiers (Station, Network, Channel, and Location), and improving the waveform retrieval formats

7.4 EVT_FAST

In order to provide Web access to the NCSN waveforms before the SEED conversion and instrument response for the NCSN has been completed, the NCEDC implemented EVT_FAST, and interim email-based waveform request system similar to the BREQ_FAST email request systems. Users can email EVT_FAST requests to the NCEDC and request NCSN waveform data based on the NCSN event id. The NCSN waveform data is converted to either SAC ASCII, SAC binary, or AH format, and placed in the anonymous FTP directory so that users can retrieve the data. The EVT_FAST waveforms are currently named with the USGS's native NCSN channel names, since the SEED channel names conversion is not yet complete.

7.5 FISSURES

The FISSURES project developed from an initiative by IRIS to improve earth scientists' efficiency by developing a unified environment that can provide interactive or programmatic access to waveform data and the corresponding metadata for instrument response, as well as station, and channel inventory information. FISSURES was developed using CORBA (Common Object Request Broker Architecture) as the architecture to implement a system-independent method for the exchange of this binary data. The IRIS DMC developed a series of services, referred to as the Data Handling Interface (DHI),

using the FISSURES architecture to provide waveform and metadata from the IRIS DMC.

The NCEDC has started to implement the FISSURES Data Handling Interface (DHI) services at the NCEDC, which involves interfacing the DHI servers with the NCEDC database schema. We started with the source code for the IRIS DMC's DHI servers, which reduced significantly the implementation's time. We now have the waveform and event FISSURES services running in demonstration mode at the NCEDC. These services interact with the NCEDC database and data storage system, and can deliver NCEDC event and channel metadata as well as waveforms using the FISSURES interfaces. We are currently still performing tests on FISSURES and are waiting to import our catalog data into the database before we start running the software in production mode.

7.6 GSAC

Since 1997, the NCEDC has collaborated with UNAVCO and other members of the GPS community on the development of the GPS Seamless Archive Centers (GSAC) project. This project allows a user to access the most current version of GPS data and metadata from distributed archive locations. The NCEDC is participating at several levels in the GSAC project: as a primary provider of data collected from core BARD stations and USGS MP surveys, as a wholesale collection point for other data collected in northern California, and, in the next year, as a retail provider for the global distribution of all data archived within the GSAC system. We have helped to define database schema and file formats for the GSAC project, and for several years have produced complete and incremental monumentation and data holdings files describing the data sets that are produced by the BARD project or archived at the NCEDC so that other members of the GSAC community can provide up-to-date information about our holdings. Currently, the NCEDC is the primary provider for over 89,000 data files from over 1500 continuous and survey-mode monuments. The data holdings records for these data have been incorporated into the retailer system, which became publicly available in late 2002.

7.7 Web Pages

The NCEDC developed its Web pages in the early days of the Web. Unfortunately, time constraints have kept the pages somewhat static and limited in their use. In June of 2002, the NCEDC began an project to update and expand their Web offerings. This project was completed in October 2002, and provides the NCEDC with a uniform look-and-feel for all Web pages.

8. Acknowledgements

The NCEDC is a joint project of the BSL and the USGS Menlo Park and is partially funded by the USGS.

Doug Neuhauser is the manager of the NCEDC. Stephane Zuzlewski, Rick McKenzie, Mark Murray, André Basset, and Lind Gee of the BSL and David Oppenheimer, Hal Macbeth, and Fred Klein of the USGS Menlo Park contribute to the operation of the NCEDC. Steve Chu developed the *CalQC* program. Doug Neuhauser, Lind Gee, and Stephane Zuzlewski contributed to the preparation of this chapter.

Chapter 12

Outreach and Educational Activities

1. Introduction

The BSL is involved in a variety of outreach activities, ranging from lectures and lab tours to educational displays and the development of classroom materials for K-12 teachers. We maintain an earthquake information tape (510-642-2160) and an extensive set of Web pages, providing basic earthquake and seismic hazard information for northern and central California.

2. Outreach Overview

The BSL has several on-going outreach programs, such as the educational displays, WWW development, and the Earthquake Research Affiliates Program.

2.1 Educational Displays

As part of the BSL's outreach activities, we have made REDI earthquake data available to a number of universities, colleges, and museums as educational displays. As noted above, this year marked the expansion of this program to the K-12 environment. Participating organizations receive a REDI pager and the Qpager software to display the earthquake information. The Qpager program maps the previous seven days of seismicity, with earthquake shown as a dot. The size of the dot indicates the magnitude of the event, while the color of the dot indicates its age. These educational displays have been installed at UC Berkeley (McCone Hall, Earthquake Engineering Research Center, LHS), California Academy of Sciences, CSU Fresno, CSU Northridge, CSU Sacramento, Caltech, College of the Redwoods, Fresno City College, Humboldt State University, San Diego State University, Sonoma State University, Stanford University (Blume Engineering Center, Department of Geophysics), UC Davis, UC Santa Cruz, UC San Diego, and USC. In a pilot project initiated two years ago, the San Francisco Unified School District has been given two pager systems for use in middle school classrooms.

In addition to the seismicity displays, the BSL provides local waveform feeds for helicorders at several visitor centers associated with BDSN stations (CMB and

MHC). Organizations such as LHS, KRON, and KPIX receive feeds from BKS via dedicated phone lines for display, while the USGS Menlo Park uses data from CMB for display in the lobby of the seismology building. The BSL has also loaned a seismometer and helicorder display to the San Leandro Unified School District for their use in science classes.

2.2 WWW

Over the last year, we have continued to expand our presence on the WWW. Our primary goal has been to provide a source of earthquake information for the public, although we also provide information about the networks, such as station profiles, which benefits the research community as well. We provide such information as seminar schedules, course advertisements, descriptions of operations and research, updates on recent earthquake activity, details on Bay Area seismicity and hazards, and links to other earthquake and earth science servers. We also use the WWW server for our own information distribution, with such details as the computing and operational resources, rosters, and schedules for various purposes. Last year, we began an effort to update and revamp our Web pages, as described below.

2.3 Earthquake Research Affiliates Program

The UC Berkeley Earthquake Research Affiliates (ERA) Program is an outreach project of the BSL, the Department of Geology and Geophysics, and the Earthquake Engineering Research Center. The purpose is to promote the support of earthquake research while involving corporations and governmental agencies in academic investigation and education activities such as conferences and field trips. The ERA program provides an interface between the academic investigation and practical application of earthquake studies.

3. 2002-2003 Activities

3.1 Tours and Presentations

BSL staff spent considerable time with public relations activities during the past year. Several tours are given each month, with audiences ranging from middle-school students to scientists and engineers from China and Japan.

The BSL hosted several special groups during 2002-2003. Several of large groups visited, including a class from San Francisco State and 20 members of the Alameda County Sheriff's Emergency Communications Team. A number of schools scheduled visits, many of them in April during Earthquake Awareness Month. April was so busy this year that we actually turned away tours.

In addition to the tours, Drs. Romanowicz, Dreger, Uhrhammer, and Gee presented talks on earthquakes and related phenomena to public groups. Dr. Gee gave a presentation for the City of Berkeley, directed at visitors from Japan visiting the Bay Area.

UC Regents

The BSL held a special tour this year for the UC Regents, who visited the Berkeley campus on June 11-12th. The Regents met in the BSL conference room and heard a presentation from Dr. Gee on the BSL history, operations, and research. Fortunately, an M3.3 earthquake occurred just a few minutes before the presentation, so the Regents could see the waveforms on the live data feed and see the automatic earthquake location shown on the REDI/CUBE display and on the new CISN Display software. BSL staff put together an Quanterra datalogger with an FBA-23 as an example of seismic instrumentation. When the FBA was placed on the earthquake machine, the Regents could "make" earthquakes by turning the crank that applies a force to pull a brick along the sandpaper surface. Chancellor Bergdahl was seen jumping up and down to create earthquakes on the helicorder.

3.2 Open Houses

The BSL participated in both *Cal Day* (April 12th) and *Take Your Child to Work Day* (April 24) this year. The attendance for both festivities was quite good - visitors showed up before we opened the doors! The visitors learned about UC Berkeley's role in earthquake monitoring, watched a streaming feed of earthquake data, jumped up and down to "make a quake", played with the earthquake machine, made P and S-waves with springs, learned about earthquake preparedness, and were given sample seismograms. As a special activity during *Cal Day*, Dr. Peggy Hellweg gave two walking tours of the Hayward fault. These were quite well attended - despite the damp weather.

3.3 Quake 2003

The campus held an earthquake drill on June 5, 2000. Dr. Gee worked with Sarah Nathe and Professor Mary Comerio to design a scenario earthquake. Taking advantage of the new USGS scenario ShakeMaps, an M6.5 on the Northern Hayward Fault was selected and the BSL put together a set of Web pages similar to those routinely put together following an event of interest. The Web pages included a press release, the aftershock probabilities, and maps. With help from Johanna Fenton of OES, the scenario ShakeMaps were turned into HAZUS runs predicting regional damage. An unusual aspect of this earthquake exercise was its focus on business resumption. The drill started 48 hours after the simulated earthquake. More information about the exercise is available at <http://www.seismo.berkeley.edu/seismo/eqw/q2003/>.

3.4 1906 Centennial

The centennial of the great 1906 San Francisco earthquake is rapidly approaching! A number of Bay Area organizations are participating in the '06 Earthquake Centennial Alliance and beginning to plan activities memorializing the event and celebrating the progress we've made in reducing earthquake losses.

Although UC Berkeley was spared major damage, the 1906 earthquake did have a significant impact on the campus community. These effects were documented in an issue of the Chronicle of the University of California in 1998 which describes the refugee camps established on the campus and the dispatch of University cadets to help maintain order in San Francisco. Professor Andrew Lawson chaired the State Earthquake Investigation Commission which produced the first comprehensive government-commissioned report on an earthquake.

Given the many ties between the 1906 earthquake and fire and the University, many UC Berkeley units are beginning to coordinate plans for centennial activities. Ideas for centennial activities include new classes, public lecture series, symposia, displays on the progress of the SAFER program, exhibits of 1906 artifacts and photographs, film series, walking tours, and many others. A small group of people are meeting quarterly at the BSL to plan activities. Information about their plans is available at <http://www.seismo.berkeley.edu/seismo/1906/>.

Lawson Lecture

As part of centennial activities, the BSL established an annual lecture this year. The public lecture will be held each April and focus on issues of earthquakes and society. This year, the lecture series had a fabulous kick-off with a presentation by Dr. David Schwartz of USGS, Menlo Park. Dr. Schwartz is the leader of Working Group '02, a wide cross-section of the Earth science community, dedicated to quantifying earthquake hazards in

the San Francisco Bay Area (Figure 12.1). This lecture was part of the first public announcement of the new earthquake probabilities by Working Group '02. If you missed the lecture, don't despair! A Web cast of the talk is available at http://www.seismo.berkeley.edu/seismo/news/seismo_lecture.html.

SSA 2006

The BSL will co-host the annual meeting of the Seismological Society of America (SSA), scheduled for 4/18/2006 - 4/21/2006, with the USGS. Discussions are currently underway among SSA, the Earthquake Engineering Research Institute (EERI), and OES to create a "mega" spanning earth sciences, earthquake engineering, and disaster response and mitigation. The SSA meeting will also provide the opportunity to kick-off the centennial of the Society.

3.5 Web Pages

The BSL began a program to update and revamp their Web pages this year. Although still in progress, the new Web pages are designed to give greater focus to the research program.

3.6 Brochure

The BSL published a four-page brochure this year. This publication fills an important gap. Prior to the brochure, the best handout on BSL activities was this document - the Annual Report! The depth - and length - of the Annual Report limit its use as a general purpose publication. The brochure is also available through the BSL Web site.

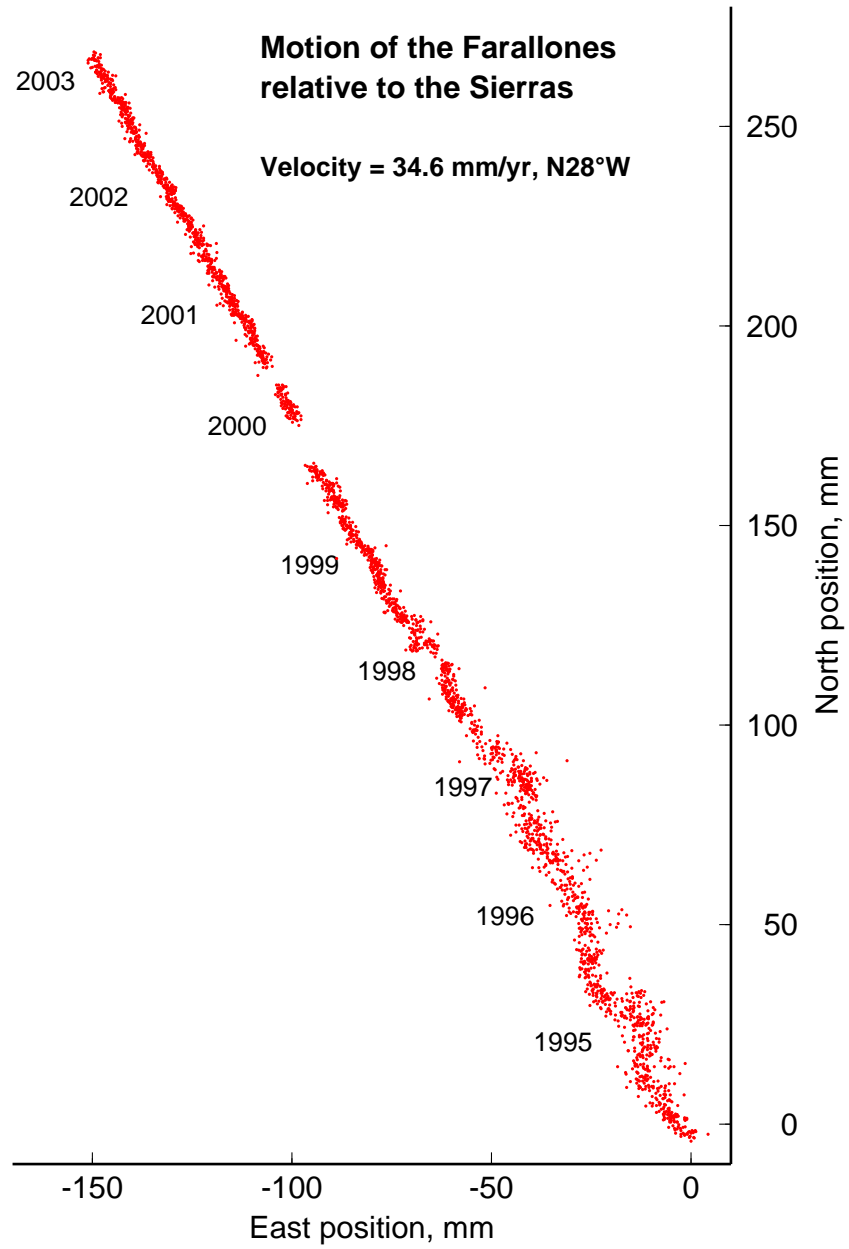
4. Acknowledgements

Lind Gee oversees the outreach activities at the BSL. Barbara Romanowicz, Bob Uhrhammer, Rick McKenzie, and many other faculty, staff, and students at the BSL contribute to the outreach activities. Lisa Krain helped with the upkeep and development of new web pages. Lind Gee contributed to the preparation of this chapter.



Figure 12.1: David Schwartz, Lind Gee, and Barbara Romanowicz at the inaugural Lawson lecture.

Part III
Ongoing Research Projects



Chapter 13

Finite Source Modeling of Great Earthquakes

Douglas Dreger

0.1 Introduction

The M_w 7.9 Denali fault, Alaska, earthquake, which occurred on November 03, 2002 at 22:12:41.0 UTC initiated on the north dipping Susitna Glacier fault with a reverse sense of motion that apparently triggered primarily strike-slip faulting over approximately 300 km of the Denali-Totschunda fault system (*Eberhart-Phillips et al.*, 2003). This complex fault geometry is similar in many respects to that of the San Andreas fault system, and therefore the study of this great earthquake provides needed insight into processes by which earthquakes may grow into large, multi-segmented ruptures involving complex fault geometries. Central to such study is a detailed analysis of the kinematic source process, and investigation of dynamic rupture models to obtain insight into the complex fault interaction. Teaming with Professor Oglesby (UCR), and Drs. Harris (USGS Menlo Park), Ratchkovski (UA, Fairbanks), and Hansen (UA, Fairbanks) we investigate the connection between the Denali rupture kinematics and the dynamic source process. This work has been submitted for publication in GRL (*Dreger et al.*, 2003).

0.2 Kinematic Source Modeling

Three data sets were employed to constrain the kinematic rupture process: observed surface offsets reported by the Denali Earthquake Field Geology Team (*Eberhart-Phillips et al.*, 2003), continuous and campaign-mode GPS data (*Hreinsdóttir et al.*, 2003), and local and regional distance seismic waveforms. The seismic data from 8 recorders, operated by several groups (e.g. US Geological Survey, the University of Alaska, Fairbanks, and the Alyeska Corporation) provide control on the spatial and temporal pattern of mainshock slip. The seismic station coverage is sparse necessitating the use of GPS data from

38 stations from the continuous Alaska Deformation Array and campaign-mode collections.

The 5-segment fault geometry used for the inversion accounts for the arcuate structure of the Denali-Totschunda fault system (Figure 13.1a), as well as the north-dipping structure of the Susitna Glacier fault, which was identified as the initial rupture plane based on a oblique-reverse first motion focal mechanism obtained by the Alaska Earthquake Information Center. The strike and dip of segment 1, representing the Susitna Glacier fault, was 262 and 48 degrees, respectively. The strikes of segments 2-5 were 83, 102, 117, and 143 all with 90 degree dip since relocated aftershocks do not clearly delineate a non-vertical dip. Each fault segment of the model has a width of 30 km, and the lengths of segments 1-5 are 30, 30, 50, 136, and 100 km, respectively. Segments 1 and 2 share a common hypocenter located at 63.520 N, 147.530 W, and a depth of 7.5 km, and they spatially overlap.

The inversion method that we used is based on the multiple time window approach of *Hartzell and Heaton* (1983). Each of the fault segments was discretized by 3.75 km by 3.75 km subfaults. We applied slip positivity, moment minimization, and Laplacian smoothing constraints (e.g. *Kaverina et al.*, 2002), and allow for spatially variable rake. The slip rise time was taken to be 2 seconds. Three time windows, each overlapping by 1 second, were employed allowing the slip rise time to vary between 2 to 4 seconds.

The seismic data were corrected for instrument response, integrated to displacement, and bandpass filtered using a two-pass, fourth-order Butterworth filter with corners of 0.01 and 0.5 Hz, and then resampled to 2 sps. GPS displacements processed and distributed by *Hreinsdóttir et al.* (2003) were used.

Seismic Green's functions were computed using a velocity model from *Ratchkovski and Hansen* (2002), which is appropriate for the region using a frequency-wavenumber integration approach. Green's functions for the GPS data were computed for a half-space elastic structure using the method of *Okada* (1985), assuming a

shear elastic stiffness of 3.52×10^{10} Pa, which corresponds to the value at 8 km depth in the velocity model used to compute the seismic Green's functions.

It was possible to fit the GPS and seismic data sets quite well with respective variance reductions of 99.4% and 44.3%. The preferred slip model is shown in Figure 13.1b. The slip on Susitna Glacier fault (S1) is confined to depths less than the intersection depth (7.5 km) with the vertical Denali fault. The slip on this portion of the fault sums to a seismic moment of 3.12×10^{19} Nm equivalent to M_w 7.0. Following the initial reverse event very little slip accumulated on the Denali fault for a distance of about 50 km to the east (S2 & S3) consistent with surface slip reports (*Eberhart-Phillips et al.*, 2003). The main Denali segment (S4) of the rupture model has 3 shallow asperities, which are principally strike-slip. The bulk of the slip is shallow (less than 10 km) consistent with the depth of relocated aftershocks (e.g. *Ratchkovski et al.*, 2003). The kinematic model presented in Figure 13.1b includes a 15 km jump in the rupture front at the Denali/Totschunda junction that is an important feature of the dynamic rupture models described below. The jump is not constrained by the seismic data however it qualitatively improves the model in the sense that the amplitude of deep slip is reduced. Slip on the Totschunda fault (S5) in the kinematic model has relatively low amplitude, and is unfortunately poorly constrained by both the GPS and seismic data sets. The total scalar seismic moment was found to be 8.45×10^{20} Nm, and the average and peak slips were 2.14 and 9.94 m.

A relatively high rupture velocity of 3.3 km/s was required to place the recovered strike-slip asperities far enough east to correlate with surface slip observations, which is consistent with the findings of *Frankel et al.* (2002). An average rupture velocity of 3.3 km/s also maximizes the level of fit to the seismic waveform data. Direct measurement of the S-wave arrival time at the closest recording station, site PS10 only 3 km from the fault, requires a rupture velocity of at least 3.3 km/s. It is evident from those records that a typical rupture velocity of 0.8β is much too slow. A 3.3 km/s rupture velocity represents 98% of the shear wave velocity at 8 km depth with respect to the velocity model we used. Infrasound recordings also suggest a relatively high rupture velocity (approximately 3.3 km/s) over the length of the Denali fault from just west of the trans-Alaska oil pipeline to the Denali/Totschunda junction in the east (*Olson et al.*, 2003).

Interestingly, the western region of the fault that requires a possibly super-shear rupture velocity also has very low levels of slip suggesting that this portion of the fault may be relatively weak. The teleseismic model of *Ozacar et al.* (2003) also shows that this region had little slip, and they report that a low Bouguer gravity anomaly in this region indicates that the low density rocks in this

region are weak; a claim also supported by the lack of aftershocks (e.g. *Ratchkovski et al.*, 2003). The dynamic modeling also required this section of the Denali fault to be weak in order to allow slip to transfer from the Susitna Glacier to the Denali fault.

Static stress drop was computed from the kinematic slip model using the relation, $\Delta\sigma = 2.44 * M_0 / A^{1.5}$, which assumes a circular fault model for each subfault. Moment (M_0) and area (A) were obtained for each of the 5 fault segments by integrating only those subfaults with non-zero slip. The stress drop varies considerably over the fault with values of 2.9, 1.0, 3.2, 5.2 and 2.4 MPa for segments 1-5, respectively.

0.3 Dynamic Source Modeling

To dynamically model the Denali event, we use the 3-D finite element method (*Oglesby*, 1999; *Whirley and Englemann*, 1993) and a slip-weakening friction law. The material and computational parameters used in our models are; V_p 6.25 km/s, V_s 3.55 km/s, density 2790 kg/m³, shear stress 8.46 Mpa, normal stress 27.63 Mpa, static friction 0.6, dynamic friction 0.12, and critical slip-weakening distance 0.624 m. The fault geometry and finite element mesh are shown in Figure 13.1c, and the discretization on the fault is 2 km by 2 km. The fault geometry is a slight simplification of that used in the kinematic models, with the Susitna Glacier fault having the same strike as the Denali fault, and meeting the Denali fault at its deepest extent. Unfortunately, the large size of the fault system requires a coarse discretization of 2-km along the fault, which in turn means that we cannot resolve the slip weakening distance of 0.624 m in our models. However, as will be argued below, this lack of resolution does not significantly affect the major features of our models. For simplicity, we use a homogeneous, infinite-Q half-space in the dynamic models, corresponding to an intermediate depth in the velocity mode used in the kinematic modeling.

The key ingredient in our dynamic models is the fault stress. *Ratchkovski and Hansen* (2002) show that the maximum principal stress is oriented approximately 85 degrees from the strike of the main Denali fault segment. However, we find it difficult to produce rupture with correct timing on all fault segments using such a simple stress field. A stress field that rotates with the fault strike is one means of solving this problem, but for simplicity we choose a principal compressive stress oriented 65 from the strike of the main Denali segment. The stress field in the western part of the fault, at the intersection between the Susitna Glacier and Denali faults, is likely to be very complicated, due to the complex fault geometry in this region. For computational reasons a simpler fault geometry in this area is used. For both these reasons, we do not attempt to use a single regional stress field to produce fault stresses in this region. Rather, for

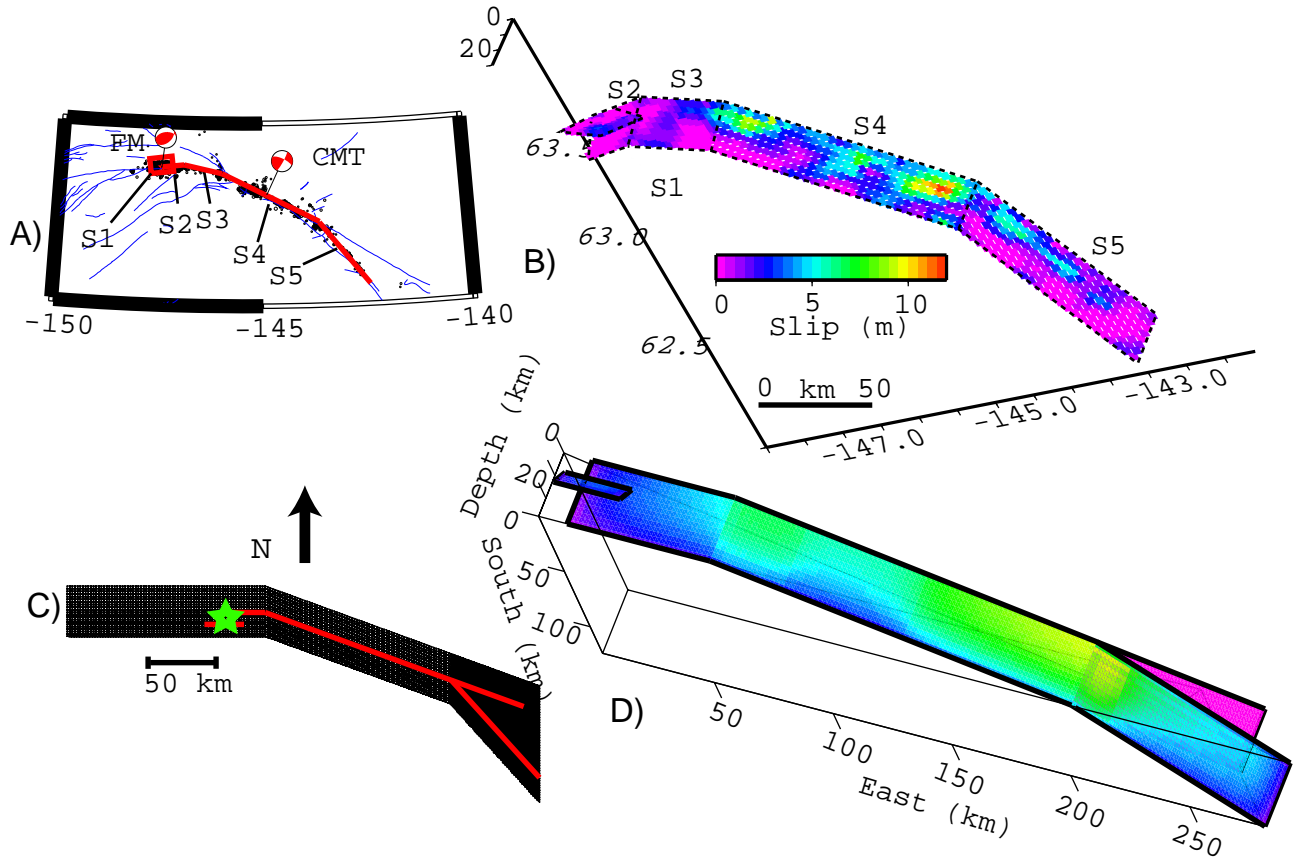


Figure 13.1: . A) 5-segment fault model, the first motion (FM) and Harvard CMT solutions for the mainshock, and regional faults (blue lines). B) 3D projection of the kinematic slip model. C) Map view of fault geometry (red) and finite element mesh used in dynamic models. The mesh is embedded in a much larger buffer mesh to eliminate spurious reflections from the model boundaries. The imposed epicenter is shown by the green star. D) Final slip distribution for the preferred dynamic model. Color version of this figure is found in Chapter IV

simplicity, we impose shear and normal stresses that give a stress drop of approximately 30 bars on the Susitna Glacier fault and 15 bars on the western 50 km of the Denali Fault. This difference in stress drop is consistent with the kinematic observations. To better match the slip distribution of the earthquake we reduce the initial shear and normal stress by 50% between 82 and 130 km along the main Denali Segment, reduce the shear stress by 50% on the Totschunda fault starting 20 km from the branching point and continuing to the end of the segment, and reduce the shear stress to zero in the top 2 km of the Totschunda and eastern Denali faults.

The slip for our preferred dynamic model is shown in Figure 13.1d. The seismic moment in this model is 7.28×10^{20} Nm, corresponding to M_w 7.9. While we do not match the fine details of the kinematic model, we match many of the main features, including patches of high slip at both ends of the main Denali branch. The modeled surface slip matches the mapped surface slip

quite well in both pattern and amplitude. Most importantly, rupture propagates to the Totschunda fault, and abandons the Denali fault at the branch in the east, although the rupture propagates (with relatively low slip) for about 40 km. In our model, this propagation pattern is a direct result of the more favorable orientation of the Totschunda fault with respect to the discussed regional stress field, coupled with the dynamic effect that slip on the Totschunda fault sends the eastern Denali segment into a stress shadow (e.g. *Kame et al.* (2003); *Bhat et al.* (2002)) Another interesting feature of the dynamic model is that rupture propagation is discontinuous: Due to the more favorable orientation of the Totschunda fault near the western branch, stress waves from the Denali fault trigger slip on the Totschunda segment approximately 14 km ahead of the primary rupture front. Experiments with finer fault discretization in the branching region show similar jumping patterns, indicating that the discontinuous rupture is not an artifact of

our low spatial resolution. Minor changes to the stress field produce slightly different jumping lengths, but the main effect remains. Interestingly, stress fields that do not produce jumping rupture also tend to allow significant slip on the eastern Denali segment, in conflict with observations.

0.4 Conclusions

Regional seismic waveforms, continuous and campaign-mode GPS data, and surface slip measurements were used to obtain a kinematic model of the rupture process of the November 3, 2002 M_w 7.9 Denali, Alaska, earthquake. The event initiated as a M_w 7.0 reverse slip event on the north-dipping Susitna Glacier fault with subsequent right-lateral slip distributed over approximately 300 km of the Denali fault system. Near-shear rupture velocity was inferred from direct measurement of S-wave arrival time and the kinematic modeling. The average and maximum slips were found to be 2.14 m and 9.94 m. Static stress drop varies from 1 to 5.2 MPa over the 5-segment fault model. The dynamic models point toward the possibility of discontinuous rupture propagation in this event. Such discontinuous rupture propagation has been implied in kinematic models of earlier events (e.g., the 1984 Morgan Hill event (*Beroza and Spudich, 1988*)), but in this case the dynamic source of the effect is identified in terms of the fault geometry rather than heterogeneity in strength on a planar fault. In addition to qualitatively improving the kinematic slip model for this event, discontinuous rupture propagation may help to explain some of the apparent rapid rupture propagation, and aid in the abandonment of the Denali segment, in agreement with observations.

0.5 Acknowledgements

We thank Jeff Freymueller and Sigrun Hreinsdóttir for providing their GPS solutions for both the continuous and campaign-mode sites, and Mark Murray for his help with GPS solutions at the initial stages of this study.

0.6 References

Beroza, G.C., and P. Spudich, Linearized inversion for fault rupture behavior: application to the 1984 Morgan Hill, California, earthquake, *Bull. Seism. Soc. Am.*, *93*, 6275-6296, 1988.

Bhat, H.S., R. Dmowska, J.R. Rice, and N. Kame, Testing theory for fault branching: Denali to Totschunda, Alaska, November 3, 2002, *EOS Trans. AGU*, *83*, Fall Meet. Suppl., Abstract S72F-1364, 2002.

Dreger, D. S., D. Oglesby, R. Harris, N. Ratchkovski, and R. Hansen, Kinematic and dynamic rupture models of the November 3, 2002 M_w 7.9 Denali, Alaska, earthquake, *Geophys. Res. Lett.*, *submitted*, 2003.

Eberhart-Phillips, D., et al., The 2002 Denali fault earthquake, Alaska: A large magnitude, slip-partitioned event, *Science*, *300*, pp. 1113-1118, 2003 DOI 10.1126/science.1082703.

Frankel, A. D., N. N. Biswas, A. H. Martirosyan, U. Dutta, and D. E. McNamara, Rupture Process of the M7.9 Denali Fault, Alaska, Earthquake Determined from Strong-Motion Recordings, *EOS Trans. AGU*, *83*, Fall 2002 AGU meeting S72F-1340, 2002.

Hartzell, S. H., and T. H. Heaton, Inversion of strong ground motion and teleseismic waveform data for the fault rupture history of the 1979 Imperial Valley, California, earthquake, *Bull. Seism. Soc. Am.*, *73*, 1553-1583, 1983.

Hreinsdóttir, S., J. T. Freymueller, H. J. Fletcher, C. F. Larsen, and R. Brügmann, Coseismic slip distribution of the 2002 MW7.9 Denali fault earthquake, Alaska, determined from GPS measurements, *Geophys. Res. Lett.*, *30*, 1670, doi:10.1029/2003GL017447, 2003.

Kame, N., J.R. Rice, and R. Dmowska, Effects of pre-stress state and rupture velocity on dynamic fault branching, *J. Geophys. Res.*, *108*, 2265, doi:10.1029/2002JB002189, 2003.

Kaverina, A., D. Dreger, and E. Price, The combined inversion of seismic and geodetic data for the source process of the 16 October, 1999, M_w 7.1 Hector Mine, California, earthquake, *Bull. Seism. Soc. Am.*, *92*, 1266-1280, 2002.

Okada, Y., Surface deformation due to shear and tensile faulting in a halfspace, *Bull. Seism. Soc. Am.*, *75*, 1135-1154, 1985.

Oglesby, D.D., Earthquake dynamics on dip-slip faults, Ph. D. thesis, *University of California, Santa Barbara*, 1999.

Olson, J.V., C.R. Wilson, and R.A. Hansen, Infrasound associated with the 3 November, 2002 Denali Fault, Alaska earthquake, *Geophys. Res. Lett.*, *submitted*, 2003.

Ozakar, A.A., S.L. Beck, and D.H. Christensen, Source process of the 3 November 2002 Denali fault earthquake (central Alaska) from teleseismic observations, *Geophys. Res. Lett.*, *30*, 1638, doi:10.1029/2003GL017272, 2003.

Ratchkovski, N. A., and R. A. Hansen, New constraints on tectonics of interior Alaska: earthquake locations, source mechanisms, and stress regime, *Bull. Seism. Soc. Am.*, *92*, 998-1014, 2002.

Ratchkovski, N.A., A. Hansen, J.C. Stachnik, T. Cox, O. Fox, L. Rao, E. Clark, M. Lafeyers, S. Estes, J.B. MacCormack, T. Williams, and K.R. Kore, Aftershock sequence of the MW 7.9 Denali, Alaska, earthquake of 3 November, 2002 from the regional seismic network data, *Seism. Res. Lett.*, *in press*, 2003.

Whirley, R.G., and B.E. Engelmann, DYNA3D: A Nonlinear, Explicit, Three-Dimensional Finite Element Code for Solid and Structural Mechanics - User Manual,

*University of California, Lawrence Livermore National
Laboratory, 1993.*

Chapter 14

Accuracy of the Hypocenter Location and Fault Plane Orientation for Near Realtime Finite Fault Inversion

Wu-Cheng Chi, Asya Kaverina, and Doug Dreger

0.1 Introduction

Recently there has been a push within the seismological community to produce maps of ground shaking intensity in near real time for emergency response purposes. In densely instrumented regions, such as Southern California, Japan, and Taiwan, these maps can be generated using ground-truth measurements. However, other approaches are needed for regions with sparse station coverage. One of them is to derive finite source parameters in near real time, then forward model the ground shaking in the regions of interest (e.g. *Dreger and Kaverina, (2000)*). To successfully predict ground motion we need to have good waveform fits at all azimuths from the hypocenter. An initial set of good source parameters will dramatically reduce the time required to derive a good slip model and enable us to generate synthetic ground shaking information. It is also beneficial to have correct finite source information soon after the earthquake. The information then can help to identify the causative fault plane, design temporary portable seismic networks to monitor the aftershocks surrounding the main event, and forward calculate the stress perturbation due to the earthquake.

We inverted strong motion data for the finite source parameters of 6 large aftershocks of the 1999 Chi-Chi, Taiwan earthquake. The locations and origin times are depicted in Figure 1. For each event, we derived a preferred model by testing different focal mechanisms, hypocenters, and other source parameters in more than 1000 inversions. We documented how the fits between the observed waveforms and the corresponding synthetics deteriorated as the hypocenter and focal mechanism deviate from those of the preferred model. These results will

help to determine how accurate these parameters must be if we wish to derive slip models in near real-time for generating ShakeMaps.

0.2 Data Analyses and Results

More than 6 Chi-Chi, Taiwan Earthquake aftershocks with M_w 5.8-6.4 were well-recorded by a strong motion network maintained by the Central Weather Bureau of Taiwan. They provided an unprecedented opportunity to study the finite source process of moderate sized earthquakes. Each aftershock was recorded by more than 200 strong motion stations. We use only data from stations that had no apparent timing errors and provide good azimuthal coverage. We have converted each waveform from digital counts to cm/s^2 , removed the mean offset, integrated from acceleration to velocity, and band-pass filtered between 0.02 and 0.5 Hz with a four-pole acausal Butterworth filter before resampling the data to 10 sps. Using a frequency-wave number code from Chandan Saikia (*Saikia, 1994*), we calculated a catalog of Green's functions for an average 1D velocity model taken from a 3D tomographic study by *Rau and Wu (1995)*. This 1D model had been tested in routine regional moment tensor studies of local and regional events and performed well for the finite fault inversions of Chi-Chi mainshock and aftershock. The Green's functions were then subjected to the same signal processing as the observed waveforms. We used strong motion data to invert the representation theorem for parameters of the finite source using a method pioneered by *Hartzell and Heaton (1983)*. For each event we tested a range of values for each of the source parameters: the slip vector, fault orientation, location, hypocentral depth, rupture velocity, and dislocation rise time. In this modeling we assumed that the rupture velocity and dislocation rise time were constant and did not vary spatially. For each event, we performed more than 1000 sensitivity tests by

varying the source parameters used in the inversions and we documented the influence these parameters have on the slip model and the waveform fits. The preferred models derived after these extensive tests usually gave more than 20% improvement in waveform fits.

We found that, if the deviation in hypocenters and focal mechanisms were less than 5 km and 20° , respectively, we generally recovered more than 80% of the preferred model's synthetic waveform fit, measured by variance reduction. The length of 5 km (Figure 14.1) is similar, and maybe related, to the widths of the slip patches we modeled. For the thrust events, the input dip angle of the fault must be correct to within 20° . For the strike-slip event, the input fault strike must also be within 20° of the true strike (Figure 14.2).

0.3 Conclusion

For each of the six Chi-Chi, Taiwan aftershock events, we performed more than 1000 sensitivity tests by varying the source parameters used in the inversions and we documented the influence these parameters have on the slip model and the waveform fits. Good waveform fits can mostly be achieved if the errors in hypocenters and focal mechanisms are within 5 km and 20° , respectively. However, in some cases good waveform fits can also be achieved outside of the preferred ranges of the input source parameters. These results provide the criteria needed to evaluate the performance of the seismic network if we want to invert the finite fault parameters of magnitude 6 earthquakes in real time and use the source model to forward-model the ShakeMaps, which can be used by the seismic response authorities for seismic mitigation purposes.

0.4 Acknowledgements

We thank Dr. Willie Lee for providing the strong motion data from Central Weather Bureau (CWB) of Taiwan and Dr. Win-Gee Huang for the strong motion data from IES, Academia Sinica of Taiwan. We thank CWB for providing their aftershock seismicity data. This research is funded by NSF Grant EAR-0000893 and PEER Lifelines 1E06.

0.5 References

Dreger, D., and A. Kaverina, Seismic remote sensing for the earthquake source process and near-source strong shaking: A case Study of the October 16, 1999 Hector Mine Earthquake, *Geophys. Res. Lett.*, it 27, 13,1941-1944, 2000.

Hartzell, S.H., and T.H. Heaton, Inversion of strong ground motion and teleseismic waveform data for the fault rupture history of the 1979 Imperial Valley, California, Earthquake, *Bull. Seism. Soc. Am.*, 73, 1553-1583, 1983.

Rau, R.-J., and F. Wu, Tomographic imaging of lithospheric structures under Taiwan, *Earth Planet. Sci. Lett.*, 133, 517-532, 1995.

Saikia, C.K., Modified frequency-wave-number algorithm for regional seismograms using Filon's quadrature-modeling of L(g) waves in eastern North America, *Geophys. J. Int.*, 118, 142-158, 1994.

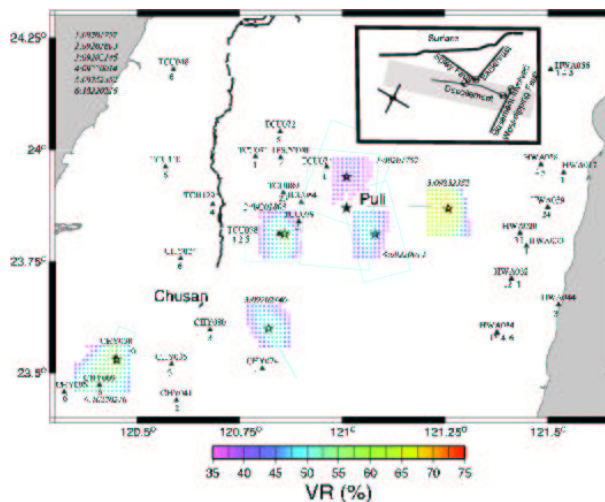


Figure 14.1: Preferred locations of the aftershock events studied are marked as stars. The origin times for these events are shown at the upper left corner. The dot color shows the variance reduction derived from inversions using that particular location as epicenter. It shows how rapidly the waveform fits, measured by variance reduction (VR), deteriorate if the epicentral information is incorrect. In general, the VR will drop 20% if the epicenter is off by 5 km. Results for Event 5 are shifted to the east for clear presentation. The blue rectangles are the fault dimensions of the preferred slip models. The cross section in the upper right corner shows a schematic with possible rupture scenarios for the aftershocks we studied.

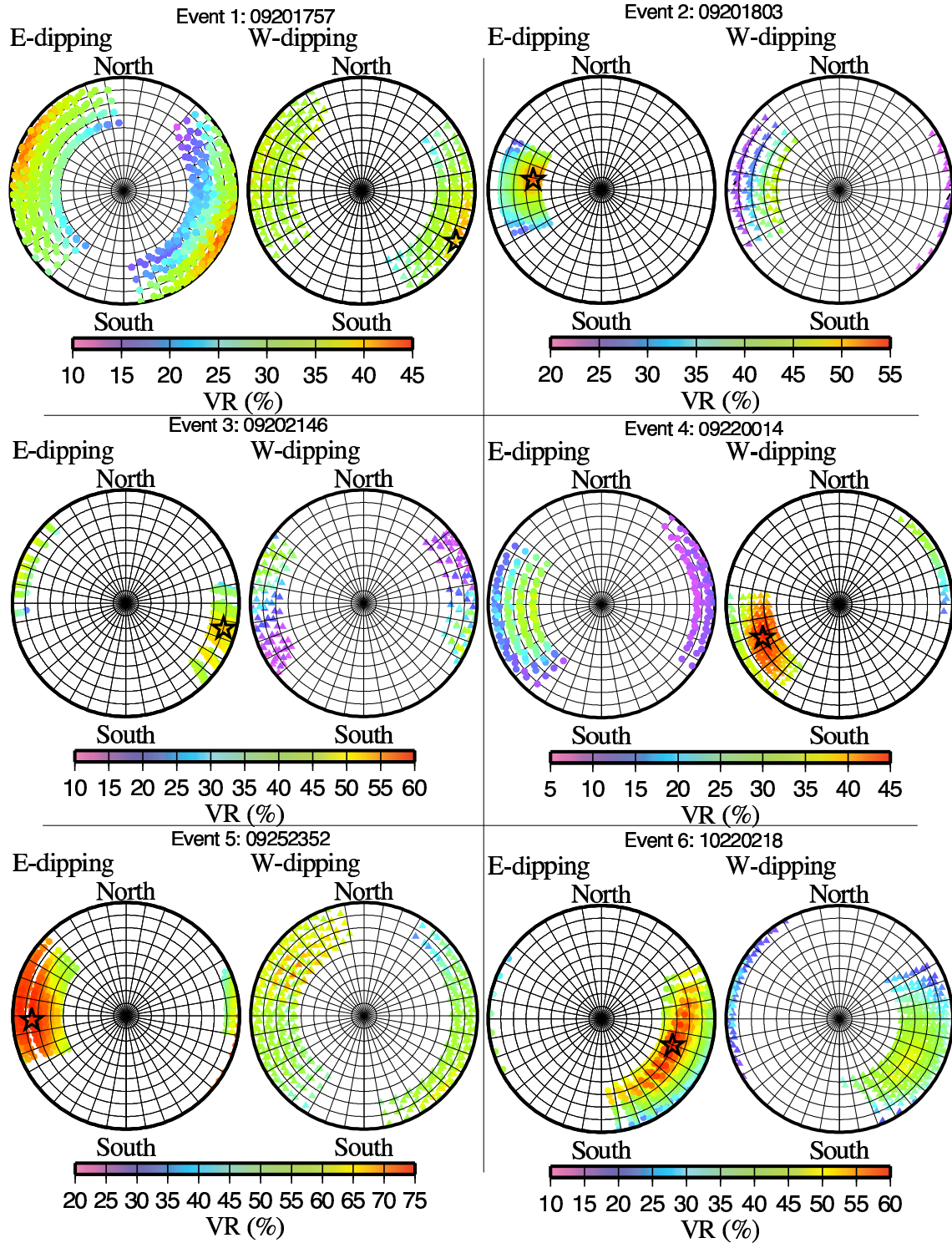


Figure 14.2: The results of sensitivity tests on the focal mechanism for each event. The P axis of each focal mechanism tested is plotted in lower hemisphere stereonet projection. The left stereonets show the east-dipping fault planes, the right ones the west-dipping planes. The color shows the variance reduction. Note VR deteriorates fastest when the plunge of the P axis changes, implying the waveform fits are most sensitive to the dip, and possibly rake, of the focal mechanism for the thrust events. For the strike-slip aftershock (Event 3), VR is more sensitive to strike. We interpreted this to be the result of the amplitude of the S wave radiation pattern, which controls the inversion results. The star shows the P axis of the preferred focal mechanism. Overall, the waveform fits are pretty good if the fault orientation is accurate within 20 degrees.

Chapter 15

Historical Earthquake Re-analysis Project

Robert A. Uhrhammer

0.1 Introduction

The objective of this USGS NEHRP funded two-year project, that commenced in March, 2000, is to characterize the spatial and temporal evolution of the San Francisco Bay Region (SFBR) seismicity during the initial part of the earthquake cycle as the region emerges from the stress shadow of the great 1906 San Francisco earthquake.

The fundamental problem is that the existing BSL seismicity catalog for the SFBR, which spans most of the past century (1910-present), is inherently inhomogeneous because the location and magnitude determination methodologies have changed, as seismic instrumentation and computational capabilities have improved over time. As a result, the SFBR seismicity since 1906 is poorly understood. Creation of a SFBR catalog of seismicity that is homogeneous, that spans as many years as possible, and that includes formal estimates of the parameters and their uncertainty is a fundamental prerequisite for probabilistic studies of the SFBR seismicity.

The lack of a homogeneous catalog of earthquake for the SFBR which spans most of the past century, the availability of the invaluable BSL seismological archive, the interest in the Working Group on California Earthquake Probabilities (WGCEP, 1999), the funding of an initial effort with support from the USGS-PG&E CRADA, and the purchase and loan of a high-resolution wide-format digitizer by the USGS, combine to provide both an incentive and an unique opportunity to systematically re-process, using modern algorithms, the BSL seismographic records and data for SFBR earthquakes and to produce a homogeneous catalog of earthquakes for the region.

Our approach is to systematically re-analyze the data acquired from the archive to develop a homogeneous

SFBR catalog of earthquake location, local magnitude (M_L), moment magnitude (M_w), and seismic moment tensor (mechanism), including formal uncertainties on all parameters which extends as far back in time as the instrumental records allow and which is complete above appropriate threshold magnitudes. We anticipate being able to compile a new SFBR catalog of location and M_L which spans 1927 to the present and is complete at the $M_L \sim 3$ threshold, and of M_w which spans 1911 to the present and which is complete at the $M_w \sim 4.5$ threshold.

0.2 Previous Effort

During the summer of 1998, the USGS funded two students, via a USGS-PG&E CRADA, to transcribe the data from the original BSL reading/analysis sheets to computer readable form. With this funding, they were able to transcribe the reading/analysis sheets for SFBR earthquakes, working back in time from 1983 through 1944 (1984 onward was already in a computer database).

The Wood-Anderson maximum trace amplitude data used in the determination of M_L were not registered on the original reading/analysis sheets kept in the BSL archive, so we read the maximum trace amplitudes recorded by the Wood-Anderson seismograms in order to calculate M_L and its uncertainty. The manpower intensive task of reading the maximum trace amplitudes registered by the Wood-Anderson seismograms for Berkeley (BRK), Mt. Hamilton (Lick Observatory; MHC), Palo Alto (Banner Station; PAC), and San Francisco (USF) that are kept on store in the BSL seismogram archive in Edwards Stadium, which began with the 1950 Wood-Anderson records and worked backward in time and finished with the earliest Wood-Anderson records (circa 1927), was completed in June 2001. At the same time we also completed the process of transcribing the data from the original reading/analysis sheets to computer readable flat files bank through 1927.

We finished transcribing the 1910-1927 data (pre-Wood-Anderson instrument) data from the original read-

ing/analysis sheets to computer readable flat files in December 2001. Prior to the advent of the Wood-Anderson seismographs, there were only two seismic stations operating in the Berkeley network, namely at the Student Observatory on the Berkeley Campus (BRK) and at the Lick Observatory at Mt. Hamilton (MHC). During the pre-1927 era, the primary seismic instrumentation at BKS and MHC consisted of Bosch-Omori and Wiechert seismographs which operated at low magnification (100x) and recorded on smoked paper.

We began the time consuming task of scanning and digitizing selected pre-1932 seismograms in September 2001. Obtaining digital representations of the Bosch-Omori and Wiechert smoked paper seismograms is crucial particularly because the earliest smoked paper records, kept on store in the Berkeley Seismogram Archive, are becoming quite brittle and difficult to handle. We have been scanning these seismograms mostly on a flat bed scanner because some of the records could be damaged if they are passed through the rollers in the large format scanner. In February, 2002, the project received a six-month no-cost extension to complete this labor intensive scanning and digitizing effort.

See previous Annual Reports for more detailed information.

0.3 Progress During the Past Year

The task of scanning and digitizing the pre-1933 seismograms was completed in August 2002. Figure 15.1 compares the E-component signals recorded by co-sited Bosch-Omori, Galitzin, and Wood-Anderson seismometers located at BRK on the Berkeley campus. The quality of these images is fairly typical of the types of images that can be obtained by scanning the old paper seismograms kept on store in the BSL seismogram archive. A comparison of the Bosch-Omori, Galitzin, and Wood-Anderson records for ten SFBR earthquakes which occurred in 1931 and 1932, when all three types of instruments were on operation at Berkeley, was used to empirically calibrate the magnitude estimates for SFBR events which occurred prior to the installation of the Wood-Anderson seismographs.

We found that the existing earthquake location algorithms do not provide robust solutions when using the potentially imprecise data available from the sparse four-station pre-1960 SFBR seismic network. Consequently, a fuzzy logic based algorithm was developed to facilitate the determination of robust earthquake locations (Uhrhammer, 2001). The algorithm inherently has a high tolerance for imprecision in the observed data and it can yield robust sparse network solutions without requiring that the problematic observed data be either identified, down-weighted, or removed. This characteristic also renders the algorithm ideally suited for use in automated systems, such as the REDI Project, which provide rapid

earthquake information.

The ultimate goal of this project has been the development of a uniform and internally consistent catalog of SFBR seismicity for instrumentally recorded earthquakes which have occurred during the past century in the region and to make the data and the results of this study available on-line via the Northern California Earthquake Data Center at <http://quake.geo.berkeley.edu>.

As a part of this goal, we also developed a calibration procedure for obtaining robust earthquake locations throughout a time when the number of SFBR seismic stations evolved from the initial two stations (BRK and MHC) at the turn of the last century to the more than 100 seismic stations at present (Uhrhammer, 2003). The complex geology and faulting observed in the SFBR results in seismic wave propagation times which scatter significantly over differing propagation paths in the region.

The final effort to place all the raw and processed data on the NCEDC is underway. The goal is to have all the raw data and the results in a searchable format and to be available on-line circa September 2003.

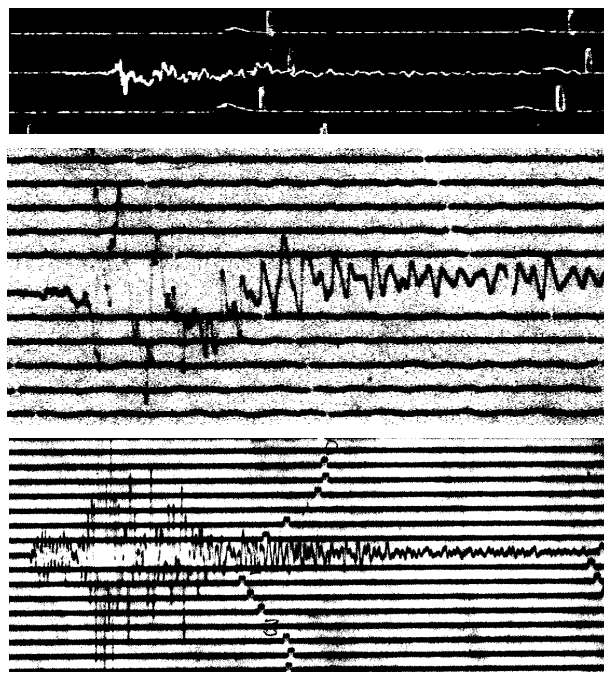


Figure 15.1: Example of scanned seismograms. Shown are the BRK E-component Bosch-Omori (top), Galitzin (middle), and Wood-Anderson (bottom) seismograms for a M_L 4.5 earthquake which occurred on June 14, 1932 at 09:44:13 UT. The epicenter is located along the San Andreas Fault approximately 2 km N of Castle Rock State Park and 71 km SSE of Berkeley. For reference, the distance between adjacent traces is 10 mm, 2.5 mm and 2.5 mm on the original Bosch-Omori, Galitzin, and Wood-Anderson seismograms, respectively.

0.4 Acknowledgements

We thank William Bakun of the USGS who encouraged us to pursue this project. UC Berkeley students Tom Fournier and Gabe Trevis participated in this project during the past year and we thank them for their efforts.

This project was supported by the USGS, through the NEHRP External Grants Program.

0.5 References

Bolt, B. A. and R. D. Miller, Catalog of Earthquakes in Northern California and Adjoining Areas: 1 January 1910 - 31 December 1972, *Seismographic Stations, University of California, Berkeley*, iv + 567 pp., 1975.

Uhrhammer, R. A., The San Francisco Bay Region Historical Earthquake Re-analysis Project: A progress report and locating pre-1960 instrumentally recorded earthquakes using a fuzzy-logic-based algorithm, *Seism, Res, Lett.*, 72, 245, 2001.

Uhrhammer, R. A., Historical Earthquake Re-analysis Project: San Francisco Bay Region, *Seis. Research Lett.*, 74, p. 217, 2003.

Chapter 16

Northern California Seismicity Project

Robert A. Uhrhammer

0.1 Introduction

The Northern California Seismicity Project (NCSP) is a counterpart to the San Francisco Bay Region (SFBR) - Historical Earthquake Re-analysis Project (HERP) reported in the research section on HERP. The initial objective of this project which commenced in August, 2000, is to transcribe the pre-1984 data for $M_L \geq 2.8$ earthquakes which have occurred in Northern and Central California (NCC) (outside of the SFBR covered by HERP), from the original reading/analysis sheets, kept on store in the Berkeley Seismological Archives, to a computer readable format.

As is the case with HERP, characterization of the spatial and temporal evolution of NCSP seismicity during the initial part of the earthquake cycle as the region emerges from the stress shadow of the great 1906 San Francisco earthquake is the long term goal. The problem is that the existing BSL seismicity catalog for the SFBR, which spans most of the past century (1910-present), is inherently inhomogeneous because the location and magnitude determination methodologies have changed, as seismic instrumentation and computational capabilities have improved over time. As a result, NCC seismicity since 1906 is poorly understood.

Creation of a NCC seismicity catalog that is homogeneous, that spans as many years as possible, and that includes formal estimates of the parameters and their uncertainty is a fundamental prerequisite for probabilistic studies of the NCC seismicity. The existence of the invaluable BSL seismological archive, containing the original seismograms as well as the original reading/analysis sheets, coupled with the recently acquired BSL capability to scan and digitize historical seismograms at high resolution allows the application of modern analytical algorithms towards the problem of determining the source parameters of the historical SFBR earthquakes.

0.2 Background and Motivation

Although the 1910 to present BSL catalog of earthquakes for NCC appears to be a simple list of events, one must remember that it really is a very complex data set. It is easy to misinterpret observed variations in seismicity if we do not understand the limitations of this catalog. The existing 1910 to present BSL catalog of earthquakes for NCC is inhomogeneous in that it suffers from the three types of man-made seismicity changes identified by *Habermann, 1987*, namely detection changes, reporting changes, and magnitude shifts. The largest change in the detection capability of the BSL seismic station network occurred starting circa 1927 with the installation of the Wood-Anderson and Benioff seismometers at several sites in NCC (see Figure 16.1) and the resulting increase in sensitivity lowered the threshold for detection of NCC earthquakes by about 2 M_L units. The most significant reporting change occurred circa 1942 when the BSL began determining M_L for some earthquakes and by 1948 M_L was routinely determined and reported for all SFBR earthquakes listed in the BSL Bulletin (*Romney and Meeker, 1949*). A magnitude shift occurred in 1954 when the response of the Wood-Anderson seismographs changed (owing to changing the free period from 1.0 to 0.8 seconds) (*Bolt and Miller, 1975*).

The lack of a homogeneous catalog of earthquake for the SFBR which spans most of the past century, the availability of the invaluable BSL seismological archive, the interest in the Working Group on California Earthquake Probabilities (WGCEP, 1999), the funding of an initial effort with support from the USGS-PG&E CRADA, and the purchase and loan of a high-resolution wide-format digitizer by the USGS, combine to provide both an incentive and a unique opportunity to systematically re-process, using modern algorithms, the BSL seismographic records and data for SFBR earthquakes and to produce a homogeneous catalog of earthquakes for the region.

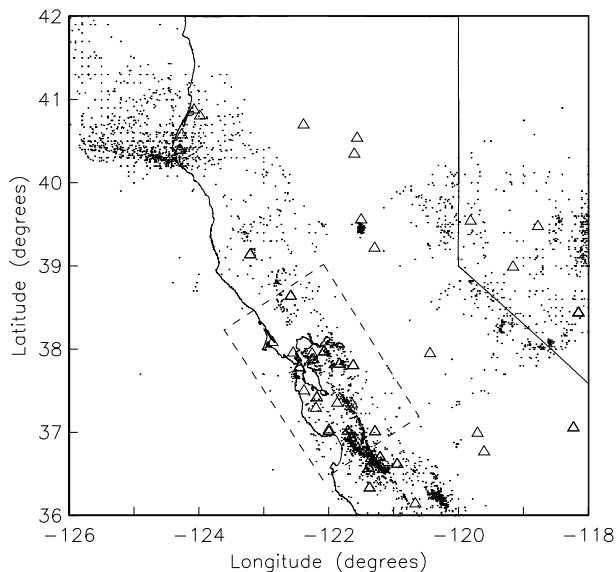


Figure 16.1: Map of the NCC Region showing the 1951-1983 $M_L \geq 2.9$ seismicity (small dots). The triangles are the seismic stations, operated by Berkeley and adjacent networks between 1951 and 1983, for which data are available. Events occurring in the dashed inset box are being transcribed and analyzed via HERP (see the previous section).

0.3 Current Effort

To expedite the transcription process, we converted all relevant available data from the online NCEDC event catalogs and the in-house phase data to the flat transcription file format as shown in Figure 16.2 for the years 1978 through 1983. We also acquired a copy of the International Data Center (ISC) CDROM which contains events and associated station data published in the ISC Bulletins from January 1964 through December 1977 (Version 1.2). This ISC data set includes event and station data contributed by Berkeley and the CDROM also contains an algorithm to search the database and extract and translate the ISC coded phase Berkeley data to a readable print format for years 1963 through 1977. This enabled us to start with transcription files that contained approximately half of the data that is on the original reading/analysis sheets for the years 1964 through 1983. The primary data from the original reading/analysis sheets, that was not included in this process, was the Wood-Anderson maximum trace amplitude data that is crucial for the determination of local magnitude.

During the past year two students worked on the process of transcribing the data from the original BSL reading/analysis sheets to computer readable form. They started by transcribing the original reading/analysis sheets from 1963 and they have been working back in time. The data from 1952 through 1983 has now been

```

NEIS 1977/01/09 23:24:39 39.50N 121.64W 2 14 Northern California
NEIS M-L3.3(BRK), AFTER BRK.
NEIS IO=V MM AT DOBBINS. ALSO FELT AT GRIDLEY, GOLD RUN, RACKERBY,
BRK 1977/01/09 23:24:39 39.50N 121.64W 2 3.4L Northern California
ISC *1977/01/09 23:24:37 39.55N 121.53W 2 15 Northern California

ORV 0.02 84 -iP Pn 23:24:42.00 -2.6
KPK 0.17 80 iPN Pn 23:24:44.10 -2.7
MIN 0.79 356 +iP/PKP Pn 23:24:56.00 0.4
WDC 1.29 323 +iP/PKP Pn 23:25:02.60 -0.1
WCN 1.39 99 iPN Pn 23:25:05.10 0.9
BKS 1.76 198 +iP/PKP Pn 23:25:09.00 -0.5
BKS S/(SKS) 23:25:30.00 -2.9
JAS 1.82 152 +iP/PKP Pn 23:25:10.20 -0.1
ARN 2.20 181 ePN Pn 23:25:15.60 -0.2
MHC 2.21 183 iP/PKP Pn 23:25:16.00 0.1
SAO 2.78 178 P/PKP Pn 23:25:24.00 -0.1
MNV 2.86 112 eP/PKP Pn 23:25:26.00 0.9
FRI 2.93 150 +iP/PKP Pn 23:25:26.90 0.7
BMN 3.42 74 ePN Pn 23:25:34.30 1.1
TNP 3.67 112 ePN Pn 23:25:37.40 0.7
EUR 4.30 89 iP Pn 23:25:46.00 0.4 A1.56E01 T 0.4
EUR i 23:26:53.80

```

Figure 16.2: Example of printer file of data for Berkeley network data extracted from ISC CDROM.

transcribed.

We are currently transcribing reading/analysis sheet data from 1951. Since none of the data on the pre-1964 reading/analysis sheets exists in a computer readable form, all data has to be transcribed and consequently it takes more time to transcribe each event. Also, the pre-1951 reading/analysis sheets data do not contain Wood-Anderson maximum trace amplitude data which is used in the calculation of local magnitude so that the original Wood-Anderson seismograms will have to be retrieved from the archive and the amplitudes read. This quite labor intensive component of the project is planned for the coming year.

```

E 010977 232439.5 39-30.1 121-38.6 2.0 3.4
C 5KM SOUTHWEST OF OROVILLE, CALIFORNIA
F MMI V at Oroville
F Also felt at Gridley, Gold Run, Rackerby, Marysville and
F Brownsville
P BKS Ben Z e P c 232509.0
P BKS Ben E e S - 232529.5
A BKS WA - 0.65 0.7
P MIN Ben Z i P c 232456.0
A MIN WA - 5.2 6.0
P PCC Ben Z e (P) - 232515
A PCC Ben 11 - -
P MNV Ben Z e P - 232526.-
P PRI Ben Z e - - 232538
P ORV Ben Z i P d 232442.0
P JAS Ben Z e P c 232510.2
P WDC Ben Z i P c 232502.6
P BRK Ben Z e (P) - 232510
A BRK Ben 6 - -
P SAO Ben Z e (P) - 232524.2
P FRI Ben Z e P c 232526.9
P MHC Ben Z e P (c) 232516.0
A MHC WA - 0.35 0.25
P GCC Ben Z e - - 232520
P PRS Ben Z e (P) - 232530.8
P LLA Ben Z e - - 232527
A LLA Ben 19 - -
P FHC Ben Z e - - 232518
X

```

Figure 16.3: Example of completed transcription file format for the event shown in Figure 16.2.

0.4 Acknowledgements

UC Berkeley students Tom Fournier, Karin Spiller, Gabe Trevis, Maxwell Wilmarth, and Jennifer Epstein participated in this project and we thank them for their efforts.

This project was partially supported by the USGS funding of the Northern California Earthquake Data Center.

0.5 References

Bolt, B. A. and R. D. Miller, Catalog of Earthquakes in Northern California and Adjoining Areas: 1 January 1910 - 31 December 1972, *Seismographic Stations, University of California, Berkeley*, iv + 567 pp., 1975.

Habermann, R. E., Man-made changes of seismicity rates, *Bull. Seism. Soc. Am.*, *77*, 141-159, 1987.

Romney, C. F. and J. E. Meeker, Bulletin of the Seismographic Stations, *University of California Press*, *18*, pp. 89, 1949.

Chapter 17

Parkfield Research

Robert M. Nadeau, Lane R. Johnson and Tom V. McEvilly

0.1 Earthquake Forecasting

In its various reports since 1988, the Working Group on California Earthquake Probabilities (WGCEP) has consistently made use of statistical models of time-dependent earthquake recurrence to help estimate earthquake probabilities in California. In all WGCEP reports, the need for a larger database of earthquake recurrence intervals is emphasized. Additional data are necessary to select from competing statistical models of earthquake recurrence and to better define the model parameters. The most recent working group reports (*WG99*, 1999; *WG02*, 2002) introduced recurrence intervals from numerous small and characteristically repeating microearthquake sequences occurring along the San Andreas fault and, in particular, at Parkfield (*Ellsworth et al.*, 1999). They included only a small fraction of the Parkfield data yet that nearly doubled the available data base from which estimates of the model parameters were made. However, even this expanded data set was considered less than adequate by the working groups. At Parkfield a significantly larger set of small repeating sequences than was used by the working groups exists (184 total sequences composed of 1073 events and 889 recurrence intervals; compared to 17 Parkfield sequences of 117 events and 100 recurrence intervals used for the WG model) and many additional sequences and events have recently been identified by our research group along the central SAF between Parkfield and the southeast terminus of the Loma Prieta rupture (*Nadeau and McEvilly*, 2003). In total, our group has now identified a total of 515 sequences yielding 2079 recurrence intervals from sequences whose characteristic magnitudes range from M_w -0.7 to M_w 3.5 (Figure 17.1).

The potential of such a large data set for helping select and refine time-dependent recurrence models is considerable, yet serious questions remain regarding the use of small earthquake data for forecasting large earthquakes (e.g. Is the variance of earthquake recurrence intervals independent of magnitude, and what normalization (if any)

could be used to account for variations in magnitude among characteristic sequences?). *Nadeau and Johnson* (1998) found that the average recurrence interval of sequences scales reasonably well for sequence magnitudes ranging from -0.7 to 6 under similar fault loading conditions. However, they did not analyze the variance of intervals as a function of magnitude. *Ellsworth et al.* (1999) analyzed magnitude dependent variance for the small data used by the working groups, and noted that the variance for both the small and large sequences was comparable. However results of their analysis, admittedly based on a small data set, had a large uncertainty. Adding to the difficulties in evaluating magnitude dependent variance are problems associated with spatial and temporal variations of fault loading rates on recurrence time variance. For example if significant slip rate transients occur over time scales comparable to the recurrence intervals of sequences (as has been observed at Parkfield) the variance of the intervals should be significantly greater than for sequences whose recurrence times are long compared to the transients.

Previous efforts at variance determinations have also relied on data dependent normalizations where the intervals for each sequence were divided by the average recurrence time of the sequences (Figure 17.1, top). However as pointed out by *Matthews et al.* (2002), this significantly under estimates the variance for typical characteristic sequences where the total number of repetitions are typically small. *Matthews et al.* also point out that discrimination between competing probability models of interval variance for earthquakes is a difficult task, even when normalization is ignored and relatively large synthetic data sets are used (e.g. 50 intervals).

0.2 Preliminary Findings

The unique attributes of our recurrence interval data set and auxiliary geodetic measurements of fault loading rates have the potential of overcoming many of these difficulties and of greatly expanding our understanding of the time-dependent earthquake recurrence process. Since our data set is large and since recurrence times scale with magnitude, our data can also be used to establish a

scaling relationship between average recurrence time and magnitude that is relatively insensitive to the average intervals of any individual sequence. This scaling can then be used to normalize the entire recurrence interval data set in a way that is also insensitive to the average recurrence intervals. This approach effectively circumvents the small sample bias problem discussed by *Matthews et al.* The bottom panel of Figure 17.1 shows our first attempt at normalizing our data set in this way. A significantly better fit to a lognormal-like distribution is observed compared to the distribution shown in the top panel of Figure 17.1 where individual sequence average recurrence intervals are used for normalization. Also of significance is the larger intrinsic uncertainty determined for our scale normalized data (0.63 compared to 0.46). This result is entirely consistent with the remarks of *Matthews et al.*, and supports the potential of the scaled normalization for overcoming bias problems associated with the sequence average recurrence interval normalization approach. The large number of data also significantly reduces the confidence bounds of the intrinsic uncertainty estimate.

Our 2079 recurrence intervals significantly exceed the 50 used by *Matthews et al.* in their synthetic dataset used for assessing the practicality of discriminating between competing recurrence models. This leaves some hope that discrimination between models may be feasible after all using real earthquakes and a scale-normalized dataset. Further investigation of the characteristics of the recurrence-magnitude scaling and normalization will be required before reliable conclusions can be reached in these regards, but our initial results do appear promising. The spatial and temporal characteristics of fault loading rate variations are also exceptionally well characterized in the regions where most of our repeating sequences are occurring. This information can be used to remove and/or assess any bias in the variance of recurrence interval data that variations in spatial and temporal fault loading rates introduce into their distributions. Though our dataset contains only small magnitude events, the "range" in magnitude that it spans is over 4 magnitude units. This should also allow us to test (at least for small magnitudes) the validity of the hypothesis that recurrence interval variance is independent of magnitude, an implicit assumption used by *WG99* and *WG02*.

Finally, an additional attractive feature of our dataset is that it continues to increase in size as ongoing repeating events (typically repeats for each of the 515 sequences occur on the order of every few years or less). Using these ongoing events to continually add to the recurrence interval data set can not only provide more data for constraining the forecast model parameters, but it also can be used to test forecast models on real events. This can be done by making probabilistic forecasts for the future small and frequently recurring earthquakes using competing models and then by assessing the success and failure rates of

the various forecasts.

Our future research plans include integration of the auxiliary fault loading rate and recurrence interval data as discussed above, augmentation of the recurrence interval archive with the ongoing small characteristic events, parameterizing competing forecast models using our recurrence and other available recurrence interval data, making small earthquake forecasts using the competing models and comparing the forecasts' relative success rates.

0.3 Acknowledgements

We appreciate support for this project by the USGS NEHRP program through grant numbers 02HQGR0067 and 03HQGR0065, by NSF through award number 9814605, and by the U.S. Department of Energy (DOE) under contract No. DE-AC03-76SF00098.

0.4 References

- Ellsworth, W.L., M.V. Matthews, R.M. Nadeau, S.P. Nishenko, P.A. Reasenberg, and R.W. Simpson, A physically based earthquake recurrence model for estimation of long-term earthquake probabilities, U.S. Geol. Surv. Open-File Rept. 99-522, 1999.
- Matthews, M.V., W.L. Ellsworth and P.A. Reasenberg, A Brownian Model for Recurrent Earthquakes, *Bull. Seism. Soc. Am.*, 92, 2233-2250, 2002.
- Nadeau, R.M. and L.R. Johnson, Seismological Studies at Parkfield VI: Moment Release Rates and Estimates of Source Parameters for Small Repeating Earthquakes, *Bull. Seismol. Soc. Amer.*, 88, 790-814, 1998.
- Nadeau, R.M. and T.V. McEvilly, Periodic Pulsing of the San Andreas Fault, *Science*, *submitted*, 2003.
- Working Group on California earthquake Probabilities (*WG99*), Earthquake probabilities in the San Francisco Bay Region: 2000 to 2030—a summary of findings, *U.S. Geol. Surv., Open-File Rept. 99-517*, 1999
- Working Group on California earthquake Probabilities (*WG02*), Earthquake probabilities in the San Francisco Bay Region: 2003 to 2032—a summary of findings, *U.S. Geol. Surv., Open-File Rept. (to be determined)*, 2002.

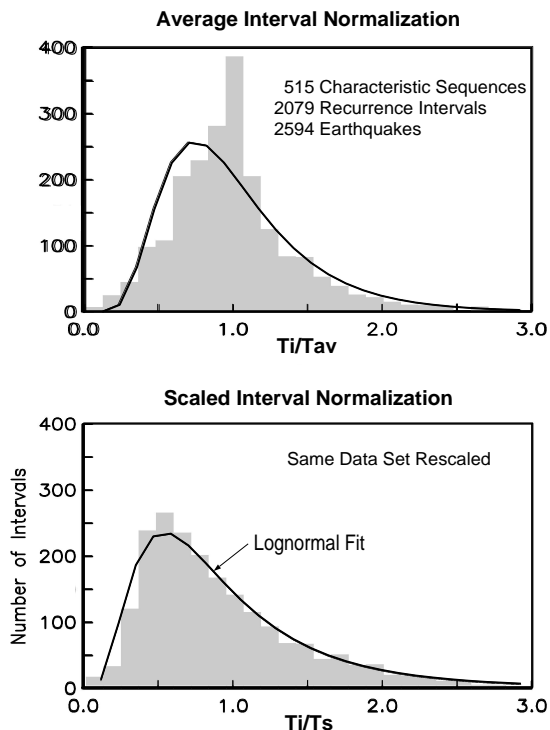


Figure 17.1: Normalized recurrence interval distributions from repeat times of 2594 characteristic small earthquakes ($-0.8 < M_w < 3.6$) occurring along the central SAF from 15 km southeast to 160 km northwest of Parkfield, CA. (Top) Histogram and lognormal fit to recurrence intervals normalized by the average interval for each sequence. (Bottom) Histogram and fit for data normalized by the empirical scaling relationship of average recurrence time with magnitude for all the data. No corrections for spatial or temporal variations in fault slip rates have been applied, and all sequences, regardless of the number of member events, have been included. The exceptionally large number of characteristically repeating small earthquakes makes normalization by the scaling relationship insensitive to the biases that plague T_{av} normalized data. The surprisingly well behaved T_s scaled results and the large number of intervals available suggest it might be possible to discriminate between competing time-dependent earthquake recurrence models and to test the assumption used by the *WG99* and *WG02* recurrence model subgroup that aperiodicity of earthquake recurrence is scale independent.

Chapter 18

The Evolution of the Seismic-Aseismic Transition during the Earthquake Cycle: Constraints from the Time-Dependent Depth Distribution of Aftershocks

Frédérique Rolandone, Roland Bürgmann and Robert Nabelek

0.1 Introduction

We have demonstrated that aftershock distributions after several large earthquakes show an immediate deepening from pre-earthquake levels, followed by a time-dependent postseismic shallowing (Rolandone *et al.*, 2002). We use these seismic data to constrain the depth variations with time of the seismic-aseismic transition throughout the earthquake cycle. Most studies of the seismic-aseismic transition have focussed on the effect of temperature and/or rock composition and have shown that the maximum depth of seismic activity is well correlated with the spatial variations of these two parameters. However, little has been done to examine how the maximum depth of seismogenic faulting varies locally, at the scale of a fault segment, with time during the earthquake cycle.

The mechanical behavior of rocks in the crust is governed by frictional behavior and at greater depth by plastic flow. The coupling between the brittle and ductile layers and the depth extent and behavior of the transition zone between these two regimes is a fundamental question. Mechanical models of long-term deformation (Rolandone and Jaupart, 2002) suggest that the brittle-ductile transition is a wide zone where deformation is caused both by slip and ductile flow. Geologic observations (Sibson, 1986; Scholz, 1990; Trepmann and Stockhert, 2002) indicate that the depth of the seismic-aseismic transition varies with strain rate and therefore is also ex-

pected to change with time throughout the earthquake cycle. The maximum depth of seismogenic faulting is interpreted either as the transition from brittle faulting to plastic flow in the continental crust, or as the transition in the frictional sliding process from unstable to stable sliding. The seismic-aseismic transition therefore reflects a fault zone rheology transition or a more distributed transition from brittle to ductile deformation mechanisms.

0.2 Results

We investigate the time-dependent depth distribution of aftershocks in the Mojave Desert. We apply the double difference method of Waldhauser and Ellsworth (2000) to the region of the M 7.3 1992 Landers earthquake to relocate earthquakes. Time-dependent depth patterns of seismicity have been identified in only few previous studies (Doser and Kanamori, 1986; Schaff *et al.*, 2002) and never quantified. This was mainly due to the problem of the accuracy of the hypocenter locations. Accurately resolving depth is the most challenging part of earthquake location. With new relocation techniques, we can investigate the time-dependent depth distribution of seismicity to reveal more intricate details in the patterns of deformation which take place during an earthquake cycle.

In this study, we focus on quantifying the temporal pattern of the deepest aftershocks. We calculate the d_{95} , the depth above which 95% of the earthquakes occur, and we also calculate the $d_{5\%}$, the average of the 5% of the deepest earthquakes for a constant number of events. We compare our results with the same statistics for the Hauksson relocations (catalog from Hauksson (2000) with a vertical error cutoff of 1.5 km). We specifically in-

investigate (1) the deepening of the aftershocks relative to the background seismicity, (2) the time constant of the postseismic shallowing of the deepest earthquakes. Figure 18.1 shows the time-dependent depth distribution of seismicity for the Johnson Valley fault that ruptured in the 1992 Landers earthquake. Our analysis reveals a strong time-dependence of the depth of the deepest aftershocks. In the immediate postseismic period, the aftershocks are deeper than the background seismicity, followed by a time-dependent shallowing. Figure 18.2 shows the same data but in the form of histograms and relate them to the deepening of the brittle-ductile transition after the mainshock. The temporal variations of the depth of the brittle-ductile transition reflect the strain-rate changes at the base of the seismogenic zone.

The analysis of seismic data to resolve the time-dependent depth distribution of the seismic-aseismic transition provides additional constraints on fault zone rheology, which are independent of geodetic data. Together with geodetic measurements, these seismological observations form the basis for developing more sophisticated models for the mechanical evolution of strike-slip shear zones during the earthquake cycle.

0.3 Acknowledgements

This research is supported by the Southern California Earthquake Center and an IGPP/LLNL grant.

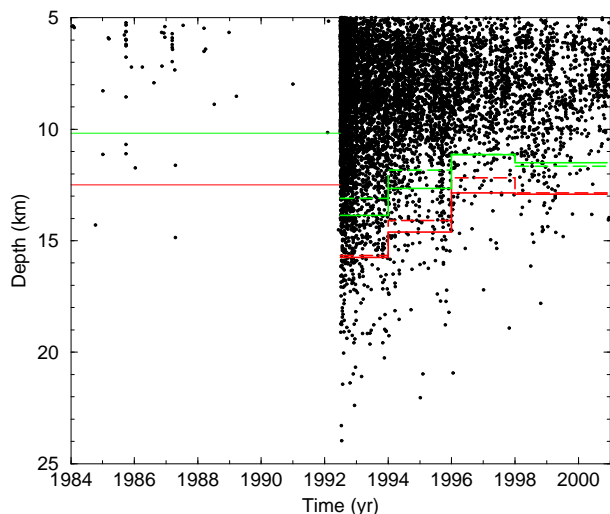


Figure 18.1: Time-dependent depth distribution of seismicity for the Johnson Valley fault. The red curve shows the statistics for the $d_{5\%}$ and the green for the d_{95} (see text). The dashed lines show the same statistics for the Hauksson relocations and are in very good agreement with our results.

0.4 References

- Doser, D.I., and Kanamori H., Depth of seismicity in the Imperial Valley region (1977-1983) and its relationship to heat flow, crustal structure, and the October 15, 1979, earthquake. *J. Geophys. Res.*, *91*, 675-688, 1986.
- Hauksson, E., Crustal structure and seismicity distribution adjacent to the Pacific and North America plate boundary in southern California, *J. Geophys. Res.*, *105*, 13,875-13,903, 2000.
- Rolandone, F., and C. Jaupart, The distribution of slip rate and ductile deformation in a strike-slip shear zone, *Geophys. J. Int.*, *148*, 179-192, 2002.
- Rolandone, F., R. Bürgmann and R.M. Nadeau, Time-dependent depth distribution of aftershocks: implications for fault mechanics and crustal rheology, *Seism. Res. Lett.*, *73*, 229, 2002.
- Schaff, D.P., G.H.R. Bokelmann, G.C. Beroza, F. Waldhauser and W.L. Ellsworth, High resolution image of Calaveras Fault seismicity, *J. Geophys. Res.*, *107* (B9), 2186, doi:10.1029/2001JB000633, 2002.
- Scholz, C.H., Earthquakes and friction laws *Nature*, *391*, 37-42, 1998.
- Sibson, R.H., Earthquakes and rock deformation in crustal fault zone, *Ann. Rev. Earth Planet. Sci.*, *14*, 149-175, 1986.
- Trepman, C.A., and B. Stockhert, Cataclastic deformation of garnet: a record of synseismic loading and postseismic creep, *J. Struct. Geol.*, *24*, 1845-1856, 2002.
- Waldhauser, F., and W. L. Ellsworth, A double-difference earthquake location algorithm: method and application to the northern Hayward fault, California, *Bull. Seismol. Soc. Am.*, *90*, 1353-1368, 2000.

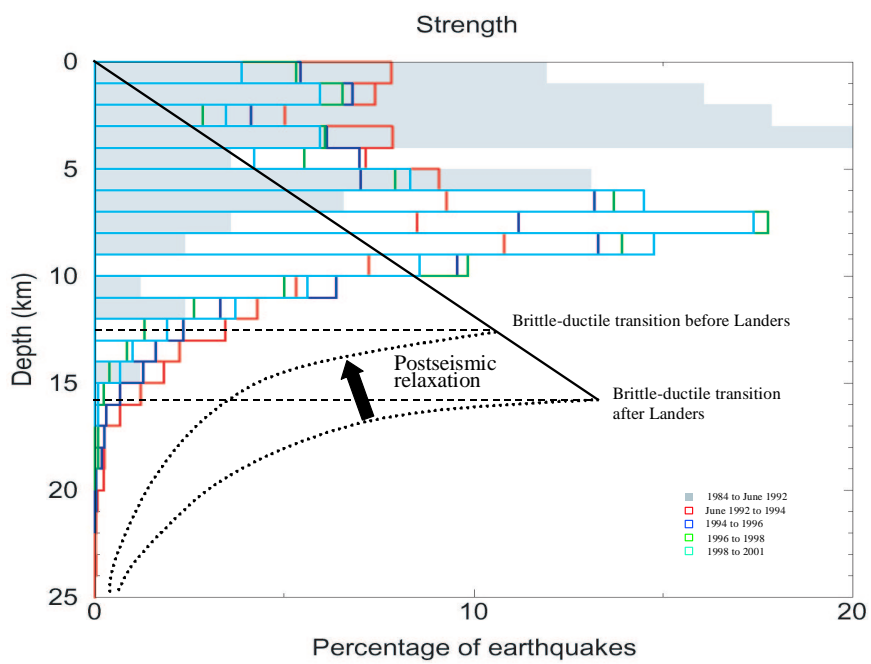


Figure 18.2: Histograms of the depth distribution of seismicity for different time periods. Overlaid is the strength of the brittle and ductile materials.

Chapter 19

Detection of Seismic Stress-Drop Anomalies in the Mendocino Transform Using Coda-Derived Spectra

Gilead Wurman and Douglas S. Dreger

0.1 Introduction

The Berkeley Digital Seismic Network (BDSN) records many regional-scale events in Northern California each year. At present, only a few of these events are assigned moment magnitudes due to the limitations of moment tensor (MT) inversion codes in use today (*Pasyanos et al.*, 1996). Complete-waveform MT inversions require good records at several stations (usually three or more) to obtain well-constrained solutions. Due to high signal to noise levels for small events such coverage is not possible, limiting the reliability of M_w estimates. In the regional context of Northern California this applies to small events with $M_w \leq 3.5$, and here the goal is to create a continuous M_w scale over as broad a range of magnitudes as possible. Additionally, there is interest in getting stable M_w determinations in other, sparsely instrumented regions, where reliable MT inversions cannot be done for events of even moderate magnitude.

The moment magnitude and seismic stress drop of an event can be quickly and accurately determined by fitting the decay rate of L_g or S_n phase coda via the method of *Mayeda et al.* (2003). The coda is composed of seismic waves which are multiply randomly scattered by 3-D inhomogeneities in the upper crust, and sample a broader swath than direct waves. As a result, path and distance corrections can take the form of average crustal properties and simple geometrical spreading relations, and source radiation patterns are washed out. After a station is calibrated for site response the correction holds for all future events. Because the coda method uses a continuum of arrivals rather than a small number of discrete direct arrivals a single station gives a much more robust measurement of M_w than a single station MT inversion.

In a densely instrumented region like Northern California coda-derived M_w determinations can then be made over a much broader range of earthquake sizes (from $M_w \approx 2$ through 8). The coda method also provides stable determinations of earthquake moment-rate spectra, which can be used to examine E_s/M_0 scaling in the study region.

0.2 Coda Decay Method

The coda method measures the narrowband envelopes of the horizontal component of ground motion and fits them to the relation (given a narrow frequency band and epicentral distance)

$$A_c(t|f,r) = A_0 \cdot H\left(t - \frac{r}{v(r)}\right) \cdot \left(t - \frac{r}{v(r)}\right)^{-\gamma(r)} \cdot e^{-b(r) \cdot \left(t - \frac{r}{v(r)}\right)}$$

where H is the Heaviside step function, v is the group velocity as a function of distance, and b and γ are decay functions of distance representing average crustal properties of logarithmic and power decay. These three variables are fixed by fitting theoretical functions to data from multiple calibration events at (ideally) multiple stations. Then for each event at each station the amplitude coefficient A_0 can be fit, representing the power received in that narrow passband. A range of passbands is processed, providing broadband analysis. This power needs to be corrected for site response, and this is done by taking several calibration events (events with good MT solutions) and forcing level spectra at frequencies below the theoretical corner frequency for the corresponding magnitude. Making such corrections over a range of magnitudes yields overall spectra that resemble Brune-model theoretical spectra in corner frequency, DC level and ω^{-2} falloff beyond the corner frequency (*Brune*, 1970).

When the calibration for region and individual stations is complete, any subsequent event must be processed into narrowband envelopes, and A_0 must be fit at each passband. M_w can then be determined from the low fre-

quency power level (lowest two passbands), and energy release and Orowan stress drop can be calculated (Figure 19.1) by integrating the square of the moment-rate spectrum of the event (*Mayeda and Walter, 1996*).

0.3 Performance in the Mendocino Area

The coda method has been applied to 88 offshore events in the Mendocino transform and the Gorda plate with reasonable success. Due to possible source anomalies in transform events the list of good calibration events is fairly small (10 events). The method has been applied with more success in Northern California (*Mayeda*, unpub. data).

A significant number of events in the Mendocino transform exhibit source spectra which depart from the Brune model in characteristic ways. These events exhibit significant enrichment in low-frequency content (below 0.5 Hz) and low corner frequencies for a given M_w . These events have low Orowan stress drops and have been characterized as slow earthquakes (*Abercrombie and Ekström, 2003*), which may indicate lubrication of faults (e.g., *Okal and Stewart, 1982*).

After calibrations are performed on BDSN stations WDC and YBH, the rms magnitude discrepancy between coda and complete-waveform M_w is 0.14 above M_w 3.5 for events that were not in the calibration (Figure 19.2). This scatter is probably due to uncertainties in both methods arising from the anomalous source physics noted above.

0.4 Real-Time Applications

The method, described briefly above, currently requires extensive user input at various stages, in particular to pick the start and end of the coda, and for quality control in the final results. The method could be modified to procedurally pick the coda based on slope, coda length and signal to noise constraints. While the calibration phase would still require human input, subsequent detections and measurement of M_w and stress drop could be done automatically, yielding results within five minutes. The coda method needs approximately 20 minutes of coda to make good measurements, and taking into account telemetry and other processing delays, a robust magnitude determination can be made within 30 minutes of an earthquake.

0.5 Acknowledgements

The authors gratefully acknowledge the help of Kevin Mayeda and Fumiko Tajima in creating the codes to process the raw NCEDC data into the final results. This project was funded through IGPP grant no. 03-GS-031.

0.6 References

- Abercrombie, R.E. and G. Ekström, Earthquake slip on oceanic transform faults, *Nature (London)*, *410*, 74-77, 2001.
- Brune, J.N., Tectonic stress and the spectra of seismic shear waves from earthquakes, *J. Geophys. Res.*, *75*, 4997-5009, 1970.
- Mayeda, K. and W.R. Walter, Moment, energy, stress drop, and source spectra of Western United States earthquakes from regional coda envelopes, *J. Geophys. Res. B*, *101*, 11,195-11,208, 1996.
- Mayeda, K., A. Hofstetter, J.L. O'Boyle and W.R. Walter, Stable and transportable regional magnitudes based on coda-derived moment-rate spectra, *Bull. Seism. Soc. Am.*, *93*, 224-239, 2003.
- Okal, E.A. and L.M. Stewart, Slow earthquakes along oceanic fracture zones: evidence for aesthenospheric flow away from hotspots?, *Earth Planet. Sci. Lett.*, *57*, 75-87, 1982.
- Pasyanos, M.E., D.S. Dreger and B. Romanowicz, Towards real-time estimation of regional moment tensors, *Bull. Seism. Soc. Am.*, *86*, 1255-1269, 1996.

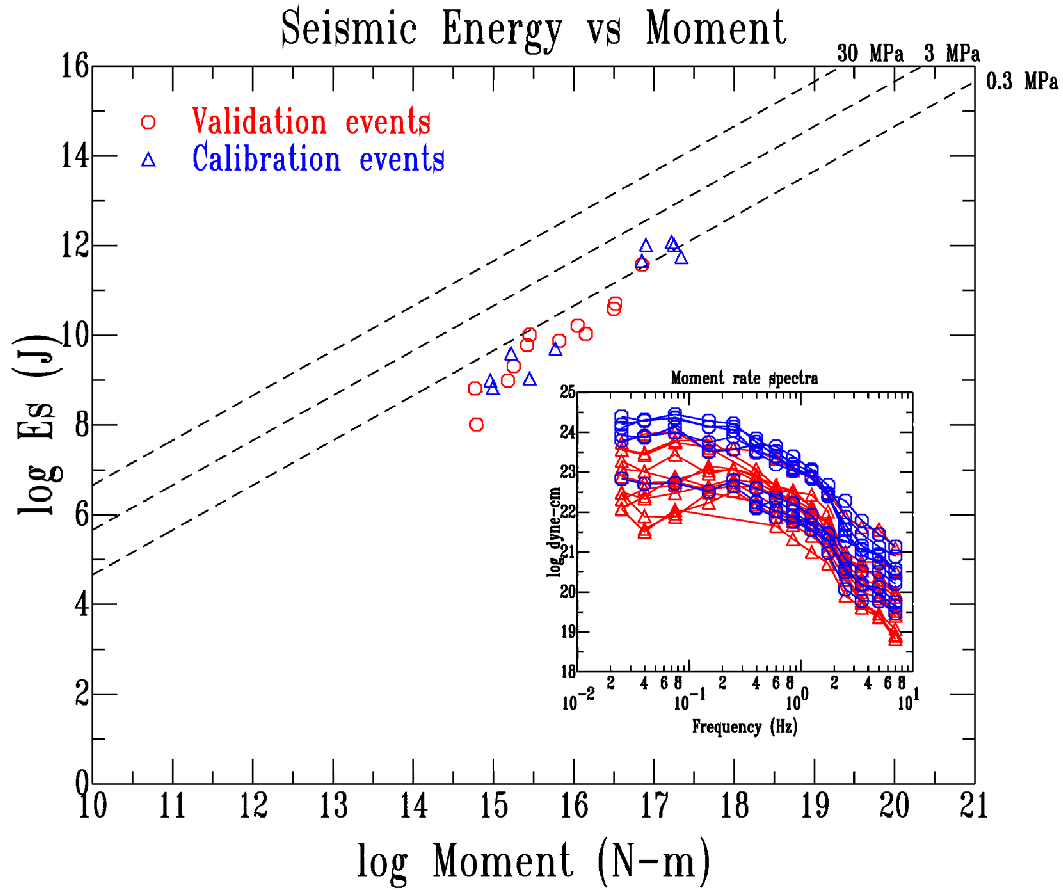


Figure 19.1: Moment-energy scaling relationship for events in the Mendocino region. Dashed lines represent constant Orowan stress drop. Inset: typical source spectra for events in the Mendocino region (averaged over stations WDC and YBH).

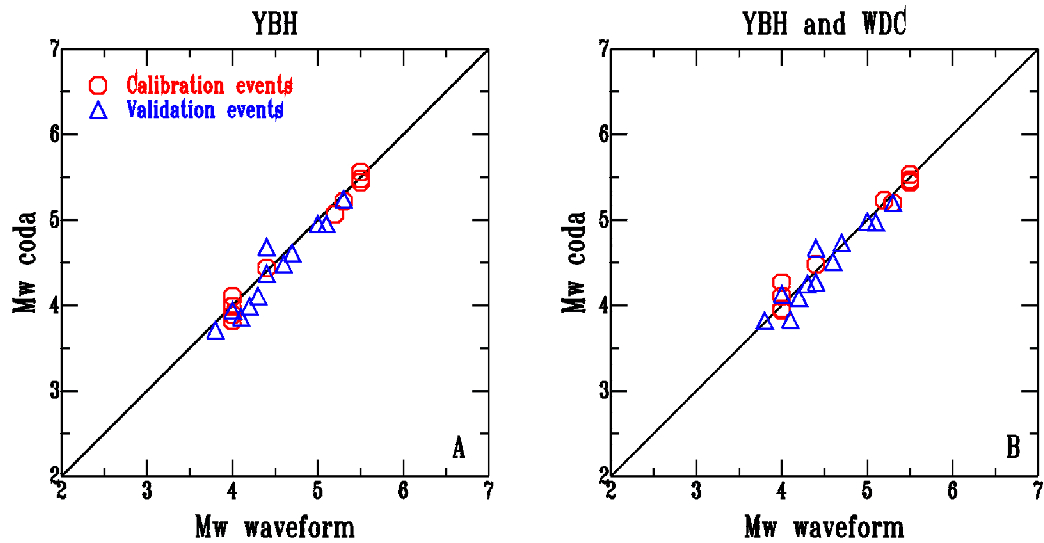


Figure 19.2: Complete-waveform M_w vs. Coda-derived M_w from station YBH (a) and averaged over stations YBH and WDC (b).

Chapter 20

Long-Period Microtremor Observations in the Santa Clara Valley, California

David Dolenc and Doug Dreger

0.1 Introduction

The 3D velocity structure of the Santa Clara Valley (SCV) was previously investigated by modeling the teleseismic P-waves (Dolenc, 2001) recorded by the 41 seismic stations of the SCV Seismic Experiment (USGS/UCB/PASSCAL, 6/98-12/98). To complement these results, we now focused on the microseisms that were recorded during the same SCV seismic experiment.

0.2 Results

Microseisms are generated by the pressure variations on the sea floor due to the ocean waves and can be observed in the 0.1 to 5 Hz frequency range. We first compared the noise level of several earthquake-free periods to the ocean wave heights recorded at the Santa Cruz weather buoy and showed that the two are correlated (Dolenc, 2001).

Horizontal to vertical (H/V) spectral ratios of microtremor signals for a 5-day earthquake-free period were then calculated for each station. The H/V spectral ratios for the 5-minute segments at the beginning of each hour were first calculated and then averaged over the 5 days. The results showed that the dominant period of the H/V spectral ratios in the 0.1 to 1 Hz frequency range is stable with time and is location dependent (Figure 20.1). The longer periods can be observed for the stations above the two basins and the shorter periods for the stations in-between the basins. The period of the H/V peaks as a function of the basin depth from the USGS model (Jachens, 2000) is shown in Figure 20.2.

There was no correlation between the amplitudes of the H/V spectral ratios and the USGS model basin depths.

In addition we applied the H/V method to the two local earthquakes recorded during the SCV seismic experiment (San Juan Bautista, $M_L=5.4$, and Gilroy, $M_L=4.0$).

The results showed that for most SCV seismic stations the peaks of the H/V spectral ratios in the 0.1 to 1 Hz frequency range coincided with microseism H/V spectral ratio peaks.

The observations of the microseisms on the SCV stations show that the presence of the basins can be observed even for the time periods without earthquakes. Future work will include modeling the response of the sedimentary layers using the 1D structure from the USGS model under each SCV seismic station.

0.3 Acknowledgements

This research was supported by the USGS grants 99HQGR0057 and 00HQGR0048. The USGS velocity model provided by Robert C. Jachens of the U.S. Geological Survey was used. Ocean wave data were obtained from the National Data Buoy Center.

0.4 References

Dolenc, D., Basin structure influences on the teleseismic wave propagation in the Santa Clara Valley, California, *MS Thesis*, University of California, Berkeley, 2001.
Jachens, R.C., Personal communications, 2000.

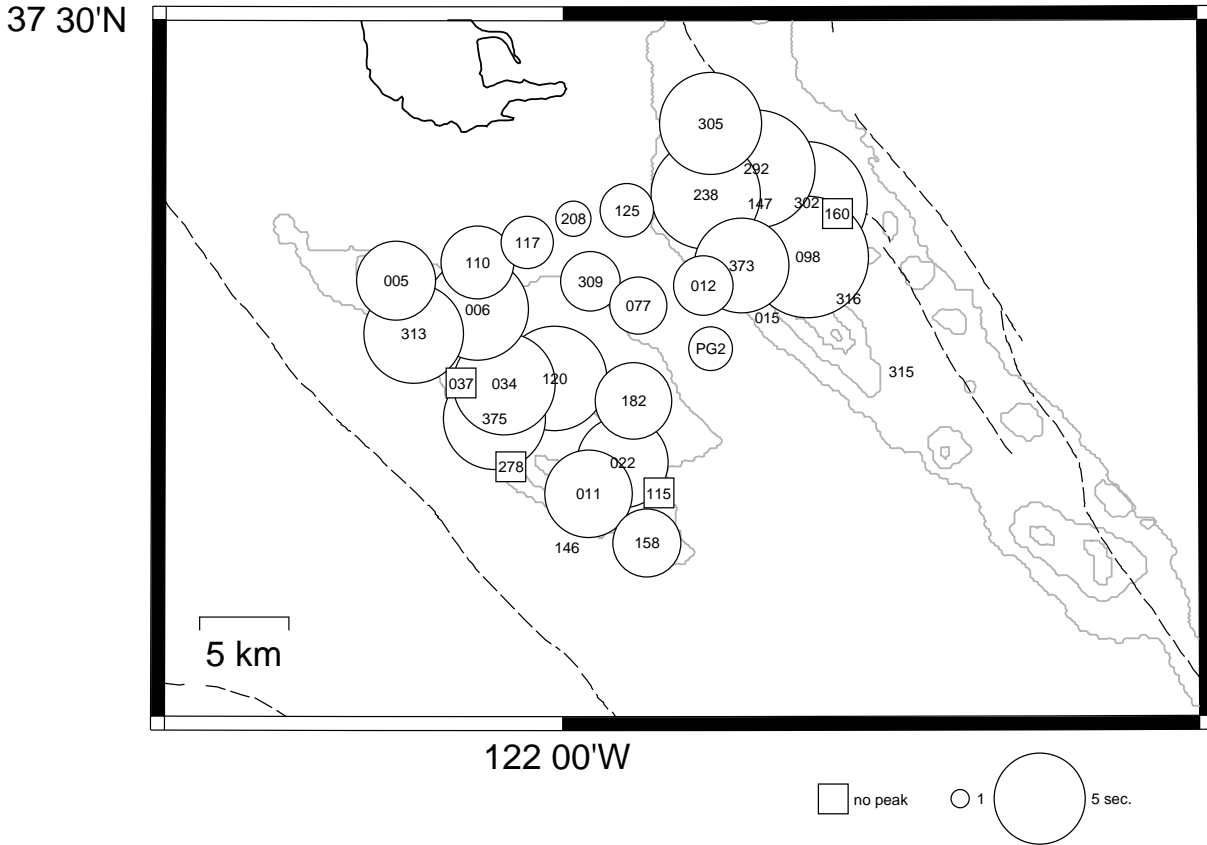


Figure 20.1: The periods of the dominant H/V spectral peaks in the 0.1 to 1 Hz frequency range. The numbers indicate locations of the SCV seismic stations and the circles indicate the periods of the H/V spectral peaks. Stations that showed no peak in the 0.1 to 1 Hz frequency range are shown by squares. Contours of the basins from the USGS model at 1 km, 3 km, 5 km, and 6 km are shown in gray. Dashed lines are the active faults in the region.

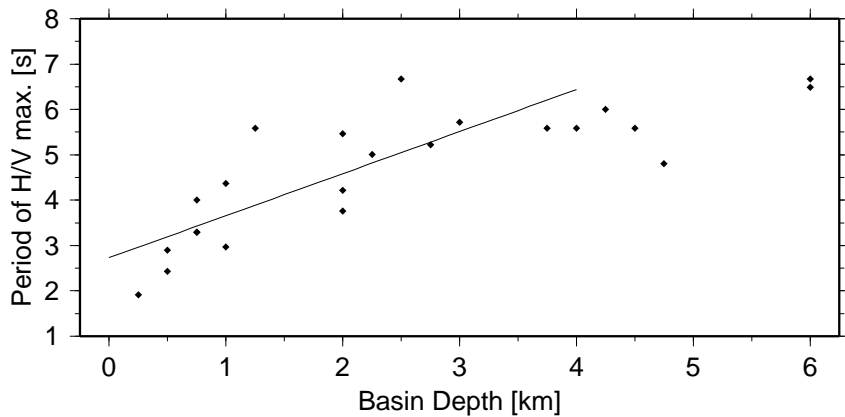


Figure 20.2: The period of the dominant H/V peaks as a function of the basin depth from the USGS model. Stations located above shallower than 4 km basins were used in regression and the resulting line fit is shown ($y=0.93x+2.73$, $R\text{-squared}=0.61$).

Chapter 21

Fluid Influenced Faulting in the Long Valley Volcanic Region

Dennise Templeton and Douglas Dreger

0.1 Introduction

We aim to better understand how an evolving hydrothermal system in an active volcanic region directly influences local earthquake production. Our ultimate interest is in the underlying source mechanism of these fluid influenced earthquakes and the factors that affect it. Towards that goal, we first determined the extent of fluid influenced faulting in the Long Valley volcanic region by computing moment tensor solutions from regional broadband data.

The Long Valley volcanic region, located in eastern California within the Sierra Nevada frontal fault system, includes the well-known active magmatic systems under Long Valley caldera and the Mono/Inyo Craters. For over two decades, the Long Valley caldera has been the center of unrest in the region exhibiting periods of increased seismicity, ground deformation, localized increases in concentrations of volcanic gases and subsurface magma movement (*Langbein et al.*, 1995 ; *Sorey et al.*, 1998). The Mono/Inyo Craters are a series of craters extending north from the caldera and are thought to have been created from a series of dikes over the past 40,000 years (*Bursik and Sieh*, 1989). To the south of the caldera is the Sierra Nevada mountain block, where there have been equivocal indications of magma existence even though there is a lack of evidence for recent volcanic or geothermal activity (*Hough et al.*, 2000 ; *Peppin et al.*, 1989).

In this study, we focused on a 100 km wide circular area centered at Long Valley caldera which includes the Mono/Inyo Craters and the seismically active Sierra Nevada block and comprehensively searched for events with coseismic volume changes.

0.2 Method and Results

Full moment tensor inversions solve for the complete moment tensor and can be decomposed into double-couple (DC), compensated-linear-vector-dipole (CLVD), and isotropic (i.e. volumetric) components. The presence of a significant volumetric component could indicate that fluids were involved in the source process of an earthquake. Deviatoric solutions a priori constrain the volumetric component to be zero. In this active geothermal and volcanic region, we did not wish to make this assumption. Therefore, we solved for both the deviatoric and full moment tensor solutions using three-component Berkeley Digital Seismic Network data at regional distances.

We studied 130 events with magnitudes greater than 3.5 since 1993. Seven stations were chosen for these inversions that provided the best azimuthal coverage and data quality. In practice however a solution would have a subset of these seven stations in its inversion depending on station availability and data quality issues. Green's functions were computed using the SoCal velocity model which is appropriate for the eastern California and Sierra Nevada regions (*Dreger and Helmberger*, 1993). Both data and Green's functions were bandpass filtered between 0.02 to 0.05 Hz using a causal Butterworth filter.

We used a nested F test to determine the probability that the additional volumetric component in the full moment tensor solution represented a true aspect of the source mechanism rather than being simply an added non-physical parameter in the inversion. We identified significant volumetric components if the improvement in fit to the data was at the 99 percent significance level between the deviatoric and full moment tensor solution.

Of the 130 earthquakes we originally identified, we were able to compute solutions for 83 events. The ensuing moment tensor catalog allowed us to determine the prevalence of events characterized by isotropic components. From these results we identified 17 earthquakes that had significant volumetric components as well as

good station coverage and data quality (Figure 21.1). These events all had between four and six stations in their inversions.

This investigation showed that fluid influenced earthquakes are fairly unique in the Long Valley volcanic region. The majority of these events were located within the Long Valley caldera or near the rim of the caldera. The remaining seven events were located in the seismically active Sierra Nevada block south of the caldera.

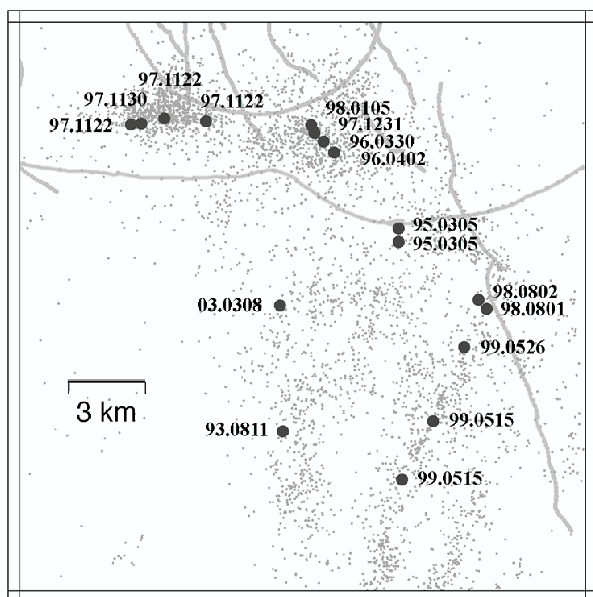


Figure 21.1: Location of events occurring between 1993-2003 with significant volumetric components labeled as YY.MMDD. Background seismicity is plotted as small gray dots. Faults, caldera rim, and resurgent dome plotted as solid gray lines.

0.3 Discussion

All events with significant volumetric components in the Long Valley caldera are located in the south moat or near the adjacent caldera rim. Seven of these events occurred in or near the location or time period of the November 1997 earthquake swarm. During and after this swarm there was also extensive independent evidence of magma migration from EDM, GPS, strainmeters, tiltmeters, and volcanic gas discharge rates. This magma migration could have affected the surface hydrothermal system in such a way as to cause these fluid influenced faulting events. The remaining two events were located near the epicenter of a M_L 6.1 May 1980 quake that had a large non-double couple component (*Julian and Sipkin, 1985*). It was never determined if this event had a volumetric component which would have conclusively

determined if fluids were involved. Long Valley caldera has an active geothermal system and thus it is not unexpected to find events with large isotropic components in this area (*Lachenbruch et al., 1976*).

It was surprising that earthquakes did not occur in or near the vicinity of the Mono/Inyo Craters. There is extensive evidence for the existence of magma under this volcanic chain and it is the expected location of the next volcanic eruption from this system (*Hill et al., 1985*; *Bursik and Sieh, 1989*). Perhaps this points to differences in the hydrothermal system or heat flux found in this area and with that found in the Long Valley caldera.

The most interesting result of this study was the number of fluid influenced earthquakes within the Sierra Nevada block when there has been no conclusive evidence of recent geothermal or magmatic activity in the area. However, there has been indirect evidence reported of magma bodies south of the caldera from pre-S phases and S-wave shadowing studies (*Peppin et al., 1989*). *Hough et al. (2000)* also identified several lines of equivocal evidence of magma or magmatic fluid involvement during an August 1998 earthquake sequence near the Hilton Creek fault. Earthquake activity in the Sierra Nevada block has always been assumed to be tectonic due to the absence of recent volcanism and present day geothermal features. However two major earthquakes occurring between 1978 and 1980 had large non-double couple components (*Julian and Sipkin, 1985*). Again, it was never determined if either of these events had large volumetric components.

Perhaps tectonic adjustment in the Sierra Nevada block could be providing a convenient conduit for hydrothermal fluids to migrate from their origin in the caldera to the mountain block via the north striking faults found in the area. In later studies we plan to explore the connection between fluid influenced faulting, the shallow hydrothermal system, and the deeper magmatic system.

0.4 Acknowledgements

We appreciate support for this project by NSF through contract EAR-0087147.

0.5 References

- Bursik, M. and K. Sieh, Range Front Faulting and Volcanism in the Mono Basin, Eastern California, *J. Geophys. Res.*, *94*, 15,587-15,609, 1989.
- Dreger, D.S. and D.V. Helmberger, Determination of source parameters at regional distances with three-component sparse network data, *J. Geophys. Res.*, *98*, 8107-8125, 1993.
- Hill, D.P., R.A. Bailey, and A.S. Ryall, Active tectonic and magmatic processes beneath LVC, eastern California: a summary, *J. Geophys. Res.*, *90*, 11,111-11,120, 1985.

Hough, S.E., R.S. Dollar, and P. Johnson, The 1998 earthquake sequence south of Long Valley Caldera, California: hints of magmatic involvement, *Bull. Seism. Soc. Am.*, *90*, 752-763, 2000.

Julian, B.R. and S.A. Sipkin, Earthquake Processes in the Long Valley Caldera Area, California, *J. Geophys. Res.*, *90*, 11,155-11,169, 1985.

Lachenbruch, A.H., M.L. Sorey, R.E. Lewis, and J.H. Sass, The Near-Surface Hydrothermal Regime of Long Valley Caldera, *J. Geophys. Res.*, *81*, 763-768, 1976.

Langbein, J., D. Dzurisin, G. Marshall, R. Stein, and J. Rundle, Shallow and peripheral volcanic sources of inflation revealed by modeling two-color geodimeter and leveling data from Long Valley caldera, California, 1998-1992, *J. Geophys. Res.*, *100*, 12,487-12,495, 1995.

Peppin, W.A., W. Honjas, T.W. Delaplain, and U.R. Vetter, The case for a shallow-crustal anomalous zone (magma body?) near the south end of Hilton Creek fault, California, including new evidence from an interpretation of pre-S arrivals, *Bull. Seism. Soc. Am.*, *79*, 805-812, 1989.

Sorey, M.L., W.C. Evans, B.M. Kennedy C.D. Farrar, L.J. Hainsworth, and B. Hausback, Carbon dioxide and helium emissions from a reservoir of magmatic gas beneath Mammoth Mountain, California, *J. Geophys. Res.*, *103*, 15,303-15,323, 1998.

Chapter 22

Source Mechanisms of Volcanic Induced Seismicity – Miyakejima, Japan, 2000

Sarah E. Minson, Douglas S. Dreger, and Roland Bürgmann (2001). In this study, all of the events were separately inverted in two frequency ranges: 0.01 to 0.033 Hz, and 0.02 to 0.05 Hz. Two types of moment tensor inversions were used: deviatoric and full moment tensor. In deviatoric inversions, the trace of the moment tensor is assumed to be zero, which implies that there is no volume change.

0.1 Introduction

Mount Oyama is a volcano on Miyakejima, Japan, part of the Izu Islands volcanic chain located south of Honshu. The most recent period of unrest at Mount Oyama began in June 2000, and this eruptive sequence included the largest recorded earthquake swarm in Japan (*Japan Meteorological Agency (JMA)*, 2000). More than 100,000 earthquakes were recorded in the next two months (*Ito and Yoshioka*, 2002). The seismic activity showed complex variations in space and time (*JMA*, 2000), but its most notable feature is that it migrated northwest with an offshore dike intrusion. Many of these earthquakes have large non-double-couple (NDC) components which might be indicative of fluid involvement in the seismic source process. In this study, linear moment tensor inversions in two passbands were used to establish the mechanism of eighteen of these earthquakes; GPS data were used to independently invert of the mechanism of two of these earthquakes and to forward predict the observed seismograms.

0.2 Moment Tensor Inversions

The methods of *Dreger et al.* (2000) and *Dreger and Woods* (2002) were used to investigate the mechanisms of eighteen events which occurred from June 29 to July 18, 2000 (UT). These eighteen events are comprised of the twelve events which the F-net network determined to have moment magnitudes of 5.5 or larger, plus six smaller events which were chosen because the F-net moment tensors had anomalous characteristics such as large NDC components or solutions with large variances.

Linear moment tensor inversions (*Pasyanos et al.*, 1996; *Dreger et al.*, 2000; *Dreger and Woods*, 2002), were used to invert complete, three-component, broadband seismograms recorded by the F-net network (Figure

22.1). In this study, all of the events were separately inverted in two frequency ranges: 0.01 to 0.033 Hz, and 0.02 to 0.05 Hz. Two types of moment tensor inversions were used: deviatoric and full moment tensor. In deviatoric inversions, the trace of the moment tensor is assumed to be zero, which implies that there is no volume change.

The depth of each event was established by performing independent moment tensor inversions at a range of depths to find which one produces the best fit to the data, and the ability of the synthetics to fit the data was assessed by the variance reduction (VR) (for example, *Dreger and Woods*, 2002), where a VR of 100% implies a perfect fit between the data and the synthetic seismograms. The stability of both the full moment tensor inversions and the deviatoric moment tensor inversions was examined by use of the jackknife test, in which data from every subset of the stations used in the original inversion are used to invert for the mechanism. Another type of source mechanism investigated was comprised only of isotropic and double-couple components (ISO+DC).

0.3 GPS Inversions

Data from ten GPS stations (Figure 22.1) operated by the Geographical Survey Institute of Japan (GSI) were used to determine displacements caused by EVT3 and EVT15, the two largest earthquakes in this sequence. The station located on the Izu peninsula was used as a reference station, and GPS displacements were calculated using the coordinates of each GPS station from the day before and after each earthquake. The nonlinear inversion methods of *Bürgmann et al.* (1997) were used to determine slip and rupture geometry. The length and width of the fault were constrained by the empirical scaling relationships between magnitude and rupture length and width which were reported in *Wells and Coppersmith* (1994), and the fault determined by the GPS inversion was required to be located within 5 km of the earthquake hypocenter reported by JMA.

0.4 Results

The majority of the events studied have large CLVD components which are consistent with the opening of a vertical crack (Figure 22.2, Figure 22.3). The results of the jackknife tests show that nearly all of the mechanisms are extremely stable. Extensional CLVD mechanisms such as the ones determined by this study have been repeatedly observed in volcanic areas and have been theorized to be the result of fluid injection (for example, *Kanamori et al., 1993; Julian and Sipkin, 1985*).

The full moment tensor inversions have an additional model parameter relative to the deviatoric inversions and ISO+DC grid searches. Therefore, it is necessary to determine whether the better fit of the full moment tensor mechanisms is statistically significant. The significance was examined by the use of multiple types of F-tests, but the partial F-test proposed by *Helsel and Hirsch (1992)* is considered to be most appropriate for this study. In the *Helsel and Hirsch (1992)* formulation, the F-test analyzes whether the specific parameter which was added to the model yields significant explanatory power in the presence of the other variables in the model. The results indicate that for at least twelve of these earthquakes, the moment tensors in both passbands have isotropic components which are statistically significant with more than 90% confidence, and half of the isotropic components are statistically significant with more than 99% confidence.

CLVD components can be caused by shear slip on two fault planes, but isotropic components cannot be formed from double-couples (*Julian et al., 1998*). Therefore, complex shear faulting can definitely be eliminated as the source of the NDC components of the mechanisms with statistically significant isotropic components. The orientation of the CLVD components of the earthquakes relative to the strike of the inferred dike (*Ito and Yoshioka, 2002; Toda et al., 2002*) and the observed seismicity indicate that these mechanisms may be consistent with tensile faulting due to opening along the dike.

The GPS data for EVT15 independently predict a mechanism that is very similar to the mechanism determined by the moment tensor inversions. Furthermore, synthetic seismograms generated using the mechanism determined by the GPS inversions fit the observed seismograms with a VR of 89.9%. This is particularly noteworthy because it shows that the GPS data can predict a completely independent data set.

The results of the GPS inversions for EVT3 are less conclusive. The GPS displacements on Miyakejima are consistent with deflation related to the magma chamber that was inferred to exist beneath the island, and they do not appear to be related to EVT3. Therefore, it was necessary to introduce a deflation source beneath the island in order to fit the GPS data, and this other deformation source probably affects the GPS inversion for the slip and geometry of the earthquake fault. The GPS data

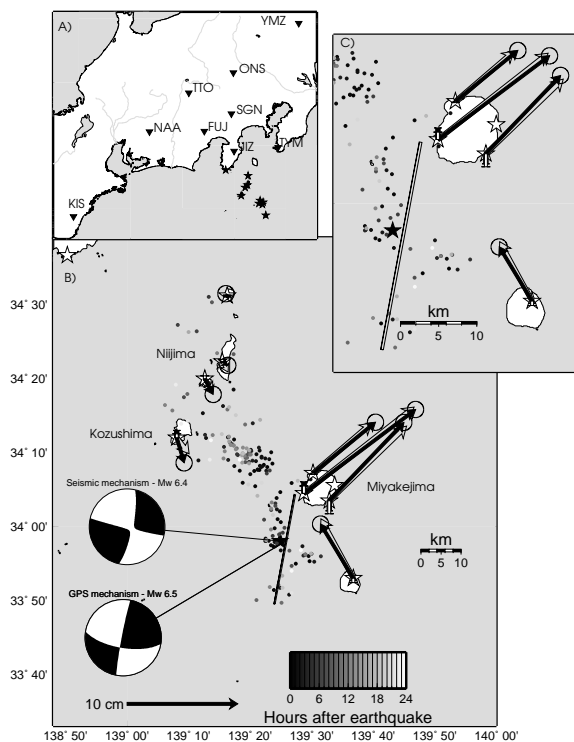


Figure 22.1: Study area and GPS inversion results for EVT15. **A.** Map showing location of F-net broadband seismograph stations and GSI GPS stations used in this study. F-net stations are denoted by triangles, and GSI stations are marked with stars. **B.** GPS inversion results for EVT15. Black arrows and vertical bar represent observed horizontal and vertical displacements, respectively. Clear arrows and yellow bars are predicted displacements. The fault determined by the GPS inversion is plotted as long with the seismicity reported in the Japan Meteorological Agency (JMA) catalog for the twenty-four hours following EVT15. The model fits the GPS data with a weighted residual sum of squares (WRSS) of 24.0053. **C.** Same as B. for the area near Miyakejima.

for EVT3 are clearly better fit by NDC mechanisms, just as the seismic data are much better fit by a NDC mechanism. However, the synthetic seismograms generated from the NDC GPS models do not fit the observed seismograms.

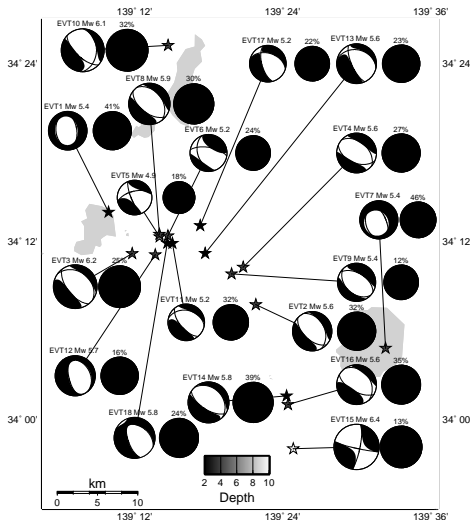


Figure 22.2: Full moment tensor mechanisms for the eighteen events in this study. The mechanisms in this figure were determined by full moment tensor inversions in the 0.02 to 0.05 Hz passband.

0.5 Conclusions

Moment tensor inversions for deviatoric, full moment tensor, and ISO+DC mechanisms in two frequency passbands were performed for eighteen earthquakes related to the eruption on Miyakejima, Japan in 2000. The majority of these events have large CLVD components which are consistent with the opening of a vertical crack (Figure 22.2). The orientation of these mechanisms relative to the dike intrusion and the observed seismicity indicate that these mechanisms might reflect tensile faulting related to inflation along the dike. Inversions of GPS data for EVT15 yield a slip model and fault geometry which does an excellent job of forward predicting the observed seismograms for that earthquake. However, the GPS data for EVT3 do not converge to a mechanism which fits the seismic data as well as the results of the GPS inversions for EVT15 do.

0.6 References

Bürgmann, R., P. Segall, M. Lisowski, and J. Svarc, Postseismic strain following the 1989 Loma Prieta earthquake from GPS and leveling measurements, *J. Geophys. Res.*, 102(3B), 4933-4955, 1997.

Dreger, D., and B. Woods, Regional distance seismic moment tensors of nuclear explosions, *Tectonophysics*, 356, 139-156, 2002.

Dreger, D. S., H. Tkalčić, and M. Johnston, Dilational processes accompanying earthquakes in the Long Valley Caldera, *Science*, 288, 122-125, 2000.

Helsel, D. R., and R. M. Hirsch, *Statistical Methods in Water Resources, Studies in Environmental Science*, 49, pp. 296-299, Elsevier Science Publishers, Amsterdam, 1992.

Ito, T., and S. Yoshioka, A dike intrusion model in and around Miyakejima, Niijima, and Kozushima in 2000, *Tectonophysics*, 359, 171-187, 2002.

Japan Meteorological Agency, Recent seismic activity in the Miyakejima and Niijima-Kozushima region, Japan - the largest earthquake swarm ever recorded, *Earth Planets Space*, 52(8), i-vii, 2000.

Julian, B. R., and S. A. Sipkin, Earthquake processes in the Long Valley Caldera area, California, *J. Geophys. Res.*, 90(B13), 11,155-11,169, 1985.

Julian, B. R., A. D. Miller, and G. R. Foulger, Non-double-couple earthquakes, 1: Theory, *Rev. Geophys.*, 36(4), 525-549, 1998.

Kanamori, H., G. Ekstrom, A. Dziewonski, J. S. Barker, and S. A. Sipkin, Seismic radiation by magma injection: An anomalous seismic event near Tori Shima, Japan, *J. Geophys. Res.*, 98(B4), 6511-6522, 1993.

Pasyanos, M. E., D. S. Dreger, and B. Romanowicz, Toward real-time estimation of regional moment tensors, *Bull. Seismol. Soc. Am.*, 86(5), 1255-1269, 1996.

Toda, S., R. Stein, and T. Sagiya, Evidence from the AD 2000 Izu islands earthquake swarm that stressing rate governs seismicity, *Nature*, 419, 58-61, 2002.

Wells, D. L., and K. J. Coppersmith, New empirical relationships among magnitude, rupture length, rupture width, rupture area, and surface displacement, *Bull. Seismol. Soc. Am.*, 84(4), 974-1002, 1994.

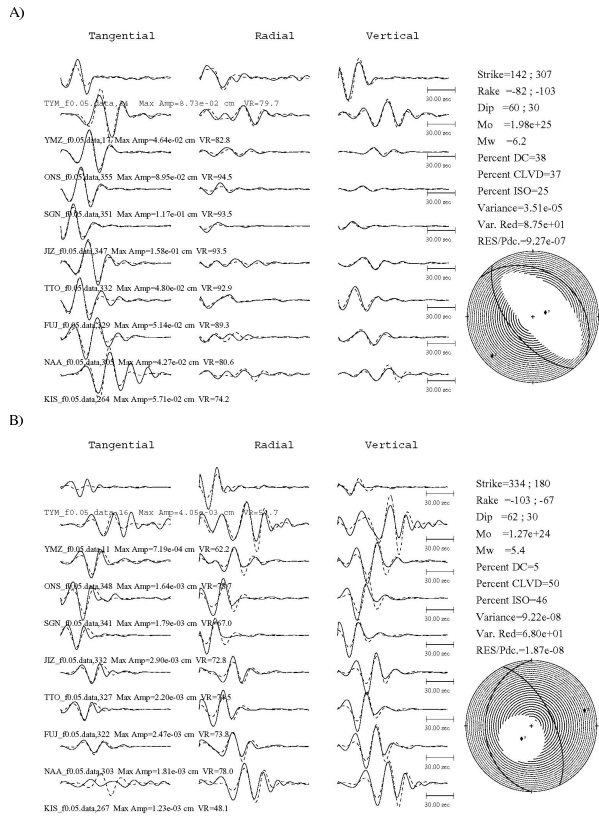


Figure 22.3: Waveform comparisons in the 0.02 to 0.05 Hz passband. **A.** Full moment tensor mechanism for EVT3. This mechanism has a large positive isotropic component which is consistent with inflation due to fluid injection. **B.** Full moment tensor mechanism for EVT7. The Phase of the Rayleigh waves does not appear to change, which is indicative of isotropic radiation. But the transverse seismogram has large amplitudes, and SH radiation should not be produced by an isotropic component. Therefore, this earthquake may have a complex mechanism consisting of both shear slip and an isotropic component, or it may have an inclined single-force mechanism. The depth of this event is unclear from the moment tensor inversions. But all three components are fit well at shallow depths which are consistent with inferred magma chamber depths. EVT7 occurred on the same day as a caldera began to form on Miyakejima, and it may be related to caldera collapse.

Chapter 23

Identifying and Removing Noise from the Ocean Bottom Broadband Seismic Data

David Dolenc, Barbara Romanowicz, and Bob Uhrhammer

0.1 Introduction

Ocean bottom broadband seismic observations show increased noise level when compared to land recordings. The signal-generated noise following the arrival of the seismic phases is one type of the observed noise, which is due to reverberations in the soft sediments and the water layer. Increased background noise, on the other hand, is generated, among others, by infragravity waves and ocean currents. Both types of noise can at least partially be removed from the seismic signal.

The data recorded at MOBB (Monterey Ocean Bottom Broadband station) were used. MOBB was installed 40 km offshore in the Monterey Bay at a water depth of 1000 m in April 2002 in a collaboration between Berkeley Seismo Lab and Monterey Bay Aquarium Research Institute (MBARI) (McGill *et al.*, 2002; Uhrhammer *et al.*, 2002). It comprises a three-component broadband seismometer with a temperature sensor, a water current meter measuring current speed and direction, and a differential pressure gauge (DPG). The station is continuously recording data which are retrieved every three months using the MBARI ROV "Ventana".

0.2 Signal-Generated Noise

An example of a large deep teleseism recorded at MOBB (black) and at the nearby island station FARB (gray) is shown in Figure 23.1. A strong signal-generated noise is observed at MOBB, probably due to reverberations in the mud layer in which MOBB seismometer is installed. This type of noise may be unavoidable in shallow buried installations. The transfer function describing the signal-generated noise in the sediments layer was calculated by the spectral division of the first 50 seconds of the MOBB and FARB records. The transfer function was then removed from the longer MOBB record to eliminate

the signal-generated noise (dashed).

Our future work will include analysis of other teleseismic events to obtain a robust transfer function, as well as 1D modeling of the soft sediments and water layer.

0.3 Background Noise

A comparison of a power spectral density (PSD) of the background noise recorded on the vertical component at MOBB and at three stations of the Berkeley Digital Seismic Network is shown in Figure 2. Data for a quiet and for a stormy day (determined from the wave height recordings from a nearby weather buoy) are shown. The background noise PSD between 30 and 500 sec is significantly different at MOBB. The observed peak is probably related to ocean currents and infragravity waves (Webb *et al.*, 1991; Webb, 1998). It is interesting that a similar peak can be observed at the island station FARB on the stormy day.

In our future work we plan to find the coherence between background noise and the ocean current, DPG data, temperature, and the ocean tides, and design filters to remove the coherent part of the noise. Previous studies successfully removed noise due to infragravity waves and ocean currents (Webb and Crawford, 1999; Crawford and Webb, 2000; Stutzmann *et al.*, 2001).

The results from this work may suggest future installation improvements for the deployment of permanent or temporary off-shore seismic broadband stations, such as have been discussed in the framework of the Ocean Mantle Dynamics (OMD) workshop (Snowbird, Fall 2002).

0.4 References

Crawford, W.C., and S.C. Webb, Identifying and removing tilt noise from low-frequency (<0.1 Hz) seafloor vertical seismic data, *Bull. Seism. Soc. Am.*, 90, 952-963, 2000.

McGill, P., D. Neuhauser, D. Stakes, B. Romanowicz, T. Ramirez, and R. Uhrhammer, Deployment of a long-term broadband seafloor observatory in Monterey Bay,

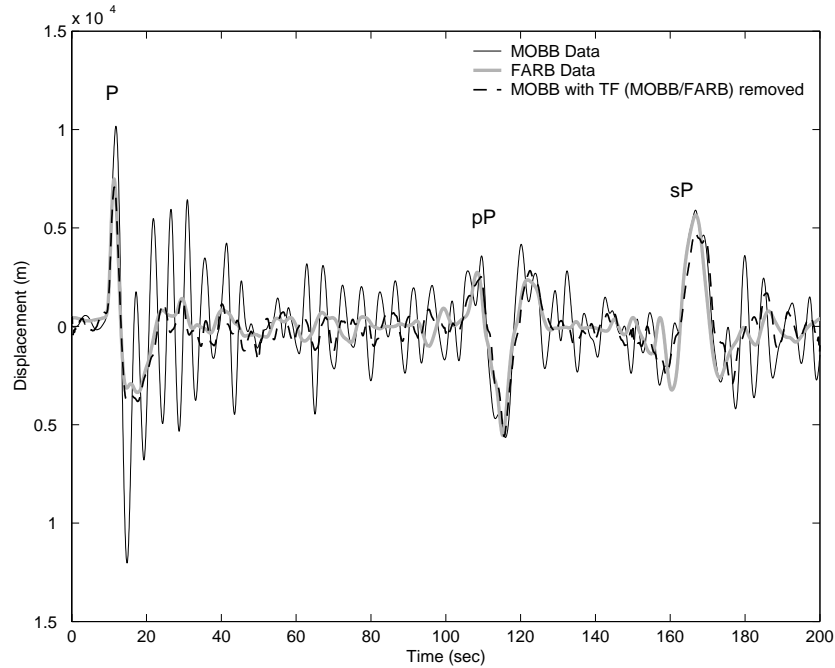


Figure 23.1: Vertical component recordings of a teleseism (Kurile Islands, 11/17/02, $M_w=7.3$, depth=459 km) at MOBB (black) and at the nearby island station FARB (gray). The two records were bandpass filtered between 0.03 and 0.3 Hz. Also shown is the MOBB record with the signal-generated noise removed (dashed). The arrivals of the P-, pP-, and sP-waves are indicated.

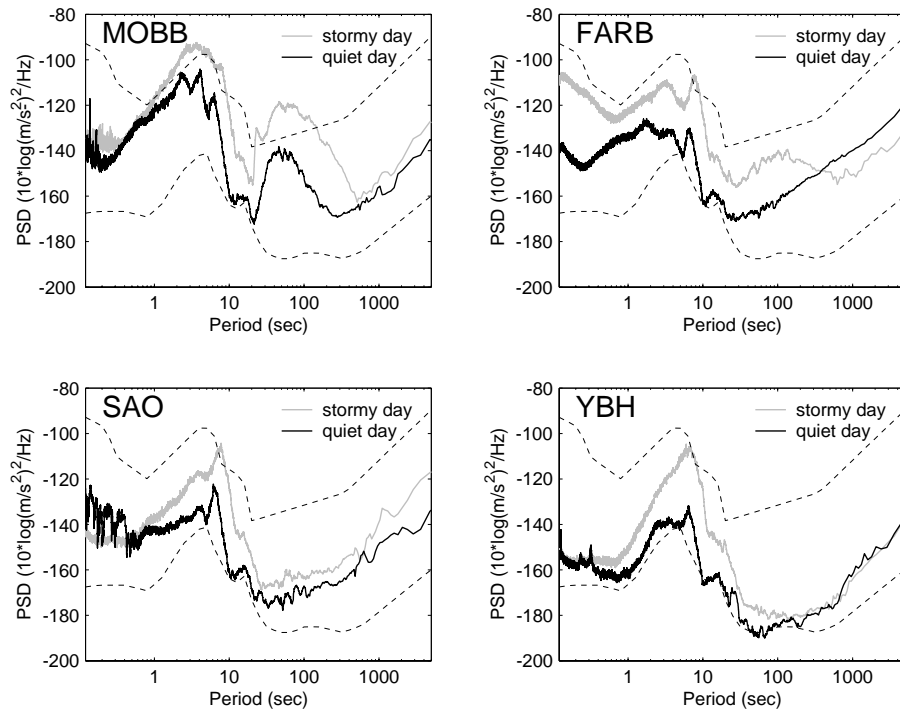


Figure 23.2: Background noise PSD observed at MOBB, FARB, SAO, and YBH vertical components. Shown are 4 hours data on a stormy (gray; 12/16/02), and on a quiet day (black; 05/23/02). The USGS high- and low-noise models for land stations are also shown (dotted).

EOS Trans. Amer. Geophys. Un., 83, F1008, 2002.

Stutzmann, E., J.-P. Montagner, A. Sebai, W.C. Crawford, J.-L. Thiot, P. Tarits, D. Stakes, B. Romanowicz, J.-F. Karczewski, J.-C. Koenig, J. Savary, D. Neuhauser, and S. Etchemendy, MOISE: A prototype multiparameter ocean-bottom station, *Bull. Seism. Soc. Am.*, 91, 885-892, 2001.

Uhrhammer, R., B. Romanowicz, D. Neuhauser, D. Stakes, P. McGill, and T. Ramirez, Instrument testing and first results from the MOBB Observatory, *EOS Trans. Amer. Geophys. Un.*, 83, F1008, 2002.

Webb, S.C., X. Zhang, and W. Crawford, Infragravity waves in deep ocean, *J. Geophys. Res.*, 96, 2723-2736, 1991.

Webb, S.C., Broadband seismology and noise under the ocean, *Rev. Geophys.*, 36, 105-142, 1998.

Webb, S.C., and W.C. Crawford, Long-period seafloor seismology and deformation under the ocean waves, *Bull. Seism. Soc. Am.*, 89, 1535-1542, 1999.

Chapter 24

Detection of Long Period Surface Wave Energy

Junkee Rhie and Barbara Romanowicz

0.1 Introduction

Since the 1960s, array seismology has been developed mainly due to the need for detection of nuclear tests. Now there are many seismic arrays of various sizes in the world which are used for detecting nuclear tests, but also very weak but important seismic phases for refining fine-scale structure of the deep earth.

In this study, we are interested in weak low-frequency surface waves. Low-frequency surface waves are usually the dominant phases in waveforms generated from earthquake. They have been widely used for determining global earth structure and for the retrieval of earthquake source parameters. In addition, they can be used for detecting the existence of special types of seismic sources, such as slow/silent earthquakes (*Beroza and Jordan, 1990*), back ground free oscillations (*Ekström, 2001*) and other unknown sources. Usually, the low-frequency surface waves generated from these kinds of sources are too weak to be detected by a single station.

The main goal of this study is to detect weak energy from some low-frequency seismic sources and locate them. To do that, we need to design an optimal array method and guarantee this method to work. Hereafter we call this optimal method an array-based method.

0.2 An Array-Based Method

Most array methods are based on beam forming method (*Rost and Thomas, 2002*). Beam forming method can enhance the amplitudes of the same phases with an identical horizontal slowness \mathbf{u} . For body waves, each phase has a constant slowness, but surface waves are dispersive, that is, slowness is a function of frequency. Our array-based method is also based on beam forming, but it does not use constant slowness, it uses the dispersive property of surface wave. The following equation

describes the propagation of surface waves over a distance x from the source, in the frequency domain.

$$D(\omega, \theta, x) = S(\omega, \theta) \exp\left(\frac{-i\omega x}{C(\omega)}\right) \exp\left(\frac{-\omega x}{2U(\omega)Q(\omega)}\right)$$

where D is waveform in frequency domain at distance x and θ is an azimuth. C , U and Q are phase, group velocity and quality factor respectively. These parameters are obtained from a reference 1D model such as PREM (*Dziewonski and Anderson, 1981*). Although surface wave propagation is also affected by lateral heterogeneities, ellipticity and rotation of the Earth, PREM is a good approximation when the frequency band that we are interested in is low enough. By using the above equation we can align the surface waves with respect to a reference point within one array. The relative propagation distance is just a function of back azimuth when we assume plane wave propagation. The relation between back azimuth and waveform cannot be represented as a linear equation. Thus a model parameter search method can be used to measure back azimuth. The detailed process is as follows. We assume any back azimuth and imagine an imaginary source at 90 deg. away from the reference point (center of the array). Epicentral distances for all stations are calculated from an imaginary epicenter. We get relative distances between stations and the reference point by subtracting 90 deg. from calculated epicentral distances. The mapped waveform into reference point from each station can be calculated by using the above equation. Next process is to stack mapped waveforms to enhance coherent surface waves and reduce incoherent noise. The stacking can increase the possibility of detection by increasing the S/N ratio. Because neither do we have very dense distribution of stations nor all of them are quiet, stacking may not be able to increase the S/N ratio significantly. But in most cases, it can be helpful. The most common stacking method is a simple mean process, but we used N-th root stacking method. The advantage of this method is that it can severely reduce incoherent noises relative to a simple mean process,

but it can distort the waveforms after stacking (Muirhead and Datt, 1976). Now we have one stack from original recordings for a given back azimuth. If a given back azimuth is close to real one, amplitude of surface wave is preserved and incoherent noise is reduced. The final step is to apply moving time window and take averaged amplitude of recording in time window. The definition of averaged amplitude is

$$S\left(\frac{t_1 + t_2}{2}\right) = \sqrt{\frac{\int_{t_1}^{t_2} (v(t)w(t))^2 dt}{\int_{t_1}^{t_2} w(t)^2 dt}}$$

where $w(t)$ is a taper function. The length and shift of time window will be different with respect to the applications and frequency content. In this study, we use a duration of 500 sec, shift of 100 sec and band pass between 50-200 sec. The above procedure is repeated for all possible back azimuths and then finally we can obtain averaged amplitudes as a function of time and back azimuth. We applied this array based method for three different arrays in the world during the period of January 2000.

0.3 Discussion

Our detection method is not completely established. Although we still need more refined detector which can identify signal from noise, the detection of the signal from large events ($M_w > 6.0$) is obvious because they have much larger amplitudes relative to the back ground amplitude level. Figure 24.1 shows maximum averaged amplitudes in back azimuth as a function of time calculated for three different arrays - FNET (Japan), GRSN (Germany) and BDSN (Northern California). Because low-frequency displacement amplitudes are proportional to scalar seismic moment, maximum averaged amplitudes can be tied to M_w by introducing a scaling factor. Most signals due to large events can be clearly identified in all three arrays. The background noise levels are different for three arrays, GRSN shows much larger noise level than other two networks. This difference can be explained partly by different internal noise of seismometer in GRSN. GRSN consists of STS-2, but STS-1 is installed on other stations which are used in this study..

The final goal of application of array-based method is to detect and locate seismic sources. To check the reliability of the current method, we manually detect signals and compare their arrival time and back azimuth with those calculated from the earthquake catalog (Harvard CMT). There were 13 events with M_w larger than 6 in January, 2000. All 13 events are clearly detected for three arrays. Comparison result is written in following table.

As you can see in the table, all measured back azimuths are within 20 deg. from actual back azimuths and time differences between measured and calculated times are not significant. It indicates that we can locate the

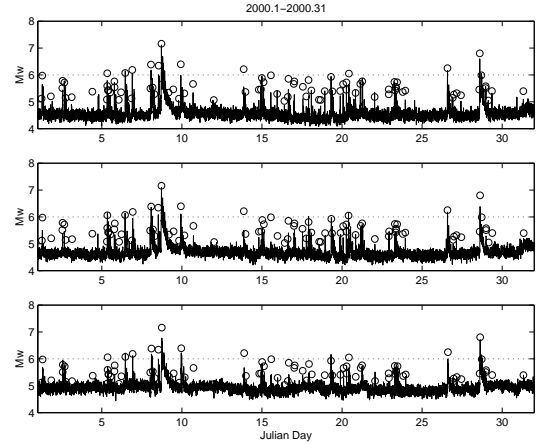


Figure 24.1: Maximum averaged amplitude plot for January, 2000. Amplitudes for FNET, BDSN and GRSN are shown from top to bottom. Small circles indicate arrival times and M_w for events listed in CMT. An arrival time is corrected by assuming group velocity of 3.8 km/sec

Event ID	Mw	Array	Time diff.	Baz1	Baz2
C010100B	6.0	FNET	-17 sec	172.20 deg	165 deg
		BDSN	-185 sec	214.64 deg	225 deg
		GRSN	249 sec	128.86 deg	115 deg
C010500C	6.1	FNET	19 sec	145.78 deg	140 deg
		BDSN	27 sec	251.38 deg	255 deg
		GRSN	92 sec	38.02 deg	40 deg
C010600C	6.1	FNET	24 sec	38.44 deg	45 deg
		BDSN	44 sec	337.46 deg	335 deg
		GRSN	121 sec	342.75 deg	345 deg
C010800A	6.4	FNET	80 sec	150.85 deg	145 deg
		BDSN	-3 sec	255.68 deg	255 deg
		GRSN	114 sec	42.74 deg	50 deg
C010800F	6.3	FNET	29 sec	69.11 deg	75 deg
		BDSN	117 sec	133.82 deg	135 deg
		GRSN	83 sec	248.76 deg	250 deg
C010800G	7.2	FNET	49 sec	130.20 deg	130 deg
		BDSN	31 sec	232.58 deg	235 deg
		GRSN	44 sec	8.06 deg	25 deg
C010900D	6.4	FNET	-39 sec	141.12 deg	135 deg
		BDSN	-165 sec	239.75 deg	240 deg
		GRSN	31 sec	28.35 deg	35 deg
C011300B	6.2	FNET	129 sec	134.42 deg	130 deg
		BDSN	-159 sec	236.03 deg	240 deg
		GRSN	165 sec	28.35 deg	15 deg
C011500C	6.0	FNET	-400 sec	137.17 deg	135 deg
		BDSN	-196 sec	233.03 deg	235 deg
		GRSN	95 sec	16.87 deg	20 deg
C012000D	6.1	FNET	-68 sec	50.73 deg	50 deg
		BDSN	21 sec	316.58 deg	300 deg
		GRSN	40 sec	331.01 deg	335 deg
C012600A	6.2	FNET	-35 sec	130.22 deg	130 deg
		BDSN	-39 sec	232.40 deg	235 deg
		GRSN	60 sec	8.23 deg	25 deg
C012800B	6.8	FNET	-88 sec	44.19 deg	50 deg
		BDSN	-64 sec	307.41 deg	305 deg
		GRSN	77 sec	31.02 deg	35 deg
C012800C	6.0	FNET	139 sec	230.22 deg	225 deg
		BDSN	-85 sec	305.34 deg	300 deg
		GRSN	38 sec	55.76 deg	55 deg

Figure 24.2: Table of detection result. Time difference means arrival time difference between observed and calculated ones. BAZ1 is back azimuth calculated from CMT and BAZ2 is measured back azimuth.

source from measured parameters. This result shows an array-based method can measure arrival time and back azimuth precisely enough to locate the source when energy released from the source is quite large. We still need to know the limit of detection and whether there is any detectable signal due to sources that are not standard events. To do that, we will apply this method on whole data of 2000 and look at other frequency bands.

0.4 References

Beroza, G. and T.H. Jordan, Searching for slow and silent earthquakes using free oscillations, *J. Geophys. Res.*, *95*, 2485-2510, 1990.

Dziewonski, A.M. and D.L. Anderson, Preliminary reference Earth model (PREM), *Phys. Earth Planet. Inter.*, *25*, 289-325, 1981

Ekström, G., Time domain analysis of Earth's long-period background seismic radiation, *J. Geophys. Res.*, *106*, 26,483-26,493, 2001.

Muirhead, K.J. and R. Datt, The N-th root process applied to seismic array data, *Geophys. J. R. Astr. Soc.*, *47*, 197-210, 1976.

Rost, S. and C. Thomas, Array seismology: Methods and applications, *Rev. Geophys.*, *40(3)*, 1008, doi:10.1029/2000RG000100, 2002.

Chapter 25

Automated Moment Tensor Software for Monitoring the Comprehensive Test Ban Treaty

Margaret Hellweg, Douglas Dreger, Barbara Romanowicz, Jeffrey Staley, and SAIC

0.1 Introduction

Seismology makes an important contribution toward monitoring compliance with the Comprehensive Test Ban Treaty (CTBT). An important task at the testbed of the Center for Monitoring Research (CMR, Washington DC, USA) and the International Data Center (IDC) of the Comprehensive Test Ban Treaty Organization (CTBTO, Vienna, Austria) is to detect, locate and characterize seismic events in order to distinguish between natural sources of seismic waves such as earthquakes, and other sources which might possibly be nuclear tests. For large events, this is not particularly difficult. However, small events, whether natural or man-made, present a greater challenge. While their epicenters and magnitudes can be determined fairly precisely using standard seismological methods, seismic moment tensor analysis can help in two ways. It gives information about the size and mechanism of a source in terms of its seismic moment and the moment tensor components. It provides, in addition, an estimate of the source's depth, which cannot always be reliably determined using normal location techniques. Thus, if an event has a large non double-couple component ($> 50\%$) its source may be an explosion, possibly a nuclear explosion, while tectonic earthquakes typically have more than 70-80% double couple movement (*Dreger and Woods, 2002*). The source depth determined from moment tensor analysis may also help to weed out deep tectonic events from among the more than 100000 events of magnitude 4 and greater that occur annually. Only events at shallow depths need be scrutinized as part of the monitoring process of the Comprehensive Test Ban Treaty (CTBT).

This project's goal is to implement the procedure for

using seismic moment tensors routinely used in real-time at the University of California at Berkeley (UCB, *Romanowicz et al., 1993; Dreger and Romanowicz, 1994; Pasyanos et al., 1996*) on the testbed at CMR. Although the moment tensor procedure will not run in real-time on the testbed, in its final implementation it will run automatically, triggered from the Reviewed Event Bulletin (REB) and will be an additional, potentially powerful method for screening events (*Pechmann et al., 1995; Dreger and Woods, 2002*).

0.2 The Denali Sequence

The earthquakes which occurred in Alaska in October and November, 2002, provide an excellent opportunity for testing the moment tensor procedures. On the map in Figure 25.1A, the dots represent aftershocks in the sequence, while the locations of the mainshock, the foreshock and the four aftershocks we analyzed are shown as the large, medium-sized and small stars, respectively. We applied the CW moment tensor method to data from the foreshock on 23 Oct 2002, (FS, $m_b(\text{NEIC})$ 6.1 and $m_b(\text{REB})$ 5.5), and four aftershocks (AS1: 5 Nov, 07:50 UTC, $m_b(\text{NEIC})$ 4.9 and $m_b(\text{REB})$ 4.6; AS2: 08 Nov, 04:04 UTC, $m_b(\text{NEIC})$ 5.3 and $m_b(\text{REB})$ 5.1; AS3: 08 Nov, 17:34 UTC, $m_b(\text{NEIC})$ 5.2 and $m_b(\text{REB})$ 5.0; AS4: 08 Nov, 20:29 UTC, $m_b(\text{NEIC})$ 5.0 and $m_b(\text{REB})$ 4.7). The moment tensor calculated for the foreshock using data from three primary stations of the IMS network that had been filtered between 30 s and 100 s (mechanism south of FS) agrees well with that given in the Harvard CMT catalog. The fits between the synthetics and data are very good. It was notable that to achieve this fit, we had to use GFs for distances 100 km too short. This is very likely due to the fact that we use Greens functions calculated from the iasp91 velocity model. The actual seismic velocities under the North American continent are probably faster than those given

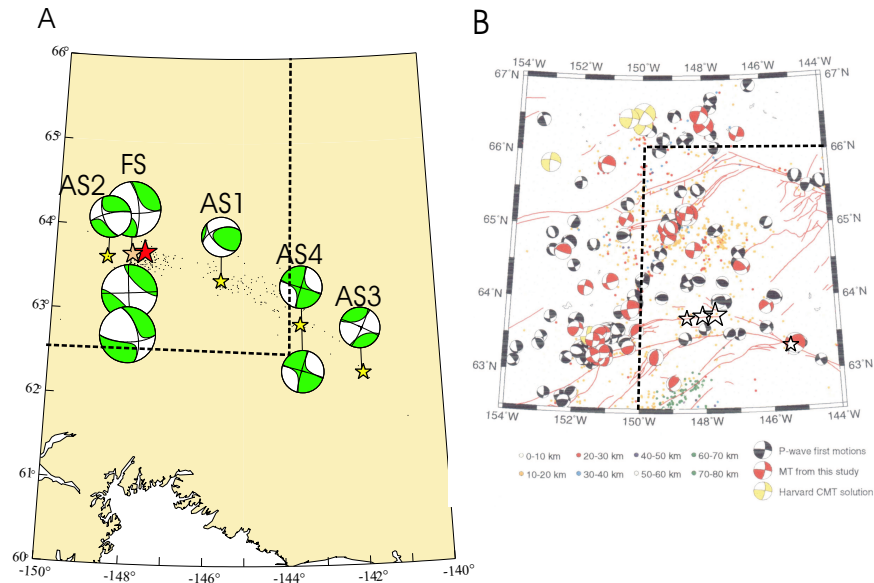


Figure 25.1: A: Epicentral locations of the Denali mainshock (large star), foreshock (medium-sized star) and the four aftershocks (small stars) analyzed. The dots show the epicenters other events in the sequence. Moment tensor solutions north of the epicenters were calculated using data filtered between 20 s and 50 s, those to the south were calculated from data filtered between 30 s and 100 s. The second solution south of FS was calculated using data for all stations. B: Mechanisms for recent Alaska seismicity given by *Ratchkovski and Hanson (2002)*. The dotted lines mark the areas of overlap between the two maps. Stars mark the locations of the mainshock, foreshock and the two aftershocks in the region of overlap.

in the model. *Ratchkovski and Hanson (2002)* have investigated recent seismicity in Alaska, producing mechanisms of many events in a region overlapping with some of the seismicity from the Denali sequence. Figure 25.1B shows their results. Both the foreshock and two of the aftershocks lie within the limits of their study. It is notable that the mechanisms north of the epicenters in Figure 25.1A, determined using data and GFs filtered between 20 and 50 s agree very well with the solutions for previous events located along the Denali Fault.

0.3 Acknowledgements

This research is sponsored by the Defense Threat Reduction Agency under contract DTRA01-00-C-0038.

0.4 References

Dreger, D. and B. Romanowicz, Source characteristics of events in the San Francisco Bay Region, *USGS Open-file report*, 94-176, 301-309, 1994.

Dreger D. and B. Woods, Regional Distance Seismic Moment Tensors of Nuclear Explosions, *Tectonophysics*, 356, 139-156, 2002.

Pasyanos, M., D. Dreger, and B. Romanowicz, Toward real-time estimation of regional moment tensors, *Bull. Seism. Soc. Am.*, 86, 1255-1269, 1996.

Pechmann, J.C., W.R. Walter, S.J. Nava, and W.J. Arabasz, The February 3, 1995, M_L 5.1 seismic event in the Trona mining district of southwestern Wyoming, *Seis. Res. Lett.*, 66, 25-34, 1995.

Ratchkovski, N.A., Hansen, R.A., New Evidence for Segmentation of the Alaska Subduction Zone, *Bull. Seism. Soc. Am.*, 92, 1754-1765, 2002.

Romanowicz, B., M. Pasyanos, D. Dreger, and R. Uhrhammer, Monitoring of strain release in central and northern California using broadband data, *Geophys. Res. Lett.*, 20, 1643-1646, 1993.

Chapter 26

The Bay Area Velocity Unification (BĀVŪ); Bringing Together Crustal Deformation Observations from throughout the San Francisco Bay Area

Matthew A. d'Alessio, Ingrid A. Johanson, Roland Bürgmating, and the UC Berkeley Active Tectonics Group

0.1 Introduction

In an effort to put together the most comprehensive picture of crustal deformation in the San Francisco Bay Area, The UC Berkeley Active Tectonics Group has begun work on the Bay Area Velocity Unification (BĀVŪ “Bay-View”). This dataset unites campaign GPS data for nearly 180 GPS stations throughout the greater San Francisco Bay Area from Sacramento to San Luis Obispo. The BĀVŪ dataset includes data collected from 1991 to 2003 by U. C. Berkeley, the U.S. Geological Survey, the California Department of Transportation, Stanford University, U. C. Davis and the Geophysical Institute in Fairbanks, AK. These are combined with continuous GPS data from the BSL’s Bay Area Regional Deformation (BARD) network. The BĀVŪ dataset will form a consistent velocity field that will serve as the basis for monitoring fault slip and strain accumulation throughout the greater San Francisco Bay region.

0.2 Technical Overview of GPS Data Collection and Processing

Data Collection

At UC Berkeley we occupy each benchmark in our campaign GPS networks yearly. When possible, we collect data for at least two continuous 24 hour sessions, with some occupations spanning as long as seven days. However, much of the study area is in urban or suburban

unattended and limiting the occupation time to the logistical limits of the human operator. For these sites, occupations may be as short as 6 hours or as long as 12 hours, depending upon the time it takes to travel to the site and the efficiency of the operator. We usually repeat surveys of these sites at least once. Other agencies contributing data to the BĀVŪ dataset generally follow the same guidelines and provide at least 6 hours of data per site per day.

Processing Baselines

We process campaign GPS data using the GAMIT/GLOBK software package developed at the Massachusetts Institute of Technology, which uses double-difference phase observations to determine baseline distances and orientations between ground-based GPS receivers. Along with campaign data, we process five global stations from the International GPS Service (IGS) network and four to six nearby continuous stations from the BARD network. Cycle slips are automatically identified and fixed using the AUTCLN routine within GAMIT. We use standard models for satellite radiation pressure and tropospheric delay. Ambiguities are fixed using the widelane combination followed by the narrowlane, with the final position based on the ionospheric free linear combination (LC or L3). For baselines shorter than 500 meters, we calculate an additional solution using only L1 data. Baseline solutions are loosely constrained (100 m) until they are combined together.

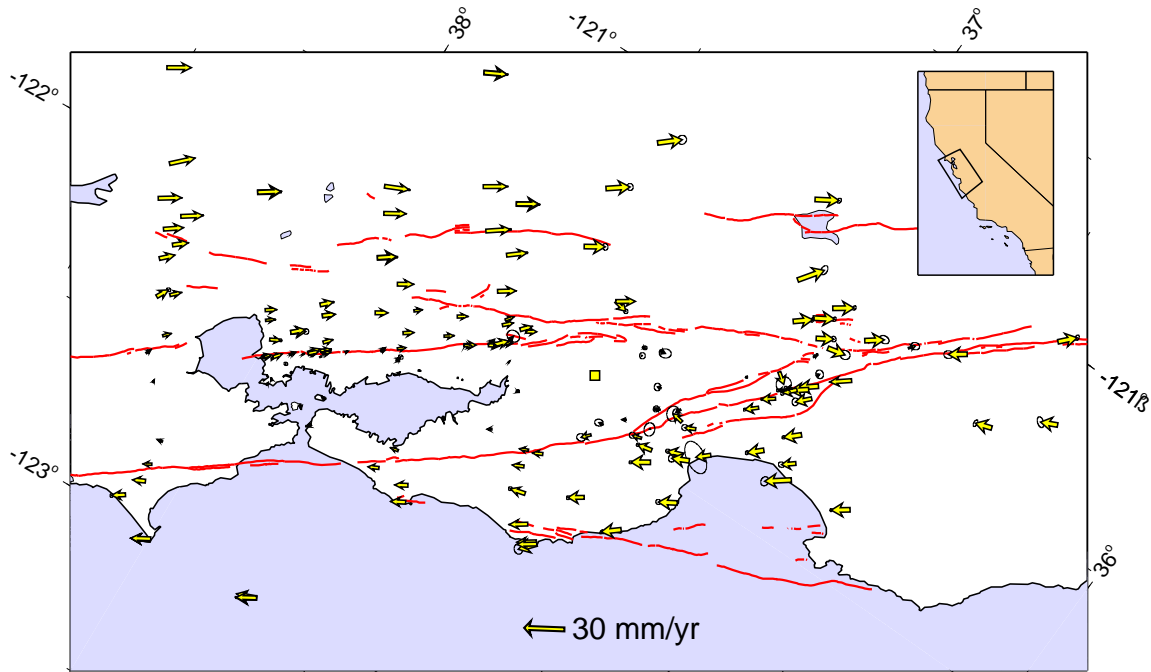


Figure 26.1: Map of the San Francisco Bay area in a Pacific Plate–Sierra Nevada block projection with GPS Velocities from 1994–2003 relative to station LUTZ in the Bay Block (yellow square). Velocities consistent with a small circle path predicted from the Euler pole of the Pacific Plate–Sierra Nevada block rotation show up as horizontal arrows.

Combining Solutions

We combine daily ambiguity-fixed, loosely constrained solutions using the Kalman filter approach implemented by GLOBK. Within a given day, we include data processed locally as well as solutions for the full IGS and BARD networks processed by and obtained from SOPAC at the University of California, San Diego. During this combination, we weight each solution file relative to the other solution files for that day proportionally to the pre-fit chi-squared for the file when run through the Kalman filter independently. We uniformly scale the covariances of the entire combination so that the prefit chi-squared for the combined daily solution is approximately 1.0. Using the Kalman filter, we combine all daily solutions with equal weight to estimate the average linear velocity of each station in the network. We fix the final positions and velocities into the global reference frame using the GLOBK stabilization routine, allowing for rotation and translation of the network. Our final covariance matrix and the uncertainty estimates derived from it are scaled by the a posteriori chi-squared for the full combination. GLOBK also allows for the modeling of uncertainty using a benchmark wobble, but our current solutions have not included this effect.

0.3 GPS Results

Figure 26.1 shows GPS velocities for the entire BÄVÜ dataset relative to station LUTZ on the Bay Block. Be-

tween UC Davis and the Farallon Islands, we observe $33\text{mm}\text{yr}^{-1}$ of relative displacement between the Pacific plate and the Sierra Nevada–Great Valley block of the North American plate. The Bay block shows up as a relatively undeformed block with many of the stations having velocities relative to LUTZ that are so small that they plot as dots in the figure.

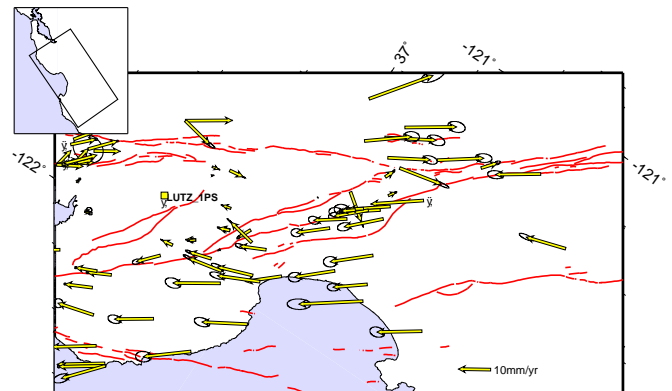


Figure 26.2: Map of deformation near the transition zone of the San Andreas Fault. Velocities relative to LUTZ on the Bay block.

Southern Bay Area

The southern section of the BÄVÜ dataset includes the region affected by postseismic deformation following the Loma Prieta earthquake (Fig. 26.2). To avoid "contamination" of the regional deformation pattern by transient processes, we have not included data in this area collected before 1994. The southern Bay Area exhibits mostly fault-parallel right-lateral motion, with no indication of the fault-normal compression observed in the Foothills thrust belt immediately after the Loma Prieta Earthquake (Bürgmann, 1997). Other transient processes such as several slow earthquakes on the Central San Andreas fault are captured by the dataset, but their effect is likely small when spread over several years. The future inclusion of InSAR data in the BÄVÜ dataset will allow the identification of some transient deformation events that the GPS networks are too sparse to capture. It should also improve our ability to measure surface creep.

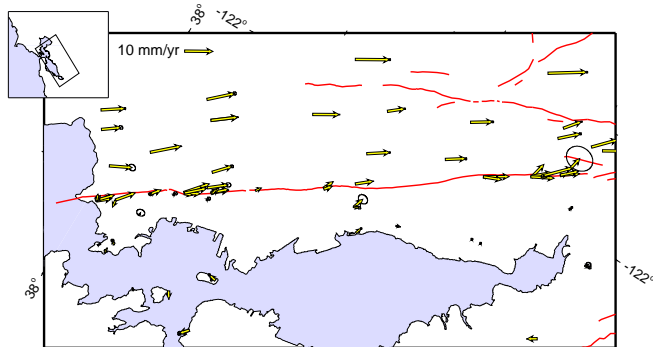


Figure 26.3: Map of deformation near the Hayward fault. Velocities relative to LUTZ on the Bay block.

Hayward Fault

BÄVÜ includes 64 stations within 15 km of the Hayward fault distributed along strike and in profiles perpendicular to the fault (Fig. 26.3). Creep along the Hayward fault allows the Bay block to slide past the East Bay Hills block with only minimal internal deformation and strain accumulation within either block. The BÄVÜ model allows us to quantify the exact creep rate and place relative displacement across the fault in a regional context to quantify strain accumulation. Figure 26.4 shows observed variations in creep rate along strike of the Hayward fault.

These variations reflect both the spatial distribution of strain accumulation and temporal variations in creep rate. This is highlighted by comparisons between the BÄVÜ GPS data and trilateration and triangulation collected by the US Geological Survey for the past several decades (grey lines in Fig. 26.4). Places where BÄVÜ deviates most from the long-term observations by the USGS are places where the USGS indeed shows different

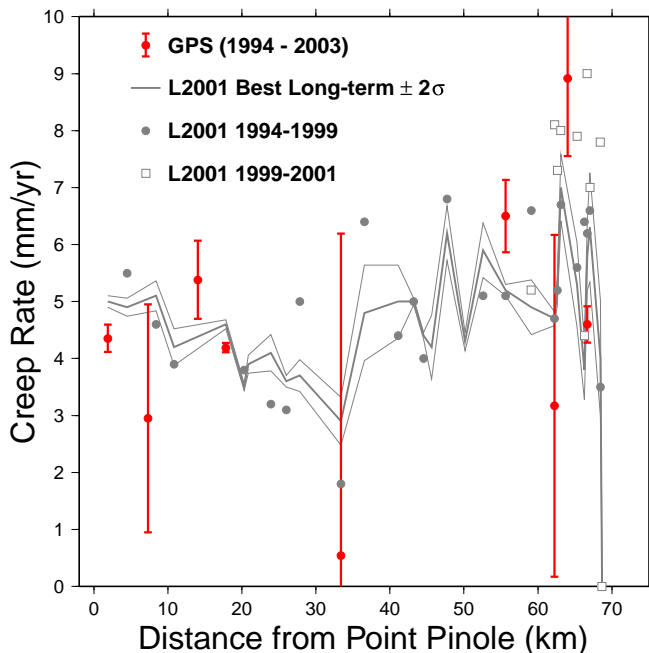


Figure 26.4: Variations in surface creep rate as a function of distance along strike of the Hayward fault. GPS data from the BÄVÜ model agree fairly well with the terrestrial geodetic results of Lienkaemper, 2001 ("L2001"). Note how the creep rate from L2001 is different for different time periods. Because BÄVÜ and L2001 cover slightly different time periods, some of the differences between the two results likely reflects actual temporal fluctuations in creep rate.

creep rates on shorter time scales (grey circles and open squares in Fig. 26.4). Observations from five to ten year periods (such as the nine-years covered in BÄVÜ) can deviate from longer-term observations by more than 2σ . These fluctuations in creep rate must therefore be considered when using observations from BÄVÜ to estimate long-term elastic strain accumulation and probabilistic earthquake magnitudes.

0.4 References

- Bürgmann, R., L. P. Segall, M. Lisowski, and J. Svarc, Postseismic strain following the 1989 Loma Prieta earthquake from GPS and leveling measurements, *J. Geophys. Res.*, 102(B3), 4933-4955, 1997.
- Lienkaemper, J.J., J.S. Galehouse, and R. W. Simpson, Long-term monitoring of creep rate along the Hayward fault and evidence for a lasting creep response to 1989 Loma Prieta earthquake, *Geophys. Res. Lett.*, 28 (11), 2265-2268, 2001.

Chapter 27

Crustal Deformation Along the Northern San Andreas Fault System

Mark H. Murray

0.1 Introduction

The San Andreas fault system in northern California includes three sub-parallel right-lateral faults: the San Andreas, Ma'acama, and Bartlett Springs. This northernmost segment is the youngest portion of the fault system, forming in the wake of the northwestwardly propagating Mendocino triple junction where the Pacific, North America, and Gorda (southern Juan de Fuca) plates meet. The Pacific plate moves about 35-40 mm/yr relative to central California across a broad ~ 100 -km zone in northern California. Additional deformation in eastern California and the Basin and Range province contribute to the total relative Pacific-North America motion of ~ 50 mm/yr. The San Andreas fault itself has been essentially aseismic and accumulating strain since it last ruptured in the great 1906 San Francisco earthquake, and no major earthquakes have occurred during the historical record on the more seismically active Ma'acama, and Bartlett Springs faults, which are northern extensions of the Hayward-Rodgers Creek and Calaveras-Concord-Green Valley faults in the San Francisco Bay area.

In *Frey Mueller et al.* (1999) we used GPS data collected in 1991-1995 along two profiles crossing the faults near Ukiah and Willits (Figure 27.1). GPS velocities from these profiles constrain the total deep slip rate on the San Andreas fault system to be $39.6^{+1.5}_{-0.6}$ mm/yr (68.6% confidence interval). Although deep slip rates on the individual faults are less well determined due to high correlations between estimated slip rates and locking depths, and between slip rates on adjacent faults, the slip rate on the Ma'acama fault ($13.9^{+4.1}_{-2.8}$ mm/yr) implies that it has now accumulated a slip deficit large enough to generate a magnitude 7 earthquake and therefore poses a significant seismic hazard.

In this renewed and ongoing study, we are resurveying

the original profiles and adding two new profiles to the north and south (Covelo and Healdsburg, respectively, in Figure 27.1). Most of the monuments were last observed in 1993 or 1995, so the new observations significantly improve the velocity estimates, and we expect they will improve models of average interseismic strain accumulation, including possible spatial variations along the fault system. These 10-station profiles every 50 km from Pt. Reyes to Cape Mendocino form a primary monitoring network for future observations to detect temporal variations in deformation. We plan to survey 40 additional stations in the southern portion of the network in Fall 2003 to provide better monitoring along the Rodgers Creek and Ma'acama faults.

0.2 Geodetic Measurements

The survey of the 4 primary profiles was conducted during January-March 2003 after verifying the benchmarks were still suitable for GPS observations, and picking or installing substitutes at the few that were not. Most of the stations were occupied for 6.5-8 hours on two different days. Some sites in the Central Valley or in the higher portions of the Coast Ranges that were not occupied due to weather or logistical considerations will be included in the Fall 2003 survey. Altogether, 43 site positions were measured during 94 session occupations, with the assistance of students and staff of the BSL.

We processed the data using GAMIT/GLOBK software using many of the same techniques used to process the BARD observations (*Murray and Segall*, 2001). These distributed processing methods allow the solutions to be combined in a self-consistent fashion with other solutions, such as for the BARD network, and for more global networks provided by the SOPAC analysis center, using Kalman filtering techniques, providing a well-defined velocity reference frame with respect to the stable North America. We are now reprocessing the older observations in GAMIT/GLOBK to tie all the northern California observations together in a self-consistent manner.

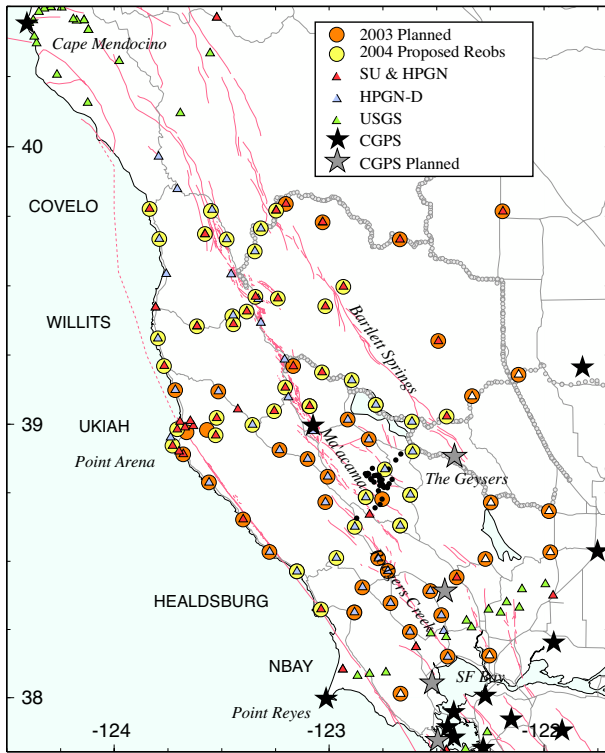


Figure 27.1: GPS sites along the northern San Andreas fault system. Light circles, sites that were observed in early 2003. Dark circles, stations with planned occupations in Fall 2003. Profile names are capitalized. USGS conduct surveys along the NBAY profile and near Cape Mendocino. Only one continuous GPS station (HOPB) currently operates in this region.

These data sets include Stanford surveys of the profiles, NGS surveys of the HPGN network, USGS surveys of the Covelo profile, and Caltrans surveys of the HPGN-Densification sites.

0.3 Deformation

Figure 27.2 shows site velocities for the 1994-2003 period relative to stable North America, as defined by a set of 20 fiducial stations. Most of the velocities were derived from data spanning 8-10 years, whereas those with the largest error ellipses include data from only a 4 year span (most of these stations will be reoccupied in Fall 2003). The easternmost stations exhibit motions typically associated with Sierran-Great Valley block (ORLA: 12.5 mm/yr NW). The westernmost sites are moving close to the Pacific plate rate (PTAR: 45.9 mm/yr NW). Fault-normal contraction is observed east of the Ma'acama fault, in the region of the Coast Ranges near the Central Valley where similar contraction has been observed elsewhere (e.g., Murray and Segall, 2001).

The North America reference frame used in this anal-

ysis is an improvement over the single-station approach used in the Freymueller *et al.* (1999) study, and allows us to apply angular velocity-fault backslip modeling techniques (e.g., Murray and Segall, 2001) to account for both far-field plate motions and interseismic strain accumulation. We are modifying a set of algorithms provided by Brendan Meade of MIT that sums backslip on rectangular dislocations to extend our simple 2D method to more complex, 3D fault systems (including subduction zones and extensional provinces). We are currently testing it on a variety of problems, such as the Adriatic region with M. Battaglia and R. Bürgmann, and it appears to be well suited to study the northern San Andreas fault system and its transition to the Cascadia subduction zone.

The velocity orientations do not closely follow the mapped traces of the faults in the northernmost section, as one might expect from pure elastic strain accumulation on the faults. We will assess whether this is a result of the Sierran-Great Valley block impinging on the San Andreas fault system, or a strain effect caused by the Mendocino fracture zone. We will determine realistic uncertainties of our strain accumulation models using the bootstrap techniques, and test methods for adding geologic and other information using Bayesian techniques to test whether the additional information can reduce the correlations and provide better resolution on other parameters. For example, the slip-rate and locking depth (10.5-22.6 mm/yr and 4.7-44.6 km, 95% confidence) on the San Andreas fault should be much better resolved by applying constraints derived from other seismic, geodetic, and paleoseismic observations.

0.4 Acknowledgements

We appreciate support for this project by the USGS NEHRP through grant numbers 02HQGR0064 and 03HQGR0074. We thank André Basset, Maurizio Battaglia, Dennise Templeton, and especially Todd Williams for assistance conducting the survey.

0.5 References

- Freymueller, J. T., M. H. Murray, P. Segall, and D. Castillo, Kinematics of the Pacific-North America plate boundary zone, northern California, *J. Geophys. Res.*, *104*, 7419-7442, 1999.
- Murray, M. H., and P. Segall, Modeling broadscale deformation in northern California and Nevada from plate motions and elastic strain accumulation, *Geophys. Res. Lett.*, *28*, 4315-4318, 2001.

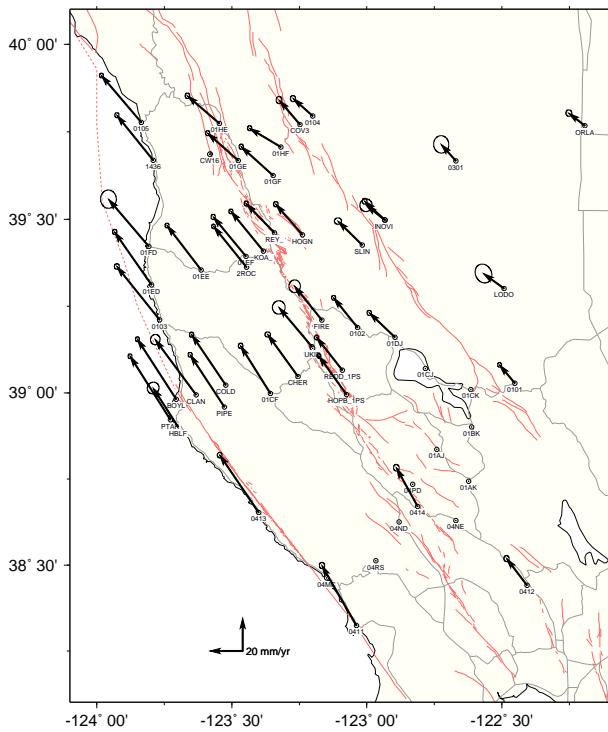


Figure 27.2: Velocities of sites in the Coast Ranges relative to North America, with 95% confidence regions assuming white-noise process only. Sites without velocities were observed in early 2003; data from their initial occupation in 1994 or 1999 is currently being processed.

Chapter 28

Surface Creep Measurements from a Slow Earthquake on the San Andreas Fault Using InSAR

Ingrid A. Johanson and Roland Bürgmann

0.1 Introduction

The ubiquity of slow earthquakes (SEQs) on faults (both dip-slip and strike-slip), suggests that they are a fundamental mode of strain release. The fact that they characteristically occur in the transition region between steadily slipping and locked faults may allow us to draw general conclusions about the mechanism by which faults transition between locked and creeping. To date, the San Andreas Fault near San Juan Bautista is the only location where slow earthquakes have occurred on an accessible strike-slip fault. The slip in these events was much closer to the surface than in the typical subduction zone events, making it a unique and potentially very effective location to study the mechanics of slow slip. Three slow earthquakes occurred along the SAF in 1992, 1996 and 1998; each with moment magnitude close to that of the largest seismic earthquakes in the area (M_w 5.5). In this report we focus on the 1998 SEQ, whose shallow depth (less than 5 km) and compact size of the slow earthquakes (relative to subduction zone SEQs), provides the opportunity to apply the high spatial resolution and good precision of InSAR to observing the deformation pattern of SEQs (Johanson and Bürgmann, 2002).

0.2 1998 SEQ

The 1998 M_w 5.0 slow earthquake was immediately preceded by the M_w 5.1 San Juan Bautista earthquake (Uhrhammer *et al.*, 1999) (Large blue circle in Fig. 28.1). The two events were located in the same region, with the slow earthquake rupturing the portion above 5km (Gwyther *et al.*, 2000). The earthquake and SEQ ruptures were of comparable size and resulted in similar

amounts of slip. An interferogram spanning from Aug. 18 1997 to Oct. 12 1998 contains adequate coherent data along the central San Andreas to observe near fault movement (Fig 28.2). The interferogram contains a sharp phase gradient aligned with the fault trace. If the range-change signal is attributed to purely strike-slip motion on the San Andreas Fault, then the interferogram indicates right-lateral slip of about the same amount observed by creepmeters. It is expected, however, that the measured range change will contain some vertical motion and may also contain atmospheric errors. We are working on incorporating ascending track frames and increasing the total number of available interferograms to account for these effects.

0.3 Near Field Fault Motion

Fig. 28.3 compares surface creep measurements made using InSAR to those from creepmeters. Red points were obtained by averaging phase values every 350 meters along strike and 50 meters away from each side of the fault. Pairs of average phase measurements were differenced and converted to San Andreas parallel strike-slip movement. Error bars are the standard deviations of values in each bin. Though the InSAR and creepmeter data match well, the InSAR data suggest that fault movement is much more variable than would be inferred from creepmeters alone. However, the variability may be the result of a poorly defined fault trace. Figure 28.3 also makes it apparent that the contribution of the slow earthquake to surface slip during the time spanned by the interferogram is small; the difference between the blue and green triangles. The contribution of interseismic creep must therefore be accounted for before slip is attributed to the SEQ. The variability in the InSAR data makes it a requirement that we use interseismic creep rates with similar spatial sampling. We are working on creating interferogram stacks using a patch-work method that will

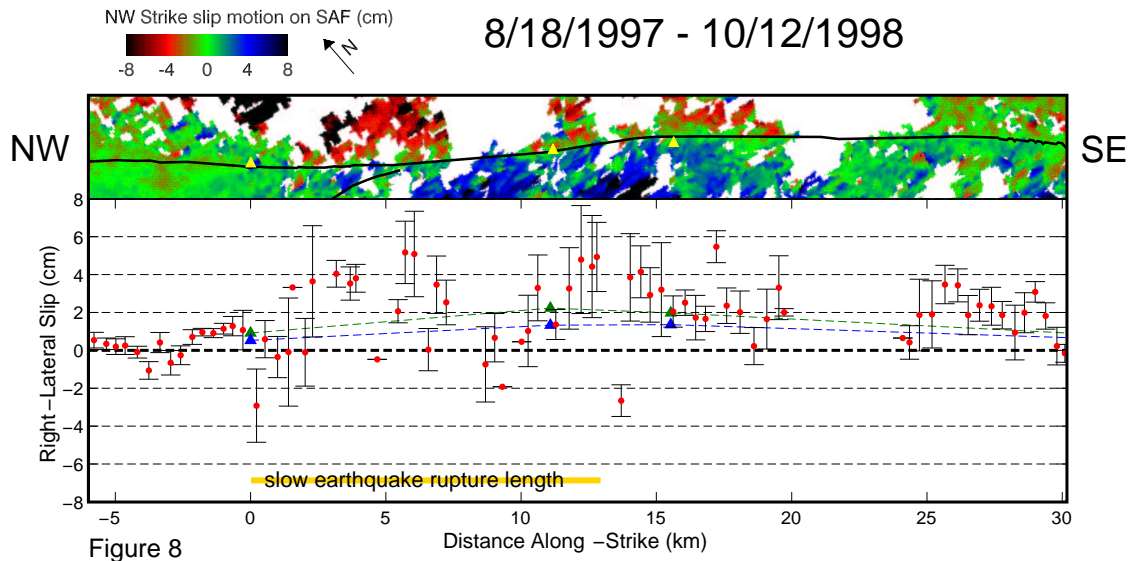


Figure 8

Figure 28.3: Comparison of near field motion measured using InSAR and creepmeters XSJ, XHR and CWN. Green triangles are the total amount of creep measured by creepmeters during the time span of the interferogram and includes secular creep, the 1998 slow earthquake and the San Juan Bautista earthquake. Blue triangles are the amount of creep expected without the 1998 slow earthquake or San Juan Bautista earthquake. The interferogram shown is a subset of Track 299 Frame 2861; its location is shown in Figure 28.1.

allow us to define average creep rates along the San Andreas.

0.4 Conclusions

InSAR is capable of measuring small scale movement such as creep. The interferogram shown here suggests that creep along the Central San Andreas varies considerably along strike. Future modelling of the fault system will benefit from the dense spatial sampling of InSAR. However, the contribution of the 1998 San Juan Bautista slow earthquake to the total range change is very subtle and will require careful removal of the interseismic signal.

0.5 References

Gwyther, R. L., C. H. Thurber, M. T. Gladwin, and M. Mee, Seismic and aseismic observations of the 12th August 1998 San Juan Bautista, California M5.3 earthquake, *3rd San Andreas Fault Conference*, Stanford University, 209-213, 2000

Johanson, I. A. and R. Bürgmann, An investigation of slow earthquakes on the San Andreas Fault using InSAR, *EOS Transactions, AGU*, 83(47), 357, 2002

Uhrhammer, R., L. S. Gee, M. H. Murray, D. Dreger and B. Romanowicz, The M_w 5.1 San Juan Bautista, California earthquake of 12 August 1998, *Seismological Research Letters*, 70(1), 1999.

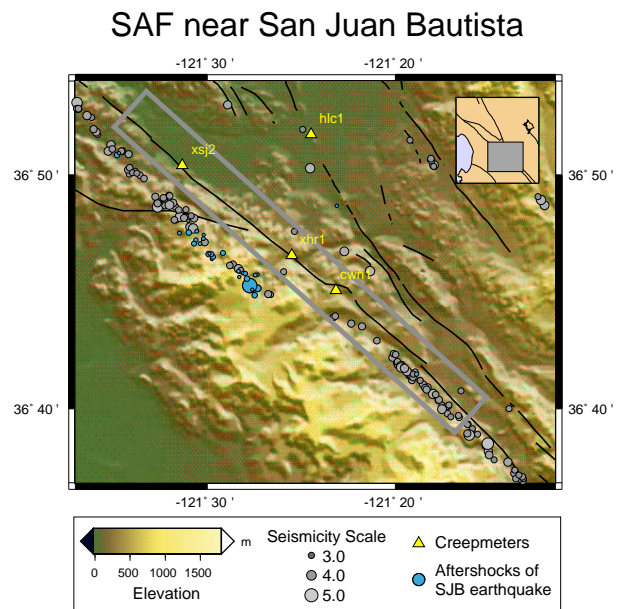
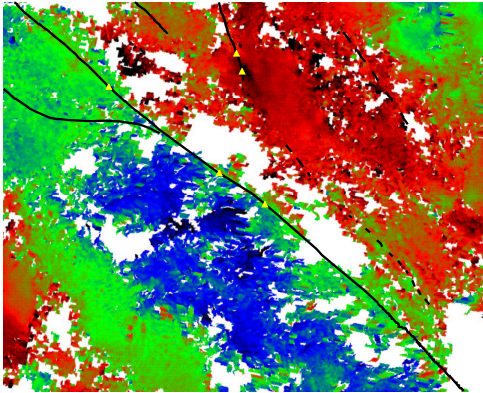


Figure 28.1: Location map of the Central San Andreas Fault showing local background seismicity and creepmeter locations. Also shown is the main and aftershocks of the 1998 San Juan Bautista earthquake (in blue). The grey box outlines the profile shown in Figure 28.3.

8/18/1997 - 10/12/1998



Time Span = 1.15 yrs
⊥ Baseline = 69 m

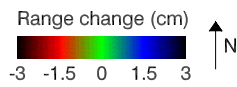


Figure 28.2: Subset of an interferogram from Track 299 Frame 2861 corresponding in area to the location map in figure 28.1. The interferogram contains significant topography correlated signal which are probably atmospheric errors. However, creep occurs on a scale much smaller than most atmospheric errors

Chapter 29

Evidence of Powerlaw Flow in the Mojave Mantle

Andrew Freed and Roland Bürgmann

0.1 Introduction

Laboratory experiments suggest that rocks in the lower crust and upper mantle (shallower than 200 km) should deform by dislocation creep, characterized by a strain rate proportional to stress raised to a power, n (e.g., Kirby and Kronenberg, 1987; Carter and Tsepp, 1987). Dislocation creep has not yet been confirmed by geodetic observations. We use GPS campaign and continuous time-series data associated with 1992 Landers and 1999 Hector Mine earthquakes to infer rheologic properties of the Mojave lithosphere in southern California. The coupled nature of these earthquakes (20 km and 7 years apart) makes them ideal for a stringent rheology study in that a candidate rheologic model must satisfy the postseismic observations associated with both events. To infer the nature of viscous flow we developed a finite element model of this earthquake sequence that simulates coseismic slip associated with both events (Wald and Heaton, 1994; Dreger and Kaverina, 2000), a regional background strain rate (Savage and Svarc, 1997), and temperature dependent powerlaw rheologies (Hirth et al., 2001; Kronenberg and Tullis, 1984; Shelton and Tullis, 1981; Jaoul et al., 1984; Hansen and Carter, 1982). We consider a range of powerlaws (for felsic and mafic, wet and dry rocks) reflecting uncertainty in the mineralogy of the lithosphere and in the extrapolation from laboratory to geologic conditions. Thermal gradients are constrained from surface heat flow measurements (Williams, 1996) and regional seismic velocities (Melbourne and Helmberger, 2001). For comparison purposes, we also consider models with a Newtonian (strain rate linearly proportional to stress) rheology.

0.2 Results

Our results show that the spatial and temporal evolution of transient surface deformation following the Landers and Hector Mine earthquakes can be successfully explained by powerlaw flow ($n = 3.5$), predominantly in a warm and wet upper mantle. These results are characterized by model and data comparisons shown in Figure 29.1. We can rule out Newtonian flow as a reasonable explanation of both the spatial and temporal patterns of postseismic transient motions, implying that the common assumption of Newtonian flow in numerical models of ductile deformation within the crust and upper mantle (e.g., Thatcher et al., 1980; Miyashita, 1987; Deng et al., 1998; Pollitz et al., 2001, 2002) may be invalid. These results suggest that recovery-controlled dislocation creep is the dominant mechanism of viscous flow following earthquakes. The model results also preclude significant flow in the lower crust, supporting the contention that, at least beneath the Mojave Desert, the mantle is the weaker region.

The stress dependence of powerlaw flow inferred by our calculations means that the viscosity of the upper mantle changes as a function of time after an earthquake. This has implications for models of regional stress changes and fault interaction. For example, the influence of earthquake induced stress changes on neighboring faults will evolve more rapidly early on, but will last many decades longer than would be inferred from a Newtonian model. Furthermore, as viscosities are lowest where stresses are highest, a powerlaw rheology leads to a more localized shear zone beneath faults where coseismic stresses are highest. For example, our calculations show that a Newtonian model of post-Landers relaxation leads to a broad, diffuse shear zone in the mantle beneath the Landers rupture zone about 250-300 km wide. In contrast, post-Landers relaxation of a powerlaw rheology leads to a relatively narrow shear zone 70-90 km wide, with much of the shear concentrated in a central zone only 15 km wide.

0.3 Acknowledgements

Funding provided by NSF grant #EAR 0207617

0.4 References

Carter, N. L. and M. C. Tsenn, Flow properties of continental lithosphere, *Tectonophysics*. 136, 27-63, 1987.

Deng, J., M. Gurnis, H. Kanamori, E. Hauksson, Viscoelastic flow in the lower crust after the 1992 Landers, California, earthquake, *Science* 282, 1689-1692, 1998.

Dreger, D. and A. Kaverina, Seismic remote sensing for the earthquake source process and near-source strong shaking; a case study of the October 16, 1999 Hector Mine earthquake, *Geophys. Res. Lett.*, 27, 1941-1944, 2000.

Hansen, F.D. and N.L. Carter, Creep of selected crustal rocks at 1000 MPa, *Trans. Amer. Geophys. Union* 63, 437, 1982.

Hirth, G., C. Teyssier, W. J. Dunlap, An evaluation of quartzite flow laws based on comparisons between experimentally and naturally deformed rocks, *Int. J. Earth Sci.* 90, 77-87, 2001.

Hudnut, K.W., N.E. King, J.G. Galetzka, K.F. Stark, J.A. Behr, A. Aspiotes, S. van-Wyk, R. Moffitt, S. Dockter, F. Wyatt, Continuous GPS observations of postseismic deformation following the 16 October 1999 Hector Mine, California, earthquake ($M_w = 7.1$), *Bull. Seismo. Soc. Amer.* 92, 1403-1422, 2002.

Jaoul, O., J. A. Tullis, A. K. Kronenberg, The effect of varying water contents on the creep behavior of Heavitree Quartzite, *J. Geophys. Res.* 89, 4298-4312, 1984.

Kirby, S.H. and A.K. Kronenberg, Rheology of the lithosphere; selected topics, *Rev. Geophys.* 25, 1219-1244, 1987.

Kronenberg, A. K. and J. A. Tullis, Flow strengths of quartz aggregates; grain size and pressure effects due to hydrolytic weakening, *J. Geophys. Res.* 89, 4281-4297, 1984.

Melbourne, T. and D. Helmberger, Mantle control of plate boundary deformation, *Geophys. Res. Lett.*, 28, 4003-4006, 2001.

Miyashita, K., A model of plate convergence in Southwest Japan, inferred from leveling data associated with the 1946 Nankaido earthquake, *J. Phys. Earth* 35, 449-467, 1987.

Pollitz, F.F., G. Peltzer, and R. Brügmann, Mobility of continental mantle; evidence from postseismic geodetic observations following the 1992 Landers earthquake, *J. Geophys. Res.*, 105, 8035-8054, 2000.

Pollitz, F.F., C. Wicks, and W. Thatcher, Mantle flow beneath a continental strike-slip fault; postseismic deformation after the 1999 Hector Mine earthquake, *Science* 293, 1814-1818, 2001.

Savage, J.C. and J.L. Svarc, Postseismic deformation associated with the 1992 $M (sub w) = 7.3$ Landers earth-

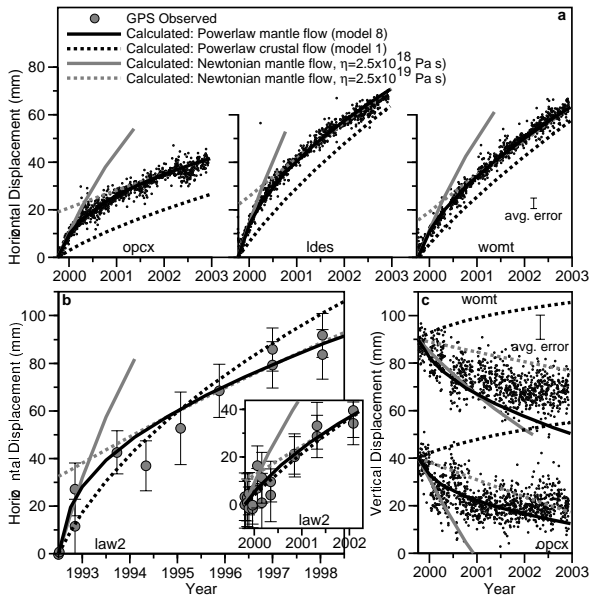


Figure 29.1: Comparison of representative observed and calculated postseismic displacement time-series following the 1992 Landers and 1999 Hector Mine earthquakes. (a) Horizontal displacements at 3 continuously monitored GPS stations following 1999 Hector Mine earthquake. (b) Horizontal displacements at campaign GPS station law2 following the 1992 Landers quake (22). Inset shows campaign data at station law2 following the Hector Mine quake. (c) Vertical motions at 2 continuously monitored stations following 1999 Hector Mine earthquake. Powerlaw mantle flow model (solid black curves) is a model of aplite and wet olivine. Powerlaw crustal model (dotted black curves) is a model of wet quartzite and dry olivine. Newtonian models consider purely mantle flow with low viscosity (2.5×10^{18} Pa s, solid grey curves) and an order of magnitude higher viscosity (dotted grey curves) that match early and late time-series slopes, respectively. Curves associated with the high viscosity Newtonian model have been raised to show where the slopes match the observed time-series. These results show that a powerlaw model of flow in the mantle can satisfy that time-series data, but not a model of lower crustal or Newtonian flow.

quake, Southern California, *J. Geophys. Res.*, *102*, 7565-7577, 1997.

Shelton, G. and J. A. Tullis, Experimental flow laws for crustal rocks, *Trans. Amer. Geophys. Union* *62*, 396, 1981.

Thatcher, W., T. Matsuda, T. Kato, and J. B. Rundle, Lithospheric loading by the 1896 Riku-u earthquake, northern Japan; implications for plate flexure and asthenospheric rheology *J. Geophys. Res.*, *85*, 6429-6435, 1980.

Wald, D.J. and T. H. Heaton, Spatial and temporal distribution of slip for the 1992 Landers, California, earthquake, *Bull. Seismol. Soc. Am.*, *84*, 668-691, 1994.

Williams, C.F., Temperature and the seismic/ aseismic transition; observations from the 1992 Landers earthquake, *Geophys. Res. Lett.*, *23*, 2029-2032, 1996.

Chapter 30

Intraplate Strain Accumulation in the New Madrid Seismic Zone

Mark H. Murray, Mark D. Zoback (Stanford University), Paul Segall (Stanford University)

0.1 Introduction

The New Madrid seismic zone (NMSZ) in the central United States is the most seismically active intraplate region in North America. It includes two SW-NE-trending zones of right-lateral strike-slip faulting on subvertical faults and a zone of thrust faulting on 30° SW-dipping plane at a left step-over between the strike-slip fault zones (Figure 30.1). Three widely felt magnitude ~7–8 earthquakes occurred in the ~250 km zone in the the winter of 1811–1812, and the central thrust zone was sufficiently displaced during the 7 February 1812 event to create a waterfall on the Mississippi river.

The NMSZ is located within a failed rift that was active about 600 million years ago, followed by period of magmatic reactivation and igneous intrusion of mafic plutons 80 to 60 million ago. These episodes of activity introduced heterogeneities into the crust that may act as stress concentrators for the late Holocene seismicity, possibly initiated by the most recent deglaciation event (*Grolimund and Zoback, 2001*). Paleoseismic evidence indicates that 1811–1812 sized events have occurred throughout the late Holocene, most recently around 1450 and 900 A.D., but the small cumulative fault offsets inferred from seismic reflection data suggest that the current high level of seismic activity initiated recently, and there is scant paleoseismic evidence for more than 4 episodes prior to the historic events.

Low rates of strain and the lack of apparent active surface tectonics suggest that the central and eastern U.S. are within the stable interior of the North America plate. Geodetic studies of broadscale deformation within this region generally find that relative station velocities are consistent (< 1 mm/yr) with a rigid plate with strain rates not significantly differing from zero. High strain rates (~100 nanostrain/yr) were reported within a network spanning the southern NMSZ based on a 1991 GPS

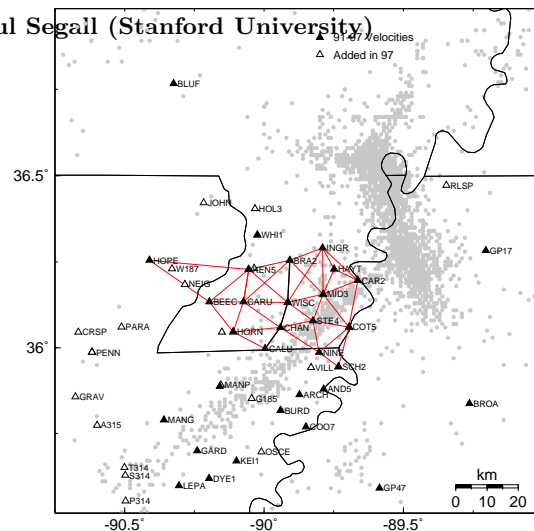


Figure 30.1: GPS and triangulation networks along the southern New Madrid seismic zone. Circles are earthquake epicenters. Solid triangles are sites occupied in the 1991, 1993, and 1997 surveys with estimated velocities. Open triangles are sites installed in the 1997 survey. Thin lines connecting some of the sites represent the triangulation network that was occupied in the 1950's. *Liu et al. [1992]* estimated uniform shear strain rates for the entire network, as well as the east and west portions divided by the bold line.

survey and triangulation data collected in the 1950's (*Liu et al., 1992*). We present new strain rate estimates within this southern NMSZ network from GPS surveys conducted in 1993 and 1997 that show the recent deformation rates are not significantly greater than zero.

0.2 Geodetic Measurements

The primary network consists of triangulation benchmarks installed in the mid-1950's that were reoccupied

using GPS in 1991 by NGS. Enough of the benchmarks had survived to allow 40-year averaged shear-strain rates to be estimated. This network was reoccupied by GPS in 1993 and 1997 and stations were added to better span the southern seismic zone and the western rift boundary (Figure 30.1).

We processed the data from the 3 GPS surveys using GAMIT/GLOBK software using many of the same techniques used to process the BARD observations (*Murray and Segall, 2001*). Definition of a self-consistent reference frame is complicated by major changes to the global fiducial network that occurred between the 1991 and 1993 surveys. To better define the velocity frame throughout this period, we included SOPAC global solutions obtained for 45 days, at 64-day intervals, between March 1991 and December 1998. These solutions provide sufficient observations to estimate the positions and velocities of the fiducial stations included in our NMSZ analysis during each interval between significant changes of the station equipment and reference monuments. We defined a North America frame by minimizing the horizontal velocities of 15 stations, which had an rms deviation of 3.5 mm in position and 0.5 mm/yr in velocity.

0.3 Deformation

The velocities of 32 sites in the NMSZ region are well determined with respect to the North America frame (Figure 30.2). The average horizontal velocity of the 32 stations relative to North America is 1.7 ± 0.8 mm/yr at $N8^\circ E$, which significantly differs from zero (all quoted uncertainties are 95% confidence). The apparent average northward motion is due primarily to stations located in the interior of the network, whereas the average motion of the outlying stations (BLUF, HOPE, GP47, BROA, GP17) is 1.0 ± 1.4 mm/yr, $N10^\circ E$, consistent with their being on stable North America.

We estimated strain rates using 1950's triangulation data to compare with the *Liu et al. (1992)* results. Because triangulation data are relatively insensitive to distances and the scale of the network, we estimated engineering shear strain rates, $\dot{\gamma}_1 = \dot{\epsilon}_{EE} - \dot{\epsilon}_{NN}$ and $\dot{\gamma}_2 = \dot{\epsilon}_{EN} + \dot{\epsilon}_{NE}$, from which the maximum shear-strain rate $\dot{\gamma}$ and direction of maximum contraction can be derived. *Liu et al. (1992)* found that shear-strain rates in a 22-station network (Figure 30.1) were significantly greater than zero, particularly in the western half of the network that spans the rift boundary, with $\dot{\gamma} = 248 \pm 140$ nanoradian/yr. Using the same stations, but including GPS data from all 3 years, we find the estimated shear strain rates in all cases do not significantly differ from zero. For example, $\dot{\gamma}$ using all or just the western stations is 64 ± 68 or 134 ± 140 nanoradian/yr, respectively. Therefore, in contrast to the 1992 study, we find no evidence for high strain rates in the southern New Madrid seismic zone.

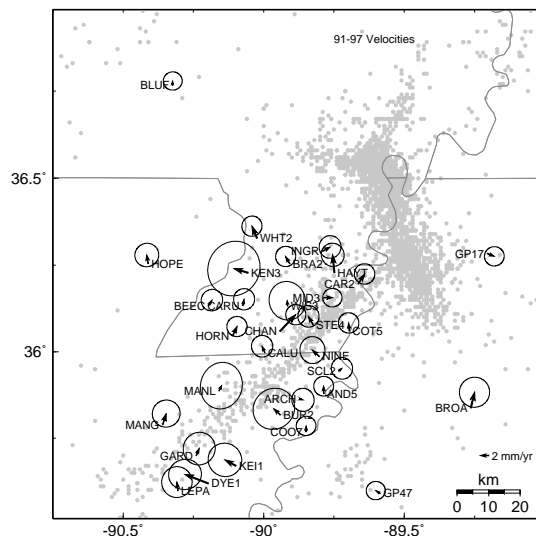


Figure 30.2: Velocity of stations relative to stable North America estimated from the 1991, 1993, and 1997 surveys. The error ellipses represent 95% confidence regions that assume formal errors scaled by the misfit scatter plus $2 \text{ mm yr}^{-1/2}$ random walk to account for possible benchmark instability, which could be significant for the shallowly anchored benchmarks in 500-m deep Mississippi embayment sediments.

The average motion of the interior stations relative to the outlying stations is 1.0 ± 0.6 mm/yr, $N6^\circ E$, with the most central stations tending to have velocities slightly elevated above this level. The spatial coherence of this pattern suggests that some deformation—albeit marginally significant—may be present in the region. Projecting the average motion onto the $N45^\circ E$ seismic trend yields 0.7 parallel and -0.6 mm/yr perpendicular components, which is opposite of that predicted by simple elastic strain dislocation models that assume zero far-field deformation and backslip on the faults defined by seismic and paleoseismic studies. We are currently investigating alternative explanations for this tantalizing signal, such as from a gravitational instability of the underlying rift pillow (*Pollitz et al., 2002*), or from the relaxation of a weakened lower crustal zone proposed by *Kenner and Segall (2000)*. This latter model, which predicts low rates of strain consistent with our geodetic observations, shows that low strain rates do not necessarily preclude the possibility of repeating large intraplate earthquakes, and that the seismic hazards in the NMSZ are still likely to be high.

0.4 Acknowledgements

We appreciate previous support for this project by the NSF. We thank Stacy Kerkela, Stephanie Prejean, and the staff and students of CERI in Memphis, Tennessee

for assistance conducting the 1997 survey.

0.5 References

Grollmund, B., and M. D. Zoback, Did deglaciation trigger intraplate seismicity in the New Madrid seismic zone?, *Geology*, 29, 175-178, 2001.

Kenner, S. J., and P. Segall, A mechanical model for intraplate earthquakes: Application to the New Madrid seismic zone, *Science*, 289, 2329-2332, 2000.

Liu, L. B., M. D. Zoback, and P. Segall, Rapid intraplate strain accumulation in the New Madrid seismic zone, *Science*, 257, 1666-1669, 1992.

Murray, M. H., and P. Segall, Modeling broadscale deformation in northern California and Nevada from plate motions and elastic strain accumulation, *Geophys. Res. Lett.*, 28, 4315-4318, 2001.

Pollitz, F. F., L. Kellogg, and R. Bürgmann, Sinking mafic body in a reactivated lower crust: A mechanism for stress concentration in the New Madrid Seismic Zone, *Bull. Seismol. Soc. Am.*, 91, 1882-1897, 2002.

Chapter 31

The Adriatic Region: An Independent Microplate within the Africa-Eurasia Collision Zone

Maurizio Battaglia, Mark H. Murray and Roland Bürgmann

model of regional deformation. This approach incorporates the secular velocities from GPS, fault geometry estimates and elastic-strain accumulation, making possible to determine how different tectonic hypothesis are compatible with geodetic data.

0.1 Introduction

In this study we use surface velocities recorded by GPS measurements and block modeling to investigate the active deformation of the Adriatic region, a component of the zone of distributed deformation between the African and Eurasian plates. The region includes the relatively stable Adriatic area (Po Valley, Adriatic Sea and Apulia), surrounded on the eastern, northern and western margins by a mountain belt which includes the Albanides, the Dinarides, the Alps and the Apennines. The southern margin of the Adriatic region, representing the boundary with the African plate, is still undefined. This study was prompted by a need to resolve the uncertainty surrounding the tectonic representation of this area, alternatively viewed as a promontory of North Africa or as a microplate within the Africa-Eurasia plate boundary.

The absence or low level of seismic activity in the Adriatic Sea indicates that its behavior is that of a relatively rigid plate within a deforming region. The bulk motion of the plate can be described as rigid rotation about an Euler pole in North Italy. Fault plane solutions suggest that the motions at the boundaries of the Adriatic area may not reflect directly Africa-Eurasia convergence. Some authors question the existence of an independent Adriatic plate, suggesting that a counterclockwise rotation of the Adriatic block, driven by impingement of the Africa plate against the Calabrian Arc, may explain the major tectonic events in the region, such as the opening of the Tyrrhenian basin, the evolution of the Apenninic-Maghrebian chain, the extension in the northern Ionian basin, and the shortening process along the Alps-Dinarides-Ellepidonides. On order to test the competing tectonic models proposed, we plan to develop a block

0.2 Deformation Velocities

We employ publicly available GPS observations made at 30 stations of the European Reference Permanent Network (EUREF) and the Italian Space Agency (ASI) continuous GPS networks to estimate deformation in the Adriatic region (Figure 31.1). We analyze the data using the GAMIT/GLOBK software in a three step approach described by (*McCluski et al*, 2000). To improve the realization of a stable reference frame for the velocity solution, additional sites from the International GPS Service (IGS) and EUREF networks are included through the publicly available global regional loosely constrained solutions performed by the Scripps Orbit and Permanent Array Center (SOPAC). Given the small velocities (from 2 to 5 mm/yr) recorded along the Italian peninsula, the choice of the appropriate definition of a stable Eurasian frame of reference may be critical.

The velocities shown in Figure 1 are referenced to the stable Eurasian frame, based on 15 stable sites in Europe and Asia (*McCluski et al*, 2000). All together, our solution includes data spanning 4 years from 138 stations, including 45 in the Mediterranean area. We incorporate 50 additional sites from publicly available solutions (*McCluski et al*, 2000) to resolve the deformation in the Eastern Mediterranean and Caucasus. To better assess the real uncertainties of the GPS solutions, we scale the covariances of the daily and monthly average to be consistent with the internal residual scatter of their combinations (i.e., chi-square statistics are approximately 1). These scalings do not compensate for systematic reference frame biases, possible non-Gaussian errors or pos-

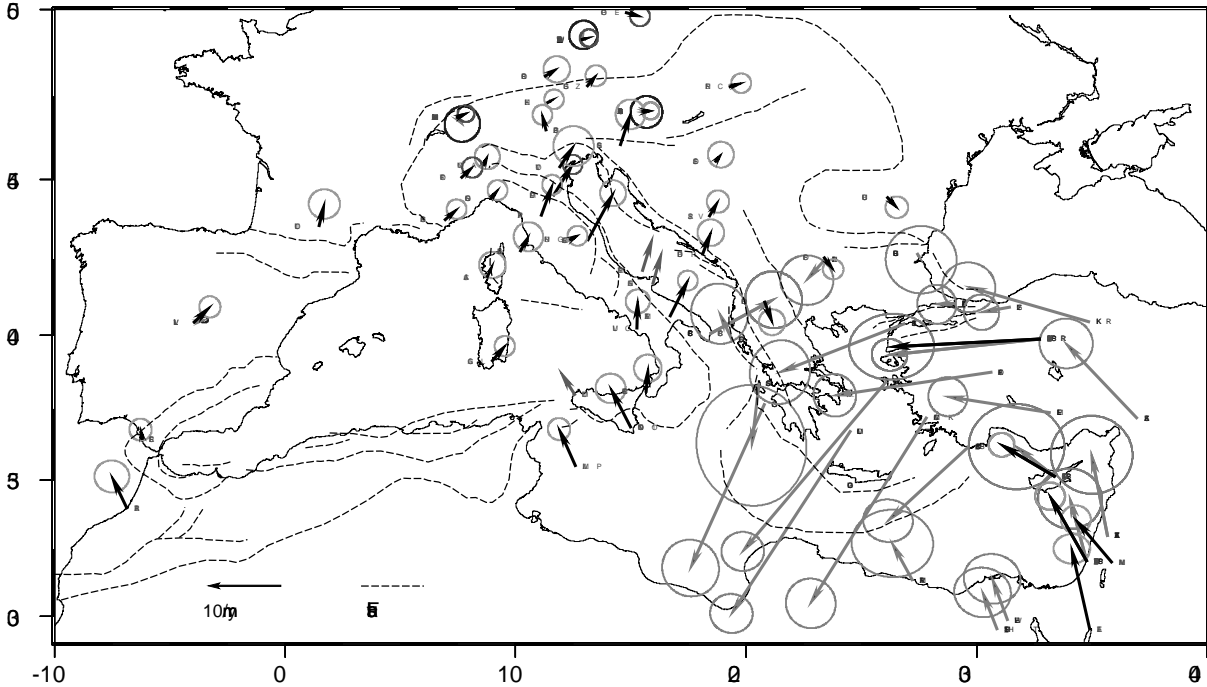


Figure 31.1: GPS horizontal velocities and their 95% confidence ellipses in a Eurasia-fixed reference frame for the period 1999-2002. Black arrows: velocities from this study. Gray arrows: publicly available velocities (McCluski et al., 2000). Dark gray arrows: velocities by E. Serpelloni (INGV, personal communication)

sible correlations between solutions. Monthly combinations of daily solutions, which tests suggest have white-noise characteristics, provide sufficient observations to obtain robust chi-square statistics on the residuals about the linear trends to properly weight the velocities. We compute velocity solutions using the monthly combinations, and scale the formal errors by the square root of chi-square of the solution. We allow a random walk of 1 mm/yr to take into account possible monument instability.

The active deformation in the Adriatic region (Figure 31.1) is highly variable with velocities decreasing from south (~ 5 mm/yr) to north (~ 2 mm/yr). Preliminary motion estimates (1999-2002) for stations located on the northern edge of the African plate (RABT, LAMP, NOTO, MATR, HELW and MEST) show a north-westward motion (N 23 ± 2 W) at 6 ± 1 mm/yr. Sites in Corsica (AJAC) and North-western Italy (ELBA, GENO, TORI, NOVA, UNPG) show no significant deformation, while the stations on the Italian peninsula close to the Adriatic sea (VOLT, VENE, CAME, TREM, ANGE, MATE, SPEC) are characterized by a north-eastward motion (N 29 ± 3 E) at 5 ± 1 mm/yr. Stations located on the eastern edge of the Adriatic Sea (GSR1, DUBR, SRJV) move in the same direction (N 23 ± 7 E) at a somewhat slower rate (3 ± 1 mm/yr). The northward displacement (N 3 ± 4 E at 3 ± 1 mm/yr) of sites in the

southern Italian peninsula (TGRC, VLUC) may reflect a transition between the African plate and the Adriatic region.

0.3 Acknowledgements

This work has been partially funded by the Istituto Nazionale di Oceanografia e Geofisica Sperimentale (OGS), Udine, Italy.

0.4 References

McCluski et al., Global Positioning Constraints on plate kinematics and dynamics in the eastern Mediterranean and Caucasus, *J. Geophys. Res.*, 105, 5695, 2000.

Chapter 32

Global Waveform Tomography with Spectral Element Method

Yann Capdeville, Barbara Romanowicz, Yuang-Cheng Gung

0.1 Introduction and Research Objectives

Because seismogram waveforms contain much more information on the earth structure than body wave time arrivals or surface wave phase velocities, inversion of complete time-domain seismograms should allow much better resolution in global tomography. In order to achieve this, accurate methods for the calculation of forward propagation of waves in a 3D earth need to be utilized, which presents theoretical as well as computational challenges.

In the past 8 years, we have developed several global 3D S velocity models based on long period waveform data, and a normal mode asymptotic perturbation formalism (NACT, *Li and Romanowicz, 1996*). While this approach is relatively accessible from the computational point of view, it relies on the assumption of smooth heterogeneity in a single scattering framework. Recently, the introduction of the spectral element method (SEM) has been a major step forward in the computation of seismic waveforms in a global 3D earth with no restrictions on the size of heterogeneities (*Chaljub, 2003*). While this method is computationally heavy when the goal is to compute large numbers of seismograms down to typical body wave periods (1-10 sec), it is much more accessible when restricted to low frequencies ($T > 150\text{sec}$). When coupled with normal modes (e.g. *Capdeville et al., 2000*), the numerical computation can be restricted to a spherical shell within which heterogeneity is considered, further reducing the computational time.

Here, we present a tomographic method based on the non linear least square inversion of time domain seismograms using the coupled method of spectral elements and modal solution. SEM/modes are used for both the forward modeling and to compute partial derivatives. The parameterization of the model is also based on the spec-

tral element mesh, the "cubed sphere", which leads to a 3D local polynomial parameterization. This parameterization, combined with the excellent earth coverage resulting from the full 3D theory used for the forward modeling, leads to a very stable inversion scheme. Synthetic tests show that, with a limited number of events (between 50 and 100), using long period records ($>150\text{s}$) and representative background seismic noise, it is possible to recover both amplitude and phase of the earth model with high accuracy.

0.2 Method

Our aim is to find the "best" Earth model that explain our seismic data set. Let assume we wish to solve the inverse problem with a classical least square inversion with a complete modeling theory that is the Spectral Element Method (SEM) applied to the wave equation. Classical inversion processes require to compute the partial derivative matrix

$$\mathbf{A} = \left[\frac{\partial \mathbf{f}(\mathbf{x})}{\partial \mathbf{x}} \right]_{\mathbf{x}}. \quad (32.1)$$

where \mathbf{x} the set of parameters which describe the model, and \mathbf{f} is the "function" that produce a synthetic data set \mathbf{d} for a given set of model parameters \mathbf{x} .

In most of the classical tomographic methods, the forward problem is solved using the Born approximation within the normal modes framework which leads to a linear relation between the set of parameters and the synthetic data, and this relation matrix is \mathbf{A} . Our case is different since there is no way to compute directly the partial derivative matrix or kernel with the SEM but using brute force with a finite differences formula:

$$\left[\frac{\partial \mathbf{f}(\mathbf{x})}{\partial \mathbf{x}} \right]_{\mathbf{x}=\mathbf{x}_0} \simeq \frac{\mathbf{f}(\mathbf{x}_0 + \delta \mathbf{x}) - \mathbf{f}(\mathbf{x}_0)}{\delta \mathbf{x}}. \quad (32.2)$$

Therefore, in order to compute the partial derivative matrix, one need to compute the whole data set, that is as many runs as the number of sources, for each parameter of the model. This will be obviously the most expensive

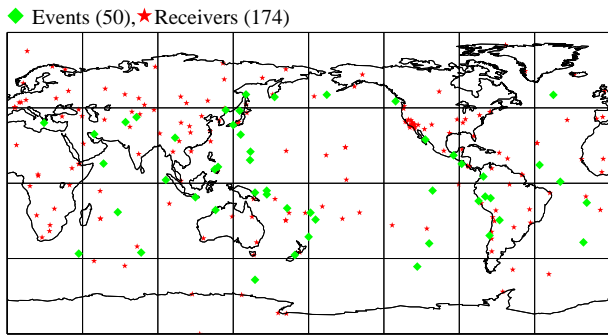


Figure 32.1: Distribution of the sources and stations used in this experiment.

part of the inversion. An estimation of the computing time shows that computing the partial derivative matrix might takes years, even on large computers.

Here we used a scheme that reduce the computation by a factor equal to the number of sources and make the process possible within a reasonable amount of time.

We now show a synthetic inversion to test the scheme. The “data” are produced with the SEM in a known model that we try to retrieve. The source-receiver distribution is shown on Figure 32.1. The parameterization used here to describe the model is based of the spectral element mesh. We use here a mesh roughly equivalent to a degree 8 in spherical harmonics as shown on Figure 32.3 . We show results of the 2 first iterations of the inversion on Figure 32.2. The model is represented in a linear way: the velocity contrast are shown as a function of the parameter number. It is sorted such that the left part is the lower mantle and the right part is the upper mantle. The residual between the wanted model an the obtained model shows an excellent agreement.

A description of the coupled method with illustrations can be found on <http://www.seismo.berkeley.edu/~yann>

0.3 Acknowledgements

Most of the computation were made using the computational resources of the NERSC, especially the IBM SP, under repo mp342.

0.4 References

Capdeville, Y., B. Romanowicz and A. To (2003). Coupling Spectral Elements and Modes in a spherical earth: an extension to the “sandwich” case. *Geophys. J. Int.* Vol 154, pp 44-57

Chaljub, E. Capdeville, Y. and Vilotte, J.P. (2003) Solving elastodynamics in a solid heterogeneous 3D-sphere: a parallel spectral element approximation on non-conforming grids. *J. Comp Phy.* Vol. 183 pp. 457-

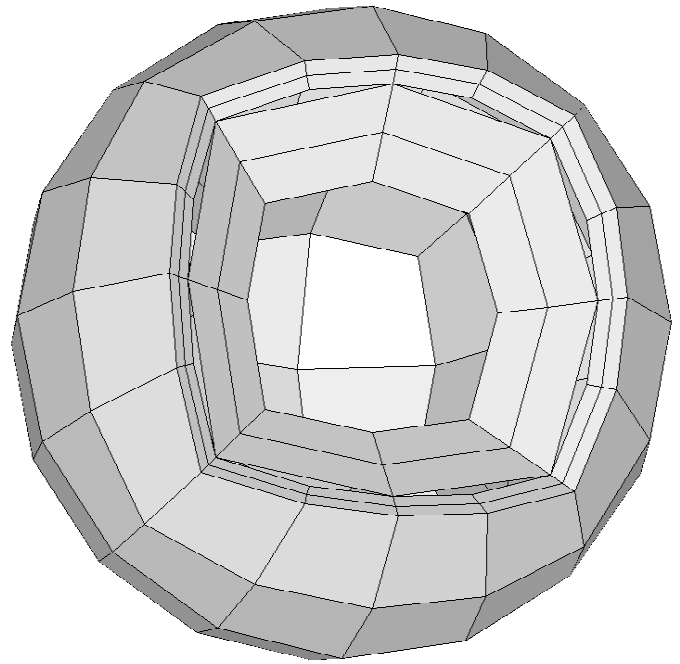


Figure 32.2: Mesh used for the parameterization of the experiment

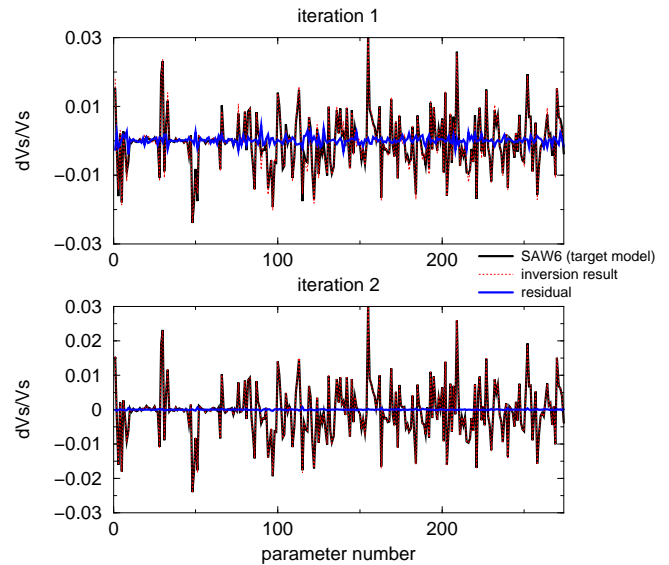


Figure 32.3: Synthetic inversion model results of the two first iterations in a linear representation (see text). The residual between the wanted model an the obtained model shows an excellent agreement

Capdeville Y., E. Chaljub, J.P. Vilotte and J.P. Montagner (2003). Coupling the Spectral Element Method with a modal solution for Elastic Wave Propagation in Global Earth Models. *Geophys. J. Int.*, Vol 152, pp 34–66

Capdeville Y., C. Larmat, J.P. Vilotte and J.P. Montagner (2002) Numerical simulation of the scattering induced by a localized plume-like anomaly using a coupled spectral element and modal solution method. *Geoph. Res. Lett.* VOL. 29, No. 9, 10.1029/2001GL013747

Capdeville Y., E. Stutzmann and J. P. Montagner (2000). Effect of a plume on long period surface waves computed with normal modes coupling. *Phys. Earth Planet. Inter.*, Vol 119 pp. 57–74.

Li, X. B. and Romanowicz, B. (1996) . Global mantle shear velocity model developed using nonlinear asymptotic coupling theory *J. Geophys. Res.* Vol 101, pp 11,245–22,271.

Chapter 33

Global Anisotropy and the Thickness of Continents

Yuancheng Gung, Mark Panning and Barbara Romanowicz

0.1 Introduction

For decades there has been a vigorous debate about the depth extent of continental roots (*Jordan, 1975*) The analysis of heat flow (*Jaupart et al., 1998*), mantle xenoliths (*Rudnick et al., 1998*) and electrical conductivity (*Hirth, 2000*) indicate that the coherent, conductive part of continental roots is not much thicker than 200-250 km. Some global seismic tomographic models agree with this estimate but others indicate much thicker zone of fast velocities under continental shields, reaching at least 400km in depth. This is manifested by a drop in correlation between some models from ~ 0.80 at 100km to less than 0.45 at 300 km depth (Figure 33.1a), which casts some doubt on the ability of global tomography to accurately resolve upper mantle structure.

However, although global V_S models differ from each other significantly in the depth range 200-400km under the main continental shields, these differences are consistent when they are classified into three categories, depending on the type of data used to derive them: *SV* (mostly vertical or longitudinal component data, dominated by Rayleigh waves in the upper mantle), *SH* (mostly transverse component data, dominated by Love waves), and (3)*hybrid* (three component data). *SH* and *hybrid* models are better correlated with each other than with *SV* models. This difference is accentuated when the correlation is computed only across continental areas, as shown in Figure 33.1b. The reduced correlation in the depth range 250-400 km between *SH* and *hybrid* models and *SV* models is strongly accentuated over continents.

On the other hand, global tomographic studies that account for seismic anisotropy, either by inverting three component data for V_{SV} and V_{SH} using isotropic kernels (*Ekström and Dziewonski, 1998*), or in the framework of more general anisotropic theory (*Montagner and Tani-moto, 1991*), have documented significant lateral varia-

tions in the anisotropic parameter $\xi (= (V_{SH}/V_{SV})^2)$ on the global scale. Until now, attention has mostly focused on the strong positive $\delta \ln \xi (= 2(\delta \ln V_{SH} - \delta \ln V_{SV}))$ observed in the central part of the Pacific Ocean in the depth range 80-200 km. The presence of this anisotropy has been related to shear flow in the asthenosphere, with a significant horizontal component. Deeper anisotropy was suggested, but not well resolved in these studies, either because the dataset was limited to fundamental mode surface waves, or because of the use of inaccurate depth sensitivity kernels. In particular, it is important to verify that any differences in V_{SV} and V_{SH} observed below 200km depth are not an artifact of simplified theoretical assumptions, which ignore the influence of radial anisotropy on depth sensitivity kernels.

0.2 Results

We have developed an inversion procedure for transverse isotropy using three component surface and body waveform data, in the framework of normal mode asymptotic coupling theory (*Li and Romanowicz, 1995*), which in particular, involves the use of 2D broadband anisotropic sensitivity kernels appropriate for higher modes and body waves.

Figure 33.2 shows the distributions of $\delta \ln \xi$ in the resulting degree 16 anisotropic model *SAW16AN*. At 175 km depth, the global distribution of $\delta \ln \xi$ confirms features found in previous studies, and is dominated by the striking positive $\delta \ln \xi > 0$ ($V_{SH} > V_{SV}$) anomaly in the central Pacific and a similar one in the Indian Ocean. However, at depths greater than 250 km, the character of the distribution changes: positive $\delta \ln \xi$ emerges under the Canadian Shield, Siberian Platform, Baltic Shield, southern Africa, Amazonian and Australian cratons, while the positive $\delta \ln \xi$ fades out under the Pacific and Indian oceans. At 300 km depth, the roots of most cratons are characterized by positive $\delta \ln \xi$, which extend down to about 400 km. These features are emphasized in depth cross sections across major continental shields (Figure 33.3), where we compare V_{SH} and V_{SV} distri-

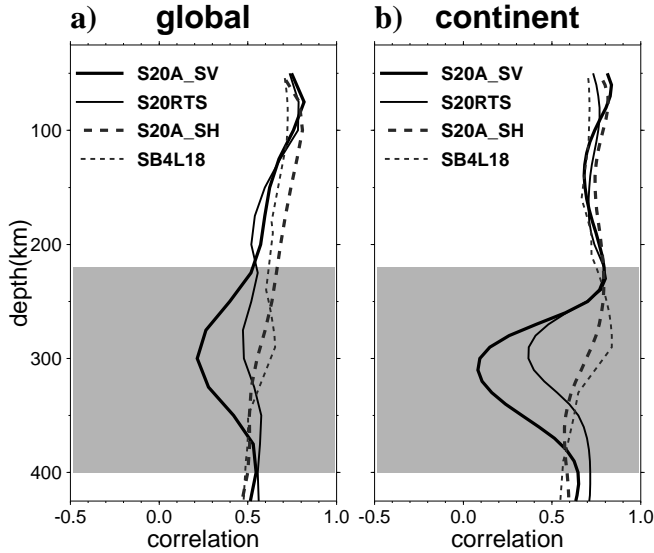


Figure 33.1: Correlation coefficient as a function of depth between model *SAW24B16* (Mégnin and Romanowicz, 1999), an *SH* model, and other global tomographic *S* velocity models. (a) over the whole globe; (b) over continental areas only. *S20ASH* (Ekström and Dziewonski, 1998) is an *SH* model, *SB 4L18* (Masters et al., 1996) is a hybrid model and *S20ASV* (Ekström and Dziewonski, 1998) and *S20RTS* (Ritsema et al., 1999) are both *SV* models.

butions, consistently showing deeper continental roots in V_{SH} . Interestingly, the East Pacific Rise has a signature with $\delta \ln \xi < 0$ down to 300km, indicative of a significant component of vertical flow. At 400km depth, we also note the negative $\delta \ln \xi$ around the Pacific ring, consistent with quasi-vertical flow in the subduction zone regions in the western Pacific and south America.

0.3 Discussions

Temperatures in the 250-400 km depth range exceed 1000°C , and are therefore too high to allow sustained frozen anisotropy in a mechanically coherent lithospheric lid on geologically relevant time scales (Vinnik et al., 1992). Therefore we infer that the $V_{SH} > V_{SV}$ anisotropy under continental roots we describe here must be related to present day flow-induced shear, with a significant horizontal component.

We note the similarity of the character of $V_{SH} > V_{SV}$ anisotropy, in the depth range 200-400km under cratons, and 80-200km under ocean basins, and we suggest that both are related to shear in the asthenosphere, the difference in depth simply reflecting the varying depth of the asthenospheric channel. Although our inference is indirect, it reconciles tomographic studies with other geophysical observations of lithospheric thickness based on

heat flow, xenoliths and mantle electrical conductivity.

Another contentious issue is the nature of the Lehmann discontinuity (L), and in particular the puzzling observation that it is not a consistent global feature, but is observed primarily in stable continental areas and not under oceans (Gu et al., 2001). Since the $V_{SH} > V_{SV}$ anisotropy under continental cratons is found deeper than 200 km, we propose that L actually marks the top of the asthenospheric layer, a transition from weak anisotropic lowermost continental lithosphere to anisotropic asthenosphere. Under oceans, the lithosphere is much thinner, and the lithosphere/asthenosphere boundary occurs at much shallower depths. There is no consistently observed discontinuity around 200-250 km depth. On the other hand, a shallower discontinuity, the Gutenberg discontinuity (G), is often reported under oceans and appears as a negative impedance reflector (Revenaugh and Jordan, 1991). The difference in depth of the observed $\delta \ln \xi > 0$ anisotropy between continents and oceans is consistent with an interpretation of L and G as both marking the bottom of the mechanically coherent lithosphere, in areas where it is quasi-horizontal (Figure 33.4).

0.4 Conclusion

Thus, the inspection of radial anisotropy in the depth range 200-400 km allows us to infer that continental roots do not extend much beyond 250km depth, in agreement with other geophysical observations. The part of the mantle under old continents that translates coherently with plate motions need not be thicker than 200-250km. Tomographic models reveal the varying depth of the top of the anisotropic asthenospheric channel, marked by a detectable seismic discontinuity called L under continents (about 200-250km depth), and G under oceans (about 60-80km depth). Finally, seemingly incompatible tomographic models obtained by different researchers can thus also be reconciled: the relatively poor correlation between different models in the depth range 250-400 km is not due to a lack of resolution of the tomographic approach, but rather to the different sensitivity to anisotropy of different types of data.

0.5 Acknowledgements

We thank the National Science Foundation for support of this research.

0.6 References

- Ekström, G., and A.M. Dziewonski, The unique anisotropy of the Pacific upper mantle, *Nature*, 394, 168-171, 1998.
- Gu, Y., A.M. Dziewonski, W.-j. Su, and G. Ekström, Models of the mantle shear velocity and discontinuities in

the pattern of lateral heterogeneities, *J. Geophys. Res.*, *106*, 11,169-11,200, 2001.

Gung, Y., M. Panning and B. Romanowicz, Global anisotropy and the thickness of continents, *Nature*, *422*, 707-711 2003.

Jordan, T.H., The continental lithosphere, *Rev. Geoph. Space Phys.*, *13*, 1-12, 1975.

Hirth, G., Evans, R.L. and Chave A. D. Comparison of continental and oceanic mantle electrical conductivity: Is the Archean lithosphere dry?, *Geochem. Geophys. Geosyst.*, *1*, 2000GC000048, 2000.

Jaupart, C., Mareschal, J.C. and Guillou-Frottier, L., Heat flow and thickness of the lithosphere in the Canadian Shield, *J. Geophys. Res.*, *103*, 15,269-15,286, 1998.

Li, X.-D. and B. Romanowicz, Comparison of global waveform inversions with and without considering cross-branch modal coupling, *Geophys. J. Int.*, *121*, 695-709, 1995.

Masters, G., S. Johnson, G. Laske, and H. Bolton, A shear-velocity model of the mantle, *Phil. Trans. R. Soc. London*, *354* 1,385-1,410, 1996.

Mégnin, C., and B. Romanowicz, The 3D shear velocity structure of the mantle from the inversion of body, surface and higher mode waveforms, *Geophys. J. Int.*, *143*, 709-728, 2000.

Montagner, J.P., and T. Tanimoto, Global upper mantle tomography of seismic velocities and anisotropies, *J. Geophys. Res.*, *96*, 20,337-20,351, 1991.

Revenaugh, J. and Jordan, T.H., Mantle layering from ScS reverberations, 3. The upper mantle, *J. Geophys. Res.*, *96*, 19781-19810, 1991.

Ritsema, J., van Heijst, H. and Woodhouse, J. H., Complex shear wave velocity structure imaged beneath Africa and Iceland, *Science*, *286*, 1925-1928, 1999.

Rudnick, R., McDonough, W. and O'Connell, R. Thermal structure, thickness and composition of continental lithosphere, *Chem. Geol.*, *145*, 395-411, 1998.

Vinnik, L.P., Makeyeva, L.I., Milev, A. and Usenko, Y., Global patterns of azimuthal anisotropy and deformations in the continental mantle, *Geophys. J. Int.*, *111*, 433-447, 1992.

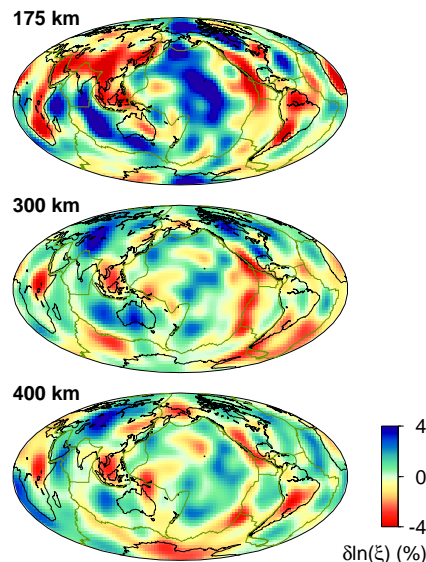


Figure 33.2: Maps of relative lateral variations in ξ of model *SAW16AN* at 3 depths in the upper mantle. Lateral variations are referred to reference model *PREM*, which is isotropic below 220km depth, but has significant $\delta \ln \xi > 0$ at 175km depth.

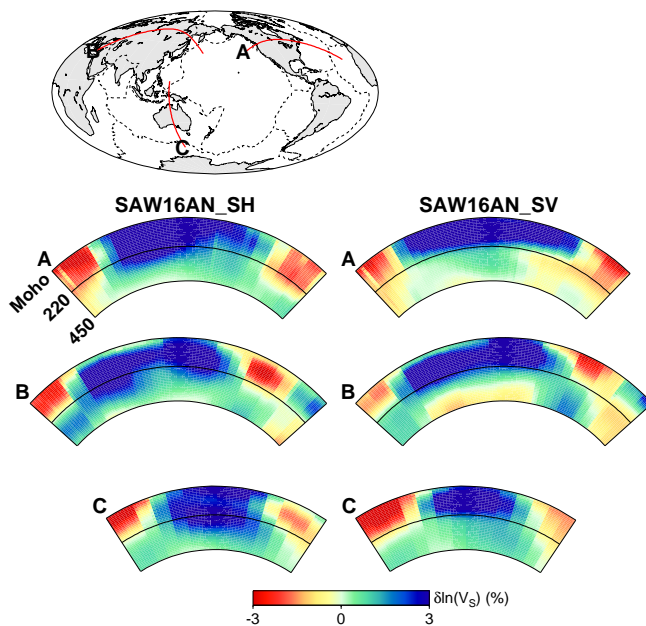


Figure 33.3: Depths cross-sections through 3 continents showing the *SH* (left) and *SV* (right) components of anisotropic model *SAW16AN*. The *SH* sections consistently indicate fast velocities extending to depths in excess of 220 km, whereas the *SV* sections do not.

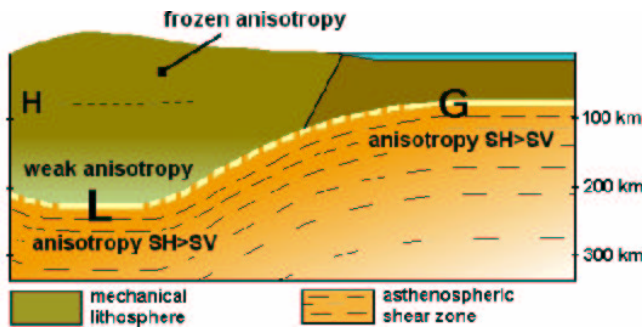


Figure 33.4: Sketch illustrating our interpretation of the observed anisotropy in relation to lithospheric thickness, and its relationship to Lehmann (L) and Gutenberg (G) discontinuities. The Hales discontinuity (H) is also shown. H is generally observed as a positive impedance embedded within the continental lithosphere in the depth range 60-80km. H and G may not be related.

Chapter 34

Large Scale Anisotropy Near the Core-Mantle Boundary from Global Waveform Inversion

Mark Panning and Barbara Romanowicz

0.1 Introduction

The Earth's core-mantle boundary (CMB) is both a thermal and chemical boundary layer between the solid silicate mantle and the fluid iron outer core. The mantle-side portion of this layer (D''), is therefore the site of dynamic processes that may involve both thermal and chemical heterogeneity at various scales. Additionally, this area also functions as a mechanical boundary layer for the convection of the overlying mantle, leading to intense deformation. This deformation can lead to detectable seismic anisotropy, either through the alignment of anisotropic crystals in the strain field or through the alignment of layering or inclusions of materials with strongly contrasting elastic properties (Karato, 1998; Kendall and Silver, 1996).

Anisotropy in D'' has been well established in several regions, including under the Pacific, northern Asia, Alaska, and central America, from the observation of S waves diffracting (S_{diff}) or reflecting (S_{cS}) at the CMB (Vinnik *et al.*, 1989; Kendall and Silver, 1996; Lay *et al.*, 1998). However, these studies only sample limited areas of D'' , and therefore interpretation is difficult. A more global picture of long-wavelength anisotropic D'' structure would clearly aid interpretation both in terms of dynamic flow modeling as well as mineral physics.

With this in mind we have adapted our global waveform tomography approach (Méglin and Romanowicz, 2000) to develop a 3D model of radial anisotropy throughout the mantle using a large dataset of three component time-domain waveforms of both surface and body waves.

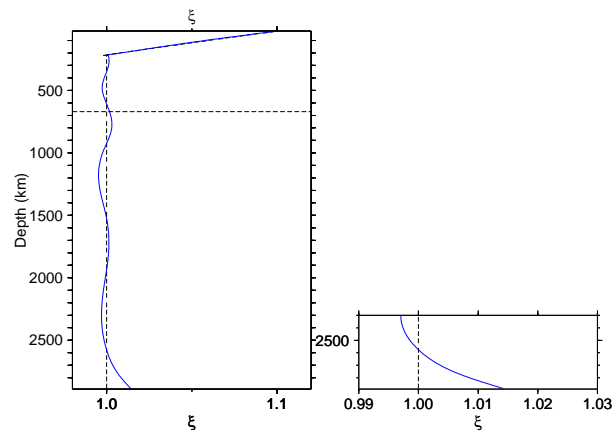


Figure 34.1: Radially symmetric values of ξ as a function of depth in the model. The values for PREM, the starting model, are shown by the dashed line, and the 670 discontinuity is shown by the dotted line. Notice the strong increase at the base of the mantle, similar but smaller in magnitude to that seen in the upper mantle.

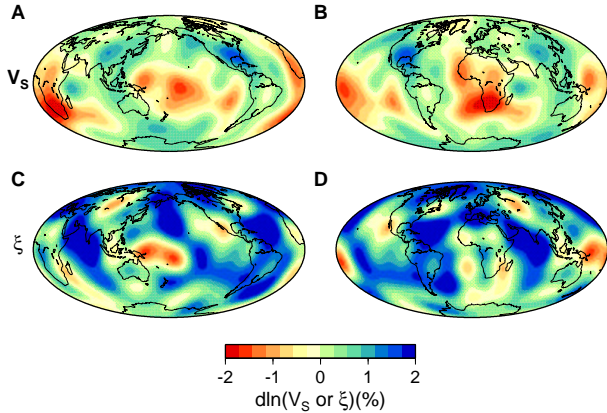


Figure 34.2: $\delta \ln V_S$ (A and B) and $\delta \ln \xi$ (C and D) shown at a depth of 2800 km. Slices are shown centered under the Pacific (A and C) and Africa (B and D).

0.2 D'' Anisotropic Model

The model is parameterized in terms of isotropic V_S and the anisotropic ξ parameter ($\xi = V_{SH}^2/V_{SV}^2$), which is directly related to radial anisotropy in shear velocity. In our model, D'' is characterized by a strong radially symmetric signature of radial anisotropy, as seen in the uppermost mantle in previous anisotropic models such as PREM (*Dziewonski and Anderson, 1981*). Similar to the uppermost 200 km of the mantle, this signature is a positive $\delta \ln \xi$, indicating that horizontally polarized shear velocity, V_{SH} , is faster than vertically polarized shear velocity, V_{SV} (Figure 34.1).

The 3D isotropic velocity imaged in D'' in this study is consistent with earlier tomographic models of shear velocity in this depth range (*Masters et al., 1996; Mégnin and Romanowicz, 2000*), and is characterized by a strong degree 2 component representing a fast ring surrounding two low velocity features (often called superplumes) centered beneath the central Pacific and Africa (Figure 34.2, A and B). In the ξ model, the strong degree 0 component appears to be limited to the lowermost 300 km (Figure 34.1, inset), but the regions that differ most from this average structure correlate well with the locations of the superplumes, with reduced values of $\delta \ln \xi$ under the central Pacific, Africa, and the south Atlantic, including patches with negative values ($V_{SV} > V_{SH}$).

The long-wavelength anisotropic features imaged in our model generally agree with more localized studies of D'' anisotropy. Specifically, these studies imaged areas with positive $\delta \ln \xi$ beneath central America and Alaska. The central Pacific appears to be more variable with some areas showing negative $\delta \ln \xi$ (*Lay et al., 1998*).

0.3 Conclusions

Our study extends to a global scale the results obtained so far for limited regional sampling of D''. The dominant $V_{SH} > V_{SV}$ found as one approaches the CMB suggests that the anisotropy observed in D'' is related to the dominant horizontal flow in a mechanical boundary layer, analogous to the larger signal observed in the uppermost 200 km of the mantle. As one approaches regions of upwelling, the direction of flow changes and results in a different signature of anisotropy, as manifested in our study under the central Pacific and Africa. In reality, anisotropy in these regions bordering the large scale upwellings may be much more complex and include tilting of the vertical axis of symmetry assumed in our modeling. This could lead to azimuthal anisotropy which we do not yet attempt to model.

Although our model does not determine the microscopic causes of the observed anisotropy, the results clearly suggest that the dynamics of D'' correspond with what would be expected in a boundary layer dominated by horizontal flow, and emphasize the unique character of the two superplume regions. Although mineral physics data are not yet available for the pressure and temperature conditions at the base of the mantle, our results suggest that similar relationships between anisotropic signature and flow prevail in the uppermost and lowermost mantle.

0.4 References

- Dziewonski, A.M., and D.L. Anderson, Preliminary reference Earth model, *Phys. Earth Planet. Int.*, 25, 297-356, 1981.
- Karato, S.-I., Some remarks on the origin of seismic anisotropy in the D'' layer *Earth, Planets, Space*, 50, 1019-1028, 1998.
- Kendall, J.-M. and P.G. Silver, Constraints from seismic anisotropy on the nature of the lowermost mantle, *Nature*, 381, 409-412, 1996.
- Lay, T., Q. Williams, E.J. Garnero, L. Kellogg, and M. Wyssession, Seismic wave anisotropy in the D'' region and its implications, in *The core-mantle boundary region*, M. Gurnis, M.E. Wyssession, E. Knittle, B.A. Buffett, Eds., Amer. Geophys. Union, pp. 219-318, 1998.
- Masters, G., H. Bolton, and G. Laske, Joint seismic tomography for P and S velocities: How pervasive are chemical anomalies in the mantle? *EOS Trans. AGU*, 80 S14, 1999.
- Mégnin, C., and B. Romanowicz, The 3D shear velocity of the mantle from the inversion of body, surface, and higher mode waveforms, *Geophys. Jour. Intl.*, 143, 709-728, 2000.
- Vinnik, L., V. Farra, and B. Romanowicz, Observational evidence for diffracted SV in the shadow of the Earth's core, *Geophys. Res. Lett.*, 16, 519-522, 1989.

Chapter 35

Towards Forward Modeling of 3D Heterogeneity in D'' region

Akiko To, Yann Capdeville and Barbara Romanowicz

0.1 Introduction

The presence of strong lateral heterogeneity in D'' is now well documented, and represents a problem for seismic modeling, when using standard ray or mode approaches, because of the theoretical limits of validity of these methods. Consequently, present tomographic models are only able to represent the large scale, smooth features of the structure. They may also not reflect the amplitudes of lateral variations accurately. We use a coupled normal mode/Spectral Element Method (SEM) (Capdeville *et al.*, 2003) to compute synthetic seismograms of Sdiff in the D'' part of a 3D tomographic model (SAW24B16, Mégnin and Romanowicz, 2000) down to a corner frequency of 1/12s. This coupled method is much faster than standard SEM, as the numerical part of the computation is restricted to the D'' region. The rest of the mantle is assumed 1D, and there the wavefield is computed using efficient normal mode summation.

0.2 Comparison between Observed and Synthetic Waveforms

We compare the synthetics thus obtained with observed waveforms for a collection of 16 deep earthquakes in the Western Pacific. The results from one of the events are shown in Figure 35.1 and Figure 35.2. For deep earthquakes, the effect of strong heterogeneity in the crust and upper mantle is avoided. Observed and synthetic travel time trends are very consistent, although in most cases the observed residuals are significantly larger. Waveform amplitudes are less consistent.

We manually modify the original SAW24b16, and by trial and error try to make a better model which fit the observations (Figure 35.3). The fit becomes better in a few traces, but in many cases it is difficult to fit both amplitude and travel times (Figure 35.4).

0.3 Modification of the Velocity Model by a Genetic Algorithm

We try to apply a genetic algorithm to travel time or waveform modeling in the D''. The advantages of GAs are that there is no damping and the output models are less controlled by the starting model. These properties are appropriate for modeling strong and complex heterogeneity in the D''. The defect of the method is the high computational cost. By limiting the target to a small local region on the CMB, we reduce the number of model parameters. We use ray theory, which is the most expedient method, to calculate travel times, and examine whether a GA is useful for modeling D''.

We choose a region of 28 x 28 degree in Northern Pacific, where 58 Sdiff ray paths diffract on CMB. We divided the region to 25 boxes. The number of initial ensemble of models is 30. After 15 to 16 generations, the model converged. We were able to get 35% of variance reduction. In future, we want to apply this method using NACT with the focusing and defocusing effect.

0.4 Comparison of Travel Time between Ray Theory and Coupled Mode/SEM

We compared the predicted Sdiff travel time between ray theory and Coupled Mode/SEM (Figure 35.5). Ray theory is a most expedient way to calculate travel times. However, it is an infinite frequency approximation and not appropriate to handle diffracting waves.

For negative residuals, both residuals are almost the same. They distribute around $y=x$ with in 1 to 2 second differences. However, for positive residuals, the predictions from ray theory give larger values by up to 4 seconds. This is consistent with theoretical predictions for the wave front healing effect (e.g. Nolet and Dahlen, 2000).

0.5 Acknowledgements

We thank the National Science Foundation for support of this research.

0.6 References

Capdeville Y., B. Romanowicz and A. To, Coupling Spectral Elements and Modes in a spherical earth: an extension to the “sandwich” case. *Geophys. J. Int.*, 154, 44-57, 2003

Capdeville Y., E. Chaljub, J.P. Vilotte and J.P. Montagner, Coupling the Spectral Element Method with a modal solution for Elastic Wave Propagation in Global Earth Models, *Geophys. J. Int.*, 153, 34-66, 2003

Dziewonski A.M., and D.L. Anderson, Preliminary reference Earth model, *Phys. Earth Planet. Inter.*, 25, 297-356, 1981.

Mégnin, C., and B. Romanowicz, The shear velocity structure of the mantle from the inversion of of body, surface and higher modes waveforms, *Geophys. J. Int.*, 143, 709-728, 2000

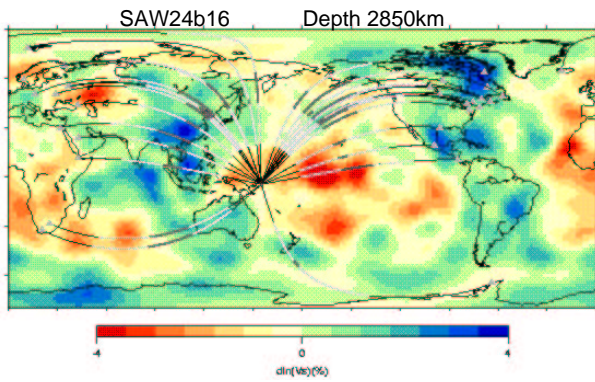


Figure 35.1: The ray paths distribution of Sdiff phase whose waveforms are shown in Figure 35.2. The event is 511.2km deep. Dark gray line: the diffracting part. Light gray line: The ray paths at the bottom 370km of the mantle, where 3D heterogeneity is included in synthetic waveform calculation.

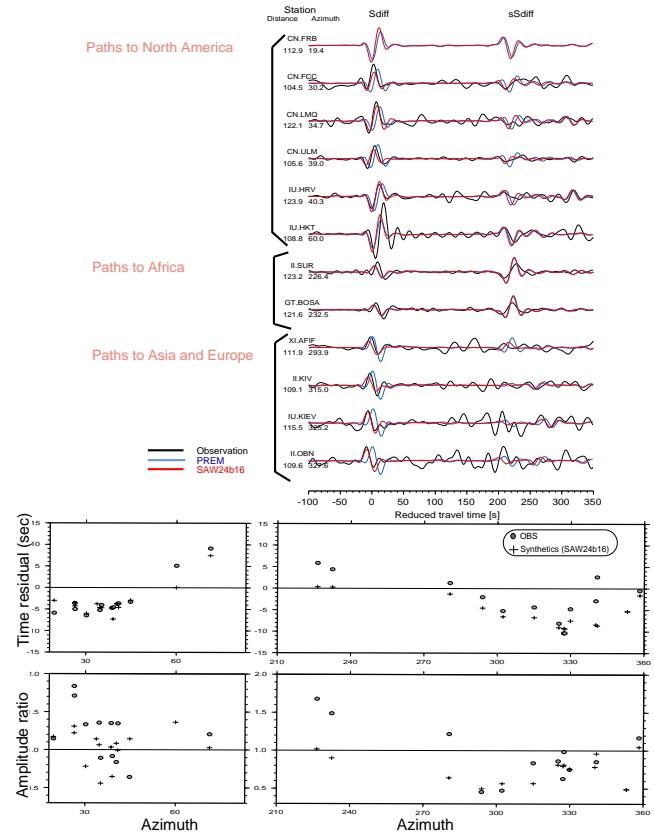


Figure 35.2: Top: Comparison of selected waveforms. Synthetic waveforms are made by couple model/SEM 3D models of the D” layer. The contribution of heterogeneity from rest of the mantle is calculated by ray theory. Bottom: Travel time residuals and maximum amplitude ratio relative to PREM (*Dziewonski and Anderson, 1981*) for all traces.

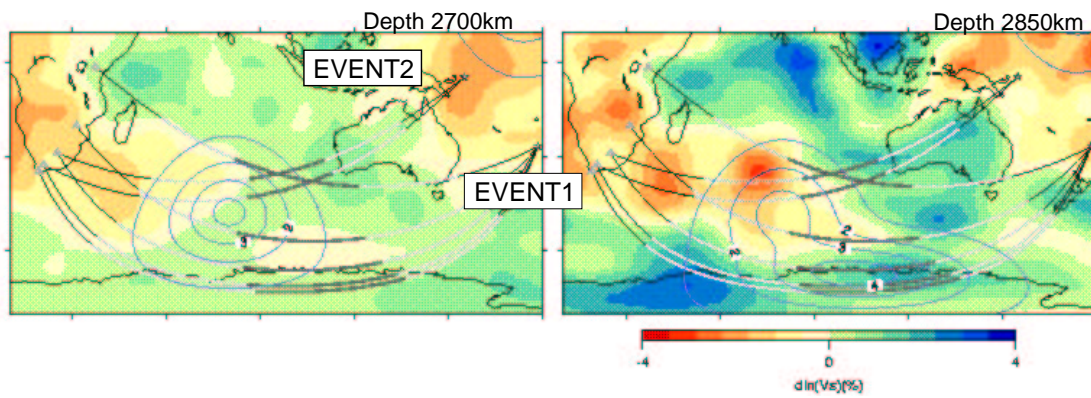


Figure 35.3: The background model is SAW24b16. The blue line shows the region where the anomaly is amplified in each depth. Numbers on the blue line show the factor of amplification. The waveforms calculated from this model is shown in Figure 35.4

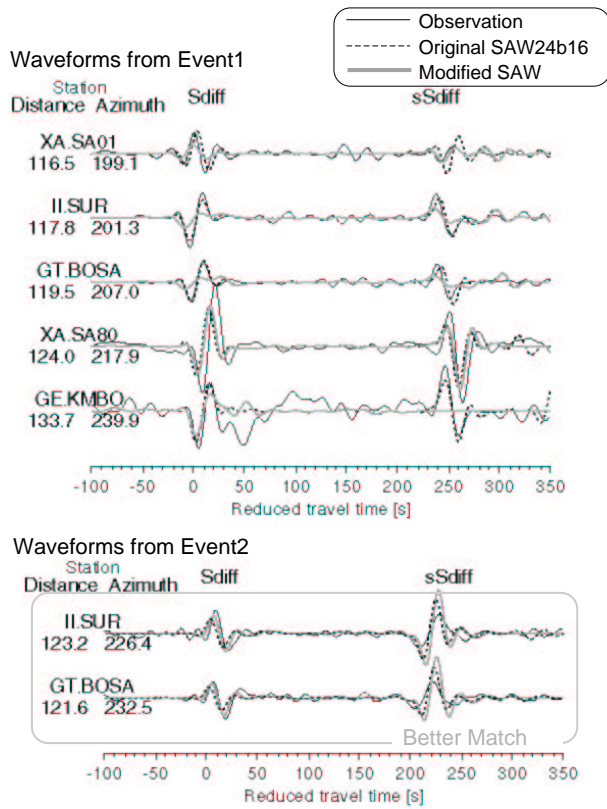


Figure 35.4: Waveforms from modified model as indicated in Figure 35.3. The two waveforms from Event2 show better fit between synthetics from the modified model and the observations. However, the fit between observation and synthetics become worse in the modified model for most of the waveforms from Event1.

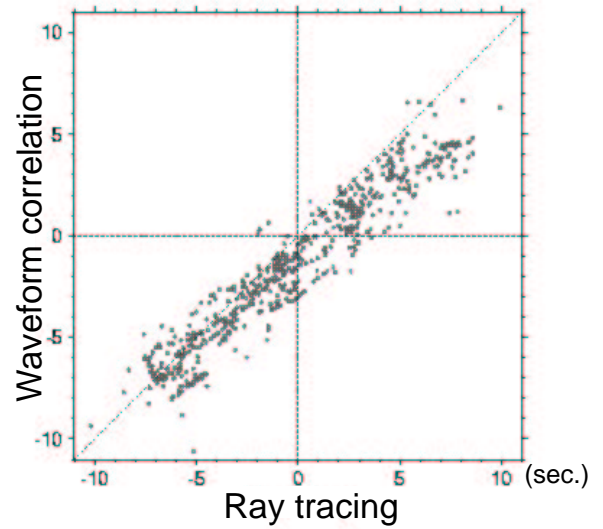


Figure 35.5: Synthetic travel time residuals with respect to PREM for 800 globally distributed Sdiff phase. The 3D velocity model used in the comparison is SAW24b16. The model has 3D heterogeneity in the bottom 370km of the mantle. The travel time residuals calculated using Coupled Mode/SEM are on Y axis. We cross correlated the waveforms constructed from the 3D model and PREM.

Chapter 36

Constraints on Density and Shear Velocity Contrasts at Inner Core Boundary

Aimin Cao and Barbara Romanowicz

0.1 Introduction

Density and shear velocity contrasts at the Inner Core Boundary (ICB) likely play a significant role in the character of the Earth's geodynamo and the evolution of the inner core. While studies of geodynamo have been made remarkable progress in the past decades (e.g., *Hewitt et al.*, 1975; *Backus*, 1975; *Gubbins*, 1977; *Loper*, 1978; *Mollett*, 1984; *Buffet et al.*, 1996; *Labrosse et al.*, 1997; *Stacey and Stacey*, 1999), the density and shear velocity contrasts at ICB are still controversial issues.

So far there are basically three distinct ways to constrain the density and shear velocity contrasts at the ICB. The first one is using the normal modes which are sensitive to the inner core structure (*Gilbert et al.*, 1973; *Gilbert and Dziewonski*, 1975; *Masters*, 1979). This technique suggested a density jump of 0.5-0.6 gcm^{-3} and a shear velocity jump of 3.45 kms^{-1} at the ICB.

The second one is using the body wave amplitude and waveform modeling of PKP and PKiKP. This technique suggested a density jump of 0-1.2 gcm^{-3} (*Hage*, 1983) and shear velocity jumps of 2.5-3.0 kms^{-1} (*Hage*, 1983), 2-4 kms^{-1} (*Cummins and Johnson*, 1988) at the ICB.

The third one is using body wave amplitude ratio of PKiKP to PcP. *Bolt and Qamar* (1970) first demonstrated this technique and estimated a maximum density jump of 1.8 gcm^{-3} at the ICB. *Souriau and Souriau* (1989) further constrained the density jump in the range of 1.35-1.6 gcm^{-3} . The latest estimation using this method was conducted by *Shearer and Masters* (1990) who suggested the density jump to be less than 1.0 gcm^{-3} and shear velocity jump to be greater than 2.5 kms^{-1} at the ICB.

Compared with the results derived from normal modes,

the constraint on the density contrast from body waves is much more rough and scattered. Therefore, right now the simulations of geodynamo usually refer to the density contrast derived from normal modes.

Nevertheless, a recent geodynamo study (*Stacey and Stacey*, 1999) explicitly pointed out that the inner core would not have existed 2 billion years ago if based on the density contrast at the ICB in the current Earth models. This is obviously against the paleomagnetic evidence, which shows that the Earth has sustained a magnetic field for at least 3 billion years (*McElhinny and Senanayake*, 1980). And the magnetic field is induced by the geodynamo that is powered by energy mainly associated with the cooling and gradual solidification of the core (*Gubbins*, 1977; *Loper*, 1978, 1991; *Gubbins et al.*, 1979). Fortunately this conflict can be readily settled if the density contrast at the ICB is somewhat higher than the assumed value in the seismic inner core models, because the energies of the geodynamo are proportional to the assumed density contrast (*Stacey and Stacey*, 1999). In this study, we try to constrain the density and shear velocity contrasts at the ICB by means of body wave PKiKP/PcP amplitude ratio taking advantage of the availability of recent high quality broadband data.

0.2 Data, Method, and Results

We systematically downloaded all of the broadband vertical component data in the epicentral distance range between 10° and 70°, from 1990 to 1999, stored in IRIS Data Management Center (DMC). Before searching for PKiKP and PcP arrivals, the event original time and hypocentral parameters were modified with the relocated earthquake catalog (*Engdahl et al.*, 1998) at first, and then theoretical arrivals (PcP, PKiKP, P, pP, PP, PPP, S, SS, and ScS) were labeled with reference to ak135 model (*Kennett et al.*, 1995) after the corrections for ellipticity. The additional 7 theoretical arrivals are the most

potential interfering sources for PcP and PKiKP phases. Then the seismograms were filtered in band pass 0.7-3 Hz (PKiKP phase is typically with 1 Hz frequency).

The picking quality is classified into three categories A, A-, and B. Quality A means there are very clear PKiKP and PcP phases within 5 seconds of their theoretical arrivals, there is no other theoretical arrival 20 seconds preceding the identified PKiKP or PcP phases (unless the potential interfering arrival can be verified from nodal plane), and the average peak-to-peak signal-to-noise ratio is less than 40%. Quality A- means there are clear PKiKP and PcP phase within 5 seconds of their theoretical arrivals, there is no other theoretical arrival 20 seconds preceding the identified PKiKP or PcP, and the average peak-to-peak signal-to-noise ratio is larger than 40%. Quality B means there is no observable PKiKP phase within 5 seconds of its theoretical arrival, but there is also no any other theoretical arrival 50 seconds preceding the theoretical PKiKP arrival, and PcP phase is very clear within 5 seconds of its theoretical arrival.

Based on above criteria, we collected 5, 16, and 62 Quality A, A-, and B data, respectively. One of the Quality A data is shown in Figure 36.1. The final measurements of PKiKP/PcP ratios were conducted directly with the peak-to-peak amplitudes of the identified PKiKP and PcP phases for Quality A and Quality A- data. For Quality B data, the maximum peak-to-peak amplitude 5 seconds around PKiKP theoretical arrival was read as the upper limit of the PKiKP amplitude (Figure 36.2).

0.3 Acknowledgements

We are grateful to the IRIS Data Management Center (DMC) and the network or station operators who contributed data to the DMC.

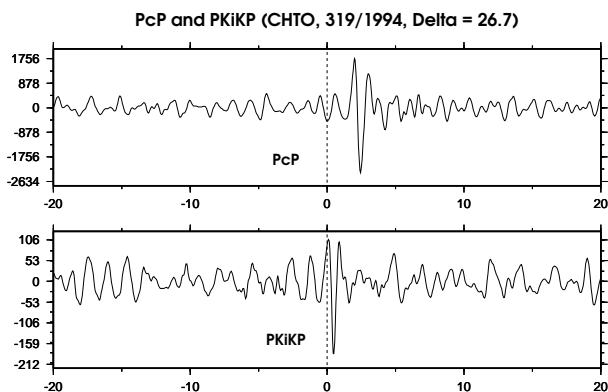


Figure 36.1: A Quality A example with very clear PKiKP and PcP phases. Dashed lines are the theoretical arrivals. The PKiKP/PcP ratio is 0.071.

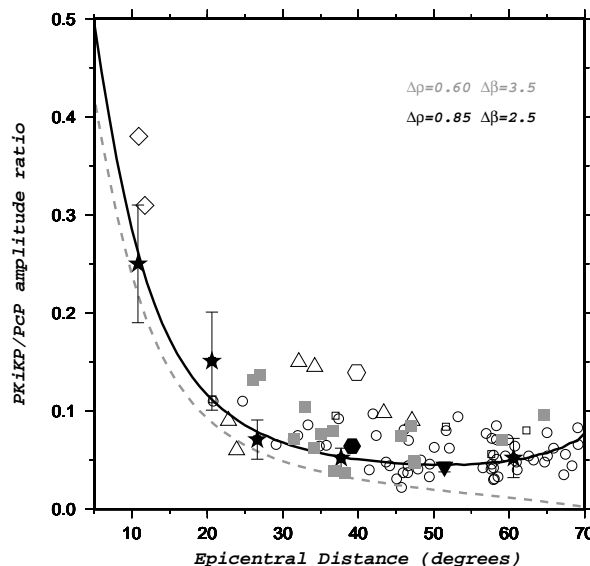


Figure 36.2: Measurements of PKiKP/PcP ratios. The stars denote the Quality A data; the grey squares denote the Quality A- data; and the open dots are the Quality B data. The curves are the theoretical functions of PKiKP/PcP with respect to PREM. Other open symbols are data from previous studies. Our current estimates favor a somewhat larger density jump at the ICB than for PREM

0.4 References

Backus, G.E., Gross thermodynamics of heat engines in deep interior of Earth, *Nat. Acad. Sci. USA*, *72*, 1555-1558, 1975.

Bolt, B.A., and A. Qamar, Upper bound to the density jump at the boundary of the Earth's inner core, *Nature*, *228*, 148-150, 1970.

Buffet, B.A., H.E. Huppert, J.R. Lister, and A.W. Woods, On the thermal evolution of the Earth's core, *J. Geophys. Res.*, *101*, 7989-8006, 1996.

Cummins, P., and L.R. Johnson, Short-period body wave constraints of properties of the Earth's inner core boundary, *J. Geophys. Res.*, *93*, 9058-9074, 1988.

Gilbert, F., A.M. Dziewonski, and J.N. Brune, An informative solution to a seismological inverse problem, *Proc. Natl. Acad. Sci.*, *70*, 1410-1413, 1973.

Gilbert, F., and A.M. Dziewonski, An application of normal mode theory to the retrieval of structural parameters and source mechanisms from seismic spectra. *Phil. Trans. R. Soc. Lond.*, *A278*, 187-269, 1975.

Gubbins, D., Energetics of the Earth's core, *J. Geophys.*, *43*, 453-464, 1977.

Hage, H., Velocity constraints for the inner core inferred from long-period PKP amplitudes, *Phys. Earth Planet. Inter.*, *31*, 171-185, 1983.

Hewitt, J.M., D.P. McKenzie, and N.O. Weiss, Dissipative heating in convective flows, *J. Fluid Mech.*, *68*, 721-738, 1975.

Labrosse, S., J.P. Poirier, and J.L. LeMouel, On cooling of the Earth's core, *Phys. Earth Planet. Int.*, *99*, 1-17, 1997.

Loper, D.E., The gravitationally powered dynamo, *Geophys. J. R. Astron. Soc.*, *54*, 389-404, 1978.

Masters, G., Observational constraints on the chemical and thermal structure of the earth's deep interior. *Geophys. J. R. Astron. Soc.*, *57*, 507-534, 1979.

Mollett, S., Thermal and magnetic constraints on the cooling of the Earth, *Geophys. J. R. Astron. Soc.*, *76*, 653-666, 1984.

Souriau, A., and M. Souriau, Ellipticity and density at the inner core boundary from sub-critical PKiKP and PcP data, *Geophys. J. Int.*, *98*, 39-54, 1989.

Stacey, F.D., and C.H.B. Stacey, Gravitational energy of core evolution: implications for thermal history and geodynamo power, *Phys. Earth Planet. Int.*, *110*, 83-93, 1999.

Chapter 37

Investigating Mantle's Density Resolution Using the Neighborhood Algorithm

Sébastien Rousset and Barbara Romanowicz

0.1 Introduction

Unlike travel times or waveform data, normal mode data are directly sensitive to density. However, the sensitivity kernels for density are much smaller than those for velocities, so the controversy about the possibility of resolution of the mantle's density is still vivid, especially since the publication of model SPRD6 (*Ishii and Tromp, 1999*). Several authors (*Resovsky and Ritzwoller, 1999, Romanowicz, 2001, Kuo and Romanowicz, 2002*) objected that density cannot yet be constrained and the controversy is still going.

However the inversion processes used by previous studies all rely on least-square inversions and require the use of a starting model, the choice of which is critical for the reliability of the results. Unlike this simple inversion scheme whose result is one "best" model, stochastic methods sample the parameter space, and their result is a set of models whose statistical properties reflect the likelihood function. In this study, in order to investigate the resolution, we use the Neighborhood Algorithm (*Sambridge 1999a,b*). The first step of the algorithm generates a set of models that samples the parameter space preferentially where the fit is better. The second step approximates the posterior probability density (ppd) in the parameter space using the previously generated set and quantitative information is extracted from this approximate ppd by a Bayesian approach.

0.2 Data Set and Parameterization

Our data set consists in a set of splitting coefficients (*Giardini and al., 1988*) inverted from normal mode spectra. These coefficients are linearly related to the aspheri-

cal structure of the Earth considered as a perturbation δx of the elastic parameter x of our reference model PREM, integrated over depth:

$$C_{st} = \int_0^a \left(\frac{\delta x}{x}\right)_{s,t}(z) K_s^x(z) dz \quad (37.1)$$

where s, t are degree and order in spherical harmonic expansion and a the Earth's radius. The sensitivity kernel K_s^x is calculated for the reference model and depends only on the degree s of the expansion.

A first data set used 63 well constrained modes (*He and Tromp, 1996* and *Resovsky and Ritzwoller, 1998*), corrected for the contribution of the crust; tests proved that the choice of the crustal model has little impact on the correction. Another data set adds a large number of upper mantle modes (*Widmer, 2002*); these modes are less well constrained but may improve the resolution in the upper mantle.

The Model Parameter Space

We search the degree 2 of the spherical harmonic expansion of the perturbation, with five coefficients $C_{2,0}$, $C_{2,1}$, $S_{2,1}$, $C_{2,2}$ and $S_{2,2}$. After trying various parameterizations for the radial variations of the perturbations, we selected a 7 (8 when more modes are included) cubic splines parameterization that gives naturally smooth variations.

To further reduce the number of parameters, only the shear velocity structure is fully discretized by splines. The bulk velocity and density structures are scaled to shear velocity structure with 3 scaling coefficients: lower mantle (bottom 2 splines), the middle mantle (3 splines) and one for the upper mantle (2 or 3 splines). Note that we are allowing lateral variations in the scaling coefficient as the scaling coefficients can be different for different spherical harmonic coefficients. Finally, the contribution of the topography of the CMB to the splitting of the

modes is also included. Parameter space dimension is then 14 (resp. 15).

0.3 Results

Sampling the Parameter Space

The neighborhood algorithm sampler (*Sambridge* 1999a) produces a set of models that sample the parameter space preferentially where the fit is good. Figure 37.1 shows 300 of the $C_{2,0}$ models for an exploration with 7 splines, V_p and ρ being scaled as described previously. While most models appear similar to the best model, a secondary minimum of misfit also appears that would be missed by a least square inversion. Note how the density in the uppermost mantle is poorly constrained in this case with a broad variety of values.

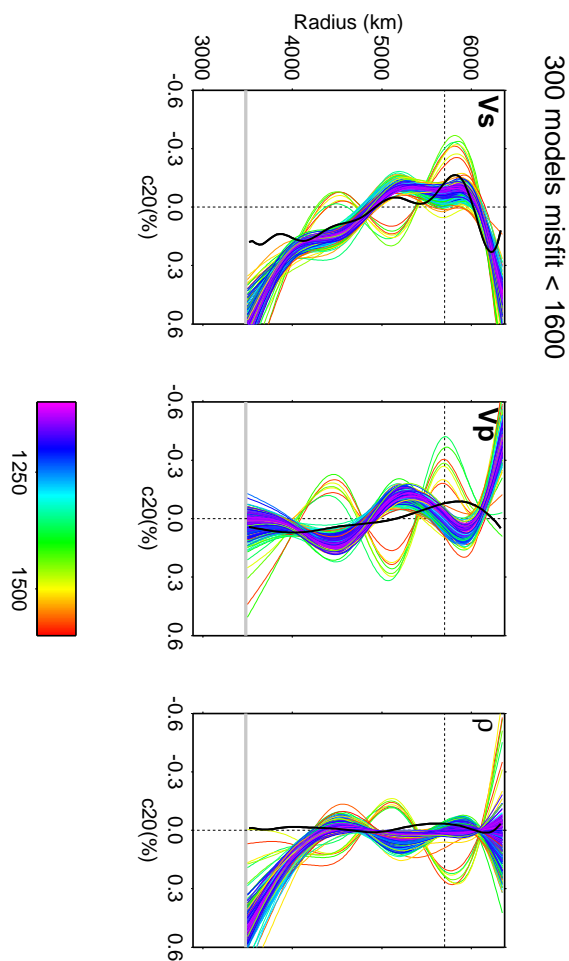


Figure 37.1: 300 good (low misfit), randomly selected $C_{2,0}$ models. The black line in front is the SPRD6 model, color/grey is given by the misfit between synthetic coefficients and data.

Quantitative Results from the Bayesian Integrals

The second program, the appraiser (*Sambridge* 1999b) uses a set of models to approximate the posterior probability density in the parameter space, and computes Bayesian integrals over this approximate ppd, allowing a quantitative use of the set of models. It is then possible to get the marginal probability for each parameter - or quantities based on these parameters. Such quantities have been estimated and are shown in Figure 37.2. The spherical harmonic coefficient shown is $S_{2,2}$, for a parameterization with 8 splines, scaling and topography of CMB. Note how the scaling values in the middle mantle (depth range 670 to 1800 km) are more poorly constrained than values in the lowermost and upper mantle. While the average shear velocity anomaly at these depths noted $\langle V_s \rangle_{mm}$ is well constrained, the scaling coefficient for bulk velocity anomaly V_p/V_s (for $d(\ln V_p)/d(\ln V_s)$) and density Rho/V_s can take a broad range of values.

0.4 Perspectives

Further work will include stability tests for the method. Preliminary tests show that the confidence intervals may not be completely reliable (!), especially for some parameters for which convergence of the Bayesian integrals is slow and/or currently insufficient. The addition of the modes of Widmer (*Widmer*, 2002) seems to help to constrain the perturbation in the upper mantle but the effect on other values remains to be investigated.

0.5 Acknowledgements

Special thanks to Malcolm Sambridge for making the NA software package available. This package, its very helpful online help and a short description of the algorithm can be found at <http://rses.anu.edu.au/~malcolm/na/na/html>. Figure 37.2 was made using a plotting utility of the package.

0.6 References

Giardini, D., X.D. Li and J. Woodhouse, Splitting functions of long-period normal modes of the Earth, *Jour. Geophys. Res.*, 93 B11, 1988.
 He, X. and J. Tromp, Normal-mode constraints on the structure of the Earth, *J. Geophys. Res.*, 102, 17981-17994, 1996.
 Ishii, M. and J. Tromp, Normal-Mode and Free-Air Gravity Constraints on Lateral Variations in Velocity and Density of Earth's Mantle, *Science*, 285, 1231-1236, 1999.
 Kuo, C. and B. Romanowicz, On the resolution of density anomalies in the Earth's mantle using spectral fitting of normal mode data, *Geophys. J. Inter.*, in press
 Romanowicz, B, Can we resolve 3D density heterogeneity in the lower mantle ?, *Geophys. Res. Lett.*, 28, 15, 1107-1110, 2001.

Resovsky, J. and M. Ritzwoller, Regularization uncertainty in density model estimated from normal mode data, *Geophys. Res. Lett.*, 26, 15, 2319-2322, 1999.

Resovsky, J. and M. Ritzwoller, New and refined constraints on 3D Earth structure from normal modes below 3mHz., *J. Geophys. Res.*, 103, 783-810, 1998.

Sambridge, M., Geophysical inversion with a neighborhood algorithm I - Searching a parameter space, *Geophys. J. Int.*, 138, 479-494, 1999.

Sambridge, M., Geophysical inversion with a neighborhood algorithm II - Appraising the ensemble, *Geophys. J. Int.*, 138, 727-746, 1999.

Widmer-Schmidrig, R., Application of regionalized multiplet stripping to retrieval of aspherical structure constraints, *Geophys. J. Int.*, 148, 1-18, 2002.

2-D Marginals

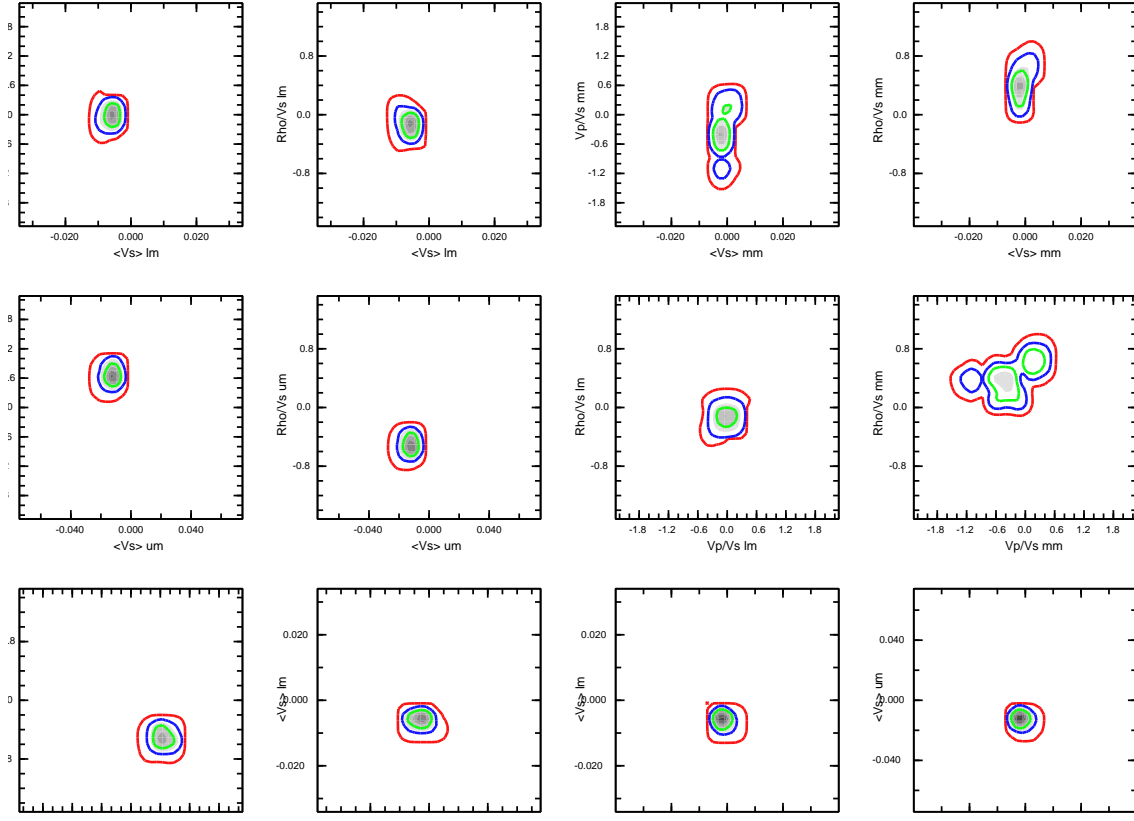


Figure 37.2: 2D marginal probabilities for the $S_{2,2}$ anomalies. Average of the shear velocity anomaly is noted $\langle V_s \rangle$, scaling coefficient from V_s to density (resp. V_p) ρ/ν_s (resp. V_p/V_s). lm stands for a value in the lower mantle, mm middle and um upper mantle.

Chapter 38

Thermochemical Convection Models of Lunar Evolution

Dave Stegman, Mark Richards, Mark Jellinek, John Baumgardner (LANL) yield a definite onset time at 4 Ga for the lunar core dynamo.

0.1 Introduction

We consider the early thermo-chemical history of the Moon and specifically address the question of how the Moon could have had an internally generated magnetic field suddenly 'switch-on' somewhat late in its evolution and then just as quickly 'switch-off'. It is commonly assumed the Moon never underwent mantle convection, given the majority of the surface geology is likely the original crust formed nearly simultaneous with the Moon. This can partially be explained by the fact that thermal evolution may well occur under the regime of stagnant-lid convection. Furthermore, there are a few tantalizing clues that perhaps the Moon possessed a brief, internally generated magnetic field (*Cisowski et al.*, 1983) and by implication, that the interior of the Moon was once convecting. Lunar samples returned from the Apollo missions provide a few which may contain a remnant thermal magnetism, possibly acquired during the Moon's 'magnetic era' (*Cisowski et al.*, 1983). These samples also reveal the near side of the Moon contains large areas flooded with volcanic material, the lunar mare. These mare (Latin for sea), erupted during a pulse of magmatism beginning 0.5 billion years after the Moon had formed and mostly ended after 1 billion years of activity. We have recently shown (*Stegman et al.*, 2003) that chemical overturn models suggested to explain the eruption of the Maria basalts may also account for the hitherto unexplained existence of a lunar magnetic field (core dynamo) at about the same time (3-4 billion years ago). We have chosen the approach of parallel computing to solve governing equations using the 3-D spherical finite element model (for which a considerable amount of effort was spent implementing a Lagrangian tracer algorithm). Our convection models bring together the main features of early lunar post-magma-ocean history, and carry an important testable prediction - that further analysis of

0.2 Generating an Early Lunar Dynamo

The Moon presently has no internally-generated magnetic field (i.e. core dynamo). However, paleomagnetic data combined with radiometric ages of Apollo samples record the existence of a magnetic field from approximately 3.9 to 3.6 Ga ('magnetic era') possibly due to an ancient lunar dynamo (*Cisowski et al.*, 1983; *Collinson*, 1993). A dynamo during this time period is difficult to explain (*Collinson*, 1993; *Stevenson*, 1983), because current thermal evolution models for the Moon (*Konrad and Spohn*, 1997) yield insufficient core heat flux to power a dynamo after 4.2 Ga. In Figure 38.1, we show that a transient increase in core heat flux following an overturn of an initially stratified lunar mantle may explain the existence and timing of an early lunar dynamo. Using a 3-D spherical convection model (*Baumgardner*, 1985), we show that a dense layer, enriched in radioactive elements ("thermal blanket"), at the base of the lunar mantle initially prevents core cooling, thereby inhibiting core convection and magnetic field generation. Subsequent radioactive heating progressively increases the buoyancy of the thermal blanket, ultimately causing it to rise back into the mantle. The removal of the thermal blanket, proposed to explain the eruption of thorium and titanium-rich lunar Mare basalts (*Hess and Parmentier*, 1995), plausibly results in a core heat flux sufficient to power a short-lived lunar dynamo.

0.3 Acknowledgements

We thank B. Buffett, C. Johnson, R. Jeanloz, M. Manga, and H-P. Bunge for helpful discussions. This work was supported by IGPP LANL, NASA CT project, NSF, Miller Institute for Basic Research. We dedicate this work to the memory of the late Stephen Zatman.

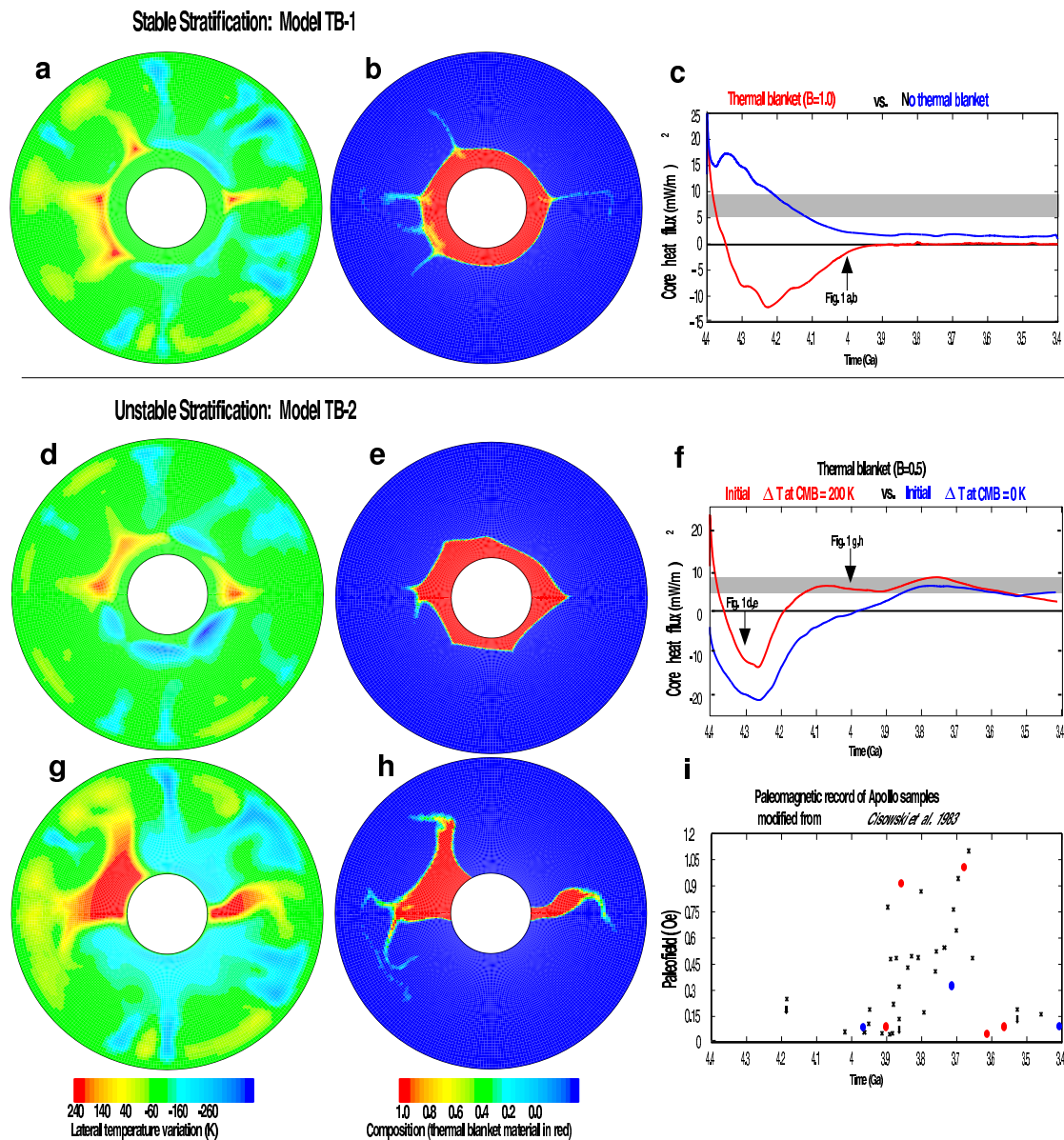


Figure 38.1: Thermochemical evolution models in stable (a-c) and unstable (d-h) thermal blanket regimes as seen in temperature (a,d,g), composition (b,e,h) and core heat flux (c,f) compared with paleomagnetic data (i). The equatorial cross-sections of (a) temperature and (b) composition for model TB-1 at 400 million years show thermal blanket material is too dense to become buoyant, but some entrainment occurs. However, equatorial cross-sections of temperature and composition for model TB-2 show a marginally stable thermal blanket interacting with mantle convection at 100 million years (d,e) and that by 400 million years (g,h) has sufficient thermal buoyancy to rise back towards lunar surface. Core thermal history (c) for reference model TB-0 shows heat flux values (blue line) well below adiabatic core heat flux (shaded region) while model TB-1 (red line) has nearly zero heat flux (black line). Such core heat flux values ranging between the black line and shaded region indicates a thermally stratified core, in which all core heat loss is by conduction and no dynamo is supported. A core heat flux equal to or above the shaded region indicates core convection and likely occurrence of a dynamo, as seen in models TB-2,3 (f). Paleointensity measurements (i) from Apollo samples (modified from Cisowski et al. 1983) where dots indicate absolute paleointensity measurements (Thellier-Thellier method in red, other techniques in blue) and crosses indicate scaled normalized relative paleointensities. In our models, asymmetric thermal blanket removal leads to a localized distribution of partially-molten thermal blanket material at relatively shallow mantle depths, confirming a plausible explanation for the eruption of high-Th, high-Ti mare basalts, similar to the models of *Zhong et al., 2000*. Our models make no attempt to evaluate melt transport to the surface.

0.4 References

Collinson, D. W., Magnetism of the Moon - A lunar core dynamo or impact magnetization? *Surv. Geophys.*, *14*, 89-118, 1993.

Stevenson, D.J., Planetary magnetic fields, *Rep. Prog. Phys.*, *46*, 555-557, 1983.

Hess, P.C. and E.M. Parmentier, A model for the thermal and chemical evolution of the Moon's interior: implications for the onset of mare volcanism, *Earth Planet. Sci. Lett.*, *134*, 501-514, 1995.

Konrad, W. and T. Spohn, Thermal history of the moon - Implications for an early core dynamo and post-accretionary magmatism, *Adv. Space Res.*, *19*, 1511-1521, 1997.

Baumgardner, J.R., Three dimensional treatment of convective flow in the Earth's mantle, *J. Stat. Phys.*, *39*, 501-511, 1985.

Stegman, D.R., A.M. Jellinek, S.A. Zaitman, J.R. Baumgardner, and M.A. Richards, An early lunar core dynamo driven by thermochemical mantle convection, *Nature*, *421*, 143-146, 2003.

Zhong, S., E.M. Parmentier, and M.T. Zuber, A dynamic origin for the global asymmetry of lunar mare basalts, *Earth Planet. Sci. Lett.*, *177*, 131-140, 2000.

Part IV

Appendices

